

Investigation of mineral-mediated photochemical processes and the development of an automated TD-GC-FID/MS system coupled to an atmospheric reaction chamber

by

Mario Schmidt

A thesis submitted in partial fulfillment of the requirements for the degree of

Master of Science

Department of Chemistry
University of Alberta

© Mario Schmidt, 2019

Abstract

The atmospheric aqueous phase is an important reaction medium for the processing of both biogenic and anthropogenic organic compounds. Particularly, the formation of aqueous-phase secondary organic aerosol (aqSOA) and the influence on ambient air quality and regional climate are of increasing interest compared to data from comparable gas-phase processes contributing to SOA formation.

A fundamental component for the investigation of atmospheric aqueous-phase reactions is the availability of a photochemical reactor. For this purpose, a multi-position photoreactor was designed and characterized with detailed comparisons of exchangeable sample adaptors regarding their stirring performance for the application in heterogeneous, aqueous-phase photochemistry.

The developed photoreactor was applied for the investigation of a new, mineral-mediated, photochemical formation mechanism of organosulfates (OS) in the aqueous phase using methacrolein, a major atmospheric oxidation product of isoprene, an abundant biogenic volatile organic compound, as precursor. Since organosulfates are known to make a significant contribution to particulate matter (PM) mass loadings and SOA, the OS formation was studied under several conditions, such as the illumination time, catalyst loading, sulfate concentration,

counterion identity, and methacrolein concentration.

SOA formation in the atmosphere also occurs from gas-phase precursors, the concentrations of which can be monitored with both optical spectroscopic techniques, such as differential optical absorption spectroscopy (DOAS) and via gas chromatographic (GC) separation and hyphenation techniques, such as flame ionization detection (FID) and mass spectrometry (MS). GC-MS is a powerful tool for the analysis and structural elucidation of gas-phase species. However, volatile organic compounds and related atmospheric oxidation products are usually detected at low concentration ranges, which require an analyte preconcentration and thermal desorption (TD) step prior to a gas chromatographic analysis. Consequently, a thermal desorption unit for GC-FID/MS coupling was designed, characterized and further developed to achieve an automated TD-GC-FID/MS system for a continuously operated analysis process of samples generated in smog chamber studies.

Preface

This thesis is based on manuscripts that have been published in or are in preparation for submission for publication. Consequently, there may be some overlap in material which is presented throughout the thesis. All manuscripts included in this thesis were written by Mario Schmidt, with critical comments provided by Sarah A. Styler. Contributions of any other authors are described below.

Chapter 1: Introduction

This chapter was written by Mario Schmidt with critical comments from Sarah A. Styler.

Chapter 2: Photochemical reactor development

All experiments for this chapter were performed by Mario Schmidt and Jiahui Zhou, under guidance of Mario Schmidt. The mechanical production of the photoreactor was performed by Vincent Bizon with contributions of Dieter Starke and Dirk Kelm. An electronic reactor control unit was built by Allan Chilton. Design considerations and the customized production of glass reactor parts were contributed by Jason Dibbs. This chapter was written by Mario Schmidt with contributions from Jiahui Zhou, and critical comments from Sarah A. Styler.

Chapter 3: Mineral-mediated photochemical organosulfate formation

All experiments for this chapter were performed by Mario Schmidt with fundamental experimental contributions from Shawn M. Jansen van Beek to establish the experimental design. SEM-EDS and XRD analyses were performed by Maya Abou-Ghanem with support from Anton O. Oliynyk for XRD data analysis. Electron microprobe analysis was performed by Andrew J. Locock. This chapter was written by Mario Schmidt and Sarah A. Styler.

Published as: Mario Schmidt, Shawn M. Jansen van Beek, Maya Abou-Ghanem, Anton O. Oliynyk, Andrew J. Locock, and Sarah A. Styler (2019). "Production of Atmospheric Organosulfates via Mineral-Mediated Photochemistry" *ACS Earth and Space Chemistry* 3(3): 424-431.

Chapter 4: TD-GC-FID/MS system

The experimental approach and final thermal desorption unit design was developed by Mario Schmidt. The mechanical production and additional design suggestions were contributed by Dieter Starke. All experiments were performed by Mario Schmidt. This chapter was written by Mario Schmidt with critical comments from Sarah A. Styler.

Chapter 5: Conclusions and future directions

This chapter was written by Mario Schmidt with critical comments from Sarah A. Styler.

“He who has a why to live for can bear with almost any how.”

Friedrich Wilhelm Nietzsche

Acknowledgements

First, I would like to thank my supervisor, Dr. Sarah A. Styler, for all her contributions to this thesis and to my entire MSc research. I would also like to give special thanks for my supervisor committee members, Dr. James Harynuk and Dr. Liang Li. I also thank Dr. Wolfgang Jäger for serving on my final examination committee. Furthermore, I had the chance to work with great, outstanding, highly motivated students including Shawn M. Jansen van Beek and Jiahui Zhou. Especially, I want to thank my group members Ming Lyu, Maya Abou-Ghanem and previous group members including Patrick Milner for realizing a friendly, supportive and organized research atmosphere. Furthermore, I am very thankful for Boyang Zhao's support related to chamber experiments. I also want to thank the extraordinarily knowledgeable, experienced and foremost very reliable staff from the chemistry department machine shop. I would not have been able to finish my degree without their great support. Hence, I am very thankful for all technical contributions and advice from Dieter Starke, Paul Crothers, Vincent Bizon and Dirk Kelm. There was no time when I was not impressed by their ability to troubleshoot research related problems. Furthermore, I want to thank Wayne Moffat for his advice and expertise regarding any questions that have been related to analytical instrumentation, including his supportive team member Jennifer Jones. Moreover, the team of the mass spectrometry service laboratory (Randy Whittal, Bela Reiz, Jing Zheng, Angelina Morales-Izquierdo) always assisted with any problems related to method development using LC-MS/MS, which was very much appreciated. I am also thanking the electronic shop team (Allan Chilton, Kim Do, Andrew Hillier) for all support provided during the development of the thermal desorption unit. Jason Dibb's support as specialist for glass blowing was highly appreciated during the photoreactor development. Finally, none of this would have been possible without the unconditioned love, support and encouragement from my family including my incredibly supportive wife Claudia, my parents, Frank and Christine, and my parents in law, Hans-Rainer and Doris. This is your achievement as much as mine.

Contents

Abstract	ii
Preface	iv
Acknowledgements	vii
List of Tables	xii
List of Figures	xvii
Abbreviations	xviii
1 Introduction	1
1.1 The atmosphere - endless space or box ?	2
1.2 Atmospheric emissions and pollution	5
1.2.1 Gas-phase emissions	5
1.2.2 Particle-phase emission	7
1.2.3 Particle properties	8
1.3 Chemistry of the atmosphere	11
1.3.1 Gas-phase chemistry	11
1.3.2 Particle-phase chemistry	14
1.3.2.1 Traditional and new pathway for SOA formation . .	15
1.3.2.2 Aqueous dust-mediated photochemistry	16
1.4 Impacts on human health and climate	18
1.5 Laboratory atmospheric simulation approaches & analytical techniques	20
1.5.1 Atmospheric reaction chambers	20
1.5.2 Differential optical absorption spectroscopy	22
1.5.3 Thermodesorption gas chromatography	25
1.5.4 Photochemical reactor development	27

1.6	Thesis introduction	28
2	Development of a multi-position photochemical reactor	30
2.1	Introduction	32
2.2	Experimental methods	34
2.2.1	Experimental apparatus	34
2.2.1.1	Photochemical reactor description	34
2.2.1.2	Reaction vessels	35
2.2.1.3	Temperature and stirring control	36
2.3	Reactor characterization	37
2.3.1	Chemical actinometry	37
2.3.2	Experimental procedure	38
2.4	Chemicals and materials	39
2.5	Results and discussion	39
2.5.1	Temperature stability	39
2.5.2	Multi-position stirring performance	40
2.5.3	Influence of the reactor cover	43
2.5.4	Efficacy of large particle suspension	45
2.6	Summary	46
3	Mineral-mediated photochemical organosulfate formation	48
3.1	Introduction	50
3.2	Materials and methods	51
3.2.1	Experimental apparatus	51
3.2.2	Experimental procedure	52
3.2.3	OS quantification and analysis	53
3.2.4	Sample collection, preparation, and characterization	53
3.2.5	Chemicals	54
3.3	Results and discussion	55
3.3.1	TiO ₂ -catalyzed production of HAS: influence of illumination time and catalyst loading	55
3.3.2	TiO ₂ -catalyzed production of HAS: sulfate concentration de- pendence and cation effects	57
3.3.3	TiO ₂ -catalyzed production of additional OS products: MACR concentration dependence and cation effects	59

3.3.4	Unexpectedly high OS production in the presence of natural mineral samples	62
3.3.5	Mineral-catalyzed OS production: implications for catalysis and atmospheric aerosol composition	63
4	TD-GC-FID/MS system	65
4.1	Introduction	66
4.2	Thermal desorption unit	69
4.2.1	Design considerations and technical design	69
4.2.2	Trap tube preparation	71
4.2.3	Electronic control and temperature monitoring	73
4.3	TD-GC-FID/MS system and chamber coupling	76
4.3.1	Instrument flow path	76
4.3.2	Analytical instrumentation and related supplies	79
4.3.3	Instrument characterization and first application	81
4.4	Summary	85
5	Conclusions and future directions	87
5.1	Photochemical reactor development	88
5.2	Mineral-mediated photochemical organosulfate formation	89
5.3	TD-GC-FID/MS system coupled to an atmospheric reaction chamber	90
	Bibliography	94
A	Photochemical reactor development	124
A.1	Supplementary Figures	125
B	Mineral-mediated photochemical organosulfate formation	145
B.1	Experimental and sample characterization details	145
B.1.1	Solar simulator and photochemical reactor	145
B.1.2	2-Nitrobenzaldehyde (2-NB) chemical actinometry	145
B.1.3	Control experiments and quality assurance / quality control (QA/QC)	146
B.1.4	Sample preparation and characterization	147
B.1.4.1	Sample preparation	147
B.1.4.2	Surface area determination	148
B.1.4.3	Electron microprobe analysis	148

B.1.4.4	Scanning electron microscopy with energy disperse X-ray spectroscopy (SEM-EDS) analysis . . .	149
B.1.4.5	X-ray diffraction (XRD) analysis	149
B.1.5	Synthesis of calibration standards	150
B.1.5.1	Potassium hydroxyacetone sulfate	150
B.1.5.2	Potassium propyl sulfate (adapted from a published synthesis of sodium ethyl sulfate[174]) . . .	150
B.1.6	Chemicals	151
B.2	2 Supplementary figures and tables	152
C	TD-GC-FID/MS system	174
C.1	Instrument Operation	174
C.2	Supplementary figures and schemes	177
D	Conclusions and future directions	184
D.1	Supplementary figures	184

List of Tables

1	Abbreviations.	xix
1.1	Common atmospheric absorbers and non-absorbers in the region of 3000Å to 7000Å, adapted from [54].	12
1.2	Categories of respiratory and heart diseases related to air pollution, adapted from [7, 77].	19
1.3	Common analytical instrumentation for chamber experiments, adapted from [84].	22
3.1	Proposed structures for the OS observed in the present experiments.	61
4.1	Overview of essential methodological parameters regarding conditions used for the application of gas chromatographic separation (GC) and detection via flame ionization (FID) and mass spectrometry (MS).	80
B.1	Summary of mass spectrometric parameters.	170
B.2	Specific surface areas (BET; m ² g ⁻¹) of three of the samples employed in these experiments.	170
B.3	Elemental composition of a) anatase, b) ilmenite, and c) mica samples obtained via electron microprobe analysis	171
B.3	Elemental composition of a) anatase, b) ilmenite, and c) mica samples obtained via electron microprobe analysis	172
B.3	Elemental composition of a) anatase, b) ilmenite, and c) mica samples obtained via electron microprobe analysis	173
C.1	Overview of the parameters for generating toluene gas-phase concentrations between 0.2 ppm and 1.0 ppm.	182

List of Figures

1.1	Layers of the atmosphere: troposphere, stratosphere, mesosphere, thermosphere	2
1.2	One box model showing four atmospheric processes: emission, chemical production, chemical loss and deposition	4
1.3	Atmospheric particle properties (particle number, surface area and volume) in dependence on the particle diameter, adapted from [47].	9
1.4	Major constituent contributions to PM ₁₀ , PM _{2.5} and PM _{coarse} from urban regions in central Europe, adapted from [49].	10
1.5	Ground level ozone production cycle	13
1.6	Simplified SOA formation pathways by (traditional) gas-particle partitioning and aqueous phase reactions.	16
1.7	Scheme for TiO ₂ -surface mediated hydroxyl radical formation in the aqueous environment.	18
1.8	Simplified chamber setup to generally introduce chamber experiments, adapted from [85].	21
1.9	DOAS scheme with possible factors causing a drop in light intensity	24
1.10	Chemical structure of Tenax TA (poly(2,6-diphenylphenylene oxide)).	27
2.1	Exploded view drawing of photoreactor setup.	35
2.2	Overview of photoreactor control showing the temperature and stirring control.	37
2.3	Linear fit for the loss of the 10 μM chemical actinometer 2-nitrobenzaldehyde (2NB) in the photochemical reactor (9-sample adaptor).	41
2.4	Comparison of <i>j</i> (2NB) values determined after illumination of 10 μM 2NB solutions and TiO ₂ (0.25 mg mL ⁻¹) suspensions using the 9-sample adaptor configuration.	43

2.5	Comparison of $j(2\text{NB})$ values determined after illumination of 10 μM 2NB solutions and TiO_2 (0.25 mg mL^{-1}) suspensions using the 1, 4 and 9-sample adaptor configurations.	45
2.6	Comparison of position dependent $j(2\text{NB})$ values determined after illumination of a 10 μM 2NB-road dust suspension.	46
3.1	Time-dependent HAS production from MACR (10 mM) in illuminated suspensions of TiO_2 in aqueous Na_2SO_4 (1 M; adjusted to pH 5) or $(\text{NH}_4)_2\text{SO}_4$ (1 M) in the absence of TiO_2	56
3.2	HAS production from MACR (10 mM) in illuminated (30 min) suspensions of TiO_2 (0.5 mg mL^{-1}) in aqueous Na_2SO_4 (1 M; adjusted to pH 5) or $(\text{NH}_4)_2\text{SO}_4$ (1 M).	57
3.3	OS production from MACR in illuminated (30 min) suspensions of TiO_2 (0.5 mg mL^{-1}) in aqueous Na_2SO_4 (1 M; adjusted to pH 5) or $(\text{NH}_4)_2\text{SO}_4$ (1 M).	60
3.4	Production of HAS (mg L^{-1} ; m/z 153) and other OS (peak area) from MACR (10 mM) in illuminated (30 min) suspensions of TiO_2 and natural mineral samples (0.5 mg mL^{-1}) in aqueous Na_2SO_4 (1 M; adjusted to pH 5).	62
4.1	Thermal desorption trap overview (A) with detailed trap tube section (B)	71
4.2	Schematic and step-wise overview of the customized production of a sorbent packed thermal desorption tube	73
4.3	Overall scheme of the integrated process automation.	75
4.4	Overview of the parameter dependent process automation.	76
4.5	Flow scheme of the whole TD-GC-FID/MS system.	78
4.6	Presentation of the dependence of the trap tube temperature on the location of the temperature sensor and the positions of the 10-port valve.	82
4.7	Calibration curve for the gas-phase sampling of toluene using a calibration gas generator.	83
4.8	Comparison between DOAS and TD-GC-FID/MS regarding the monitoring of a toluene decay inside the smog chamber.	85
5.1	Visual representation of all three exchangeable sample adaptors with one, four or nine sample positions.	89

5.2	Categorized aspects for future projects on the developed TD-GC-FID/MS system.	93
A.1	Cross-section of the reactor setup.	125
A.2	Exploded view drawing of the stirring mechanism and sample adaptor.	126
A.3	Overview of the photoreactor control unit.	127
A.4	Chromatograms of time-dependent 2NB (10 μM) decay experiments without TiO_2	128
A.5	Temperature monitoring of illuminated (400 s) and non-illuminated (400 s) reactions vessels.	129
A.6	Temperature dependence on illumination inside all reaction vessels of the 4 sample configuration.	130
A.7	Temperature dependence on illumination inside all reaction vessels of the 9 sample configuration.	131
A.8	Comparison of $j(2\text{NB})$ values determined after illumination of 10 μM 2NB solutions and TiO_2 (0.25 mg mL^{-1}) suspensions using the 4-sample adaptor configuration.	132
A.9	Linear fit of $\ln(c/c_0)$ vs illumination time for the single sample adaptor with and without TiO_2 in 2NB solution.	133
A.10	Linear fit of $\ln(c/c_0)$ vs illumination time for the 4 sample sample adaptor without TiO_2 in 2NB solution.	134
A.11	Linear fit of $\ln(c/c_0)$ vs illumination data for the 4 sample adaptor with TiO_2 in 2NB solution.	135
A.12 a)	Linear fit for $\ln(c/c_0)$ vs illumination time regarding triplicate experiments in position 1 of the 9 sample adaptor without TiO_2 . . .	136
A.12 b)	Linear fit for $\ln(c/c_0)$ vs illumination time regarding triplicate experiments in position 2 of the 9 sample adaptor without TiO_2 . .	137
A.12 c)	Linear fit for $\ln(c/c_0)$ vs illumination time regarding triplicate experiments in position 3 of the 9 sample adaptor without TiO_2 . .	138
A.12 d)	Linear fit for $\ln(c/c_0)$ vs illumination time regarding triplicate experiments in position 4 of the 9 sample adaptor without TiO_2 . .	139
A.12 e)	Linear fit for $\ln(c/c_0)$ vs illumination time regarding triplicate experiments in position 5 of the 9 sample adaptor without TiO_2 . .	140
A.12 f)	Linear fit for $\ln(c/c_0)$ vs illumination time regarding triplicate experiments in position 6 of the 9 sample adaptor without TiO_2 . .	141

A.12 g) Linear fit for $\ln(c/c_0)$ vs illumination time regarding triplicate experiments in position 7 of the 9 sample adaptor without TiO_2 . . .	142
A.12 h) Linear fit for $\ln(c/c_0)$ vs illumination time regarding triplicate experiments in position 8 of the 9 sample adaptor without TiO_2 . . .	143
A.13 Linear fits for $\ln(c/c_0)$ vs illumination time regarding single replicate experiments in positions 1,2,3,5,6,7,8 and a triplicate experiment in position 4 of the 9 sample adaptor with TiO_2	144
B.1 Schematic drawing of the photochemical reactor employed in experiments.	152
B.2 Spectral irradiance of the solar simulator employed in the present study at a working distance of 203 nm as compared to the AM1.5 reference spectrum.	153
B.3 Loss of the chemical actinometer 2-nitrobenzaldehyde (2-NB) in our photochemical reactor as a function of illumination time.	154
B.4 Recovery of hydroxyacetone sulfate (HAS) and propyl sulfate (PpS) using the MeOH cleanup procedure.	155
B.5 Representative chromatograms showing organosulfate products.	156
B.6 External calibration curve for hydroxyacetone sulfate (HAS).	157
B.7 Analysis of Edmonton road dust using scanning electron microscopy with energy dispersive X-ray spectroscopy (SEM-EDS) analysis.	158
B.8 a) XRD diffractograms of anatase	159
B.8 b) XRD diffractograms of ilmenite	160
B.8 c) XRD diffractograms of mica	161
B.8 d) XRD diffractograms of Edmonton road dust	162
B.9 ^1H and b) ^{13}C NMR spectra of hydroxyacetone sulfate in D_2O	163
B.10 ^1H and b) ^{13}C NMR spectra of propyl sulfate in D_2O	164
B.11 High-resolution mass spectra of hydroxyacetone sulfate and propyl sulfate synthesized standards.	165
B.12 Product ion scans for hydroxyacetone sulfate, propyl sulfate, the m/z 253 organosulfate.	166
B.13 TiO_2 -catalyzed (0.5 mg mL^{-1}) loss of hydroxyacetone sulfate (HAS; 7 ppm) in the presence and absence of methacrolein (10 mM) as a function of illumination time.	167

B.14	Formation of hydroxyacetone sulfate (m/z 153) as a function of methacrolein concentration.	168
B.15	Time-dependent production of a set of organosulfates with m/z 253.	169
C.1	Illustrated description of the Arduino UNO R3 board wiring to establish a relay-controlled heating mechanism.	177
C.2	Arduino sketch (code) for the relay-controlled heating mechanism presented in Figure C.1	178
C.3	Illustrated description of the Arduino UNO R3 board wiring to establish a trap tube temperature measurement.	179
C.4	Arduino sketch (code) for the temperature acquisition procedure presented in Figure C.3.	180
C.5	Exemplary FID chromatogram, total ion current for the injection of a preconcentrated toluene with a corresponding EI mass spectrum.	181
C.6	Exponentially fitted graphs for the decay of toluene in the atmospheric reaction chamber, monitoring with DOAS and TD-GC-FID/MS.	183
D.1	Possible design for a simultaneous TD trap loading and desorption process to increase the time resolution.	185
D.2	Optional addition of a dry purge valve to remove trapped water vapor.	186
D.3	Schematic description of the introduction of an 8-port valve for loop-mediated internal standard injection connected to the established 10-port valve. Shown is a double trap, double loop system.	187

Abbreviations

Table 1: Abbreviations.

Abbreviation	Explanation
2NB	2-Nitrobenzaldehyde
ATX	Advanced Technology eXtended
BET	Brunauer-Emmett-Teller
BTEX	Benzene, toluene, ethyl benzene, xylene
BVOC	Biogenic, volatile, organic compound
CCN	Cloud condensation nuclei
DIN	Deutsches Institut für Normung
DOAS	Differential optical absorption spectroscopy
EDS	Energy-dispersive spectroscopy
EPA	Environmental Protection Agency
FID	Flame ionization detection
FT-IR	Fourier transform infrared
GC	Gas chromatography
HAS	Hydroxyacetone sulfate
HEPA	High efficiency particulate air filter
HPLC	High performance liquid chromatography
ID	Inner diameter
MACR	Methacrolein
MRM	Multiple reaction monitoring
m/z	Mass-to-charge ratio
MS	Mass spectrometry
NiCr	Nickel-chromium
NMR	Nuclear magnetic resonance
NTC	Negative temperature coefficient
OD	Outer diameter
OS	Organosulfates
OVOC	Oxidized VOC
PFA	Perfluoroalkoxy
PM	Particulate matter
PTFE	Polytetrafluoroethylene
PTR	Proton-transfer-reaction
ROE	Report on the environment
SEM	Scanning electron microscopy
SIM	Single ion mode
SOA	Secondary organic aerosol
(S)VOC	(Semi-) volatile organic compounds
TD	Thermal desorption

Chapter 1

Introduction

Contributions: This manuscript was written by Mario Schmidt, with critical comments from Dr. Sarah A. Styler

1.1 The atmosphere - endless space or box ?

The area near the earth's surface can be divided into four spheres: the lithosphere (earth's crust), hydrosphere (water on planet's surface and moisture), biosphere (living organisms) and the atmosphere (gas phase around the earth) [1]. However, the term „gas phase“ does not fully describe atmospheric composition. Stable components are gases like nitrogen (78.08%), oxygen (20.94%), Argon (0.93%), carbon dioxide (0.04%) and other gases including noble gases such as methane (0.01%). Variable components are aerosols (*e.g.* water droplets, ice crystals, mineral dust, volcanic ash and carbonaceous particles from biomass burning) and water vapor, which depend on local conditions [2]. The pull of gravity holds gases of the atmosphere close to the Earth's surface. Regarding the distance from the Earth's surface, there are gradual changes in density, temperature, and composition. Furthermore, the atmosphere can be divided into four major layers: the troposphere, the stratosphere, the mesosphere, and the thermosphere. (Figure 1.1.)

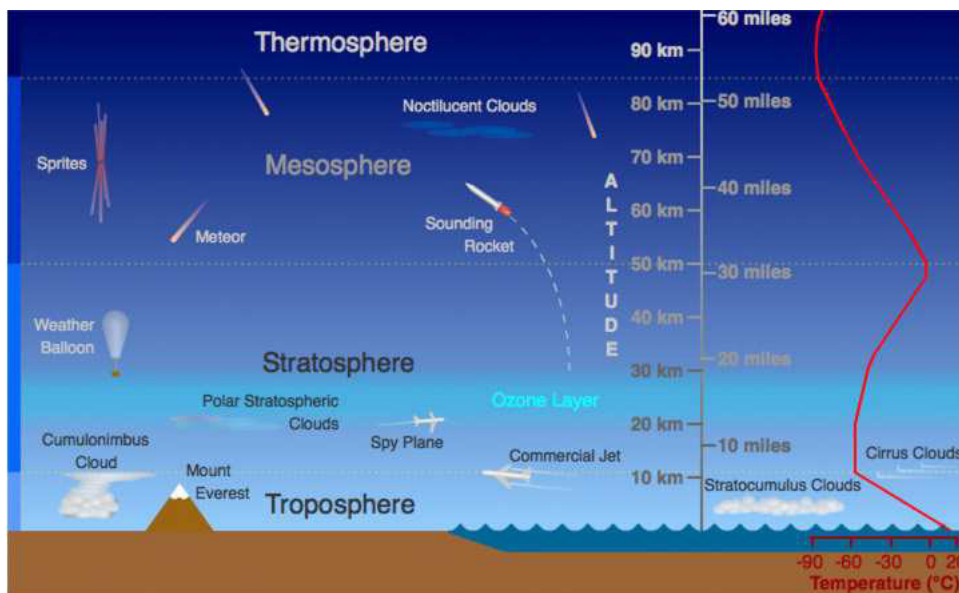


Figure 1.1: Layers of the atmosphere: troposphere, stratosphere, mesosphere, thermosphere; with kind permission for reproduction in this thesis by Dr. Randy Russell, UCAR - [3].

As shown in Figure 1.1, the troposphere extends to a distance up to 10 km approximately. The lower part of the troposphere, which interacts with the Earth's

surface, is called the boundary layer with a variable height between 0 and 3,000 m. Emitted pollutants near the ground accumulate in the boundary layer, which also is the region where most weather occurs. With an increasing height from ground to the upper troposphere, the temperature is decreasing down to approximately minus 57 °C. Furthermore, the stratosphere follows above the troposphere (together commonly referred to as the „lower atmosphere“) and extends up to approximately 50 km and is including the so-called ozone layer. The temperature in the stratosphere is gradually increasing because of UV radiation absorption by ozone, which converts radiant energy into heat. The troposphere and the stratosphere build the lower atmosphere. Finally, the upper atmosphere includes the mesosphere and thermosphere with lowest temperatures of approximately minus 90 °C in the mesosphere. Up to 1200 °C is reached in the following thermosphere by gas molecules absorbing solar radiation [2].

The atmosphere can be seen both as the surrounding gas phase that has the power to change the earth's shape due to climate change effects but also as a sphere whose composition depends on biogenic, natural or anthropogenic events on the earth's surface. This circumstance already describes the potential complexity of the atmosphere. Discussing the relationships between all four spheres leads to the recognition that also parts of the hydrosphere (water vapour, droplets from sea spray), lithosphere (mineral dust) and biosphere (*e.g.* marine microorganisms in sea spray aerosol) can be injected into and thus be part of the atmosphere being related to weather (local, atmospheric condition) or climate (long-term, average atmospheric condition). Hence, the atmosphere may be described as a huge chemical reactor, that serves as a vessel for a wide range of chemical conversions including multiphase reactions in the aqueous-, gas-, and particle phase.

The local atmospheric concentration of chemical species can be influenced by four different processes. First, the emission of chemicals from possible biogenic or anthropogenic sources can influence their ambient concentration. Second, chemical reactions in the atmosphere can either lead to the formation or removal of chemical species. Third, the transport of chemicals away from their source can be caused by winds. Finally, emitted or formed atmospheric material will eventually be deposited back to the earth. Herein, dry deposition is defined as the involvement of reactions or absorption at the surface of the earth and is characterized by a deposition velocity, which is defined as the flux of the species to

the surface divided by the concentration at some reference height. Wet deposition involves the removal of species by precipitation. An estimated ratio of dry to wet deposition (2:1) for the removal of SO_2 has been estimated for long-term transport processes in North America and emphasizes the potentially important role of dry deposition in the atmosphere [4]. In order to be able to convert a complex atmosphere into a model system for predictions and approximations (e.g. BVOC modeling), so-called box models were developed [5]. A one-box model with chemical species X is shown in Figure 1.2.

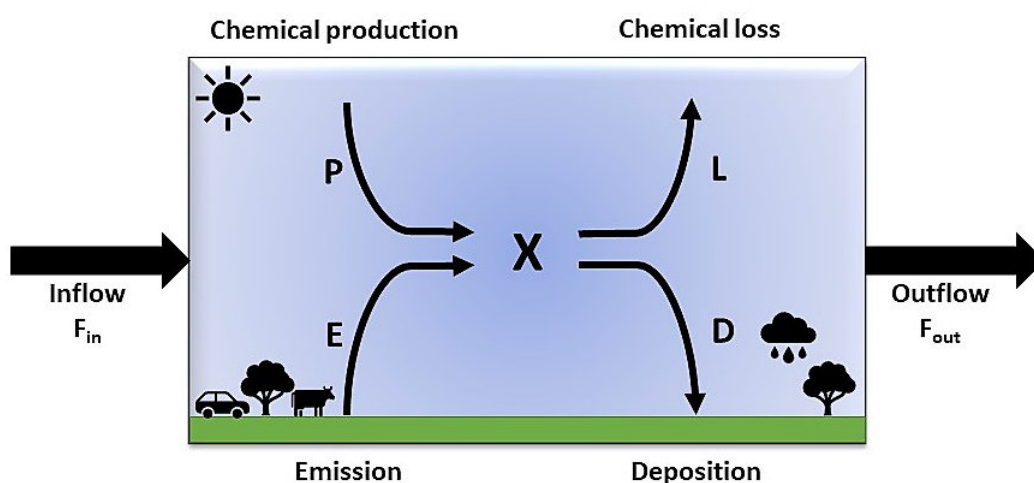


Figure 1.2: One box model showing four atmospheric processes: emission, chemical production, chemical loss and deposition; adapted from [5].

The box in Figure 1.2 represents a certain atmospheric volume, which could be a country, an urban area or the whole global atmosphere. Atmospheric transport is shown as a flow of a species X into the box (F_{in}) as well as out of the box (F_{out}). Sources of the species X are defined by the inflow, emission and chemical production, whereas sinks are possible chemical loss, deposition, and outflow. However, the one-box model does not describe concentration gradients inside the box. Instead, a simplified transport mechanism and the assumption of a well-mixed box serve as a model for predictions. Hence, an assembly of various boxes can be used to describe a certain atmospheric domain with transport

between the boxes (*e.g.* a two-box, three-box model, 3-D modelling GEOSChem [6]).

1.2 Atmospheric emissions and pollution

Throughout human history, the earth's atmosphere had two fundamental purposes. First, it provides air and thus oxygen to maintain biological processes but also for industrial activities. Second, the atmosphere serves as space for waste disposal related to the anthropogenic emission of gases and solids, which are products of combustion and other energy transforming processes. Since nature is not able to cleanse out the atmosphere as a gigantic sewer, urbanization and industrialization have led to severe air pollution episodes and a global reduction of the quality of ambient air. Hazardous risks arise also from gaseous pollutants which can't be seen, do not have an odor as well as from particles being too small to be seen [7, 8]. Furthermore, air pollutants can be classified according to two categories, which are called primary and secondary pollutants. Primary pollutants are directly emitted into the atmosphere including, for example, particulate matter, sulfur dioxide, and hydrocarbons. Symbolically, secondary pollutants can be formed as products of atmospheric, chemical reactions (*e.g.* photochemical reactions) that involve primary pollutants. Ozone is one of the best known secondary pollutants, which can be formed in large amounts over highly polluted cities with high sunlight intensities [5].

1.2.1 Gas-phase emissions

When discussing emissions that may have their origin in nature, it is common to make a distinction between naturally occurring emissions and biogenic emissions. The latter term is often associated with naturally occurring events only and thus is not further related to human activities. Large sources for biogenic emissions are plants and trees of the earth. Even though vegetation plays an important role in converting carbon dioxide to oxygen, they are also a major source of hydrocarbons in the earth's atmosphere. Especially, in regions such as North America, the emission rate of biogenic compounds is estimated to exceed anthropogenic emissions [9]. Annually, the biogenic emissions by vegetation were estimated in 1995 to be as high as 1.2 Pg carbon, which was considered as an amount

equivalent to global methane emissions [10]. Isoprene is one of the most common emitted volatile organic compounds by vegetation with an annual emission of 500 to 750 Tg of isoprene (440 to 660 Tg carbon) [11]. Other large classes of biogenically emitted compounds are monoterpenes, which are 10-carbon hydrocarbons consisting of two isoprene units as well as sesquiterpenes (C₁₅ hydrocarbons) consisting of three isoprene units. Additionally, oxygenated hydrocarbons are emitted by plants as well, including methanol during leaf expansion [12], acetone [13], methyl jasmonate and ethylene being related to plant defensive reactions [14] as well as so-called leaf alcohol and leaf aldehyde as results from damage of plants [15, 16, 17].

According to the U.S. EPA (2014b) report on the environment (ROE), anthropogenic sources of volatile organic compounds can be assigned to different inventoried source categories: fuel combustion (*e.g.* coal-, gas-, and oil-fired power plants), further industrial processes (*e.g.* production of chemicals), on-road vehicles (*e.g.* cars, trucks, buses), non-road vehicles and engines (*e.g.* farm and construction equipment, aircraft). BTEX compounds (benzene, toluene, ethylbenzene, xylenes) are a further environmentally important VOC class, which can be found in crude oil, diesel, gasoline, and are highly used as additives or precursors of other products in the industry [18]. High BTEX concentration levels were found in areas with high industrial activity or in large cities with a high traffic volume [19, 20, 21]. VOC emissions from biogenic and anthropogenic sources were estimated in 2011, and furthermore published in the U.S. EPA (2014b) report on the environment (ROE). Nationally, it was reported, that biogenic sources contributed approximately 74% to VOC emissions from all VOC sources, including emissions from wildfires and plants in the biogenic category. Moreover, a total U.S. VOC emission in 2011 was reported to be as high as 12.3 million tons, assigning 2.16 million tons to non-road vehicles and engines, 2.41 million tons to on-road vehicles, 7.10 million tons to other industrial processes and 0.63 million tons to fuel combustion [18]. Another group of gas-phase pollutants is called greenhouse gases. These are gases that trap heat in the atmosphere and include carbon dioxide with a total contribution of 81%, methane (10%), nitrous oxide (6%), and fluorinated gases (3%) [22]. The combustion of fossil fuels, industrial processes, forestry and other land use are supposed to be the major sources for CO₂ emission. Agricultural activities, waste management and biomass burning contribute to atmospheric methane emissions. Also, agricultural activities, like

the application of fertilizers, are a primary source of nitrous oxide (N_2O) emissions. Furthermore, fluorinated gases, which include hydrofluorocarbons (HFCs), perfluorocarbons (PFCs), and sulfur hexafluoride (SF_6), are emitted by industrial processes, refrigeration, and the use of consumer products [23]. However, biogenic emissions can be also linked to anthropogenic activities since several chemical species (*e.g.* NO_x and methane) can be biological in their origin but are associated with human agriculture, intensive factory farming or fertilization. In short, the impact of biogenic emissions might be underestimated when external factors like human activities are not critically discussed as an additional source for biogenic emissions [24].

1.2.2 Particle-phase emission

Particulate matter (PM) is an inherent part of the atmosphere. Atmospheric particulates need to be distinguished between PM and aerosols. PM is mostly considered as a solid particle or liquid droplet, whereas aerosol is described as fine suspended solid or liquid particles in the air [25]. Moreover, PM can be either directly emitted or formed by secondary processes in the atmosphere. Direct PM emission is called primary particulate matter, which can include biogenic sources (*e.g.* pollen, bacteria, spores, plant and animal fragments) [26, 27, 28, 29, 30, 31]. Furthermore, natural sources of primary aerosol dominate PM emission on a global scale, with sea salt as biggest contributor [32]. Anthropogenic, primary PM sources include industrial and combustion processes considering black or elemental carbon as major contribution [33] as well as general transport including tire, brake wear, and road abrasion, waste disposal processes, and agriculture including mass animal farming and open burning of agricultural residues [34, 35].

Secondary aerosol particles can be formed by nucleation including sulfuric, ammonia, other amines and water as part of this process [36, 37]. Also, organic compounds are considered to contribute to new particle formation [38]. Gas-to-particle conversion is a further pathway to form secondary PM via partitioning to existing PM by adsorption or absorption, and thus contributing to a potential SOA formation [39]. Functionalized oxidation products (*e.g.* carbonyls, carboxylic acids, alcohols, sulfates, nitrates) of primary VOCs from both biogenic and anthropogenic source are considered as potential species to undergo this SOA formation process, as they are less volatile than their precursor compounds [40]. Additionally, oligomerization of chemical species can produce humic-like

substances in the condensed phase [41], which may support SOA formation and heterogeneous reactions at particle surfaces may lead to an increased formation of species, which stay in the condensed phase [42]. Cloud processing represents another formation pathway for secondary PM during evaporation and condensation cycles, the uptake of water soluble chemical species may lead to a following oxidation in the condensed phase as well as secondary sulfate formation [43, 44].

1.2.3 Particle properties

Aerosols can be categorized according to different properties, such as particle size and distribution, chemical composition and hygroscopicity as well as general optical properties [45]. Aerosol sizes can be distinguished in four different modes, which are the nucleation mode (ultrafine), the *Aitken* mode (Scottish scientist), the accumulation mode (size depends on coagulation and condensation), and the coarse mode. Total concentrations of atmospheric aerosol particles can vary over 7 orders of magnitude (approximately 10 to 10^{11} particles per cubic centimeter), whereas the corresponding size ranges often vary over 5 orders of magnitude (approximately 1 nm to 100 μm) [46]. Aerosol particle concentrations can be described by number, surface area, volume, or mass per unit volume, which is represented by Figure 1.3. As shown in Figure 1.3, whereas small particles dominate the number concentration, the coarse mode contributes the majority of PM mass. A common method is the number concentration, which can be expressed by a set of log-normal distribution functions.

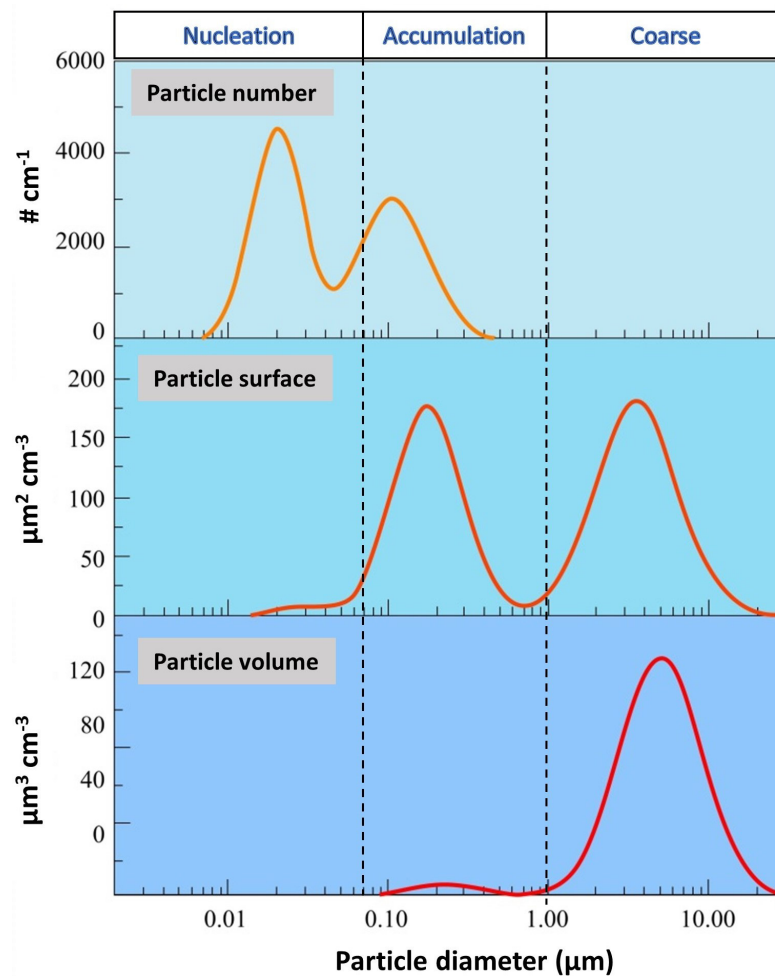


Figure 1.3: Atmospheric particle properties (particle number, surface area and volume) in dependence on the particle diameter, adapted from [47].

Furthermore, the chemical composition of aerosols can affect other properties including the hygroscopicity [45], which expresses the aerosol ability to take up water and grow in size with increasing relative humidity. The chemical composition of atmospheric aerosol particles can vary dramatically by their origin, such as mineral, sea spray, biogenic, industrial or biomass burning aerosols with different contents of organic materials (*e.g.* hydrocarbon-like, semi-volatile oxygenated, low-volatile oxygenated), inorganic materials (*e.g.* sulfate, nitrate, ammonium, chloride salts) [45, 48]. The average composition of different particle sizes including PM_{10} , $\text{PM}_{2.5}$ and $\text{PM}_{\text{coarse}}$ at urban sites was calculated for central Europe in 2010, presented in Figure 1.4, and shows large differences for mineral

dust, sulfate salts and elemental carbon according to the particle size [49].

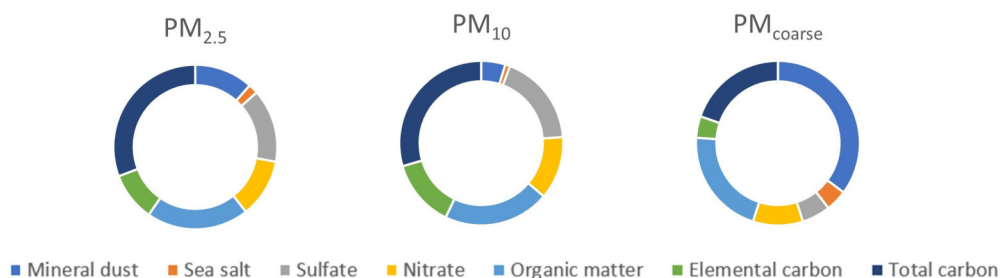


Figure 1.4: Major constituent contributions to PM₁₀, PM_{2.5} and PM_{coarse} from urban regions in central Europe, adapted from [49].

Moreover, aerosol mixtures can be distinguished between external and internal mixtures. External mixtures include particles, which are chemically pure but are mixed with other particles of different chemical composition (*e.g.* pure black carbon mixed with pure ammonium sulfate particles). In contrast, internal mixtures are characterized by different chemical constituents within each particle. Realistic mixtures are supposed to be a mix of both internal and external mixtures [50].

The chemical particle composition also affects the refractive index, which can be used for the description of aerosol optical properties, such as the general particle ability to attenuate atmospheric radiation at different wavelengths by scattering (redirecting energy to different directions) and absorption (transformation to heat). On top of the refractive index, the wavelength of incident light and the size of particles are further key parameters that govern scattering and absorption of radiation by particles. Different theories were developed for the calculation of scattering and absorption efficiencies according to the particle size. The *Mie* theory is applied when the particle size is about the same size as the wavelength of incident light. The *Rayleigh* regime describes scattering and extinction coefficients for small particles sizes compared to the wavelength. Optical properties of large particles compared with the wavelength can be characterized by the so-called geometric regime [7].

1.3 Chemistry of the atmosphere

Atmospheric chemistry still represents a relatively new, but highly complex research area. A multitude of simultaneous reactions can occur in polluted regions, which is also caused by the oxidizing environment of the Earth's atmosphere owing to the high concentration of oxygen [51]. However, gas-phase chemical reactions between two stable molecules are rare in the stratosphere and troposphere because the amount of available thermal energy is not sufficient for a reaction activation. Hence, many atmospheric reactions are driven by solar radiation. Light absorption by chemical species can lead to different reaction pathways in both the mature field of gas-phase photochemistry as well as heterogeneous, multiphase chemistry [52, 53].

1.3.1 Gas-phase chemistry

The first step for an atmospheric photochemical reaction is the absorption of a photon by a molecule (A) at an appropriate wavelength (λ), which usually produces an excited molecule (A^*).

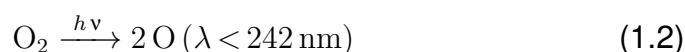


Among other reactions, molecule A^* may undergo fluorescence, collisional deactivation, dissociation, and direct reaction. Chemical change happens during the latter two processes, which is essential for photochemical reactions to occur. Consequently, the identification of common absorbers of the lower atmosphere, in the photochemically active area of the solar spectrum (ultraviolet and visible), is one step towards the determination of possible gas-phase reactions. Table 1.1 shows absorbers and non-absorbers in the region of 3000Å to 7000Å [54].

Table 1.1: Common atmospheric absorbers and non-absorbers in the region of 3000Å to 7000Å, adapted from [54].

Absorbers	Non-absorbers
Ozone	Water
Nitrogen dioxide	Carbon monoxide
Sulfur dioxide	Carbon dioxide
Nitrous acid and alkyl nitrates	Nitric oxide
Nitrous acid, alkyl nitrites, nitro compounds	Sulfur trioxide and sulfuric acid
Aldehydes	Hydrocarbons
Ketones	Alcohols
Peroxides	Organic acids
Acyl nitrites, pernitrites, nitrates	Nitrogen
Particulate matter	

The light intensity available for photochemical reactions, that reaches the earth's surface, also strongly depends on the light absorption in the stratosphere by molecular oxygen and ozone. In the year 1930, Sydney Chapman proposed the first reactions for ozone formation and destruction (Chapman cycle) leading to a steady-state, stratospheric ozone concentration, which is an atmospheric oxidant among other radical species.



However, it needs to be mentioned that this cycle does not completely describe all processes that lead to an actual stratospheric ozone concentration since several ozone sinks (*e.g.* nitrogen oxides and chlorofluorocarbons) contribute to an ozone loss.

Additionally, ozone can be formed at ground level by another mechanism, that does not depend on incident light with wavelengths under 240 nm. Instead, ozone

can be formed in a series of complex reactions involving solar radiation, nitrogen oxides (NO_x) and volatile organic compounds. Especially in large cities, which supply enough VOCs and NO_x by combustion processes among other sources, ozone can quickly accumulate during day time often with peak concentrations at noon, which is also caused by highly trafficked roads (VOC emission) during morning hours [7]. Figure 1.5 presents the ground-level ozone production cycle [55].

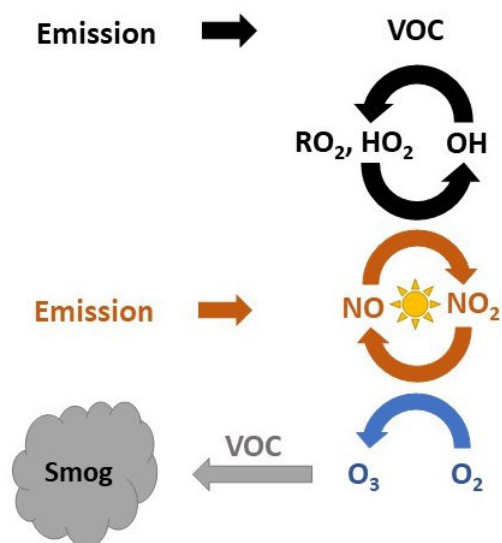


Figure 1.5: Ground level ozone production cycle; adapted from [55].

As shown in Figure 1.5, a major source for ground-level ozone is the photolysis of NO_2 , which produces oxygen atoms for the subsequent reaction with molecular oxygen to form ozone. Nitrogen dioxide in cities is mostly produced by the oxidation of nitric oxide, which in turn is emitted through fuel combustion. Moreover, emitted VOCs can be oxidized by another atmospheric radical species, called hydroxyl radical (OH). Products of these VOC oxidations are organic peroxy radicals (RO_2) and hydroperoxy radicals (HO_2), both capable to oxidize NO to NO_2 without consuming ozone. During this cycle, OH radicals are regenerated by the reaction of HO_2 radicals with NO to form NO_2 and OH. Consequently, the last step of ozone formation is represented by the photolysis of newly produced NO_2 [55].

The most important day-time radical in the troposphere is the hydroxyl radical, which causes the tropospheric degradation of many organic and inorganic pollutants and can be formed via different pathways in the gas-phase, including: [52]

- the photolysis of nitrous acid (HONO)
- the photolysis of ozone and subsequent reaction of an excited oxygen atom O(¹D) with water vapor
- the photolysis of formaldehyde

Further important atmospheric gas-phase oxidants have been reported, such as the nitrate radical (NO₃) and halogen radicals (ClO_x, BrO_x and IO_x) [56]. However, the discussed content of gas-phase chemistry described in this chapter represents only a marginal part of a highly complex but comparatively well-studied research area in contrast to heterogeneous and multiphase chemistry.

1.3.2 Particle-phase chemistry

Obviously, the atmosphere is not a homogenous gas-phase. This conclusion can be easily drawn without scientific measurements by observing common atmospheric events like dust storms, distribution of smoke from wildfires, rain or snow.

Particles or droplets such as they occur in aerosols, fog, clouds or ice crystals may provide a surface promoting surface-mediated reactions or provide bulk condensed phases promoting reactions that can't occur in the gas phase, such as hydrolysis or electron transfer. Moreover, reactions in the particle phase can also produce volatile products, which can be emitted to the gas phase and in turn may alter the gas-phase composition and corresponding reactions.

The complexity of atmospheric heterogeneous becomes more obvious by considering the large variety of available surfaces and their unique properties to promote chemical reactions. These surfaces are not limited to particles only (e.g. black carbon or mineral dust, etc.), but also include any aqueous surfaces (e.g. ocean) or man-made surfaces like glass, concrete, plaster and asphalt among many others [57]. Especially, organic aerosols (OA) are of great interest

in heterogeneous photochemistry since they contribute a mass of up to 90% to submicron particulates [48]. Sources, atmospheric processing, and removal mechanisms are still uncertain. Especially secondary OA (SOA), formed by secondary atmospheric oxidation processes of gas-phase species, accounts for a large fraction of OA [48].

1.3.2.1 Traditional and new pathway for SOA formation

The traditional understanding of SOA formation considers the gas-particle partitioning theory, which describes the partitioning of chemical species between the gas and particle phase as equilibrium. Saturation vapor pressures of the chemical species, as well as the concentration of these species in both the gas - and particle phase, are considered as influencing factors for the partitioning process among other effects. Major uncertainties in this SOA formation mechanism may be caused by neglecting the contribution of aqueous phases and inorganic compounds [39, 58]. However, SOA formation is associated with a reduced vapor pressure (by orders of magnitude) of atmospherically oxidized and thus functionalized species which can be categorized as semi-volatiles or non-volatiles [59].

Studies and field measurements have shown that the model of the traditional gas-particle partitioning theory could not explain characteristics of ambient aerosol, which firstly lead to the assumption of undetermined SOA formation pathways or unrecognized effects of different VOC precursors on the SOA formation. Consequently, it was proven that ambient SOA mass was previously underestimated and could dramatically exceed the modeled SOA formation under free tropospheric conditions [60, 61]. Despite several improvements of this SOA prediction model [62], the formation of SOA oligomeric products cannot be explained since these reactions are unlikely to occur in the gas-phase. Hence, other mechanisms including multiphase processes were investigated, resulting in the determination of atmospheric aqueous phases (aerosol liquid water, clouds, and fog) as potential reaction media for oligomeric species.

Figure 1.6 shows a simplified overview of both SOA formation mechanisms. To summarize, VOCs are emitted by anthropogenic and biogenic / natural sources and are oxidized to OVOCs (oxygenated VOCs), which are characterized by a lower vapor pressure and are more likely to nucleate or partition into the particle phase to form SOA. Furthermore, the formed OVOCs may also partition into the

aqueous phase to undergo aqueous phase reactions (radical and non-radical reactions) and form aqueous SOA via the evaporation of water. Another path of organic compounds into the aqueous phase can also occur through nucleation scavenging when particles initiate the formation of clouds or fog droplets.

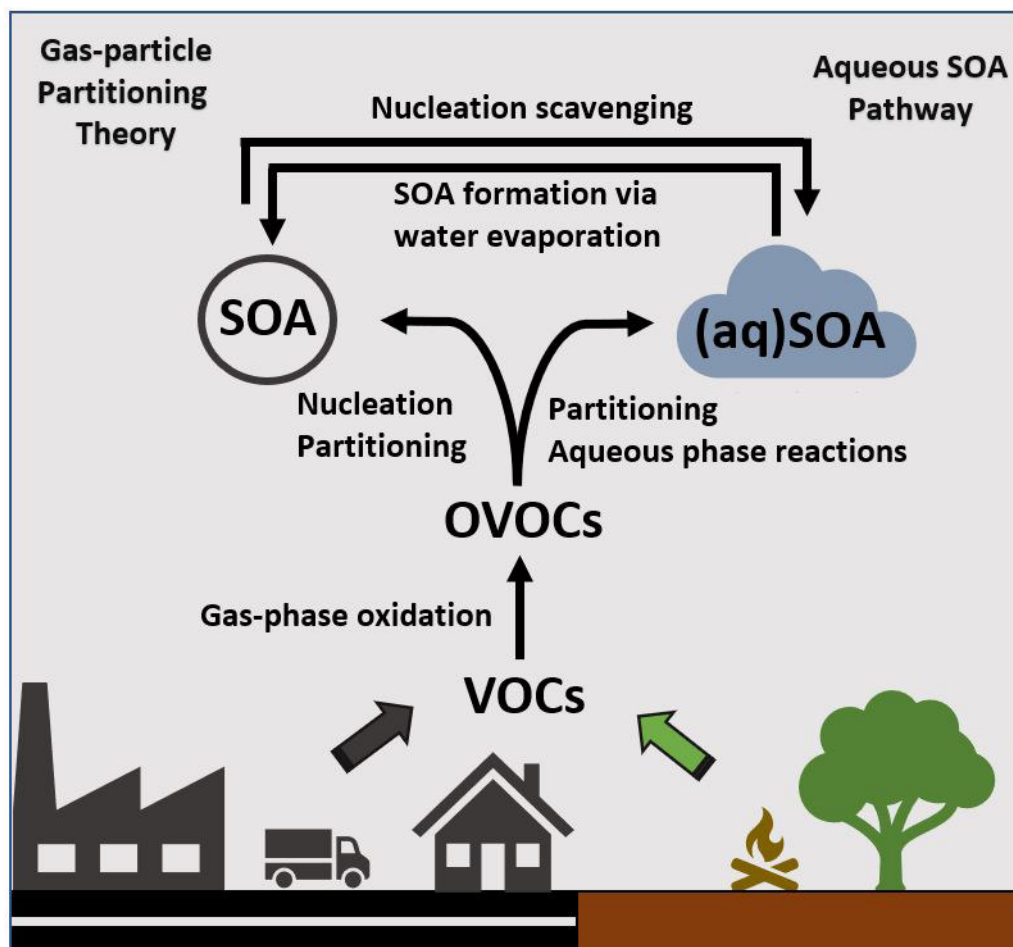


Figure 1.6: Simplified SOA formation pathways by (traditional) gas-particle partitioning and aqueous phase reactions; adapted from [63].

1.3.2.2 Aqueous dust-mediated photochemistry

Aqueous-phase reactions including radical reactions and related knowledge about kinetic insights were recently reviewed [64, 65, 66]. Potentially important aqueous-phase oxidants were reported to be hydroxyl radical, hydroperoxy radical, superoxide anion, sulfate radicals, and the nitrate radical. Probably one of

the most important aqueous-phase reactions in the atmosphere is the oxidation of S(IV) to S(VI). Hence, the gas-phase OH radical initiated oxidation of SO₂ to finally form H₂SO₄ represents an important role for new particle formation [52, 5].

Furthermore, mineral dust aerosol and TiO₂-rich minerals are known to provide reactive surfaces for heterogeneous reactions in the atmosphere and are considered as possibly underestimated factor that contributes to the photochemical formation of atmospheric oxidants, such as nitrous acid (HONO) [67], which can produce OH radicals undergoing photolysis, and as atmospheric sink for ozone by ozone uptake [68]. Moreover, in the aqueous phase TiO₂-induced photocatalysis was proposed to produce HONO in the presence of NO₂ and H₂O [69]. The aqueous SOA formation was studied in relation to aqueous organosulfate production [70], a chemical species which can contribute as much as 5% to 10% by mass of the organic fraction of fine particulate matter [71]. Since the hydroxyl radical plays an important role in aqueous oxidation reactions, also in relation to sulfate radical formation from bisulfate anions, the heterogeneous, aqueous-phase mechanism for OH radical generation will be described in the following paragraph.

Semiconductors, such as TiO₂, possess a void energy region, which does not allow for recombination of an electron and hole produced via photoactivation. This void region is called the band gap and extends from the filled valence band to the bottom of the vacant conduction band. After excitation, there is sufficient lifetime for the electron-hole pair to undergo a charge transfer process to species on the semiconductor surface. Under certain conditions, which include the continuous charge transfer to surface adsorbed species during an exothermic reaction, this process is termed heterogeneous photocatalysis. In this process, light absorption with energy equal or larger than the band gap is necessary to initiate the excitation of an electron from the valence band to the conduction band. The electron transfer induced by light absorption results from migration of holes or electrons to the surface of the semiconductor, where either an electron can be donated to electron acceptors (*e.g.* oxygen) for reduction processes or a hole can accept an electron by an electron donor species (*e.g.* water) for oxidation processes. Competitive pathways are represented by electron-hole recombinations, which may occur in the semiconductor particle volume or on the particle surface or back-donation from an adsorbed species after charge transfer occurred [72]. Figure 1.7 shows one-electron reduction steps to form

OH radicals from oxygen and two-electron oxidation steps for the formation of hydrogen peroxide from water [73].

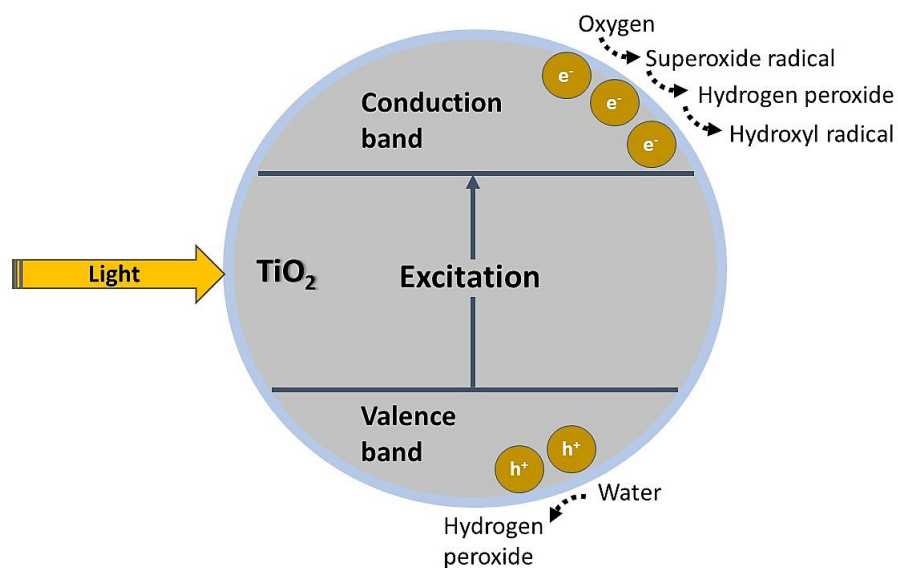


Figure 1.7: Scheme for TiO₂-surface mediated hydroxyl radical formation in the aqueous environment; adapted from [73].

1.4 Impacts on human health and climate

According to the State of Global Air 2018 report [74] and the Global Burden of Disease (GBD) project of the Institute for Health Metrics and Evaluation (IHME) [75] ambient particulate matter, household air pollution, and ozone were identified as the most important risk factors by the total number of deaths for all ages and both sexes in 2016. Especially, fine particle air pollution is considered as the largest environmental risk factor worldwide with ambient particulate matter (PM less than or equal to 2.5 μm in aerodynamic diameter, PM_{2.5}) accounting for 4.1 million deaths from heart disease and stroke, lung cancer, chronic lung disease, and respiratory infections in 2016. PM_{2.5} caused a larger number of deaths compared to well-known risk factors, such as alcohol or high sodium intake). Moreover, particulate matter in the 2.5 to 10 μm size range is also small enough for inhalation and penetration to the thoracic region of the respiratory system. Since PM can also include several metal species (cadmium, copper, nickel, vanadium, zinc) and polycyclic aromatic hydrocarbons (PAH), additionally

to other inorganic and organic components, inhalation of these particles may provide a transport pathway of these species into the blood system [76]. Already in 1970, several categories of respiratory and heart diseases were reported as part of a study about mortality and air pollution levels in New York City [77].

Table 1.2: Categories of respiratory and heart diseases related to air pollution, adapted from [7, 77].

Respiratory disease	Heart disease
Tuberculosis	Arteriosclerotic, coronary heart disease
Malignant neoplasm	Hypertensive heart disease
Asthma	Rheumatic fever, chronic rheumatic heart disease
Influenza	Other diseases of the heart, arteries, veins
Pneumonia	Certain types of nephritis, nephrosis of the kidneys
Bronchitis	
Pneumonia of newborn	

Furthermore, aerosol particles have the power to change earth's climate by absorbing or scattering light dependent on their physicochemical properties. The majority of aerosols are described as light reflecting aerosols according to their composition and color. Hence, bright or translucent particles usually tend to reflect light and dark aerosols can absorb significant amounts of radiation. For example, pure sulfates and nitrates tend to almost completely reflect/scatter incoming radiation, thus cooling the atmosphere [78]. Black carbon particles (*e.g.* from combustion processes) mostly absorb radiation, warming the atmosphere or warming the surface they are shading. Moreover, brown carbon, also called organic carbon from biomass burning, is characterized by warming as well, depending on the particle brightness [79, 80]. Sea spray aerosols (salt particles) mostly reflect encountered sunlight, whereas dust particles may reflect or absorb light depending on the composition and any possible coating with brown or black carbon [45].

1.5 Laboratory atmospheric simulation approaches & analytical techniques

1.5.1 Atmospheric reaction chambers

The determination of atmospheric conditions for the formation of smog phenomena requires the design of an instrumental setup, which allows for the control of specific reaction parameters. The monitoring of concentrations of atmospheric reactants and oxidation products is already part of established instrumentation [81] but the evaluation of parameters, such as meteorological conditions and emission rates, still represents a major challenge. In order to investigate individual conditions, it is necessary to keep several remaining parameters constant. Hence, a controlled reaction (smog) chamber is a powerful setup to investigate complex reaction mechanisms in the atmosphere.

Essential parts of smog chambers are a closed bag or container made from PTFE [82] or stainless steel [83], organic precursor compounds (*e.g.* (S)VOCs) for chemical reactions, light sources (*e.g.* blacklight lamps, xenon arc, and argon arc lamps) and suitable analytical instrumentation. Table 1.3 [84] shows a list of analytical instruments commonly used in smog chamber studies. Clean, particle-free and dry air, often from a zero air generator or cylinders, acts as an air supply for the introduction of organic compounds, oxidants or seed particles, and is also used during chamber cleaning processes. Although ambient air of smog-polluted regions has also been used for chamber experiments, it is not preferred for general experimental setups since air compositions may differ drastically and make reproducible experiments almost unfeasible [84]. An inert make-up gas like nitrogen can be applied during experiments to avoid a collapsing chamber bag. Furthermore, smog chambers can be classified into two different systems with either artificial light for indoor experiments or natural sunlight for outdoor smog chambers.

Figure 1.8 was adapted from [85] and shows a basic atmospheric reaction chamber setup with a chamber bag inlet to introduce the compound of VOC or oxidant of interest, UV lamps to provide sufficient energy for photochemical reactions, as well as an outlet for drawing samples towards several analytical instruments. For example, during SOA experiments [86] a decrease of VOC concentration can be measured with DOAS or TD-GC-FID/MS, whereas the

corresponding increase of particle mass can be monitored with a SMPS.

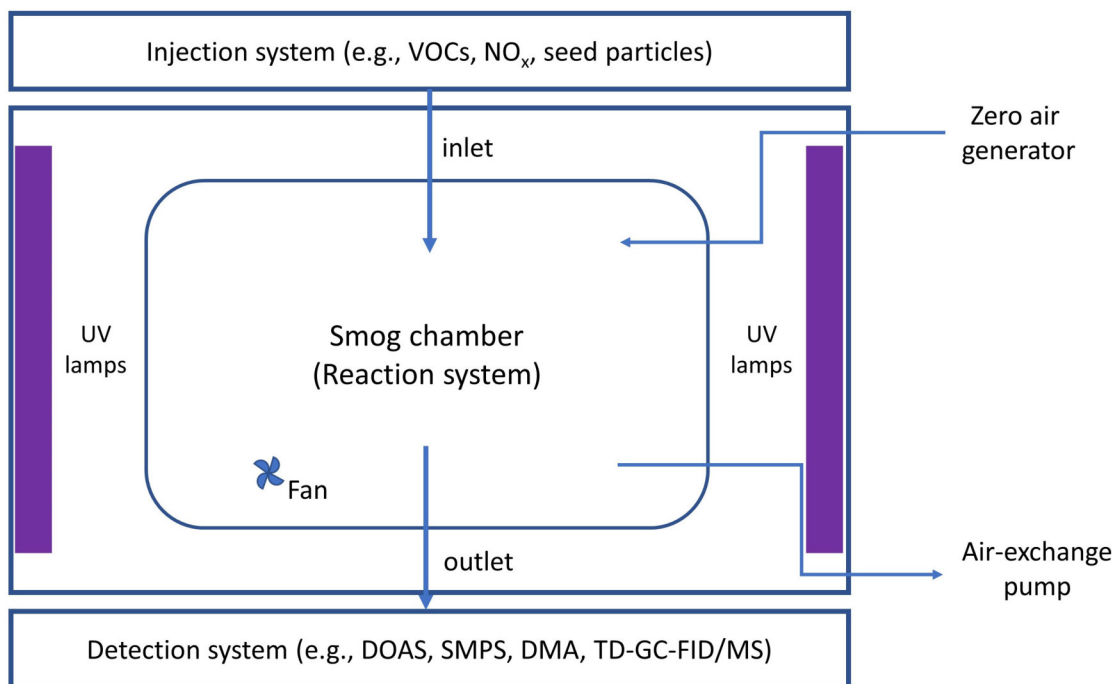


Figure 1.8: Simplified chamber setup to generally introduce chamber experiments, adapted from [85].

Major uncertainties of chamber experiments are related to wall losses, which also include potential wall contamination with previous chemical compounds or particles. Consequently, the unrealistic volume to surface ratio in an atmospheric smog chamber compared to outdoor environments may affect experimental results since both particles and gaseous compounds can be lost by wall effects [87].

Table 1.3: Common analytical instrumentation for chamber experiments, adapted from [84].

Species	Instrument
O ₃	UV photometric analyzer
NO _x	Chemiluminescence analyzer
SO ₂	Pulsed fluorescent analyzer
VOCs	GC-FID
Aldehydes	HPLC
Identification of organics	GC-MS
Aerosol size distribution	Scanning electrical mobility spectrometer Scanning mobility particle sizer
Aerosol response to humidity/temperature	Differential mobility analyzer
Aerosol total number concentration	Condensation particle counter

Additionally, organic compounds in the atmosphere can also be investigated via further techniques in optical spectroscopy like differential optical absorption spectroscopy (DOAS) or Fourier-transform infrared (FT-IR) [88].

1.5.2 Differential optical absorption spectroscopy

DOAS has become one of the most common applications to measure trace gases of the atmosphere after the first instrument for regular measurements of atmospheric ozone was developed in 1926 [89]. Principles of classical absorption spectroscopy are essential for the application of DOAS systems. Hence, the Beer-Lambert law represents a fundamental equation:

$$I(\lambda) = I_0(\lambda) \cdot \exp(-\sigma(\lambda) \cdot c \cdot L) \quad (1.6)$$

where:

$I_0(\lambda)$ = initial intensity of a light beam

$I(\lambda)$ = intensity after light beam passed through medium

L = thickness of medium

c = concentration of absorber

$\sigma(\lambda)$ = absorption cross-section at wavelength λ

A beam of light with the intensity $I_0(\lambda)$ passes through a volume containing an absorber with a concentration c over a total length L . The intensity at the end ($I(\lambda)$) of the light path is measured by a suitable detector. However, the Beer-Lambert law is subject to several limitations including a non-negligible scattering by particles. Consequently, the Beer-Lambert law needs to be expanded to include various factors which influence the light intensity. Typical factors can be the light absorption by trace gases with a concentration c_j , corresponding absorption cross-sections $\sigma_j(\lambda)$, Rayleigh scattering $\epsilon_R(\lambda)$, Mie scattering $\epsilon_M(\lambda)$, instrumental effects (*e.g.* mirrors, grating) and turbulence $A(\lambda)$ [90].

$$I(\lambda) = I_0(\lambda) \cdot \exp \left[-L \cdot \left(\sum (\sigma(\lambda) \cdot c_j) + \epsilon_R(\lambda) + \epsilon_M(\lambda) \right) \right] \cdot A(\lambda) \quad (1.7)$$

where:

$I_0(\lambda)$ = initial intensity of a light beam

$I(\lambda)$ = intensity after light beam passed through medium

L = thickness of medium

c_j = concentration of trace gases

$\sigma_j(\lambda)$ = absorption cross-sections at wavelength λ

$\epsilon_R(\lambda)$ = Rayleigh scattering at wavelength λ

$\epsilon_M(\lambda)$ = Mie scattering at wavelength λ

$A(\lambda)$ = instrumental effects and turbulence

In order to determine the true light intensity $I_0(\lambda)$ one would have to remove any possible atmospheric absorber. The solution of this dilemma lies in the measurement of the differential absorption, which represents the difference between absorption determinations at two different wavelengths. Firstly introduced in the

Dobson spectrometer (1930), the intensity of direct solar light of two different wavelengths was compared with different ozone absorption cross-sections. Figure 1.9 shows a typical scheme for a DOAS setup including possible factors which could lead to an decreasing light intensity [90].

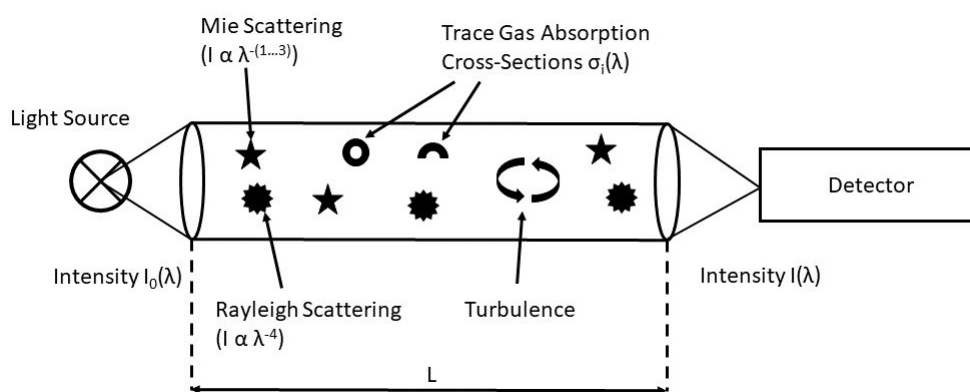


Figure 1.9: DOAS scheme with possible factors causing a drop in light intensity, adapted from [90].

Differential optical absorption spectroscopy takes advantage of very broad spectral characteristics caused by aerosol extinction processes (scattering or turbulence), which in turn can be distinguished from narrow-band absorption structures being assigned to trace gas species. Consequently, the broad spectrum can be used as new intensity spectrum substituting the true intensity for particle and absorber-free air, which then can be applied in the Beer-Lambert law again for the determination of narrow-band trace gas species. As consequence of a variety of different experimental DOAS setups, a classification was developed to distinguish between active and passive DOAS applications. In short, artificial light is used as light source for active DOAS setups in contrast to natural light sources (*e.g.* stars, solar, lunar) are used for passive DOAS measurements [90]. Despite of the advantage that DOAS represents as an on-line monitoring system also for the application in smog chambers [91, 92], it is limited regarding a general structural elucidation. Consequently, gas chromatography coupled to flame ionization and mass spectrometry is a powerful tool to investigate chemical reaction mechanisms in smog chamber experiments.

1.5.3 Thermodesorption gas chromatography

Gas chromatography (GC) is a widely used standard analytical method that supports research and development, industrial quality control as well as analyses in petrochemical industries, environmental, food, drug, and forensic sciences [93]. The origin of GC goes back to first publications in 1941 and 1952 [94, 95]. In gas chromatography, a carrier gas (mobile phase) usually consists of an unreactive gas, such as helium or nitrogen, whereas also hydrogen can be used for improved separations. Stationary phases are mostly liquid or polymeric layers on top of an inert material, inside of an inert tube (*e.g.* fused silica capillary), which is called the column. Separation can be achieved by differential partitioning of analytes between the stationary and mobile phases as the carrier gas passes over the stationary phase. Consequently, an increased interaction of analytes causes a decreased migration along the column, which leads to a delayed elution time. In contrast to packed columns, which contained more stationary phase, wall-coated open tubular columns (WCOT) are more common nowadays. Other types of capillary columns are porous layer open tubular (PLOT) columns. In general, GC columns are connected to a heated and pressurized injector and to a detector at the end of the column while they are heated inside an oven compartment [96].

The migration of an analyte is controlled by the distribution coefficient (K_c). Hence, an important factor for achieving a separation is the difference of K_c values regarding the investigated analytes. The calculation of the distribution coefficient is shown in Equation 1.8.

$$K_c = \frac{[A]_S}{[A]_M} = k\beta \quad (1.8)$$

where:

$[A]_S$ = equilibrium concentration of analyte in the stationary phase

$[A]_M$ = equilibrium concentration of analyte in the mobile phase

k = retention factor

β = phase ratio of mobile to stationary phase volume

Furthermore, the retention factor is defined as:

$$k = \frac{t_R - t_M}{t_M} \quad (1.9)$$

where:

t_R = retention time for elution of a retained analyte

t_M = holdup time for an unretained substance to transit the system from inlet to detector

The phase ratio (β) can be expressed as:

$$\beta = \frac{V_M}{V_S} \approx \frac{d_c}{4d_f} \quad (1.10)$$

where:

d_c = internal column diameter

d_f = stationary phase thickness

The equilibrium between stationary and mobile phase, and thus the distribution coefficient is temperature dependent. With an increasing column temperature, K_c is decreasing, which leads to a reduced retention time of the analyte. Consequently, temperature programming is a preferred method for complex samples that are characterized by a wide range of retention factors [96]. A similar effect is used in thermal desorption devices coupled to a gas chromatograph for the analysis of volatile organic compounds in air samples. Since concentrations of VOCs can be very low (parts per trillion), it is necessary to pre-concentrate gas-phase analytes onto a sorbent, which is then heated in a carrier gas stream to release analytes into a smaller volume of gas, and therefore a higher analyte concentration. The operation of thermal desorbers can be divided into single-stage and dual-stage mode. The single-stage operation is characterized by the collection of compounds on a sorbent tube and the direct release into the GC by heating the sorbent tube. Two-stage thermal desorbers release analyte from a sorbent tube into the carrier gas stream followed by a re-focusing step on a narrower tube (focusing trap or cold trap). This trap is then heated again to release analytes into a smaller gas volume, which improves the method sensitivity and peak shape. However, nowadays single-stage operations often are carried out with focusing traps only to reduce peak broadening [97]. For this purpose, the terminology of a micro trap was introduced. Micro traps are short fused silica or stainless steel capillaries with typical inner diameters between 0.32 mm and 1.2 mm, and can be filled with a sorbent. Traps can be

packed with a mixture of different sorbents, and sorbent selection depends on factors, such as analyte volatility, concentration and the humidity of the sample [98, 99, 100, 101, 102]. The structure of the most common sorbent material (Tenax TA[®]) is shown in Figure 1.10.

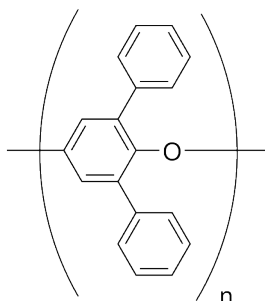


Figure 1.10: Chemical structure of Tenax TA (Tenax TA[®]) (poly(2,6-diphenylphenylene oxide)).

Tenax-TA is characterized by a high temperature limit of 350 °C and a low affinity for water. The latter properties is ideal for sampling air with a high humidity and thus to minimize the trapping of water. However, if target analytes cover a wide range of volatility, a selection of four sorbents can cover the majority VOCs in air monitoring applications: [99]

- Tenax-GR (graphitized form) - weak, hydrophobic
- Carbotrap or Carbopack B - medium strength, hydrophobic
- Spherocarb - strong, less hydrophobic
- Carboxen 1000 or Carbosieve SIII - strong, less hydrophobic

1.5.4 Photochemical reactor development

Historically, the first organic photochemical reaction was reported in 1834 by *Trommsdorff*, who observed a change of color and physical properties when crystals of a compound (α -santonin) were exposed to sunlight [103]. Since then, photochemical research experienced a rapid development related to both mechanistic investigations in organic synthesis but also the design and application of larger scale reactors. Consequently, the modeling and design of photoreactors

as the heart of a photochemical plant were subject of engineering research. Some primary factors for photoreactor development are described in the following paragraph.

Modes of operation can be distinguished in batch, semi-batch, and continuous modes, whereas usually batch type reactor are used for slow reactions, in contrast to continuously operated reactors [104]. Furthermore, the involved phases (*e.g.* single phase or multiphase) may affect the mode operation. Heat exchange needs to be considered to keep the reactor at an adequate temperature. Mixing and flow rate characteristics may be important if rate-limiting steps (*e.g.* catalyst-reactor contact) need to be considered. Also, the reactor material has to fit demands regarding necessary temperatures, pressures, possible corrosion effects, heat transfer aspects and catalytic properties of the reactor material itself [104]. Already in the year 1955 published pioneer work provided the path to active research on the design and analysis of photoreactors since commercial, plant size photoreactors were expected to work under non-uniform conditions (temperature, concentration and radiation distribution) at this time. This leads to point values of reactions (location-depend inside the reactor) being utterly different from global ones [105]. Consequently, a study about mixing in photochemical reactors discussed one of these limitations in 1965 [106] followed by a review of photochemical engineering published in 1995 providing insights into fundamentals and applications of photoreactors [107]. Whereas for industrial purposes the application and development of continuous flow photoreactors started already in the 1950s [108], it is still actively investigated in organic photochemistry [109, 110] and water treatment [111].

The development of photoreactor equipment is also important to study atmospheric reactions in the aqueous phase. Aqueous atmospheric reactions are still less investigated compared to gas-phase reactions and are of interest regarding the determination of radical initiated reaction kinetics [64], corresponding reaction mechanisms [112] and, for example, their impact on aqueous secondary organic aerosol formation [113, 65, 66, 70, 114].

1.6 Thesis introduction

The overarching goal of this thesis is to present the development of methods and techniques to investigate atmospheric reactions in both the gas phase and the aqueous phase.

In Chapter 2, a new photoreactor for the study of heterogeneous processes is reported. The reactor offers the advantage of working with an exchangeable set of multi-sample adaptors to adjust the reactor size and volume. Furthermore, the reactor was further developed to improve its low-maintenance characteristics by the addition of gear-driven, robust stirring mechanism. The reactor characterization (uniformity in illumination and stirring) is shown by acquired data related to the photochemical decay of 2-nitrobenzaldehyde (2NB) both particle-free and particle-laden aqueous samples.

In Chapter 3, the investigation of a new photochemical mechanism to produce organosulfates in the aqueous-phase is presented in the presence of mineral dust. Different reaction parameters have been changed to determine their impact on organosulfate formation, including illumination time, catalyst loading, sulfate concentration, counterion identity, and methacrolein concentration.

In Chapter 4, the development of a thermal desorption (TD) unit coupled to a GC-FID/MS is presented for the investigation of VOC oxidation experiments in an atmospheric reaction chamber. The technical design and design considerations are discussed in detail as well as the realization of an automated sampling and desorption process. Furthermore, insights into the cooling and heating capacity, and calibration data for the TD unit are shown. First TD characterization experiments are presented by coupling the TD-GC-FID/MS instrument to the smog chamber and by monitoring the decay of toluene during a dilution process with zero air with DOAS and the thermal desorption system.

Together, the work presented in this thesis provides new tools for the study of atmospheric chemistry and new insight into dust-catalyzed, aqueous photochemistry.

Chapter 2

Development of a multi-position photochemical reactor

Contributions: This manuscript was written by Mario Schmidt, with critical comments from Dr. Sarah A. Styler

2.1 Introduction

Atmospheric chemistry is mostly driven by photochemical reactions, which result from interactions between air and solar radiation [115]. However, during the past two decades more efforts have been made to improve the understanding of atmospheric heterogeneous and multiphase reactions, especially aqueous chemical reactions occurring in or on particles including aerosol particles, fog - and cloud droplets as well as their potential environmental impact [65, 116]. Photochemical studies of reactions in solution phase are of interest for atmospheric chemistry including aerosol science and technical applications such as degradation of pollutants in wastewater treatment. Atmospheric liquid reactions are characterized by a complex matrix with numerous properties including a possible uptake of soluble organic species like volatile organic compounds from the surrounding gas phase by aqueous atmospheric particles which can be potentially converted to stable and unstable products by aqueous phase reactions [64]. One example is the radical-initiated formation of sulfate esters (organosulfates) from dissolved biogenic volatile organic compounds (BVOCs) in the aqueous phase. Moreover, it has been shown that atmospheric aqueous phase reactions (*e.g.* oxidation or oligomerization) of dissolved VOCs provide pathways for the formation of aqueous secondary organic aerosols (aqSOA) [117, 118, 119, 120, 121, 70, 122].

For the investigation of laboratory aqueous phase studies in atmospheric chemistry it is still a demand to create a practical and low-cost solution of suitable reactor setups which provide a reactor application under different conditions including temperature control, adjustable reactor volume and stirring speed, on-line sampling options in a closed system during reactions involving highly volatile compounds, the introduction of atmospheric trace gases to simulate aqueous-gas phase interactions as well as multi-sample capability for the simultaneous investigation of atmospheric, heterogeneous, catalytic reactions. Batch reactors are a common reactor type for kinetic and mechanistic investigations in aqueous phase atmospheric chemistry. For this purpose, different reactor setups were published for specific experimental approaches. These photoreactors include for example a 1 L borosilicate reaction vessel with a mercury lamp in the center used for glyoxal oxidation experiments [114], 2-cm, far-UV, air-tight quartz cuvettes in a temperature controlled illumination chamber for green leaf volatile oxidation [122], a 250 mL glass reaction vessel covered by a quartz window for isoprene oxidation

experiments with a perpendicular UV source [123], a 1 L polymethylpentene bottle on the focal axis of a light-reflecting device with a wavelength range between 300-500 nm for the investigation of H₂O₂ behaviour in cloud droplets [124], a rotating disc photoreactor for the photocatalytic reduction of chromium (VI) in aqueous solutions by nano-TiO₂ or a 500 mL cylindrical and water cooled Pyrex container with a xenon lamp for carboxylic acid photooxidation [112]. However, all described reactors have several design-related limitations. Especially during heterogeneous aqueous reactions, it might be necessary to use small sample volumes because of the limited availability of particulate matter (*e.g.* collected aerosol particles or dust). Furthermore, the number of simultaneously performed experiments is mostly limited to one reaction vessel which makes comprehensive mechanistic studies time-consuming. Temperature control is another factor that may influence rate constants of atmospheric aqueous reactions, which needs to be considered when radiation of light bulbs or solar simulators affect the bulk liquid temperature and hence changes potential gas phase concentrations of volatile organic compounds. Finally, the total reactor volume influences also the light intensity profile during particle-containing experiments when homogenous stirring is not guaranteed. A decreasing profile of light intensity can be especially the case in photochemical reactors for the application of TiO₂-mediated degradation of industrial wastewater, which is improper for atmospheric, aqueous phase studies [125].

Hence, we present in detail a new exchangeable multi-position batch photoreactor, which allows for fast exchange of the overall setup regarding the number of reaction vials as well as experimental conditions and the corresponding volume of the bulk phase which is advantageous when the amount of sample (*e.g.* mineral dust) available is limited or kinetic laboratory studies require a higher bulk phase volume for continuous sampling. Constant and equal stirring at all reactor vial positions and sizes is provided by customized stirring base plates. Moreover, an exchangeable reactor size provides the opportunity to use only one light source (*e.g.* solar simulator) and one electronic control unit that includes various cooling and stirring features which finally contributes to higher flexibility and reduction of expenses.

2.2 Experimental methods

2.2.1 Experimental apparatus

2.2.1.1 Photochemical reactor description

The photochemical reactor, a schematic of which is shown in Figure 2.1 and a cross-section view in Figure A.1, represents a size-exchangeable batch reactor system that features multi-position options for the application of one single quartz disc covered reactor with an additional sealed sampling port (1-sample adaptor), four reaction vessels (4-sample adaptor) or nine reaction vessels (9-sample adaptor). A Teflon box (A) covered by a quartz glass window and a filter holder (B) serves as reactor closure for the 4 and 9-sample adaptor configuration. The single-sample reaction vessel is sealed and closed by a quartz window. Optional Swagelok® connectors can be used to introduce gas mixtures into the Teflon box for simulating reactions at the surface of solid films (*e.g.* mineral dust, aerosol extracts). The number of samples (1, 4 or 9) introduced into the reactor and hence the reactor volume can be adjusted by selecting the corresponding sample adaptor (C); here, the 9-sample configuration is shown. Each sample adaptor is permanently attached to a customized stirring mechanism (D) according to the potential number of reaction vessels being inserted. This stirring mechanism consists of a gearing unit, which serves as robust and low-maintenance actuation for brass discs with two rare-earth magnets, each disc being located underneath the actual sample vessel position. An exploded view drawing of the stirring mechanism is shown in Figure A.2. All sample adaptors sit in an aluminium housing (E), which is connected to a cooling plate containing channels for a flow of a cooling liquid (F). A fixed socket (G), which protrudes upward from the bottom part of the apparatus serves as motor shaft and is mounted to a DC motor (H) driving the stirring mechanism. It is necessary to let each adapter fit into the socket after insertion into the aluminum housing (E) by applying a low stirring motor speed until it snaps in.

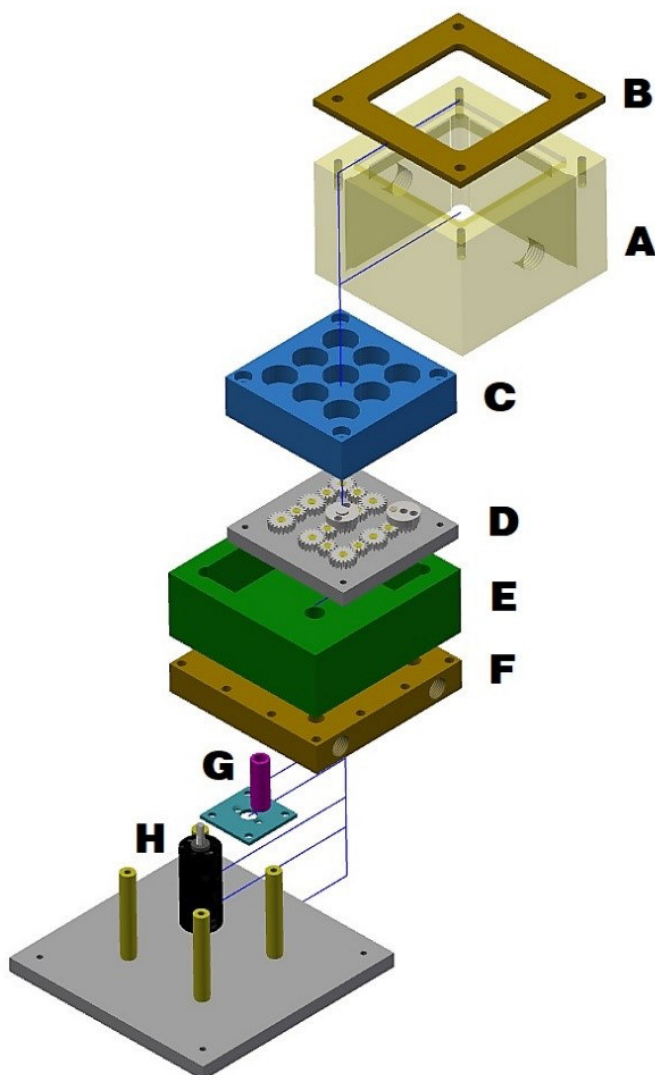


Figure 2.1: Exploded view drawing of photoreactor setup including a stirring motor (H), shaft (G), cooling plate (F), adaptor plate (E), stirring mechanism (D), sample adaptor (C), Teflon box (A), filter holder (B).

2.2.1.2 Reaction vessels

The single sample reaction vessel is constructed from a flat O-ring flange (5 cm ID; 3.8 cm height; 20 mL sample volume) equipped with a 6 mm ID sampling port. The top of the vessel is equipped with a quartz window (76 mm diameter × 6 mm thickness), which is held in place using a horseshoe clamp. Reaction vessels for

the 4 and 9 - sample adaptors are open, hence covered by the Teflon box only and are custom-built from quartz glass tubing with final dimensions of 17.68 mm ID, 20.36 mm OD, 13.87 mm height, 2 mL sample volume for 4 sample adaptor vessels and 11.76 mm ID, 13.91 mm OD, 14.22 mm height, 1 mL sample volume for 9 sample adaptor vessels. Samples were stirred using stir bars of appropriate size for each sample adaptor type (1-sample adaptor $1\frac{1}{2}$ in \times $\frac{3}{8}$ in, 4-sample adaptor $\frac{1}{2}$ in \times $\frac{1}{8}$ in and 9-sample adaptor $\frac{5}{16}$ in \times $\frac{1}{16}$ in; Fisher Scientific).

2.2.1.3 Temperature and stirring control

The reactor temperature and stirring speed are adjusted by an electronic control unit, which is shown as part (A) of an overall schematic setup in Figure 2.2. The temperature of samples is controlled by an Omega CN7500 proportional-integral-derivative (PID) controller (B), which receives a temperature feedback through a K-type thermocouple wire (C) attached to a temperature probe (D). This temperature probe is inserted into a reaction vessel filled with deionized water using the 4 and 9 - sample adaptor throughout the photoreactor application, and is introduced into the single reactor vessel through the sampling port and the corresponding septum. The PID controller (B), in turn, controls a Peltier element unit connected to a forced-air cooled aluminium heat sink (A, J in Figure A.3), which removes the heat from a circulating coolant (E, F) that is flowing through the reactor cooling plate driven by 24 V DC single-stage liquid pump (C in Figure A.3) operated at maximum flow rate using a potentiometer (G). A UV hot mirror (H) held by filter holder (I) was applied to reduce the heat transfer between the solar simulator (J) and the reactor unit (single reactor or Teflon box), which is covered by a 295 nm long-pass filter (K) and a quartz glass window (L). The DC motor (M) and thus the stirring speed are controlled by a potentiometer (N). For all electrical components a Mean Well 24 V, 600 W AC/DC converter (D in Figure A.3) is used as general power supply.

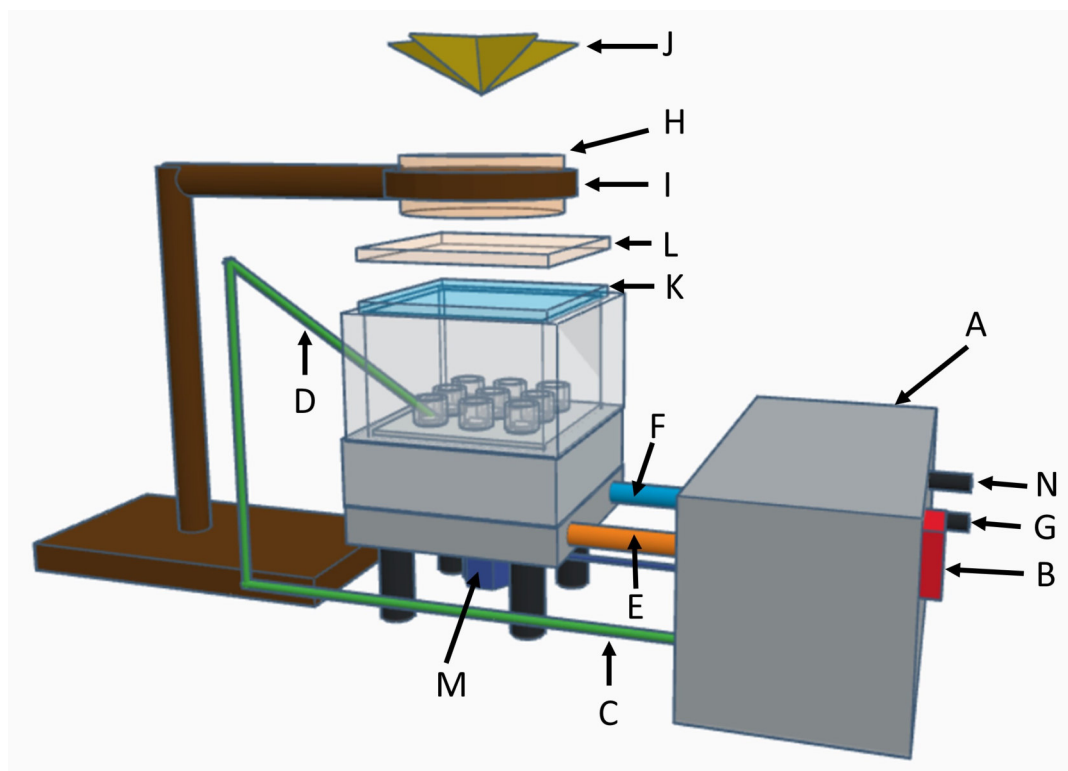


Figure 2.2: Overview of photoreactor control showing the temperature and stirring control unit (A), temperature controller (B), stirring speed potentiometer (N), pump speed potentiometer (G), coolant outlet (F) and coolant inlet (E), stirring motor (M), K-type thermoelement wire (C), K-type thermoelement temperature probe (D), UV hot mirror (H), 295 nm long-pass filter (K), Quartz glass window (L), light source (J).

2.3 Reactor characterization

2.3.1 Chemical actinometry

In order to characterize the photon flux within the sample compartments of the photoreactor chemical actinometry of 2-nitrobenzaldehyde (2NB) was used with a 10 μM aqueous 2NB solution. Under these low-light-absorbing conditions, a 2NB first-order photodegradation can be observed such that:

$$\ln \left(\frac{[2NB]_t}{[2NB]_0} \right) = -j(2NB) \times t \quad (2.1)$$

including $[2NB]_0$ and $[2NB]_t$ as concentrations of 2NB at illumination time point zero and time point t as well as the 2NB photodecay rate constant $j(2NB)$ [126]. The application of higher concentrated 2NB solutions was reported to cause an absorption of most incoming photons which leads to a zero order photodissociation of 2NB [127]. The application of 2NB as chemical actinometer was also reported for the characterization of a batch-type reactor for the photolysis of SOA solutions [128] and for microfluidic photoreactors used in photosynthetic research [129] as well as for further photochemical applications such as photoreactors for wastewater treatment [130]. An Abet Technologies SunLite solar simulator served as light source.

2.3.2 Experimental procedure

In order to characterize the general photon flux and the stirring capacity regarding different particle sizes, three sets of experiments were performed, including the illumination of particle-free 2NB solutions and particle-laden 2NB suspensions using commercially available TiO_2 and collected road dust. 2NB- TiO_2 (0.25 mg mL^{-1}) suspensions were prepared in a TiO_2 laden beaker adding a $10 \text{ }\mu\text{M}$ 2NB solution, continuously stirring to ensure a homogenous particle distribution during sample transfer into the empty photoreactor vessels. 2NB-road dust (5 mg mL^{-1} for similar opacity compared to TiO_2 experiments) suspensions were prepared by weighing road dust into the reactor vessels and adding a $10 \text{ }\mu\text{M}$ 2NB solution into each vessel. Both the solar simulator and the photoreactor cooling system were turned on 15 minutes before experiments were conducted to assure a homogeneous temperature across the photoreactor. All reactor samples were stirred for 2 min prior to illumination with a constant temperature of 293 K. For each time point (0 s; 45 s; 90 s; 180 s; 360 s; 540 s; 720 s) the solar simulator shutter was closed and samples with a total volume of 1 mL for the 4 and 9-sample adaptor, and 0.5 mL for the 1-sample adaptor were taken. Samples containing particles were filtered with nylon syringe filters ($0.2 \text{ }\mu\text{m}$ pore size). Quantification of 2NB was accomplished using an Agilent 1100 HPLC system equipped with a binary pump, autosampler, thermostatted column compartment held at $30 \text{ }^\circ\text{C}$, and a variable wavelength UV absorbance detector was set to 258 nm. Separation of 2NB from its photolysis products was performed with an Atlantis® dC18 column (Waters, $3 \text{ }\mu\text{m}$, $150 \times 2.1 \text{ mm}$) under isocratic conditions (60% acetonitrile, 40% ultrapure water) at a flow rate of 0.3 mL min^{-1} . An injection

volume of 50 μL was used for all experiments. Figure A.4 shows chromatograms of illuminated 10 μM 2NB solutions as a function of time which shows 2NB peak depletion after 39 min of illumination, with a 2NB retention time of 2.8 min and a retention time of 1.3 min for the photolysis product of 2NB. A complete signal depletion of 2NB indicates that the reported loss rates and the corresponding 2NB peak areas are only dependent on the 2NB photolysis process which is also demonstrated by a sufficient separation of both 2NB and the 2NB photolysis product.

2.4 Chemicals and materials

2-Nitrobenzaldehyde ($\geq 99.0\%$) and titanium(IV) oxide, anatase (powder, 99.8%) were obtained from Sigma-Aldrich. HPLC-grade acetonitrile (99.99%) was obtained from Fisher Scientific. Deionized water for both 2NB solution preparation and HPLC analysis was obtained from a Millipore Synergy UV ultrapure water system (resistivity = 18.2 $\text{M}\Omega\cdot\text{cm}$). Sample filtration was conducted with 25 mm nonsterile syringe filters (Fisher Scientific, Basix, nylon, 0.2 μm), which were rinsed with deionized water ($2 \times 3 \text{ mL}$) and dried overnight at 323 K prior to use. The 2NB solution was stored in a fridge in a capped glass jar wrapped in aluminium foil. Road dust was collected in December 2017 in Edmonton, Alberta (97th Street; 53°33'6.5" N, 113°29'22.0" W) with a size fraction of 45-125 μm , isolated using a Retsch AS200 analytical sieve shaker.

2.5 Results and discussion

2.5.1 Temperature stability

Given the dependence of rate constants of many reactions in the atmospheric aqueous phase on temperature [65], the ability of the photoreactor setup to keep the temperature of all reaction vessels constant, under both dark conditions and illuminated conditions, was tested. Hence, related results of the temperature monitoring are presented in Figure A.5. The temperature of the 1-sample adaptor vessel and the average temperature of all vessels of the 4 and 9-sample adaptors are shown after 400 s under dark and 400 s illumination conditions. Detailed reactor position-dependent temperatures for the multi-position adaptors are shown in

Figures A.6 and A.7. Whereas the average reactor temperature rapidly increased after opening the shutter of the solar simulator about 2°C and then stayed constant for the multi-position adaptors, the single sample adaptor showed a delayed temperature re-adjustment caused by a relatively large sample volume cooled by a smaller heat sink compared to the 4 and 9 sample adaptors which provide deeper depressions for reactions vessel, thus increasing the cooling efficiency for a small volume. Furthermore, the single sample adaptor represents a closed batch reactor system, which heats up faster compared to the 4 and 9-sample adaptors as open batch reactors.

2.5.2 Multi-position stirring performance

The investigation of photolysis rate constants for 2NB (*i.e.*, $j(2NB)$) with a multi-position reactor gives insight to a uniformity of illumination (via $j(2NB)$ for various sample adaptors) and uniformity of stirring in all reaction vessels (via $j(2NB)$ with TiO_2) to confirm a constant light intensity profile throughout the reactor positions. Both the uniformity and continuity of each reactor position were investigated by observing the photodissociation of 2NB and thus measuring the decay during illumination. Consequently, photochemical rate constants for 2NB were determined by creating a plot of $\ln[(2NB)/(2NB)_0]$ vs illumination time and using the slope of the linear fit as $j(2NB)$ value, where $(2NB)$ and $(2NB)_0$ represent the corresponding peak areas of 2NB after a certain illumination time and at time point zero. Figure 2.3 presents the photodissociation of 2NB (10 μ M) in the 9-sample adaptor as seen in Figure 2.1. 2NB exhibits first-order loss kinetics with respect to illumination time. The slope of the linear fit provides the photochemical rate constant of 2NB (*i.e.*, $j(2NB)$).

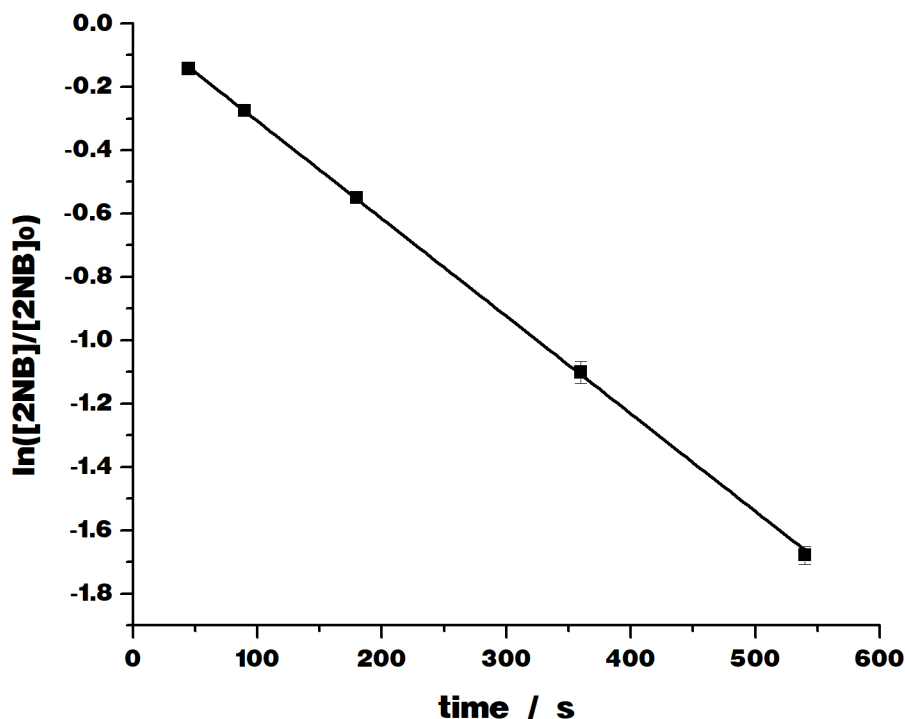


Figure 2.3: Linear fit for the loss of the 10 μM chemical actinometer 2-nitrobenzaldehyde (2NB) in our photochemical reactor (9-sample adaptor) as a function of illumination time. Each data point represents the mean of three replicates, with 1- σ error bars.

Since only the photodecay of 2NB in an aqueous solution does not proof the proper function of the 4 and 9-sample adaptor stirring mechanisms, particulate matter (TiO_2) was introduced to create a 2NB- TiO_2 suspension. Then, the $j(2\text{NB})$ values in the presence of TiO_2 were compared to those obtained in absence of TiO_2 . Figure 2.4 presents insights to the stirring uniformity of the 9-sample adaptor comparing triplicate experiments of illuminated 10 μM 2NB solutions as well as 10 μM 2NB- TiO_2 suspensions (0.25 mg mL^{-1}). As expected, the $j(2\text{NB})$ value for samples containing 2NB only ($(2.97 \pm 0.07) \times 10^{-3} \text{ s}^{-1}$) is significantly higher than with TiO_2 ($(1.14 \pm 0.04) \times 10^{-3} \text{ s}^{-1}$), which we attribute to light shielding by suspended TiO_2 . A TiO_2 -catalyzed loss of 2NB was reported to be insignificant for our experiments since photocatalytic reactions are only associated with the 2NB photolysis product (o-nitrosobenzoic acid) [131]. Considering relative standard

deviations of 2.5% and 3.76% for 2NB and 2NB-TiO₂ experiments (derived from average of all eight positions) we suppose that the application of TiO₂-related particulate matter does not introduce much additional uncertainty over that in samples containing 2NB only, which implies that the stirring of the 9-sample adaptor is uniform. Likewise, in Figure A.8 the comparison of $j(2NB)$ values is presented for the 4-sample adaptor showing a higher j -value in the absence of TiO₂ ($(2.8 \pm 0.07) \times 10^{-3} \text{ s}^{-1}$) compared to samples containing TiO₂ ($(1.36 \pm 0.06) \times 10^{-3} \text{ s}^{-1}$). In analogy to the 9-sample adaptor, the addition of TiO₂ did not add significant uncertainty over particle-free 2NB samples with relative standard deviations of 2.64% and 4.65%, respectively. Comparing both the 4 and 9 multi-position sample adaptors it becomes obvious that relative standard deviations of $j(2NB)$ values of both 2NB solutions (5.7%) and 2NB-TiO₂ suspensions (16.2%) are relatively similar but still show a divergence, which shows the importance of this reactor characterization and could be caused primarily by minor differences in the mechanical manufacturing of the 4 and 9-sample adaptors regarding the depth of the milled depressions for reaction vessels leading to different light reflection properties as well as the custom manufacturing of glass vessels which may show a low curvature at the bottom and thus could lead to different stirring properties, especially observed for the 4-sample adaptor. The single sample adaptor represents a structurally different reactor setup compared to the 4 and 9-sample configurations since its dimensions did not allow for the additional Teflon cover which was used for multi-sample adaptors. Hence, for the 1-sample adaptor and in comparison to the multi-positions configurations, a lower $j(2NB)$ value for 2NB solutions ($(1.82 \pm 0.09) \times 10^{-3} \text{ s}^{-1}$) and a higher $j(2NB)$ value for TiO₂-containing suspensions ($(1.91 \pm 0.03) \times 10^{-3} \text{ s}^{-1}$) were determined, which are discussed in the next paragraph. Additionally, supporting information are provided in Figures A.9 - A.13 showing position- and adaptor-dependent 2NB loss curves of these experiments.

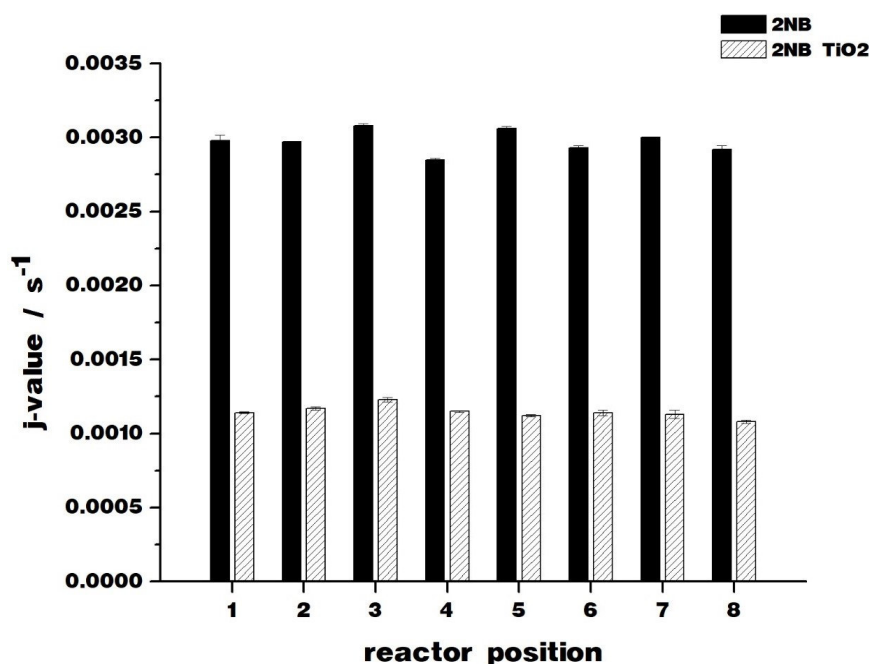


Figure 2.4: Comparison of $j(2NB)$ values determined after illumination of 10 μM 2NB solutions and TiO_2 (0.25 mg mL^{-1}) suspensions using the 9-sample adaptor configuration.

2.5.3 Influence of the reactor cover

As previously indicated in the reactor stirring evaluation part there are several structural differences between all three sample adaptor configurations, which influenced the determined $j(2NB)$ values. As shown in Figure 2.1, the Teflon box can be detached, which was required for the application of the single sample adaptor since the dimensions of this reactor vessel did not fit within the Teflon box size. Hence, all previously reported j -values were determined from 4 and 9-sample adaptors covered by the Teflon box which was another factor that could lead to differences between all reactor setups. Consequently, Figure 2.5 presents insights to covered and uncovered 4 and 9-sample adaptors compared to the permanently uncovered single sample configuration with determined $j(2NB)$ values for illuminated 2NB solutions and 2NB-TiO₂ suspensions. Experiments with uncovered 1, 4 and 9-sample adaptors resulted in overall adaptor average $j(2NB)$ values of $(2.0 \pm 0.16) \times 10^{-3} \text{ s}^{-1}$ for illuminated 2NB solutions compared to 2NB-TiO₂ suspensions resulting in $(1.97 \pm 0.05) \times 10^{-3} \text{ s}^{-1}$ with a relative standard

deviation of 5.4% among all three uncovered sample adaptor configurations considering 2NB solutions and TiO₂ suspensions at once. The addition of the Teflon box for the 4 and 9-sample adaptors increased the average $j(2NB)$ value of both configurations for 2NB solutions to $(2.89 \pm 0.07) \times 10^{-3} \text{ s}^{-1}$ and decreased the $j(2NB)$ value to $(1.22 \pm 0.08) \times 10^{-3} \text{ s}^{-1}$ for 2NB-TiO₂ suspensions compared to uncovered samples. Hence, the addition of the Teflon cover leads to an increase of the $j(2NB)$ value of 27.5% in particle-free samples and a reduction of 39% in TiO₂-containing samples. It can be assumed that an increased j -value for illuminated 2NB solutions can be traced back to an increased secondary radiation caused by light reflection from both the aluminum adaptor plate, including also back scattering from the bottom of reaction vessels, as well as from the Teflon box walls. Furthermore, a decreased j -value for 2NB-TiO₂ suspensions could be associated with particle related light shielding effects which influence the light intensity profile inside the reaction vessels by reducing both the intensity of incoming radiation from the solar simulator as well as back scattered radiation. Since backscattering of light from the reaction vessel bottom was also present during particle-including experiments without using a cover, it might be assumed that especially backscattered light from the vessel bottom, which is not reflected to the same extent anymore after using a cover, could cause the reduction of the $j(2NB)$ value. This effect might be caused by increased, complex Mie (forward) scattering which leads to an increased light shielding effect and in turn reduces the amount of backscattered light from the reaction vessel bottom. Consequently, depending on particle availability, size and material, the usage of the Teflon box cover needs to be considered as potential source for either increased or reduced reactivity in several experimental designs and thus needs to be re-evaluated prior to each changes of the photoreactor setup.

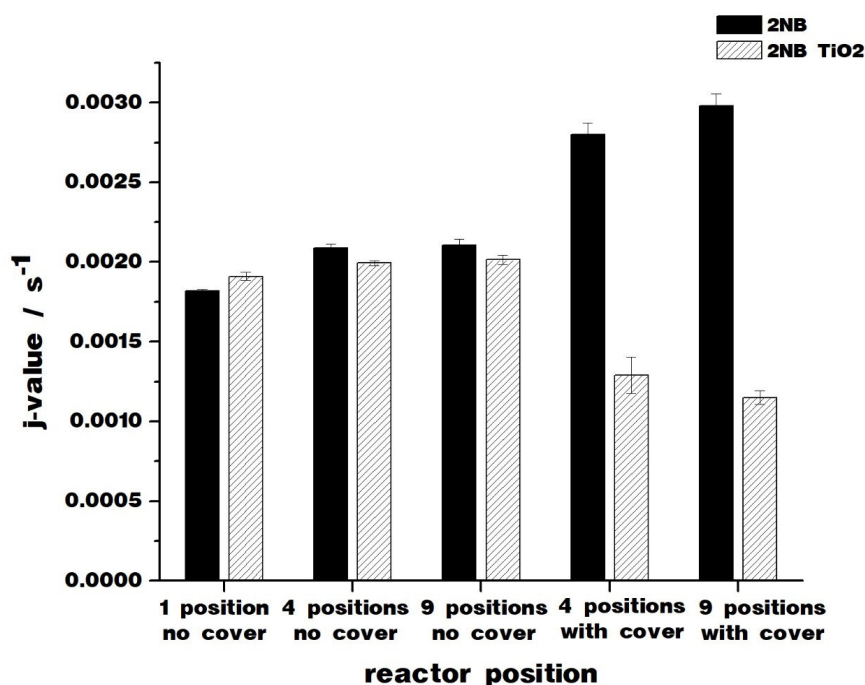


Figure 2.5: Comparison of $j(2\text{NB})$ values determined after illumination of $10 \mu\text{M}$ 2NB solutions and TiO_2 (0.25 mg mL^{-1}) suspensions using the 1, 4 and 9-sample adaptor configurations, showing the effect of the application of a Teflon box as cover for the 4 and 9-sample adaptors.

2.5.4 Efficacy of large particle suspension

All previously shown results were associated with particle containing suspensions originating from commercially available TiO_2 with an average particle diameter of $5 \mu\text{m}$. Recently, it was reported that there is also a need to investigate heterogeneous aqueous phase reactions including larger particles as hypothesized for photochemically active road dust [132]. Hence, Figure 2.6 provides results of 2NB-road dust suspensions using the 9-sample adaptor, a sieved fraction of road dust with a particle size between $45\text{-}125 \mu\text{m}$ and a reactor road dust loading of 5 mg mL^{-1} . The overall comparison of determined j -values across all eight reactor vessels gave an average $j(2\text{NB})$ value of $(1.18 \pm 0.67) \times 10^{-3} \text{ s}^{-1}$ with a relative standard deviation of 5.6%, which additionally includes also possible bias during the road dust transfer into all reaction vessels in contrast to the 2NB- TiO_2 sample preparation procedure, which consisted of a direct transfer

of a 2NB-TiO₂ suspension into the reaction vessels. Results show that the stirring mechanism of the photoreactor works also reliably with larger particle sizes and larger reactor loadings considering 5 mg mL⁻¹ road dust compared 0.25 mg mL⁻¹ TiO₂. Moreover, results in Figure 2.6 support also assumptions about the determination of low $j(2NB)$ values after illuminating TiO₂ suspensions and thus the forward scattering-related decreased photodecay of 2NB caused by TiO₂ presented in Figure 2.5. Even 20-fold higher loadings of road dust, which represents a particle class with different light scattering and light absorption properties compared to TiO₂, resulted in comparable $j(2NB)$ values, which gives a hint of the possible complex effects of particle properties in potential heterogeneous, aqueous, photochemical reactions.

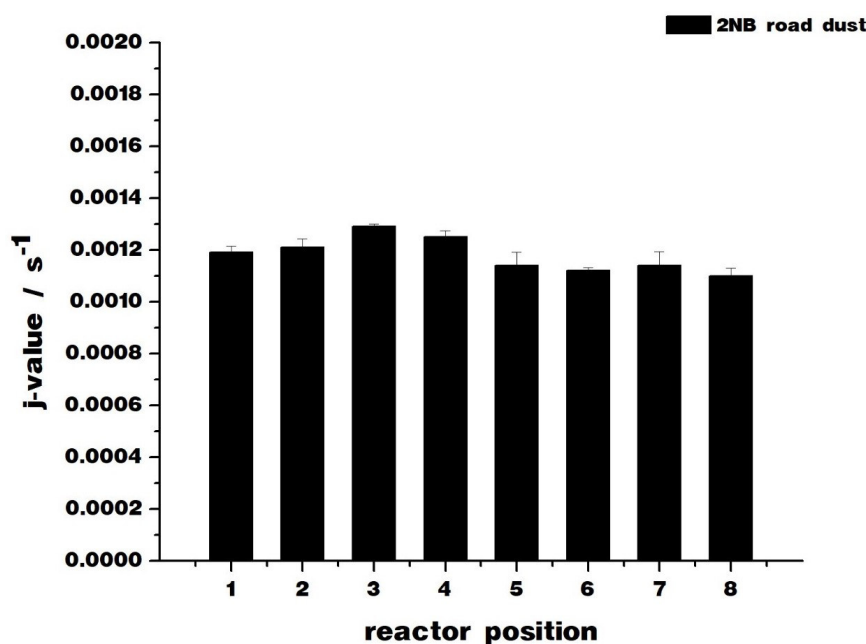


Figure 2.6: Comparison of position dependent $j(2NB)$ values determined after illumination of a 10 μM 2NB-road dust suspension with a road dust loading of 5 mg mL⁻¹ using the 9-sample adaptor.

2.6 Summary

The development and characterization of a new, multi-position reactor for heterogeneous, aqueous-phase photochemistry was presented using 2NB actinometry for the determination of first order rate constants related to the photodecay of

2NB. The photoreactor's ability of uniform stirring with particles of different sizes was proven by the application of a TiO_2 suspension with a concentration of $10 \mu\text{M}$ 2NB. An associated light-shielding dependence of the 2NB photodecay on particle availability and properties served for the evaluation of the photoreactors stirring performance. Furthermore, it was shown that the application of a reactor component, a Teflon box used as cover for the 4 and 9-sample adaptor configuration, influenced the photodecay in both 2NB solutions and 2NB- TiO_2 suspensions, which was associated with light backscattering. However, all three reactor configurations (1, 4, and 9 sample adaptor options) showed similar results without coverage using particle-free and particle containing samples. Ultimately, a temperature controlled, reactor size exchangeable photoreactor driven by a robust gear stirring mechanism was successfully applied to a 20-fold higher reactor loading using road dust as particulate matter with 5 to 25-fold larger particle sizes.

Chapter 3

Mineral-mediated photochemical organosulfate formation

Contributions: This manuscript was written by Mario Schmidt and Dr. Sarah A. Styer.

3.1 Introduction

Particulate matter (PM), whether emitted directly (*e.g.* mineral dust [133]) or formed in the atmosphere via secondary processes (*e.g.* secondary organic aerosol (SOA), which forms via the atmospheric oxidation of volatile organic compounds (VOCs) [134]), plays a role in many atmospheric processes. For example, PM influences Earth's climate directly by absorbing and scattering incoming solar radiation and indirectly by influencing the formation and optical properties of clouds; in addition, it contributes to reductions in air quality and human health [135]. PM also provides surfaces for chemical reactions and, thereby, influences the abundance and distribution of atmospheric trace gases (*e.g.* ozone and nitrogen oxides) [136].

High-resolution mass spectral analysis has revealed that heteroatom-containing compounds comprise a significant portion of the organic carbon fraction of PM [137, 138, 139, 140, 141]. One such class of compounds, organosulfates (OS, ROSO_3^-), has been measured in PM collected in a diverse range of locations, including the remote Arctic, [142] the Amazon rainforest, [143] the southern United States, [144] and urban and remote sampling sites in Asia [145]. Studies have shown that OS make a significant contribution to PM mass loadings; [146, 147, 148] for example, one large-scale study estimated that OS may make up as much as 5–10% by mass of the organic fraction of fine particulate matter (PM_{2.5}) [146]. In addition, OS have the potential to influence PM physicochemical properties, including hygroscopicity and cloud condensation nuclei (CCN) activity [149, 150, 151]. For these reasons, the formation mechanisms of this class of compounds have been the subject of much experimental interest.

Laboratory studies have provided evidence for a wide variety of pathways for OS formation, including H_2SO_4 -catalyzed esterification of alcohols, [152] nucleophilic attack by sulfate on epoxides, [153] uptake of SO_2 by long-chain alkenes and unsaturated fatty acids, [154, 155] uptake of glyoxal by SO_2 -aged $\alpha\text{-Al}_2\text{O}_3$, [156] reaction of hydrogen sulfite with unsaturated carbonyl compounds in the presence of Fe^{3+} , [157] and of particular interest to this study, the reaction of sulfate radical with organic radicals [158] and a range of unsaturated organics [149, 159, 160, 161].

In aqueous aerosol, sources of sulfate radical include the oxidation of S(IV) species in the presence of transition metal ions, [162] the hydroxyl radical oxidation of existing OS, [163] and the oxidation of hydrogen sulfate anion by the

hydroxyl radical [162]. Illumination of TiO_2 with light of energy greater than its band gap energy results in the formation of conduction band electrons and valence band holes, the latter of which can oxidize water to yield hydroxyl radical [164]. In addition, indirect evidence also exists for the production of sulfate radical via the direct, hole-mediated oxidation of sulfate at the TiO_2 surface [165]. In this context, we hypothesized that TiO_2 and Ti-containing minerals would facilitate the photochemical production of OS from unsaturated organic precursors.

In this study, we first present observations of photochemical OS formation from methacrolein (MACR) –a first-generation atmospheric oxidation product [166] of isoprene, the most abundant biogenic VOC, [167] which has been shown to be present in the atmospheric aqueous phase at concentrations much higher than those predicted by its Henry's law coefficient [168] –in aqueous suspensions of TiO_2 , where we use TiO_2 as a proxy for the photochemically active portion of atmospheric mineral dust [169]. To improve the understanding of this OS formation mechanism, OS production as a function of illumination time, TiO_2 loading, sulfate salt concentration and cation identity, and MACR concentration was measured. To provide further insight into the atmospheric importance of this mechanism, the OS production from MACR in the presence of three natural Ti-containing minerals (anatase, ilmenite, and mica) and urban road dust was explored. Together, these results provide new evidence for the role of mineral-organic interactions in OS formation and highlight the value of experiments performed using natural mineral samples.

3.2 Materials and methods

3.2.1 Experimental apparatus

Experiments were conducted in a custom-built photochemical reactor (~70 mL total volume; Figure B.1 of the Appendix B). Samples were illuminated using a solar simulator (SunLite, Abet Technologies), the spectral irradiance of which is presented in Figure B.2 of the Appendix B. Because the solar simulator spectrum exhibits a small tail extending to the blue of the actinic region, all experiments were performed with a 295 nm long-pass optical filter (Edmund Optics) located in the solar simulator light path.

To avoid sample heating, an ultraviolet (UV) hot mirror (Edmund Optics) was also placed in the light path. To compare the photon flux in our experiments to those in the ambient environment, we used chemical actinometry of 2-nitrobenzaldehyde (2-NB) [126]. Details of these experiments are presented in Appendix B and Figure B.3 of Appendix B. The photodecay rate constant for 2-NB, $j(2\text{-NB})$, obtained in these experiments was $(1.89 \pm 0.02) \times 10^{-3} \text{ s}^{-1}$, which is somewhat lower than those previously reported for a variety of ambient environments [170, 171]. Our results, therefore, represent a lower estimate for the mineral-catalyzed photochemical production of OS in the ambient atmosphere.

3.2.2 Experimental procedure

At the beginning of each experiment, the sample of interest (*i.e.*, TiO_2 or natural minerals) was placed in the photochemical reactor; then, a stir bar and 20 mL of an aqueous Na_2SO_4 (adjusted to pH 5 using 50 mM aqueous H_2SO_4) or $(\text{NH}_4)_2\text{SO}_4$ solution of the desired concentration was added. Finally, the reactor was closed; the sample port was equipped with a rubber septum; and MACR was added via a glass syringe through the septum into the stirred suspension. To minimize evaporation of MACR, all experiments were performed at 288 K. After 15 s of stirring under dark conditions, a $t = 0$ min sample was taken; then, samples were illuminated for 5–40 min. To ensure equilibration with ambient O_2 levels (*i.e.*, $\sim 3 \pm 10^{-4} \text{ M}$ dissolved O_2 at 288 K [172]), samples were gently stirred for the duration of each experiment. After illumination, samples (0.5 mL) were removed from the reactor via a syringe. To avoid injections of highly concentrated sulfate salt solutions, a methanol cleanup procedure was employed [149]. In this procedure, validation of which is described in Appendix B text and Figure B.4 of Appendix B, samples were added to a 15 mL centrifuge tube containing methanol (1.25 mL) as sulfate precipitation agent and potassium propyl sulfate (10 μL ; 5 mg mL^{-1} in water) as internal standard. The resultant mixture was vortexed for 30 s and centrifuged for 5 min at 3000 rpm; then, the supernatant was filtered (0.2 μm nylon filter, VWR) prior to analysis to remove any remaining sulfate precipitate and/or minerals. All reported OS concentrations and peak areas are corrected for dilution (*i.e.*, a dilution factor of 1.75:0.5). Because the propyl sulfate signal in our samples generally varied by $<3\%$, reported results are uncorrected. To verify that the observed OS products arose from photochemistry rather than dark reactions and that OS observed in experiments conducted using natural mineral samples

did not arise from photochemistry of mineral-associated organics, we conducted a comprehensive set of control experiments, which are described in detail in Appendix B text. No OS products were observed in any of these experiments.

3.2.3 OS quantification and analysis

Analysis of OS was accomplished using an Agilent 1100 high-performance liquid chromatography (HPLC) system equipped with a binary pump, autosampler, thermostated column compartment held at 40 °C, and Waters Micromass Quattro Micro triple quadrupole mass spectrometer as detector. Separation was performed using a Fisher Scientific Hypersil GOLD C18 column (Fisher Scientific, 3 μm particle size, 150 \times 4.6 mm) at a flow rate of 0.4 mL min⁻¹. A gradient elution was applied, with water (0.1% formic acid) as solvent A and methanol (0.1% formic acid) as solvent B: 10% B at $t = 0$; 2 min linear gradient to 90% B; 2 min hold; immediate reduction to 10% B; and hold until 15 min. An injection volume of 5 μL was used for all separations.

The analysis was run in multiple reaction monitoring (MRM) mode using negative-mode electrospray ionization. In all cases, the $[\text{M} - \text{H}]^- \rightarrow m/z 97$ transition was employed for analysis and quantification. Detailed mass spectrometric parameters are presented in Table B.1 of Appendix B, and representative chromatograms showing OS products are presented in Figure B.5 of Appendix B.

Hydroxyacetone sulfate (HAS, m/z 153) was quantified via comparison to an external calibration curve (Figure B.6 of Appendix B) prepared using synthesized potassium HAS as standard. The calibration curve was obtained at the beginning of the study. To verify signal stability over time, one low and one high standard from the points on the calibration curve were measured each day. In the absence of synthesized standards, peak areas were used for semi-quantitative comparative analysis of all other OS analytes. As shown in Figure B.5, chromatograms of several of these analytes exhibited multiple peaks, which suggests the existence of multiple isomers for these species. All reported peak areas consist of the sum of the areas of all detected peaks at a given m/z value.

3.2.4 Sample collection, preparation, and characterization

The natural minerals employed in this study were obtained through Minfind (www.minfind.com). The anatase, ilmenite, and mica samples were collected

in Pakistan, the United States, and Canada, respectively. Details regarding sample pretreatment and grinding are presented in Appendix B. The Edmonton road dust sample consists of winter street sweepings (*i.e.*, material collected from city streets in spring after winter application of sand and salt for road traction/safety purposes) and was obtained from one of four City of Edmonton (Alberta, Canada) snow storage facilities, located at 17 Street (north of Whitemud Drive at approximately 52 Avenue); its <45 μm fraction was isolated using a Retsch AS200 analytical sieve shaker.

Samples were comprehensively characterized using a variety of analytical techniques, which are briefly described here; further details are presented in Appendix B. The Brunauer-Emmett-Teller (BET) surface areas of commercial TiO_2 , anatase, and ilmenite were determined using N_2 adsorption; results are presented in Table B.2 of Appendix B. Electron microprobe analysis was used to assess the purity of the anatase, ilmenite, and mica samples; quantitative compositional data are presented in Table B.3 of Appendix B. The Edmonton road dust sample was examined using scanning electron microscopy (SEM) with energy-dispersive spectroscopy (EDS) analysis for elemental mapping. A sample EDS spectrum and representative elemental mapping results are shown in Figure B.7 of Appendix B. The mineralogy of all samples was assessed via X-ray diffraction analysis, as shown in Figure B.8 of Appendix B.

3.2.5 Chemicals

Potassium HAS and potassium propyl sulfate were synthesized according to established literature procedures, [173, 174] which are summarized in Appendix B. Nuclear magnetic resonance (NMR) spectra, high-resolution mass spectra, and product ion scans of the synthesized OS are presented in Figures B.9-B.12 of Appendix B. Deionized water was obtained from a Millipore Synergy UV ultrapure water system. All other chemicals were obtained from commercial suppliers and used as received, as outlined in Appendix B.

3.3 Results and discussion

3.3.1 TiO₂-catalyzed production of HAS: influence of illumination time and catalyst loading

Given the compositional complexity of natural mineral samples, [132] we first conducted studies of OS formation in the presence of commercial TiO₂. As shown in Figure 3.1, illumination of MACR in aqueous Na₂SO₄ in the presence of TiO₂ leads to the production of HAS, an OS not only identified in previous studies of sulfate radical-catalyzed OS formation from this precursor [149, 159, 160] but also commonly measured in ambient PM [144, 159, 175].

Figure 3.1 shows that HAS production increases linearly with illumination time and monotonically but nonlinearly with increasing TiO₂ loadings; in the absence of TiO₂, HAS is not produced. Although plateaus in TiO₂-catalyzed photochemistry at elevated catalyst loadings are generally attributed to catalyst agglomeration and light-shielding effects, [176, 177] these effects typically become important at higher loadings than those explored in these experiments. For example, even though we estimate no reduction in effective photon flux in our reactor in the presence of 0.25 mg mL⁻¹ TiO₂ (using chemical actinometry of 2-nitrobenzaldehyde [126]; results not shown), we observed nonlinear HAS production at even lower catalyst loadings (*e.g.* HAS production at 0.1 mg mL⁻¹ TiO₂ was only ~50% larger than at 0.01 mg mL⁻¹).

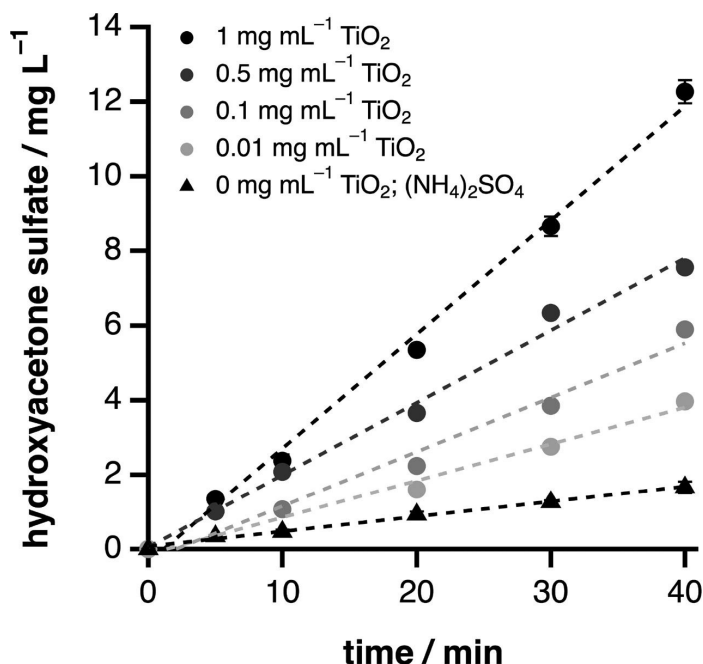


Figure 3.1: Time-dependent HAS production from MACR (10 mM) in illuminated suspensions of TiO₂ in aqueous Na₂SO₄ (1 M; adjusted to pH 5) or (NH₄)₂SO₄ (1 M) in the absence of TiO₂. For experiments at the highest TiO₂ loading, all TiO₂ loadings at 30 min, and in the presence of (NH₄)₂SO₄, data points represent the mean of three trials, with 1- σ error bars; otherwise, data points show the results of one trial. The dashed lines are linear fits to the experimental data.

We attribute the nonlinearity in HAS production with respect to TiO₂ loadings to the TiO₂-catalyzed loss of HAS, which we would expect to adsorb to the TiO₂ surface more strongly than MACR as a result of favorable electrostatic interactions between TiO₂ and its anionic sulfate moiety [164]. Support for this interpretation is provided by a set of experiments (Figure B.13 of Appendix B) showing rapid loss of HAS in the presence of 0.5 mg mL⁻¹ TiO₂, only partial inhibition of this loss in the presence of MACR, and no HAS loss in the presence of TiO₂ under dark conditions. Because all of the experiments shown in Figure 3.1 were performed at the same MACR (10 mM) and sulfate (1 M) concentrations, we would expect competitive adsorption by both MACR and sulfate anion [165] to limit HAS loss most effectively at lower TiO₂ loadings.

3.3.2 TiO₂-catalyzed production of HAS: sulfate concentration dependence and cation effects

As shown in Figure 3.2, TiO₂-catalyzed HAS production from MACR in aqueous Na₂SO₄ displays a nonlinear dependence upon sulfate anion concentration. These results are consistent with a surface reaction mechanism, in which HAS production at elevated sulfate anion concentrations is limited by the saturation of available surface sites for adsorption.

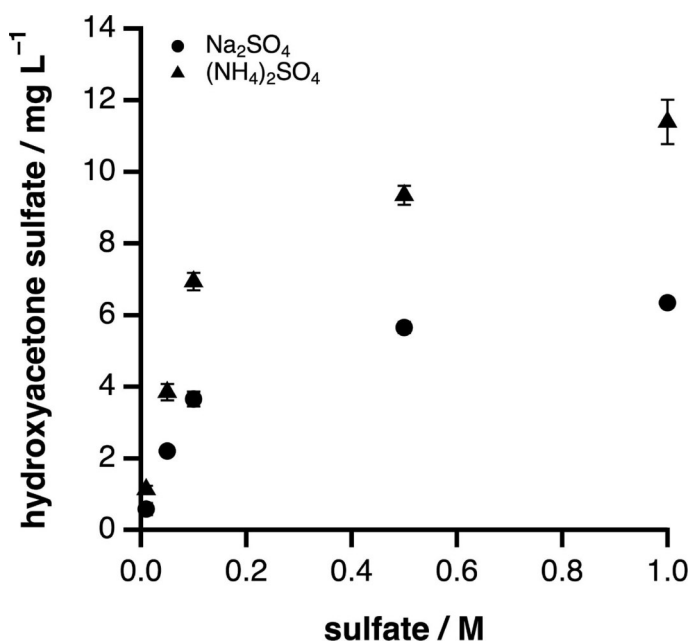
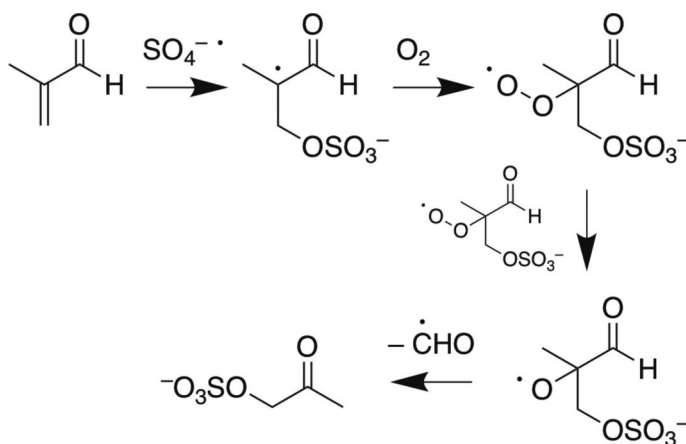


Figure 3.2: HAS production from MACR (10 mM) in illuminated (30 min) suspensions of TiO₂ (0.5 mg mL⁻¹) in aqueous Na₂SO₄ (1 M; adjusted to pH 5) or (NH₄)₂SO₄ (1 M). Each data point represents the mean of three trials, with 1- σ error bars.

In our proposed mechanism, sulfate adsorbs to the TiO₂ surface, where it undergoes one-electron oxidation, [165] and the resultant sulfate radical subsequently adds to MACR to yield HAS via the mechanism [159] shown in Scheme 3.1.



Scheme 3.1: Proposed mechanism for production of HAS (m/z 153) via sulfate radical addition to MACR.

Sulfate radical can also be formed in bulk aqueous solution via the reaction of hydroxyl radical, produced here via TiO_2 photocatalysis, [178] with hydrogen sulfate anion ($k = 3.5 \times 10^5 \text{ M}^{-1} \text{ s}^{-1}$) [179]. However, under our experimental conditions (*i.e.*, pH 5, where $[\text{HSO}_4^-] \sim 1 \text{ mM}$), the reaction of hydroxyl radical with MACR (10 mM ; $k = 9.4 \times 10^9 \text{ M}^{-1} \text{ s}^{-1}$) [113] would dominate at even the highest sulfate anion concentrations. Therefore, HAS production via this mechanism would be expected to increase linearly with increasing sulfate anion concentration, which is inconsistent with our results. In the absence of further data, we cannot exclude that the production of the hydroxyl radical itself exhibits a plateau at elevated sulfate anion concentrations. Quantification of hydroxyl and sulfate radical production in situ via the use of probe molecules [180] would provide further insight into the fundamental mechanism(s) underlying the observed results, but is beyond the scope of the current work.

Interestingly, Figure 3.2 shows that the TiO_2 -catalyzed production of HAS is higher in aqueous $(\text{NH}_4)_2\text{SO}_4$ than in aqueous Na_2SO_4 ; in addition, as displayed in Figure 3.1, illumination of MACR in aqueous $(\text{NH}_4)_2\text{SO}_4$ leads to the production of modest quantities of HAS, even in the absence of TiO_2 . This latter observation agrees with Noziere et al., who observed the formation of a range of OS upon illumination of MACR in concentrated aqueous $(\text{NH}_4)_2\text{SO}_4/\text{Na}_2\text{SO}_4$ [149]. we suggest that all of these observations can be explained by a multistep process for the formation of additional sulfate radical, involving the production of light-absorbing SOA material by the reaction of ammonium with MACR, [181] the subsequent

photolysis of this material, and the reaction of the hydroxyl radicals thus formed [128] with hydrogen sulfate anion to yield sulfate radicals. Because, as discussed above, the aqueous-phase reaction of hydroxyl radical with hydrogen sulfate anion is slow compared to its reaction with dissolved organics, sulfate radical production via this reaction would be expected to represent a minor reaction channel for photoproducted hydroxyl radical. Our observations of enhanced OS production in aqueous $(\text{NH}_4)_2\text{SO}_4$ therefore suggest that absolute hydroxyl radical production from photolysis of ammonium-MACR reaction products may be substantial. We are currently conducting *in situ* quantification of hydroxyl radical production [128] in this experimental system, which we anticipate will help to explain these observations.

3.3.3 TiO_2 -catalyzed production of additional OS products: MACR concentration dependence and cation effects

To gain further insight into TiO_2 -catalyzed OS formation, we also performed experiments as a function of MACR concentration (1-40 mM) in both aqueous Na_2SO_4 and $(\text{NH}_4)_2\text{SO}_4$. In both cases, the production of HAS does not increase with increasing MACR concentration (Figure B.14 of Appendix B). In the context of our proposed mechanism for HAS production, this observation is consistent with the reaction being sulfate radical-limited over this MACR concentration range.

As shown in Figure 3.3, the production of several OS compounds with m/z 253 [liquid chromatography-tandem mass spectrometry (LC-MS/MS) chromatograms show multiple peaks; Figure B.5 of Appendix B] increases with increasing MACR concentrations in both aqueous Na_2SO_4 and $(\text{NH}_4)_2\text{SO}_4$.

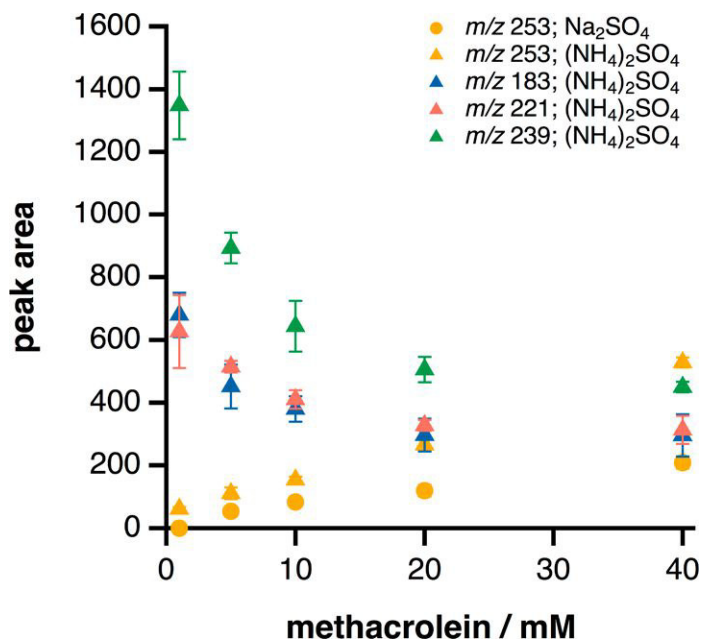
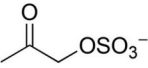
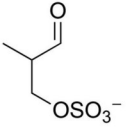
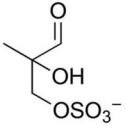
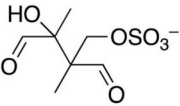
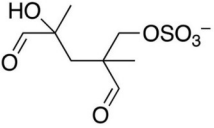


Figure 3.3: OS production from MACR in illuminated (30 min) suspensions of TiO_2 (0.5 mg mL^{-1}) in aqueous Na_2SO_4 (1 M; adjusted to pH 5) or $(\text{NH}_4)_2\text{SO}_4$ (1 M). Each data point represents the mean of three trials, with $1-\sigma$ error bars.

In addition, the total m/z 253 signal increases linearly with illumination time (Figure B.15 of Appendix B), which implies that it reflects contributions from first-generation products rather than products formed from further reaction of HAS. These results are consistent with previously proposed formation mechanisms for these species, [149, 159] in which the alkyl radical produced via sulfate radical reaction with MACR reacts with an additional molecule of MACR to ultimately form a set of isomeric OS dimers with m/z 253 (Table 3.1). In addition, these results provide insight into a recent study by Wach et al., [160] which did not report production of these dimeric OS from the solar irradiation of dilute (0.2 mM) MACR solutions containing potassium persulfate as sulfate radical precursor. Finally, we note with reference to Figure B.15 of Appendix B that the production of the m/z 253 OS increases exponentially with TiO_2 loadings, with production at 1 mg mL^{-1} approximately 4 times larger than that at 0.5 mg mL^{-1} . In the context of previous work, [159] which has shown m/z 253 to be photolytically labile, we hypothesize that these observations reflect reductions in effective photon flux in our reactor at these elevated TiO_2 loadings. Further, they imply that, unlike HAS, the dimeric m/z 253 OS do not undergo substantial TiO_2 -catalyzed loss, most

likely as a result of their relatively more hydrophobic nature and resultant lower propensity to adsorb to the TiO₂ surface.

Table 3.1: Proposed structures for the OS observed in the present experiments. (* for which LC-MS/MS chromatograms show evidence for multiple isomers.)

m/z $[M - H]^{-1}$	Proposed structure	References
153		159, 160
167		159
183*		159, 160
221*	unknown	159
239		149
253*		149, 159

Interestingly, Figure 3.3 also shows that three additional OS with m/z 183, 221, and 239 are produced when (NH₄)₂SO₄ is used as the sulfate source; these OS, as well as the m/z 253 OS, are also produced in smaller quantities in the absence of TiO₂ (results not shown). Together, these results provide additional evidence for the importance of ammonium-mediated pathways in photochemical OS formation. All three of these OS have been previously reported in one or more laboratory studies of sulfate radical-mediated OS formation; [149, 159, 160] in addition, OS with m/z 183 [149, 173] and m/z 239 [182, 183] have been reported in ambient samples. The production of these OS decreases with increasing MACR concentrations, which suggests that the ammonium-mediated OS formation pathways discussed above are suppressed by competing reaction

pathways at elevated MACR concentrations. Proposed structures for these additional OS are presented in Table 3.1.

3.3.4 Unexpectedly high OS production in the presence of natural mineral samples

To assess the environmental relevance of the TiO_2 -catalyzed OS formation pathway described in the previous sections, we also conducted experiments using natural anatase, ilmenite, and mica as well as road dust collected in Edmonton, Alberta. Interestingly, as shown in Figure 3.4, HAS concentrations resulting from illumination of MACR in aqueous Na_2SO_4 in the presence of these samples are the same order of magnitude as the HAS concentration in suspensions of commercial TiO_2 . Because we would expect these samples to have lower inherent photoreactivity than TiO_2 , these results are surprising.

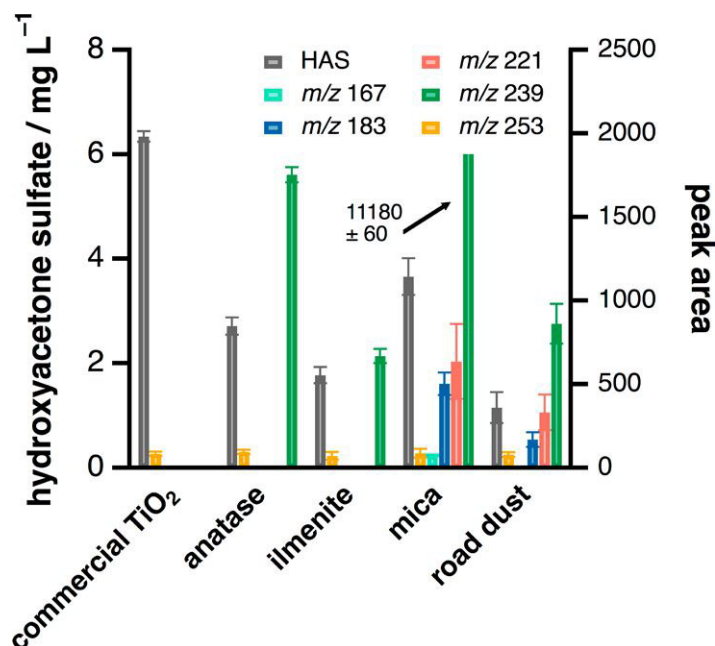


Figure 3.4: Production of HAS (mg L^{-1} ; m/z 153) and other OS (peak area) from MACR (10 mM) in illuminated (30 min) suspensions of TiO_2 and natural mineral samples (0.5 mg mL^{-1}) in aqueous Na_2SO_4 (1 M; adjusted to pH 5). Each data point represents the mean of three trials, with $1\text{-}\sigma$ error bars.

As discussed in section 3.3.1, HAS undergoes rapid TiO₂-catalyzed photodegradation, even in the presence of MACR. Although little is currently known regarding aerosol-phase OS loss pathways, these results complement those of two recent studies exploring the heterogeneous hydroxyl radical oxidation of sodium methyl sulfate [163] and 3-methyltetrol sulfate ester [184]. Because we would expect HAS loss to be influenced not only by MACR but also by competitive adsorption of sulfate at the surface of the samples employed in this study, a full understanding of HAS formation and loss kinetics in our experimental system would require experiments as a function of both MACR and sulfate concentrations for each sample type. Although these experiments are beyond the scope of the present study, our preliminary results suggest the need for further investigation of mineral-catalyzed OS loss.

Although the similarity in apparent HAS production between commercial TiO₂ and natural mineral samples may simply reflect efficient loss of HAS at the surface of TiO₂, as discussed above, we posit that it may also reflect the existence of additional OS production pathways in the presence of these more complex substrates. Support for this latter suggestion is provided by Figure 3.4, which shows production of a broader range of OS in the presence of mica and road dust than in the presence of commercial TiO₂. The OS produced in the highest quantity in these experiments is one with m/z 239, which is of interest because an OS with this mass-to-charge ratio has been reported in ambient PM, in some cases in large quantities [147, 182, 183]. In one study, Mutzel et al. [183] suggested that this OS arose via the interaction of gas-phase organic species with acidic PM; in another study, Brüggeman et al. [182] showed that formation of this OS also occurred under low-acidity PM conditions. Here, we provide evidence for a pathway for the formation of this OS that does not require acidic conditions.

3.3.5 Mineral-catalyzed OS production: implications for catalysis and atmospheric aerosol composition

In a seminal study, Abdullah et al. reported that the TiO₂-catalyzed photooxidation of organic solutes was not fully inhibited in the presence of sulfate, even though this anion would be expected to competitively occupy surface oxidizing sites [165]. These authors attributed this observation to sulfate radical production at

the TiO₂ surface and subsequent reaction of this species with the organic solutes studied. Our observations of HAS production from MACR in suspensions of TiO₂ in aqueous sulfate solution provide the first direct evidence in support of this hypothesis; in addition, they highlight the need for further mechanistic studies of the influence of inorganic anions on the product distribution resulting from TiO₂-catalyzed aqueous organic photochemistry.

More broadly and in an atmospheric context, our results also highlight the importance of mineral-mediated photochemistry for the aqueous-phase production of OS from unsaturated organic precursors. Although mineral dust is primarily emitted in remote arid regions, [185] it undergoes efficient long-range transport and can interact with potential organic OS precursors both during transport [186, 187] and upon arrival in urban [188] and/or remote [189] receptor regions; in addition, dust is often internally mixed with sulfate [190]. In this context, our results represent an important first step toward understanding the photochemical sources of OS in dust-influenced regions.

Chapter 4

TD-GC-FID/MS system

Contributions: This manuscript was written by Mario Schmidt, with critical comments from Dr. Sarah A. Styler

4.1 Introduction

Volatile organic compounds (VOCs) are emitted into the atmosphere from biogenic and anthropogenic sources, [191, 10, 192, 193, 194] and may also be formed as products of atmospheric VOC transformations [195]. Worldwide, biogenic emissions of VOCs are estimated to be as high as 750 - 1000 Tg of carbon per year from vegetation [196, 197] and comparatively approximately 100 - 160 Tg (C) per year from anthropogenic contributions [198, 199]. Once emitted into the atmosphere, VOCs can undergo chemical processes including VOC transformation (*e.g.* VOC oxidation (OVOCs) [195]. The production of OVOCs from gas-phase species is related to the formation of secondary organic aerosols (SOA) [200] accounting for a large fraction of organic aerosols (OA) [201, 60, 202, 61, 40, 203]. As submicron particle class (PM_{2.5}), OA are considered to possibly highly impact radiative climate forcing [204] and human health [205].

Smog chamber have been developed already in the 1950s as potent tools to study aerosol formation from biogenic and anthropogenic precursors. [206, 207] and have been further refined for the purpose of SOA research projects [208, 209, 210, 211, 212, 213]. Outdoor smog chambers offer the advantage to use natural sunlight, which can also turn into a disadvantage by variation of light intensity and thus causing limited reproducibility. In contrast, indoor chambers usually apply artificial light and are more accurate related to temperature and relative humidity control.

In order to better understand the rates, mechanisms, and products of VOC oxidation during chamber experiments, the atmospheric community has employed a suite of analytical instrumentation to monitor the particle and gas phase compositions [84, 81]. Techniques for monitoring the gas-phase composition during these experiments include analyzers applying optical, spectroscopic techniques (*e.g.* UV photometric, chemiluminescent, fluorescent analyzers) to detect and quantify species such as O₃, NO_x, SO₂, and CO. Organics such as VOCs and corresponding oxidation products can also be analyzed via differential optical absorption spectroscopy (DOAS) [91], gas-chromatography based techniques with hyphenation to mass spectrometry (GC-MS) [214] as well as proton-transfer-mass spectrometry (PTR-MS) [215]. Whereas DOAS is a widely used, sensitive technique also for the determination of radical species it does not provide enough information for structural elucidations of complex mixtures of chemical compounds due its dependence on the (narrowband) differential absorption cross-section and

thus is dependent on the wavelengths of light employed inside the smog chamber. PTR-MS is an excellent technique for real-time measurements of VOCs with a very short response of less than one second, low detection limits for VOCs (lower ppt) and was already further developed to detect isobaric compounds [215], has been already coupled to time-of-flight mass analyzers to increase the previously lower mass resolution [216]. However, the PTR-related soft-ionizing formation of protonated species or clusters may cause difficulties for compound identification [217]. Despite the application of alternative ionization reagents (e.g. NO^+ , O_2^+) as in selected-ion flow-tube mass spectrometry (SIFT-MS) [218], the more traditional technique using GC-MS with electron impact ionization (EI) still represents a common method for VOC analysis and was furthermore described as complementary technique with PTR-MS [219]. A major drawback of gas chromatographic on-line analyses is the relatively high cycle-time starting with sampling and sample injection, GC re-equilibration which causes a lower time-resolution in experiments. In the simplest version of on-line GC-MS gas-phase monitoring, chamber air is directed through a sampling loop for subsequent injection onto the GC column [211].

However, loop injection procedures were characterized by high detection limits and low sensitivities compared to GC systems, that include a preconcentration step via an adsorbent packed microtrap and following thermal desorption (TD) [220, 221, 222]. Analytical thermal desorption is an automatable gas-phase extraction/introduction technique for vapour-phase analytical instrumentation such as GC-FID/MS [223]. The application of adsorbent traps in general and microtraps were already reviewed in detail regarding adsorbent type, adsorbent tube handling, applications for air sampling [98, 99, 101, 102], and were also further developed for sorbent-free high-speed injections applying cryofocusing [224].

Despite the large cooling capacity of liquid cryogenes, such as N_2 and CO_2 , to quickly cool down (adsorption) traps for efficient and fast preconcentration steps after finished GC separation, there is always a demand on cryogen supply as well as a certain safety requirement that needs to be considered in closed laboratory environments. In contrast to cryogenic cooling, environmentally friendlier cooling methods such as the application of Peltier elements [225] or Stirling coolers [226] were used for the temperature control of adsorbent trap tubes, both only relying on electrical energy. Peltier elements are widely employed as small cooling devices

but cannot compete with the cooling efficiency of Sterling coolers, which are less common in thermal desorption setups. Also, different heating methods for trap tubes have been subject of research including resistively heated NiCr wires [227] or Pt wires [228] wrapped around the sorbent tube, flushing an electrical current directly through the trap tube by capacitive discharge [229, 230, 231], which is also used for 2D-GC modulation [232, 233], as well as an inductively heated trap tube setup [234].

Process automation is another key to generate reliable and traceable data. The first commercially automated thermal desorbers (ATD) was built, applied in the 1980s [235]. These instruments were further developed by different companies introducing new features such as partial sample re-collection after thermal desorption, automated internal standard injection or multi-tube measurements. However, in addition to increasing expenses for a related automated thermal desorber purchase, there is the disadvantage that an additional sampling step is necessary, which requires additional instrumentation to realize, for example, a fully automated on-line VOC monitoring including sample collection and analysis. Consequently, customized automated TD-GC systems with different hyphenation techniques were developed [236, 237, 238, 239, 240, 226].

Considering the complexity of available technical solutions, the variety of available options to realize customized thermal desorption-gas chromatography-mass spectrometry (TD-GC-MS) setups for higher time resolution compared to traditional offline VOC sampling and analysis techniques, there is always a question which analytical approaches, desorption tube types and cooling or heating efficiencies are required to achieve a robust, easily maintainable, safe and cost-efficient instrumentation for a specific scientific purpose, in this case the coupling to a smog chamber for VOC and OVOC monitoring.

Here, we present a newly developed, fully automated GC-TD-FID/MS system for smog chamber studies of VOC oxidation processes. In particular, we present the usage of a (hydrophobic) sorbent laden micro-trap, with cryogen-free cooling by a Peltier element to achieve sub ambient temperatures (e.g. 10 °C to avoid water accumulation as well as fast resistive heating above 200 °C to minimize band-broadening without a second-stage focusing trap, and give detailed mechanical, electronical information for a successful reproduction or further development by the atmospheric community.

4.2 Thermal desorption unit

4.2.1 Design considerations and technical design

Thermal desorption units usually have two main characteristics in common, which are the mechanical and electrical realization of fast trap tube cooling and heating, to preconcentrate and release formerly trapped gas phase species with a high time-resolution data acquisition. These aspects can be approached in different ways, which may depend on the final application area of the instrument (*e.g.* indoor laboratory, outdoor vehicle or planes) as well as on the analyte's concentration, vapor pressure, and adsorptive properties. Different analyte-dependent cooling techniques may be necessary to achieve a high preconcentration efficiency without compound breakthrough at low sorbent temperatures and suitable (*e.g.* weak, strong or mixed) sorbent materials. There are several, fundamental requirements for the developed thermal desorption unit.

(1) A cryogen-free, environmentally friendly cooling is desired to avoid the continuous demand for and dependence on potentially limited liquid nitrogen or carbon dioxide and the need for water vapour removal from the incoming gas stream. (2) The sorbent tube needs to be easily accessible for fast maintenance without interrupting a carrier gas supply or sampling stream, for example, due to removal of corresponding trap tube fittings to remove the trap tube from the desorption setup. (3) The contact area between Peltier cooled surfaces and heated zones are as large as possible to guarantee a fast cool down. (4) The heating method must provide the option to bake out the trap tube at a fixed temperature to remove any organic residues and heating must overcome a continuous Peltier cooling. (5) The overall signal process is designed in a way, which offers the flexibility to change single process parameters (*e.g.* heating rate, cooling temperature, sampling time) without a compromise on automation. Hence, all involved instruments and related functions need to be triggered in a signal cascade but are still available for manual adjustments to either stop or improve the parameters during a running process. (6) The overall setup is supposed to be flexible to adjustments (*e.g.* trap tube diameter) and presents also an affordable solution for a reliable on-line thermal desorption unit. Therefore, in Figure 1 a new thermal desorption unit is presented, which is based on a design modification of a consumable-free, single-stage modulator for comprehensive two-dimensional

gas chromatography, re-designed from a previous model [225] to fit our purpose for smog chamber investigations in atmospheric chemistry.

Figure 4.1A presents an overview of the general TD setup, which includes two copper plates (A1; 15 cm × 6 cm × 0.3 cm), cooled by a thermoelectric module (A2; Digi-Key#:926-1279-ND, Liard Technologies), further called Peltier element. The Peltier element is pressed between one copper plate and a heat sink (A3; Noctua NH-D9DX i4 3U; 110 mm × 95 mm × 95 mm), which is needed to cool the hot side of the Peltier element. Two fans (A4; 12 V DC, 0.28 A, 9 cm × 9 cm × 2.5 cm) are used on each side of the heat sink for active cooling and final heat transport.

An external ATX power supply (A5) extracted from a computer unit is re-used to provide a DC current for one of the two fans of the heat sink and for a Peltier element temperature controller (A6), which in turn acts as a power supply for the Peltier element and the second heat sink fan. An NTC temperature sensor (A7) is used as a temperature feedback mechanism to adjust the copper plate cooling.

Furthermore, the temperature of the trap tube surface (A8) is measured by a K-type thermocouple (A9), which feeds into a temperature acquisition box (A10) containing an Arduino UNO R3 unit with a MAX31855 cold-junction compensated thermocouple-to-digital converter. Another Arduino UNO R3 unit (A11) with a 5 VDC relay (Tongling, 10 A/250 V and 15 A/125 V) allows for time-dependent heating cycles of the trap tube, controlling a DC current (22 V, 2.323 A) supplied by a 0 - 30 V and 0 - 5 A power supply (A12; Korad KD3005D). Two banana plug cables with alligator clip ends are connected to both ends of the 30 gauge NiCr 80 wire (obtained from Master wire supply) and the corresponding Korad DC power supply unit (A12). The NiCr wire has a total length of 11.1 in, which is corresponding to approximately 13 wrappings per inch steel tube over a wrapped trap tube length of 2.2 in. A TD unit holder (A 13) with two clamps presses both copper plates together to increase the contact area with the trap tube, which is shown more in detail in Figure 4.1 B.

A Sulfinert® 304 SS stainless-steel tube (B1; 3.9 in × 0.04 in × 1/16 in) is pressed between two flexible, very high-temperature resistant and 0.004 in thick Mica sheets (B2) obtained from McMaster-Carr. The Mica sheets provide electrical insulation between the copper plates (B3) and the NiCr wire (B4), which is used for resistive trap tube heating and is wrapped around the trap tube. A glass fiber insulation sleeve (B5) is pushed over the stainless-steel trap tube to

avoid electrical contact between the trap tube and the NiCr wire, which would cause a major loss of heating efficiency. The K-type thermocouple (B6) is placed between the glass fiber sleeve and the trap tube. Milled depressions (B7) provide enough room for the trap tube setup to be squeezed in-between the copper plates. An NTC temperature sensor (B8) works as temperature feedback for a Peltier element controller, both also shown as A6 and A7 in Figure 4.1 A.

Furthermore, a sampling line (connected to the chamber/calibration gas generator) and 10-port valve heating mechanism (not shown) applying NiCr 60 alloy wire is realized by using two 12 VAC, 3 A power supplies coupled to two solid state relays (Omega, 25 A, 24-280 VAC) and two 1/32 DIN ramp/soak controllers (Omega, CN7523) for a final temperature control application.

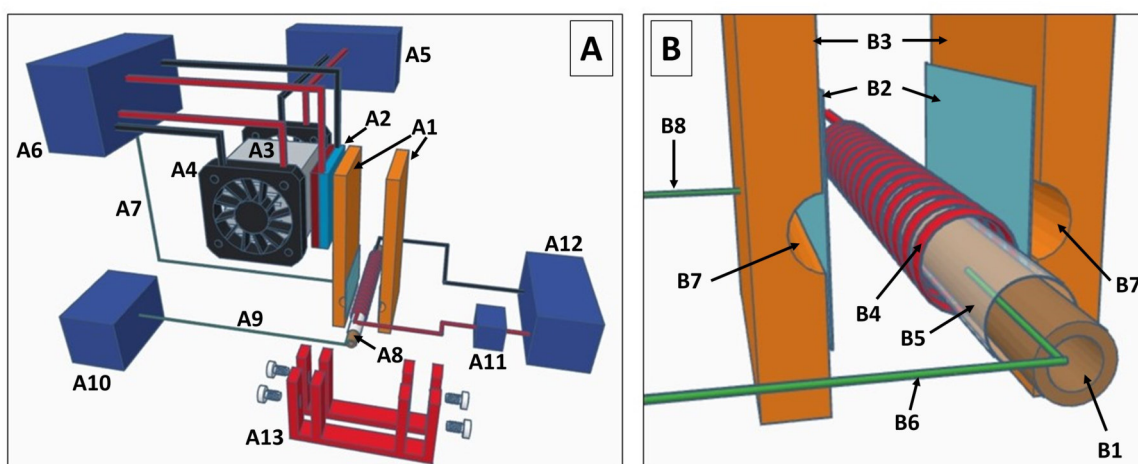


Figure 4.1: (A) Thermal desorption trap overview showing copper plates (A1), Peltier element (A2), heat sink (A3), fans (A4), ATX power supply (A5), Peltier temperature controller (A6), NTC temperature sensor (A7), stainless-steel trap tube (A8), K-type thermocouple (A9), temperature acquisition box (A10), relay control box (A11), DC power supply (A12); (B) Detailed view on the trap tube setup showing the stainless-steel tube (B1), Mica sheets (B2), copper plates (B3), NiCr80 alloy wire (B4), glass fiber insulation (B5), K-type thermocouple (B6), milled depressions (B7), NTC temperature sensor (B8).

4.2.2 Trap tube preparation

The design of a thermal desorption tube is essential for the proper function of any kind of TD-based air monitoring systems. Most commercially available TD

tubes are made from glass, stainless-steel or inert-coated stainless-steel, which can contain a sorbent material and frits (or glass wool plugs with a spring) to retain the sorbent bed in place. Stainless-steel tubes provide the advantage of a higher thermal conductivity for a fast temperature increase of the sorbent but do not offer the visual transparency of glass, which makes the sorbent filling process more difficult. The majority of prepared and purchasable TD tubes are larger in diameter than needed for the application of a microtrap. Hence, the trap tube preparation for a 1/16 in (OD) stainless-steel tube is presented in Figure 4.2. The trap tube is cut to a total length of 10 cm. During step A, a lathe machine with a Hartridge 1/16 5c collet is used to squeeze 1 cm of the tube to an inner diameter of 0.0023 in. Afterward, a vacuum supply is connected to the squeezed tube side to move a deactivated glass wool (obtained from Chromatographic Specialties Inc) plug to the narrower tube position in step B. A funnel in step C is made from a male ISO/BSP tapered thread tube adaptor with a Teflon ferrule to temporarily connect the funnel to the trap tube and for vacuum-assisted loading of the trap tube with a sorbent material (~11.5 mg of Tenax TA). In the following step D, a second glass wool plug is added with supporting vacuum and by manually pushing the plug into the tube with a stainless-steel wire. Afterward, in step E the trap tube is squeezed again, and 1/16 in stainless-steel fittings are added for a final connection to a pressurized Helium supply line in step F, which also includes the conditioning of the trap tube. Conditioning (cleaning process) is done at elevated temperatures (260 °C for 12 h followed by 310 °C for 1 h) using a temperature ramp of 10 °C/min) with a constant carrier gas flow of 20 mL min⁻¹ [99]. Both ends of the trap tube are then closed with corresponding 1/16 in stainless-steel plugs for storage until the trap tube is used.

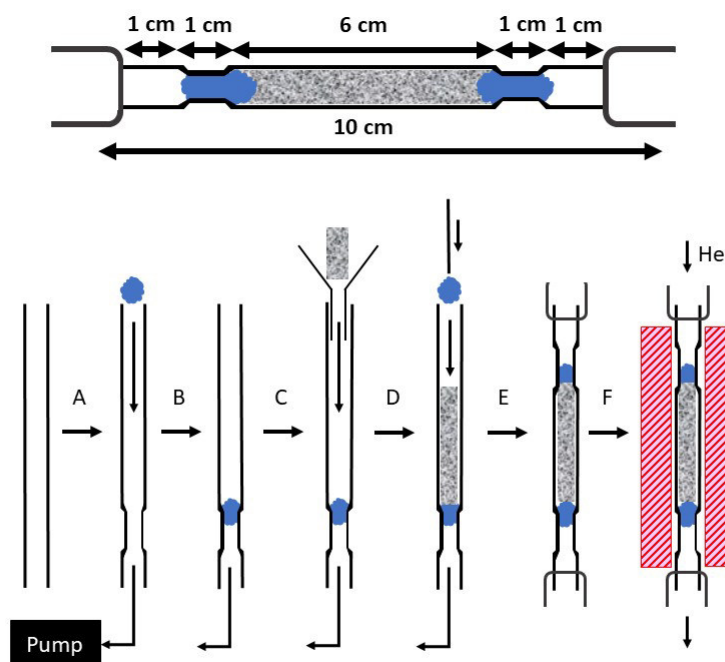


Figure 4.2: Schematic and step-wise overview of the customized production of a sorbent packed thermal desorption tube including vacuum-assisted loading of squeezed 1/16 in stainless-steel tube (A) with silanized glass wool (B), a sorbent (C) and another silanized glass wool plug (D), followed by a final squeezing step to keep sorbent material inside the tube (E) and the attachment of 1/16 in fittings (F).

4.2.3 Electronic control and temperature monitoring

In addition to the mechanical design and production of the basic TD unit parts, the realization of the communication between single components for creating an automated process of preconcentration and thermal desorption is another key aspect. Figure 4.3 presents a general overview of this process automation. Chromeleon 7.2 (ThermoFisher Scientific) is used as chromatographic data system installed on a computer to create sequence lists for several consecutive sample runs. The sequence list assigns a specific GC-/FID-MS method to each run. Since the GC method contains both the sampling and desorption step, Chromeleon 7.2 sends signals via an RS-232/USB converter to a two position actuator control unit, which is connected to the 10-port two position valve.

The two positions are assigned to either sampling (position B) or desorption (A) flow directions. Consequently, this first process can be summarized as sampling/injection control communication between the computer and the 10-port valve. A second signal pathway exists between the computer (Chromeleon 7.2) and the GC-FID/MS system via a manual valve actuation controller, which is connected to a 10-pin cable in both directions, towards the computer and towards the GC-FID/MS system. This 10-pin cable is split for coupling the first (red) pin and the third (grey) pin to the GC autosampler handshake cable, which is split as well to finally use the red and black pin. Soldering both split cables together by combining the single pins (red_{10-pin}+red_{handshake}; grey_{3rd,10-pin}+black_{handshake}) results in the realization of the feedback loop between the computer and the GC to run sequences of several samples. A third signal pathway is established between the computer and an external Arduino UNO R3 unit, which is responsible for the automated heating or cooling of the trap tube, by either turning heating on or off. Since there is another pin of the 10-pin cable left, which is assigned to transfer a signal for valve position B, this pin (fourth grey pin) is applied to trigger the Arduino UNO R3 controlled heating. Figure C.1 in Appendix C shows the Arduino board wiring for the relay thermal desorption control, which is supplemented by the Arduino sketch in Figure C.2. Furthermore, the Arduino board wiring for the temperature monitoring application is shown in Figure C.3, supplemented by the Arduino sketch in Figure C.4.

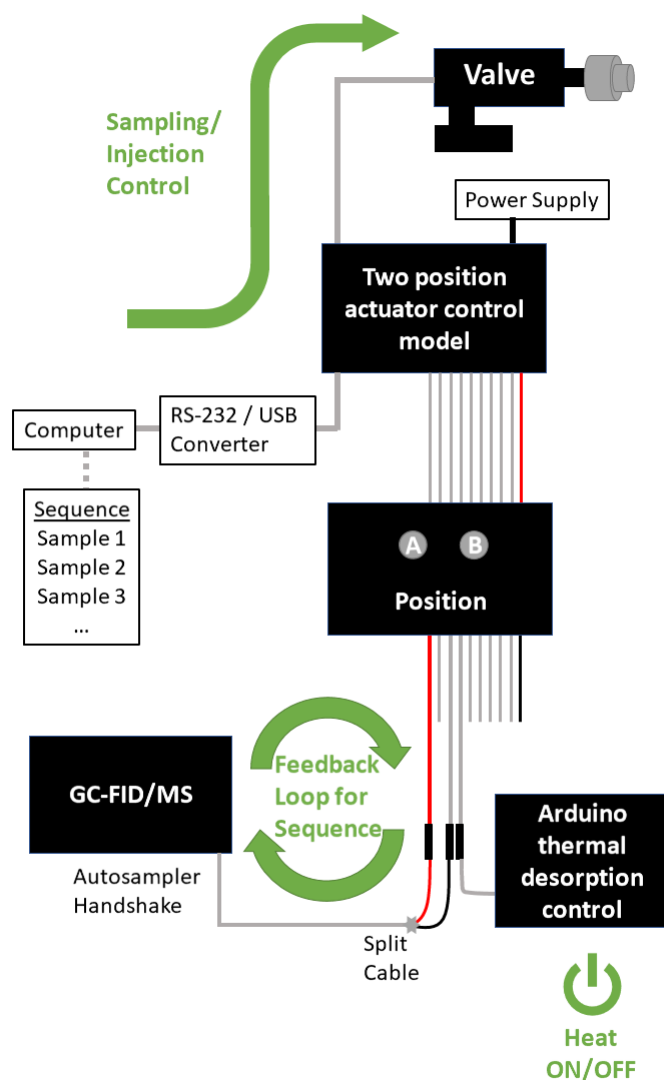


Figure 4.3: Overall scheme of the integrated process automation beginning with a created sequence list for conditional sampling and injection procedures followed by GC-FID/MS communication via a valve actuator model and the Arduino logic controlled heating or cooling mechanism of the sorbent packed trap tube.

Furthermore, a general overview of different timed parameters is shown in Figure 4.4. Two complete thermal desorption and sampling cycles are described by dashed lines, which include the change of the GC oven temperature (oven program) as well as the general time-dependent activation or deactivation of the trap cooling, trap heating, FID analysis and the MS scan over a total method time of 8 minutes for each run. The first steps in each run are the activation

of trap heating and the FID measurement followed by the initiation of the mass spectral scan after one minute of lead time. From 0.5 min until 5 minutes the oven program is performed with a temperature increase from 100°C to 150°C. After 5 minutes of method run time, the trap heating process is terminated for the following cooling process (trap tube sampling) for 3 minutes or rather until the final method run time of 8 minutes., which also includes the termination of the FID and MS scan acquisition. Afterward, the whole process is repeated for as many samples as programmed in the Chromeleon 7.2 sequence list.

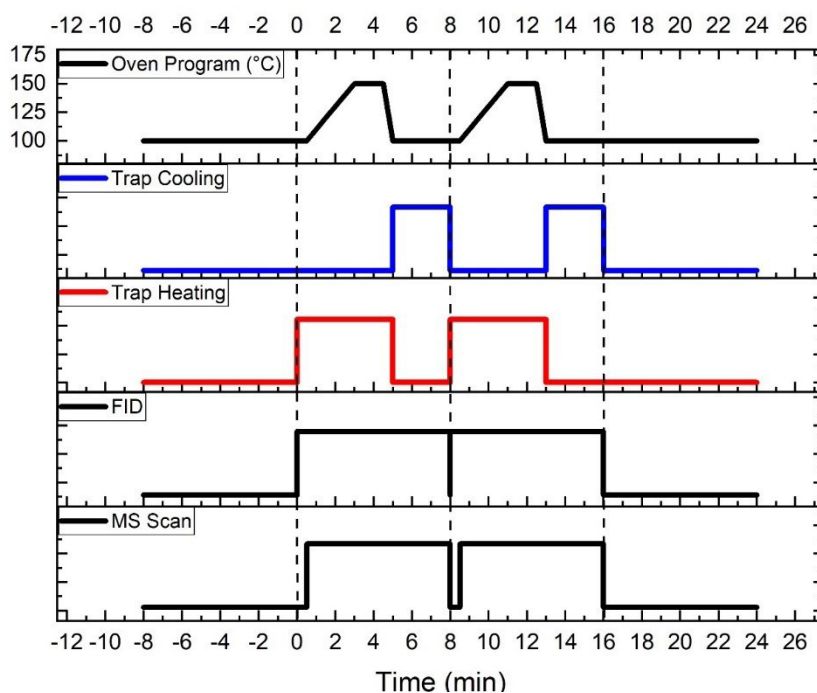


Figure 4.4: Overview of the process automation including the oven program, trap cooling and heating cycles, FID and MS data acquisition periods for 2 complete sampling and desorption operations (8 minutes each operation).

4.3 TD-GC-FID/MS system and chamber coupling

4.3.1 Instrument flow path

The 10-port valve represents a central part of the whole thermal desorption GC-FID/MS system by directing two main flow pathways regarding sampling (trap

tube loading) or thermal desorption. A key aspect is an operation in a so-called backflush mode, which can greatly extend the range of thermal desorption by eluting high-volatility and low-volatility analytes in a narrow band of vapor. The backflush mode is operated in the opposite flow direction of sample loading. The applied flow scheme using a 10-port valve is shown in Figure 4.5 for a sample injection configuration (10 port valve in position A) and a sample loading configuration (10 port valve in position B).

Sources for sampled analytes are either a calibration gas generator or a smog chamber, where the calibration gas supply line (1/4 in Teflon tube) is split to valve port number ten and a vent to prevent a pressure built-up towards the valve inlet. Consequently, the micropump draws only the amount of calibration gas through the sorbent trap, which is adjusted by a metering valve and measured by a flow meter as long as the flow rate of supplied calibration gas is higher than the pump sampling flow rate. The sampling line from the smog chamber to the 10-port valve is a 165 cm long, heated 1/8 in Sulfinert® treated stainless-steel tube to reduce potential analyte losses along the tube wall. Resistively heated and pre-cleaned stainless-steel tubes (316 SS) with dimensions of 0.04 in (ID), 1/16 in (OD) were used for all connections to valve positions 6, 7, 8, 9 as well as for the included jumper connecting valve position 1 and 4. The jumper is used to avoid an analyte concentration-related time delay, which would be caused by a paused sampling process during the desorption stage without a jumper. Hence, a permanently flushed sampling line can be achieved by on-going sampling during the desorption process towards the vent. The carrier gas and the desorbed sample are directed towards a split/splitless injector. The carrier gas flow path of the GC column is separated by a splitter for following sample analysis by a flame ionization detector and single-quadrupole mass spectrometer.

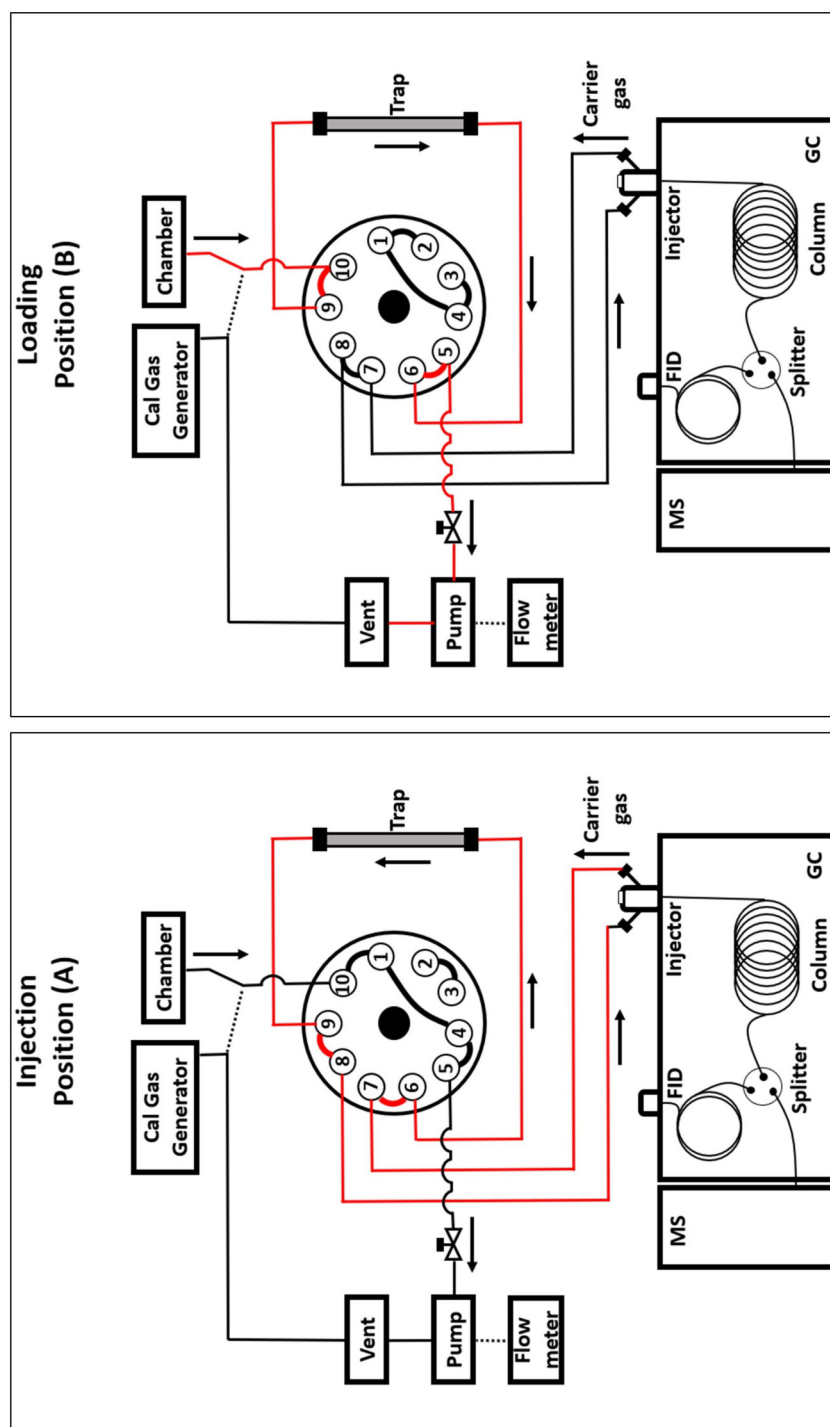


Figure 4.5: Flow scheme of the whole TD-GC-FID/MS system with two sampling sources (calibration gas generator, smog chamber), a 1/16 in stainless-steel trap tube, a 2 position 10-port valve for directing gas flows, a micropump for drawing samples through the trap tube, a vent, flow meter for adjusting the sampling rate as well as a GC-FID/MS system.

4.3.2 Analytical instrumentation and related supplies

A Thermo Fisher single quadrupole ISQ 7000 Trace 1310 GC-FID/MS system with a Zebron ZB-5 MS GC capillary column (30 m × 0.25 mm × 1.00 μm) is used for analyte separation and detection applying a ramped temperature programme (100°C to 150°C with 20°C min⁻¹). Toluene gas phase analytes are produced in concentrations between 0.2 ppm and 1.0 ppm by a Kin-Tek 491 M calibration gas generator using air generated by an Aadco 737 zero-air generator. A toluene-containing permeation tube device (Kin-Tek) is applied with a permeation rate of 2.263 ng/min at 80°C. Zero air is also used as air supply for the flame ionization detector and the atmospheric reaction chamber. Furthermore, 5.0 grade Helium (carrier gas), 5.0 grade nitrogen (auxiliary gas) and 6.0 Hydrogen (fuel) are obtained from Praxair. Helium is further purified using a Super Clean™ gas cartridge filter (ThermoScientific) to generate a 6.0 grade helium supply. Sampling and helium gas streams are changed by an external VICI Valco 2 position, high-temperature rated 10-port valve (1/16 in × 0.75 mm) with a microelectric actuator and a 6-in standoff. A 24 VDC micro diaphragm pump (Model UNMP830KNDC, KNF Neuberger Inc) with a maximum delivery of 3.1 L min⁻¹ under atmospheric pressure is used for sampling from the calibration gas generator. Pump sampling flow rates are set to 200 ccm (via the jumper configuration) with a metering valve to flush sampling lines during the desorption process. The maximum sampling flow rate (via jumper by-pass) through the trap tube is 22 ccm. Sampling flow rates are measured with a Gilibrator 2 flow meter (20 cc - 6 LPM flow cell, Sensidyne). The light source for UV DOAS measurements is a deuterium lamp with emission output from 215-400 nm (Ocean Optics D-2000-S) in combination with a grating-based UV spectrometer with a resolution of 0.118 nm (Ocean Optics, HR-2000+). Moreover, the photoreaction chamber is constructed of 0.127 mm thick perfluoroalkoxy (PFA) film with a total volume of 1.8 m³ supported by an aluminum housing. 24 fluorescent 32 W black lights with peak emission at 350 nm are the irradiation source for photochemical experiments. Further details about the chamber and the DOAS instrumentation were published in 2011 [91]. A general overview of instrumental conditions is shown in Table 4.1. Moreover, a description of the TD-GC-FID/MS operation is given in Appendix C text.

Table 4.1: Overview of essential methodological parameters regarding conditions used for the application of gas chromatographic separation (GC) and detection via flame ionization (FID) and mass spectrometry (MS).

Instrumental conditions	
GC conditions	
Inlet temperature	230 °C
Transfer line temperature	250 °C
Injection mode	Splitless
Split flow	60 mL min ⁻¹
Splitless time	0.8 min
Purge flow (He)	5.0 mL min ⁻¹
Oven equilibration time	0.1 min
Carrier gas flow (He)	1.2 mL min ⁻¹
Carrier mode	Flow control
Oven program	100 °C to 150 °C at 20 °C min ⁻¹ (Hold 1.5 min) to 100 °C at 100 °C min ⁻¹ (Hold 3.0 min) until 8 min run time
FID conditions	
Acquisition time	0 min - 8 min
Data collection rate	30 Hz
Detector temperature	225 °C
Ignition threshold	0.5 pA
Air flow rate	350 mL min ⁻¹
Nitrogen makeup gas flow rate	40 mL min ⁻¹
Hydrogen flow rate	35 mL min ⁻¹
MS conditions	
Mode	Full scan
Scan range	50 - 500 amu
Scan time	1 min - 8 min
Ionization mode	Electron impact
Ion source temperature	200 °C
Foreline pressure	27 mTorr
Electron energy	70 eV

4.3.3 Instrument characterization and first application

An important aspect of the general chamber/calibration gas sampling procedure is the proper heating of sampling lines and the 10-port valve with all corresponding stainless-steel tubes that are connected to the trap setup. Hence, the sampling line between the smog chamber and the thermal desorption system as well as the 10-port valve unit with corresponding transfer lines to the trap tube and GC inlet are resistively heated by two NiCr 60 alloy wires for establishing two different temperature zones. The sampling line is heated to 100 °C and the valve unit to 120 °C to avoid a loss of VOC analytes on tube walls.

Since the trap tube temperature during the sampling and desorption process is an important parameter for reproducibility, a temperature monitoring system (Figure C.3 and C.4) is connected to a software add-in for Microsoft Excel (PLX-DAQ). The application of this data acquisition system and hence the characterization of the heating/cooling system is presented in Figure 4.6. Temperature profiles are shown for both external valve positions A and B (sampling/cooling or desorption/heating). Moreover, the difference in temperature is given for the thermocouple placed either inside an empty trap tube or outside of a trap tube between the tube surface and the glass fiber insulation, also shown in Figure 4.1(B). A stable temperature of up to 313 °C can be achieved by applying 22.00 VDC and 2.328 A in constant voltage mode (C.V.) on the NiCr wire. The knowledge about the temperature difference between the tube inside and outside is important because under the given conditions it is not possible to measure the temperature inside the tube during experiments with a sorbent loaded trap. Hence, the tube temperature outside is used as a control value to adjust the voltage and current in order to avoid a trap tube overheating, which potentially can cause sorbent degradation. The heating efficiency for the first stage from 10 °C to 200 °C is as high as 22 °C s⁻¹, which is fast enough to quickly desorb VOCs such as BTEX (benzene, toluene, ethylbenzene, xylene) mixtures. However, as the trap tube warms up, the heating rate decreases to 120 °C min⁻¹ during the second stage (up to 300 °C). Cooling rates applying one Peltier element are as high as 122 °C min⁻¹, which is fast enough to cool down during separation of analytes until a new sampling process starts.

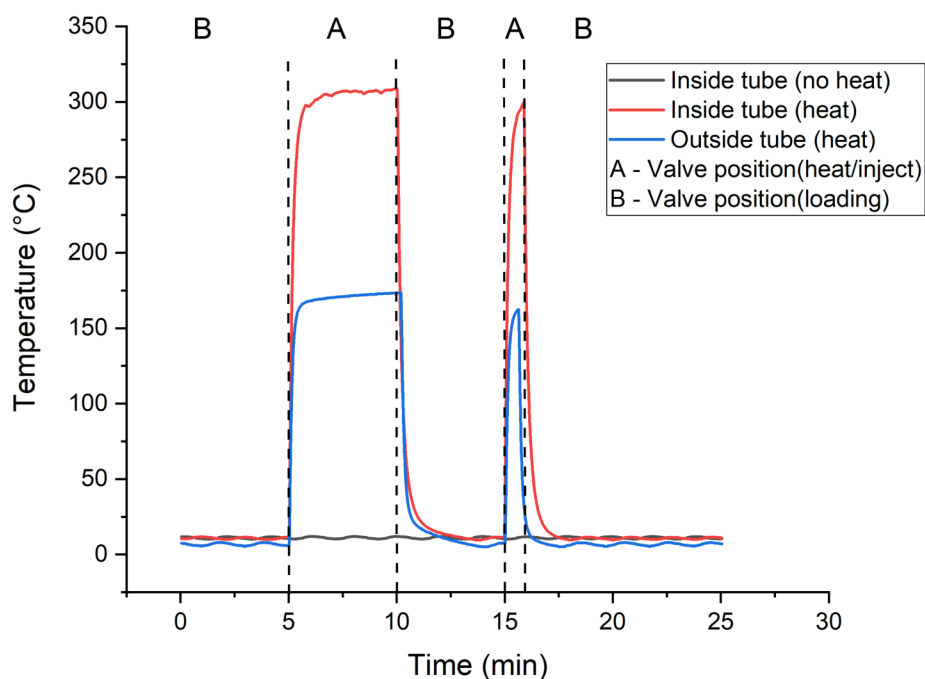


Figure 4.6: Presentation of the dependence of the trap tube temperature on the location of the temperature sensor and the positions of the 10-port valve.

Furthermore, a first approach to characterize and establish the thermal desorption unit with GC-FID/MS coupling as an alternative technique for the monitoring of chamber experiments was achieved by the quantitative comparison of toluene gas phase concentrations inside the atmospheric reaction chamber determined both with DOAS and TD-GC-FID/MS measurements. For this purpose, a calibration curve applying thermal desorption with GC-MS analysis was obtained firstly, which is shown in Figure 4.7 with a supplementary mass spectrum of toluene, a corresponding total ion current chromatogram (TIC) and an FID chromatogram in Figure C.5 acquired at a toluene concentration of 1 ppm. A KinTek 491 M calibration gas generator was used for the generation of toluene gas-phase concentrations of 0.2 ppm, 0.4 ppm, 0.6 ppm, 0.8 ppm, and 1.0 ppm. An overview of selected span gas flow rates to set up required toluene concentrations is presented in Table C.1. All remaining parameters regarding the thermal desorption, sampling process or GC-MS methodology were kept constant as described in

Table 4.1, the instrument operation description (Appendix C text) and Figure 4.4. A calibration of the DOAS system was not performed at this point but was described in a former publication [91].

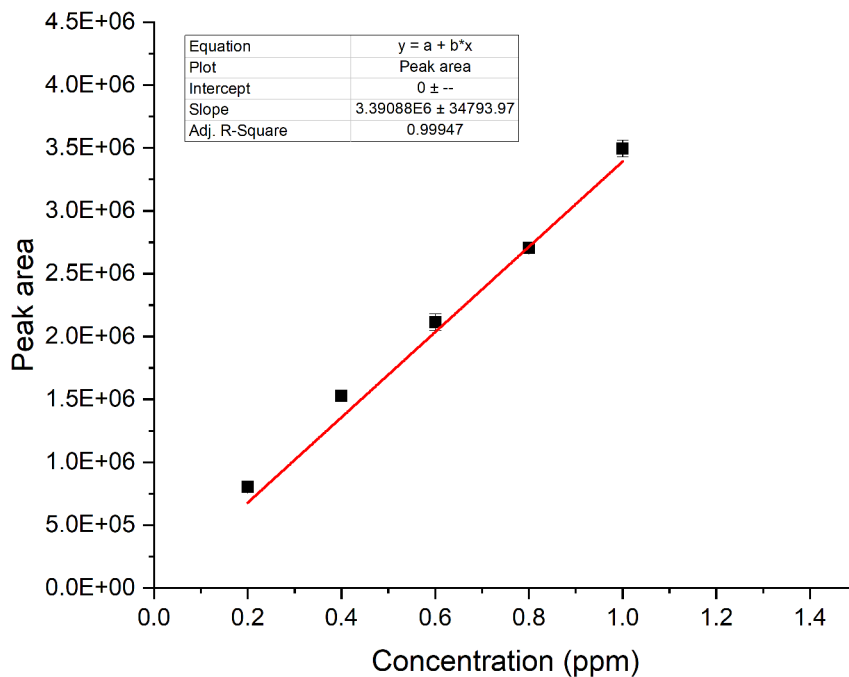


Figure 4.7: Calibration curve for the gas-phase sampling of toluene using MS detection and a calibration gas generator to produce toluene concentrations between 0.2 ppm and 1.0 ppm, showing 3 replicates for each concentration, exempting 0.6 ppm measurements with 12 replicates.

After calibration of the GC-TD-FID/MS system, the smog chamber was prepared for the first coupling with the TD-GC-FID/MS system. For this purpose, the chamber was flushed and cleaned overnight with a flow of zero air at a flow rate of 7.0 L min^{-1} with illumination by black lights. The injection of toluene into the chamber was achieved via a flow of zero air at a flow rate of 0.2 L min^{-1} over a liquid reservoir of toluene using an in-line glass bubbler, which was maintained at room temperature. The lowest possible chamber inflow is limited to 0.2 L min^{-1} by the applied mass flow controller. A total amount of 5 drops of toluene was injected into the reservoir using a Pasteur pipette. Figure 4.8 shows that

a background reference spectrum using the DOAS device was acquired for the reaction chamber (without toluene injection) over a period of 76 min. Afterward, DOAS was used to monitor the continuously increasing gas-phase concentration of injected toluene inside the chamber. After achieving a desired concentration (approximately 1 ppm of toluene), the flow over the liquid toluene reservoirs was stopped and by-passed to introduce only zero air into the chamber to monitor a loss of toluene. As a result of toluene's volatility, Figure 4.8 implies that the amount of injected toluene into the in-line bubbler was too high since a final concentration of 1.6 ppm toluene instead of 1.0 ppm was achieved. Hence, the chamber was flushed with zero air only at a flow rate of 7.0 L min^{-1} for 90 min to decrease the toluene concentration to 1.0 ppm, followed by a reduction of the zero air inflow to 3.0 L min^{-1} to slow down the dilution of toluene during the process of coupling the TD-GC-FID/MS system to the chamber. After 286 min of total chamber run time (including the background reference acquisition), the first sample for thermal desorption GC-MS analysis was taken from the chamber and the zero air inflow rate was adjusted to 9.5 L min^{-1} to accelerate the toluene loss inside the chamber again. Both the DOAS and GC-MS measurement showed a reasonable correlation related to the loss of toluene, which additionally is shown by the exponentially fitted graphs in Figure C.6.

However, the further comparison of both systems elucidates a major disadvantage of the used DOAS system, which is its higher uncertainty values of up to 200 ppb. On the other hand, the DOAS can acquire data points in a higher time resolution (2 min) compared to the thermal desorption setup with a current time resolution of 9 minutes. Moreover, DOAS chamber measurements are limited to comparably high VOC concentrations above approximately 200 ppb. The thermal desorption device has, therefore, a larger dynamic range towards lower VOC concentrations by adjusting the trap sampling time for longer preconcentration periods. Also, high VOC concentrations can be determined with the TD by either decreasing the sampling time or using a split mode injection, which reduces the amount of injected sample on the GC column. Hence, the DOAS and TD-GC-FID/MS system are valuable complementary devices to detect VOCs during atmospheric reaction chamber experiments. Whereas DOAS is not only enormously useful for setting up desired VOC concentrations, it also can be seen as a control instrument for the thermal desorption setup, because sorbents like Tenax TA™ can be subject to degradation. Furthermore, another advantage of

TD is the possibility to execute and monitor atmospheric reactions, which occur at atmospherically more relevant low-concentration conditions (lower ppb range) including SOA formation by VOC oxidation.

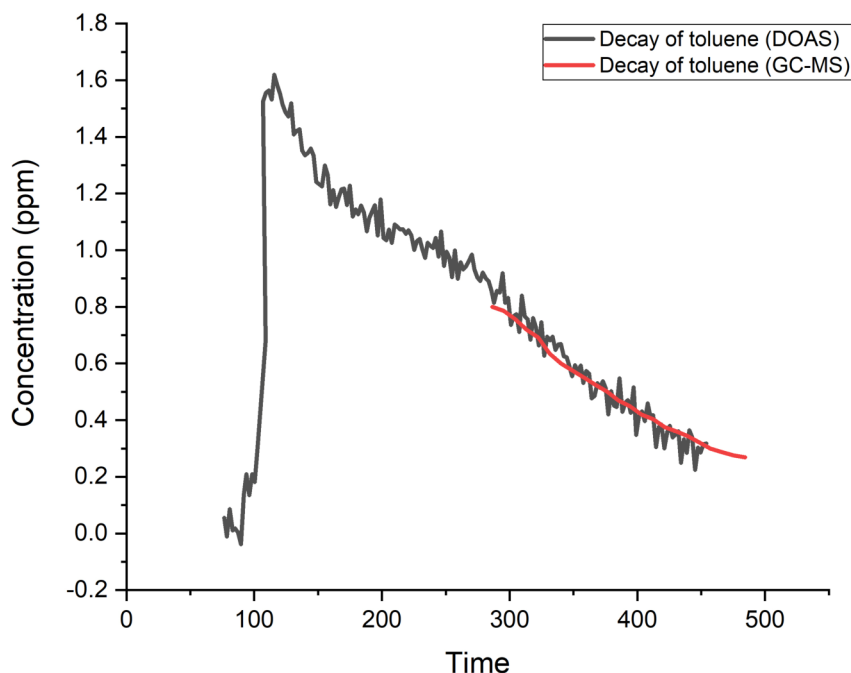


Figure 4.8: Comparison between DOAS and TD-GC-FID/MS regarding the monitoring of a toluene decay inside the smog chamber.

4.4 Summary

Atmospheric smog chamber studies are not limited to the investigation of particle formation and the corresponding characterization, but also focus on the determination of gas-phase species including their quantitative analysis and following structural elucidations. Hence, the analysis of precursors for especially secondary particle formation, in many cases either biogenic or anthropogenic volatile organic compounds, is a powerful tool to explain atmospheric oxidation processes and may provide important information for modeling studies in atmospheric chemistry.

Optical, spectroscopic methods (*e.g.* DOAS) are essential techniques to determine and monitor the concentration of gas-phase compounds. Hence, DOAS

is also a core technique used for smog chamber studies. However, it does not provide structural information and is limited in its application for low-concentration VOCs and their potential oxidation products. Hence, a new, modified thermal desorption unit coupled to a GC-FID/MS instrument was developed to complement an existing DOAS system coupled to an atmospheric reaction chamber. The detailed presentation of the technical design was supported by insights into the production of sorbent filled thermal desorption tubes. Furthermore, the electronic realization of a fully automated sampling and desorption system was discussed in depth. The operating principle of the overall TD-GC-FID/MS setup was additionally underpinned with concrete schemes regarding all occurring gas flow directions, step-wise methodological procedures as well as first performance tests related to heating and cooling efficiencies. Additionally, a very first application of the developed TD-GC-FID/MS was successfully demonstrated by its coupling to a calibration gas generator for sampling and desorbing toluene in different gas-phase concentrations for a first calibration curve. Moreover, a successful coupling of the thermal desorption setup to a smog chamber equipped with a DOAS device was achieved by monitoring the decay of toluene inside the chamber and subsequently comparing the determined concentrations of both the DOAS and the TD-GC-FID/MS system.

Hence, this work comprises a detailed description of the process of successfully developing and applying a thermal desorption system for smog chamber studies. A fully detailed TD unit characterization which includes also the application of VOC mixtures and methodological optimizations towards higher time-resolutions will need to be fulfilled in future investigations.

Chapter 5

Conclusions and future directions

Contributions: This manuscript was written by Mario Schmidt, with critical comments from Dr. Sarah A. Styler

5.1 Photochemical reactor development

In Chapter 2, the development and characterization of a multi-position photochemical reactor was presented. The multi-position option was realized by the introduction of an exchangeable sample adaptor setup to easily access 1, 4 or 9 reaction vessels as shown in Figure 5.1. The reactor temperature dependence on illumination by a solar simulator and dark conditions were investigated for all available sample adaptors and corresponding sample positions. A spatial variance of the illumination of different sample positions was evaluated and finally excluded by investigating the photochemical decay of 2-nitrobenzaldehyde (2NB) in aqueous solution upon illumination and the determination of the first order loss rate constant $j(2NB)$. Moreover, the uniform stirring performance in all adaptor-dependent sample locations was successfully proven by the application of particle laden samples of 2NB including TiO_2 as well as road dust particles as first approach to use collected samples for further environmentally relevant studies.

However, a slight temperature increase after starting illumination has shown that the cooling capacity of the photoreactor may need to be improved. The application of multiple parallel or stacked Peltier elements as well as a pump with a higher flow rate for the coolant might be considered at this point. The improvement of the cooling efficiency may be important for future aqueous phase studies which include very volatile organic compounds such as isoprene, which evaporate rapidly already at room temperature. Then, the temperature effect and thus a reduced evaporation (higher VOC concentration in the aqueous phase) could be investigated by semi-quantitative HPLC analyses. In turn, maintaining a higher aqueous VOC concentration may impact the successful investigation of multiphase (aqueous and gas-phase) reactions by finally achieving a higher concentration of oxidized VOCs in the aqueous phase. Possible reactants for multiphase reactions might be O_3 , NO_x or SO_2 , which could be introduced through fittings being connected to the Teflon box. Furthermore, the difference in $j(2NB)$ values between sample adaptors that are covered or uncovered by the Teflon box could be reduced by coloring the Teflon box black inside, which may improve the comparability of results due to a reduction of light reflection. Analogously, a following black coloring of the sample adaptor could relate photochemical reactions only to the impact of incident light.

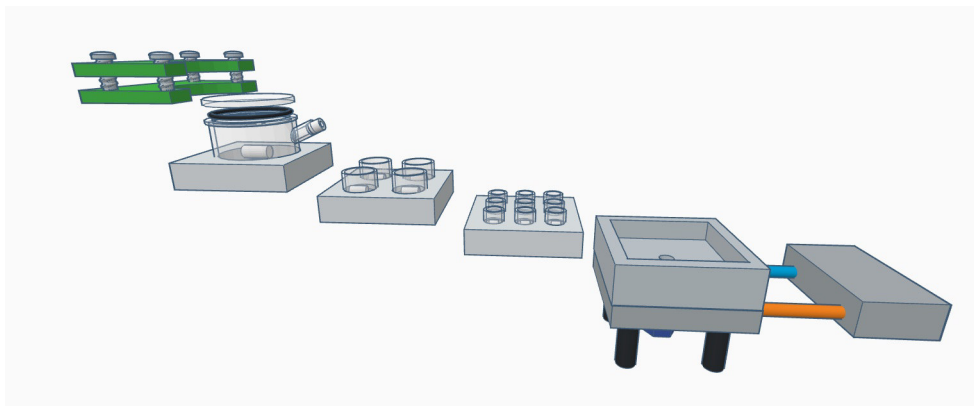


Figure 5.1: Visual representation of all three exchangeable sample adaptors with one, four or nine sample positions.

5.2 Mineral-mediated photochemical organosulfate formation

A new, mineral-mediated photochemical pathway for the formation of organosulfates (OS) was described in Chapter 3. The production of the atmospherically important organosulfate hydroxyacetone sulfate was investigated in the aqueous phase under several conditions using methacrolein as precursor. The OS production was observed as a function of illumination time, catalyst loading (TiO_2 and mineral dusts, road dust), sulfate concentration, counter-ion identity, and methacrolein concentration. Since the presented results give first insights and highlight the complexity of photochemical, aqueous-phase processes at the surface of mineral samples, further studies related to mineral-organic interactions in atmospheric OS formation are needed.

These investigations may include a screening of different VOCs from biogenic and anthropogenic sources (including green leaf volatiles). Furthermore, the investigation of aromatic organosulfates could be of interest, also by possibly using uncoated and coated commercially available TiO_2 , natural minerals or urban dust samples with semi-volatile, organic compounds (SVOCs), such as polycyclic aromatic hydrocarbons (PAHs) prior to OS formation experiments in the aqueous phase. Another key aspect for an improved organosulfate research represents the advanced synthesis of organosulfates for a broader availability of standards materials. The advantage of synthesizing OS standards comprises also the ability to work on the LC-MS/MS method development towards an improved OS

separation and detection. Moreover, organosulfate standards can be used to enhance the sample preparation of highly concentrated inorganic sulfate samples, which were present in this study and also occur during SOA sampling. Two possible directions for a sample preparation improvement are the application and investigation of solid-phase extraction (SPE) methods for OS species or the optimization of the applied MeOH cleanup procedure by concentrating the MeOH-OS mixture due to solvent evaporation and following reconstitution in a lower sample volume, similar in solvent composition to the initial gradient mixture used in HPLC analysis. This furthermore improves the HPLC method development. Finally, a potentially competitive OS loss pathway was discussed for hydroxyacetone sulfate in the presence of aqueous TiO₂ suspensions with or without methacrolein. On the basis of these results the sources and influence of loss mechanisms of different organosulfates and the corresponding formation of potential OS degradation products under different conditions (*e.g.* sulfate salt concentration or catalyst loading) may serve as further interesting directions for future OS projects.

5.3 TD-GC-FID/MS system coupled to an atmospheric reaction chamber

In Chapter 4, the development of a thermal desorption (TD) unit for the automated sampling of gas-phase analytes and the following injection into a gas chromatograph (GC) with flame ionization (FID) and mass spectrometry (MS) detection was presented as an integrated TD-GC-FID/MS system. Design aspects were discussed and shown in detail related to the basic mechanical structure and electronic control including the realization of automated processes. First instrumental characterizations were achieved by monitoring the temperature profile of different trap tube locations (*e.g.* inside and outside) as well as a first calibration with different gas-phase concentrations of toluene. Successfully, the linear response of an increasing toluene concentration at a constant sampling time could be shown for a concentration range between 0.2 ppm and 1.0 ppm. Moreover, a first successful evaluation of the thermal desorption unit was demonstrated by coupling the TD-GC-FID/MS system to an atmospheric smog chamber with differential optical absorption spectroscopy (DOAS) to monitor the loss of gas-phase

toluene inside the chamber due to dilution with zero air. Since this TD setup is a first prototype which originally was built for a possible introduction of the trap tube part into a GC oven, there are still several aspects that may be improved or added to the existing TD design. Categorized considerations for future work is shown in Figure 5.2.

Technical improvements may be approached by the introduction of a second TD system connected to the external 10-port valve, which would enhance the time-resolution of smog chamber experiments by keeping one TD unit in sampling mode whereas the second TD unit is kept in desorption mode (simultaneous trapping and injection). A possible scheme for this setup is presented in Figure D.1 of Appendix D. Furthermore, the addition of a dry purge valve (*e.g.* a DVS-3 valve available from AFP-Analytical Flow Products) to remove trapped water vapor may be useful to improve separation processes and to protect the GC column, when samples with a higher humidity should be drawn through the trap tube. Figure D.2 presents a possible technical solution to set up a dry purge step. The electronic control of this 3-port valve may be realized by splitting the fourth grey pin cable shown in Figure 4.3 to transfer the position-dependent signal of the 10-port valve to a further Arduino UNO R3 board. Furthermore, the trap tube heating efficiency and thus the corresponding analyte peak shape might be improved in future by including a modified Arduino coding that allows for a more rapid heating at an elevated current without exceeding the maximum temperature of Tenax TA. Since a high time-resolution does not only depend on fast heating and cooling of the trap tube but also on the application of a fast GC method, one aspect of fast GC - fast oven temperature ramp rates - might be applied by using a resistively heated GC column combined with possible other key points of fast GC, such as a decreased column length, higher carrier gas flow rates, a narrower inner diameter of the GC column, the application of hydrogen as carrier gas as well as a lower column film thickness. Further technical improvements may be the introduction of another external 8-port valve connected to the existing 10-port valve for injecting internal standards via a loop system onto a double trap system (previously shown in Figure D.1). Figure D.3 presents further suggestions for the development of such a loop-mediated automated internal standard injection. A particle filter (*e.g.* Teflon or HEPA filter) could be integrated in the sampling line to firstly protect the trap tube and thus the GC from particle contamination due to secondary aerosol formation. to achieve the opportunity to collect and analyze

particle phase properties additionally to gas-phase analytes.

Another essential part of further instrument validation may be the evaluation of the trap tube preparation process. Currently, it is unknown how accurate the reduced tube diameters can be reproduced for holding the glass wool and sorbent in place. This also determines maximum sampling flow rates. Hence, it might be recommended to produce and test at least three to five sorbent trap tubes on reproducibility. Furthermore, a possible loss of analytes and oxidized analytes could be investigated by comparing analyte peak areas from a heated and unheated sampling line and 10-port valve to adjust the heating temperature to an optimum value that does not cause analyte wall loss as well as oxidation product decomposition during the sampling process. Furthermore, the so-called breakthrough of analytes (volume of carrier gas that will purge an analyte through 1.0 gram of adsorbent resin in a desorption tube at a specific temperature) represents a central concern during the application of preconcentration techniques, that requires further experiments. A similar approach to investigate breakthrough might be the performance of volume variation experiments [226] by keeping the gas-phase concentration of an analyte and the sampling flow rate constant, and then changing the sampling time to increase the final sampling volume. Peak areas of analytes after different sampling times may be then compared to investigate a safe sampling volume. Lastly, the analysis methodology of oxidized VOCs (OVOCs) can be improved by the addition of a derivatization agent onto the sorbent laden trap tube. This will reduce the polarity of OVOCs by blocking reactive functions and enhance the GC response [214].

The improved and validated TD-GC-FID/MS system may then be further applied to experiments with a more atmospherically relevant character using the smog chamber for VOC oxidation experiments (*e.g.* VOC and H₂O₂ injection) [241]. The decay of VOC precursors and the corresponding production OVOCs may then be monitored and compared with both the DOAS and the TD-GC-FID/MS system. After establishing first protocols for VOC oxidation experiments, the investigation of the composition of the particle phase by collecting SOA during the gas-phase sampling process might be a another future direction. Finally, the photochemical interaction of particles (*e.g.* mineral dust) with atmospheric pollutants (*e.g.* BTEX) presents a further project direction including the chamber-coupled TD-GC-FID/MS system.

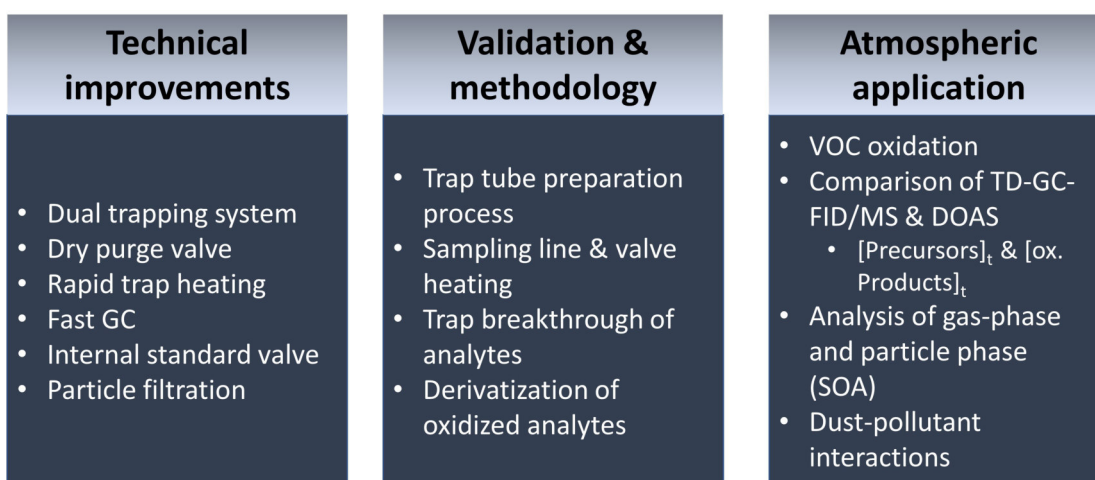


Figure 5.2: Categorized aspects for future projects on the developed TD-GC-FID/MS system.

Bibliography

- [1] A. Gillard. "On the Terminology of Biosphere and Ecosphere". en. In: *Nature* 223.5205 (Aug. 1969), pp. 500–501. ISSN: 0028-0836, 1476-4687. DOI: 10.1038/223500a0.
- [2] James Girard. *Principles of Environmental Chemistry*. 3rd ed. Burlington, Mass: Jones & Bartlett Learning, 2013. ISBN: 978-1-4496-5015-5 978-1-4496-9352-7.
- [3] Randy Russell. *Layers of the Earth's Atmosphere*. <https://scied.ucar.edu/atmosphere-layers>. 2015.
- [4] E.C. Voldner, L.A. Barrie, and A. Sirois. "A Literature Review of Dry Deposition of Oxides of Sulphur and Nitrogen with Emphasis on Long-Range Transport Modelling in North America". en. In: *Atmospheric Environment (1967)* 20.11 (Jan. 1986), pp. 2101–2123. ISSN: 00046981. DOI: 10.1016/0004-6981(86)90305-7.
- [5] Daniel J. Jacob. *Introduction to Atmospheric Chemistry*. Princeton, N.J: Princeton University Press, 1999. ISBN: 978-0-691-00185-2.
- [6] Isabelle Bey et al. "Global Modeling of Tropospheric Chemistry with Assimilated Meteorology: Model Description and Evaluation". en. In: *Journal of Geophysical Research: Atmospheres* 106.D19 (Oct. 2001), pp. 23073–23095. ISSN: 01480227. DOI: 10.1029/2001JD000807.
- [7] S.J. Williamson. *Fundamentals of Air Pollution*. Addison-Wesley, 1973. ISBN: 978-0-201-08629-4.
- [8] Wilfrid Bach. *Atmospheric Pollution*. McGraw-Hill Problems Series in Geography. New York: McGraw-Hill, 1971. ISBN: 978-0-07-002819-7.
- [9] Alex Guenther, Patrick Zimmerman, and Mary Wildermuth. "Natural Volatile Organic Compound Emission Rate Estimates for U.S. Woodland Landscapes". en. In: *Atmospheric Environment* 28.6 (Apr. 1994), pp. 1197–1210. ISSN: 13522310. DOI: 10.1016/1352-2310(94)90297-6.

- [10] Alex Guenther et al. "A Global Model of Natural Volatile Organic Compound Emissions". en. In: *Journal of Geophysical Research* 100.D5 (1995), p. 8873. ISSN: 0148-0227. DOI: 10.1029/94JD02950.
- [11] A. Guenther et al. "Estimates of Global Terrestrial Isoprene Emissions Using MEGAN (Model of Emissions of Gases and Aerosols from Nature)". en. In: *Atmospheric Chemistry and Physics* 6.11 (Aug. 2006), pp. 3181–3210. ISSN: 1680-7324. DOI: 10.5194/acp-6-3181-2006.
- [12] M. Nemecek-Marshall et al. "Methanol Emission from Leaves (Enzymatic Detection of Gas-Phase Methanol and Relation of Methanol Fluxes to Stomatal Conductance and Leaf Development)". en. In: *Plant Physiology* 108.4 (Aug. 1995), pp. 1359–1368. ISSN: 0032-0889, 1532-2548. DOI: 10.1104/pp.108.4.1359.
- [13] Robert C. Macdonald and Ray Fall. "Acetone Emission from Conifer Buds". en. In: *Phytochemistry* 34.4 (Nov. 1993), pp. 991–994. ISSN: 00319422. DOI: 10.1016/S0031-9422(00)90700-3.
- [14] E. E. Farmer and C. A. Ryan. "Interplant Communication: Airborne Methyl Jasmonate Induces Synthesis of Proteinase Inhibitors in Plant Leaves." en. In: *Proceedings of the National Academy of Sciences* 87.19 (Oct. 1990), pp. 7713–7716. ISSN: 0027-8424, 1091-6490. DOI: 10.1073/pnas.87.19.7713.
- [15] Akikazu Hatanaka. "The Biogenesis of Green Odour by Green Leaves". en. In: *Phytochemistry* 34.5 (Nov. 1993), pp. 1201–1218. ISSN: 00319422. DOI: 10.1016/0031-9422(91)80003-J.
- [16] Manuel Lerdau, Alex Guenther, and Russ Monson. "Plant Production and Emission of Volatile Organic Compounds". In: *BioScience* 47.6 (June 1997), pp. 373–383. ISSN: 00063568, 15253244. DOI: 10.2307/1313152.
- [17] Ray Fall. "Biogenic Emissions of Volatile Organic Compounds from Higher Plants". en. In: *Reactive Hydrocarbons in the Atmosphere*. Elsevier, 1999, pp. 41–96. ISBN: 978-0-12-346240-4. DOI: 10.1016/B978-012346240-4/50003-5.
- [18] *2014 National Emissions Inventory Report*. Tech. rep. United States Environmental Protection Agency.

- [19] Stuart Batterman et al. "Personal Exposure to Mixtures of Volatile Organic Compounds: Modeling and Further Analysis of the RIOPA Data". en. In: (2015), p. 99.
- [20] E. Rodolfo Sosa et al. "Levels and Source Apportionment of Volatile Organic Compounds in Southwestern Area of Mexico City". en. In: *Environmental Pollution* 157.3 (Mar. 2009), pp. 1038–1044. ISSN: 02697491. DOI: 10.1016/j.envpol.2008.09.051.
- [21] Regina Montero-Montoya, Rocío López-Vargas, and Omar Arellano-Aguilar. "Volatile Organic Compounds in Air: Sources, Distribution, Exposure and Associated Illnesses in Children". en. In: *Annals of Global Health* 84.2 (July 2018), pp. 225–238. ISSN: 2214-9996. DOI: 10.29024/aogh.910.
- [22] *Draft Inventory of U.S. Greenhouse Gas Emissions and Sinks: 1990-2017*. Tech. rep. United States Environmental Protection Agency.
- [23] Intergovernmental Panel on Climate Change and Ottmar Edenhofer, eds. *Climate Change 2014: Mitigation of Climate Change: Working Group III Contribution to the Fifth Assessment Report of the Intergovernmental Panel on Climate Change*. en. OCLC: ocn892580682. New York, NY: Cambridge University Press, 2014. ISBN: 978-1-107-05821-7 978-1-107-65481-5.
- [24] Sanford Sillman. "The Long Reach of Biogenic Emissions in the Atmosphere". In: *Challenges and Opportunities for the World's Forests in the 21st Century*. Ed. by Trevor Fenning. Vol. 81. Dordrecht: Springer Netherlands, 2014, pp. 727–737. ISBN: 978-94-007-7075-1 978-94-007-7076-8. DOI: 10.1007/978-94-007-7076-8_32.
- [25] John H. Seinfeld and Spyros N. Pandis. *Atmospheric Chemistry and Physics: From Air Pollution to Climate Change*. eng. 3rd edition. OCLC: 946547332. Hoboken, New Jersey: Wiley, 2016. ISBN: 978-1-119-22116-6 978-1-118-94740-1 978-1-119-22117-3.
- [26] Bernd R.T. Simoneit and Monica A. Mazurek. "Organic Matter of the Troposphere—II. Natural Background of Biogenic Lipid Matter in Aerosols over the Rural Western United States". en. In: *Atmospheric Environment (1967)* 16.9 (Jan. 1982), pp. 2139–2159. ISSN: 00046981. DOI: 10.1016/0004-6981(82)90284-0.

- [27] Sabine Matthias-Maser and Ruprecht Jaenicke. "Examination of Atmospheric Bioaerosol Particles with Radii $> 0.2 \text{ Mm}$ ". en. In: *Journal of Aerosol Science* 25.8 (Dec. 1994), pp. 1605–1613. ISSN: 00218502. DOI: 10.1016/0021-8502(94)90228-3.
- [28] Paulo Artaxo and Hans-Christen Hansson. "Size Distribution of Biogenic Aerosol Particles from the Amazon Basin". en. In: *Atmospheric Environment* 29.3 (Feb. 1995), pp. 393–402. ISSN: 13522310. DOI: 10.1016/1352-2310(94)00178-N.
- [29] H. E. Ahern et al. "Fluorescent Pseudomonads Isolated from Hebridean Cloud and Rain Water Produce Biosurfactants but Do Not Cause Ice Nucleation". en. In: *Biogeosciences* 4.1 (Feb. 2007), pp. 115–124. ISSN: 1726-4189. DOI: 10.5194/bg-4-115-2007.
- [30] J. Elster et al. "Composition of Microbial Communities in Aerosol, Snow and Ice Samples from Remote Glaciated Areas (Antarctica, Alps, Andes)". en. In: *Biogeosciences Discussions* 4.3 (June 2007), pp. 1779–1813. ISSN: 1810-6285. DOI: 10.5194/bgd-4-1779-2007.
- [31] S. Zhang et al. "Culturable Bacteria in Himalayan Glacial Ice in Response to Atmospheric Circulation". en. In: *Biogeosciences* 4.1 (Jan. 2007), pp. 1–9. ISSN: 1726-4189. DOI: 10.5194/bg-4-1-2007.
- [32] R. Lewis and E. Schwartz. *Sea Salt Aerosol Production: Mechanisms, Methods, Measurements and Models—A Critical Review*. en. Vol. 152. Geophysical Monograph Series. Washington, D. C.: American Geophysical Union, 2004. ISBN: 978-0-87590-417-7. DOI: 10.1029/GM152.
- [33] Tami C. Bond et al. "Historical Emissions of Black and Organic Carbon Aerosol from Energy-Related Combustion, 1850-2000: HISTORICAL BC/OC EMISSIONS". en. In: *Global Biogeochemical Cycles* 21.2 (June 2007). ISSN: 08866236. DOI: 10.1029/2006GB002840.
- [34] Zbigniew Klimont et al. "Global Anthropogenic Emissions of Particulate Matter Including Black Carbon". en. In: *Atmospheric Chemistry and Physics* 17.14 (July 2017), pp. 8681–8723. ISSN: 1680-7324. DOI: 10.5194/acp-17-8681-2017.
- [35] C.N. Davies. "Particles in the Atmosphere—Natural and Man-Made". en. In: *Atmospheric Environment (1967)* 8.11 (Nov. 1974), pp. 1069–1079. ISSN: 00046981. DOI: 10.1016/0004-6981(74)90042-0.

- [36] D. R. Benson et al. "Ternary Homogeneous Nucleation of H₂SO₄, NH₃, and H₂O under Conditions Relevant to the Lower Troposphere". en. In: *Atmospheric Chemistry and Physics* 11.10 (May 2011), pp. 4755–4766. ISSN: 1680-7324. DOI: 10.5194/acp-11-4755-2011.
- [37] Jasper Kirkby et al. "Role of Sulphuric Acid, Ammonia and Galactic Cosmic Rays in Atmospheric Aerosol Nucleation". en. In: *Nature* 476.7361 (Aug. 2011), pp. 429–433. ISSN: 0028-0836, 1476-4687. DOI: 10.1038/nature10343.
- [38] P. Vaattovaara et al. "The Composition of Nucleation and Aitken Modes Particles during Coastal Nucleation Events: Evidence for Marine Secondary Organic Contribution". en. In: *Atmospheric Chemistry and Physics* 6.12 (Oct. 2006), pp. 4601–4616. ISSN: 1680-7324. DOI: 10.5194/acp-6-4601-2006.
- [39] James F. Pankow. "An Absorption Model of Gas/Particle Partitioning of Organic Compounds in the Atmosphere". en. In: *Atmospheric Environment* 28.2 (Jan. 1994), pp. 185–188. ISSN: 13522310. DOI: 10.1016/1352-2310(94)90093-0.
- [40] M. Hallquist et al. "The Formation, Properties and Impact of Secondary Organic Aerosol: Current and Emerging Issues". en. In: *Atmospheric Chemistry and Physics* 9.14 (July 2009), pp. 5155–5236. ISSN: 1680-7324. DOI: 10.5194/acp-9-5155-2009.
- [41] M. Kalberer. "Identification of Polymers as Major Components of Atmospheric Organic Aerosols". en. In: *Science* 303.5664 (Mar. 2004), pp. 1659–1662. ISSN: 0036-8075, 1095-9203. DOI: 10.1126/science.1092185.
- [42] Jesse H. Kroll et al. "Chamber Studies of Secondary Organic Aerosol Growth by Reactive Uptake of Simple Carbonyl Compounds". en. In: *Journal of Geophysical Research* 110.D23 (2005). ISSN: 0148-0227. DOI: 10.1029/2005JD006004.
- [43] Annmarie G. Carlton et al. "Link between Isoprene and Secondary Organic Aerosol (SOA): Pyruvic Acid Oxidation Yields Low Volatility Organic Acids in Clouds". en. In: *Geophysical Research Letters* 33.6 (2006). ISSN: 0094-8276. DOI: 10.1029/2005GL025374.

- [44] Barbara Ervens et al. "Secondary Organic Aerosol Yields from Cloud-Processing of Isoprene Oxidation Products". en. In: *Geophysical Research Letters* 35.2 (Jan. 2008). ISSN: 0094-8276. DOI: 10.1029/2007GL031828.
- [45] Olivier Boucher. *Atmospheric Aerosols - Properties and Climate Impacts*. en. New York, NY: Springer Berlin Heidelberg, 2015. ISBN: 978-94-017-9648-4.
- [46] S. Matthias-Maser and R. Jaenicke. "The Size Distribution of Primary Biological Aerosol Particles with Radii $> 0.2 \mu\text{m}$ in an Urban/Rural Influenced Region". en. In: *Atmospheric Research* 39.4 (Dec. 1995), pp. 279–286. ISSN: 01698095. DOI: 10.1016/0169-8095(95)00017-8.
- [47] Istvan Lagzi et al. *Atmospheric Chemistry*. Eötvös Loránd University, 2013.
- [48] J. L. Jimenez et al. "Evolution of Organic Aerosols in the Atmosphere". en. In: *Science* 326.5959 (Dec. 2009), pp. 1525–1529. ISSN: 0036-8075, 1095-9203. DOI: 10.1126/science.1180353.
- [49] J.-P. Putaud et al. "A European Aerosol Phenomenology – 3: Physical and Chemical Characteristics of Particulate Matter from 60 Rural, Urban, and Kerbside Sites across Europe". en. In: *Atmospheric Environment* 44.10 (Mar. 2010), pp. 1308–1320. ISSN: 13522310. DOI: 10.1016/j.atmosenv.2009.12.011.
- [50] N. Riemer et al. "Aerosol Mixing State: Measurements, Modeling, and Impacts". en. In: *Reviews of Geophysics* (Mar. 2019), 2018RG000615. ISSN: 8755-1209, 1944-9208. DOI: 10.1029/2018RG000615.
- [51] N. Colin Baird. "Introducing Atmospheric Reactions: A Systematic Approach for Students". en. In: *Journal of Chemical Education* 72.2 (Feb. 1995), p. 153. ISSN: 0021-9584, 1938-1328. DOI: 10.1021/ed072p153.
- [52] Barbara J. Finlayson-Pitts and James N. Pitts. *Chemistry of the Upper and Lower Atmosphere: Theory, Experiments, and Applications*. San Diego: Academic Press, 2000. ISBN: 978-0-12-257060-5.

- [53] G. Quinkert. "Photochemistry. Von J. G. Calvert und J. N. Pitts, jr. John Wiley & Sons, Inc., New York-London-Sydney 1966. 1. Aufl., XVII, 899 S., zahlr. Abb., geb. DM 84.-". de. In: *Angewandte Chemie* 79.16 (Aug. 1967), pp. 730–730. ISSN: 00448249, 15213757. DOI: 10.1002/ange.19670791618.
- [54] Philip A. Leighton. *Photochemistry of Air Pollution*. London (UK): Academic Press Inc., 1961. ISBN: 978-0-12-442250-6.
- [55] J.A. Geddes and J.G. Murphy. "The Science of Smog: A Chemical Understanding of Ground Level Ozone and Fine Particulate Matter". en. In: *Metropolitan Sustainability*. Elsevier, 2012, pp. 205–230. ISBN: 978-0-85709-046-1. DOI: 10.1533/9780857096463.3.205.
- [56] Paul H. Wine and J. Michael Nicovich. "Atmospheric Radical Chemistry". en. In: *Encyclopedia of Radicals in Chemistry, Biology and Materials*. Ed. by Chrissyostomos Chatgililoglu and Armido Studer. Chichester, UK: John Wiley & Sons, Ltd, Mar. 2012. ISBN: 978-1-119-95367-8. DOI: 10.1002/9781119953678.rad015.
- [57] Christian George et al. "Heterogeneous Photochemistry in the Atmosphere". en. In: *Chemical Reviews* 115.10 (May 2015), pp. 4218–4258. ISSN: 0009-2665, 1520-6890. DOI: 10.1021/cr500648z.
- [58] James F. Pankow. "An Absorption Model of the Gas/Aerosol Partitioning Involved in the Formation of Secondary Organic Aerosol". en. In: *Atmospheric Environment* 28.2 (Jan. 1994), pp. 189–193. ISSN: 13522310. DOI: 10.1016/1352-2310(94)90094-9.
- [59] Jesse H. Kroll and John H. Seinfeld. "Chemistry of Secondary Organic Aerosol: Formation and Evolution of Low-Volatility Organics in the Atmosphere". en. In: *Atmospheric Environment* 42.16 (May 2008), pp. 3593–3624. ISSN: 13522310. DOI: 10.1016/j.atmosenv.2008.01.003.
- [60] Colette L. Heald et al. "A Large Organic Aerosol Source in the Free Troposphere Missing from Current Models: LARGE TROPOSPHERIC SOURCE OF OC AEROSOLS". en. In: *Geophysical Research Letters* 32.18 (Sept. 2005). ISSN: 00948276. DOI: 10.1029/2005GL023831.

- [61] Rainer Volkamer et al. "Secondary Organic Aerosol Formation from Anthropogenic Air Pollution: Rapid and Higher than Expected". en. In: *Geophysical Research Letters* 33.17 (2006). ISSN: 0094-8276. DOI: 10.1029/2006GL026899.
- [62] N. M. Donahue et al. "Coupled Partitioning, Dilution, and Chemical Aging of Semivolatile Organics". en. In: *Environmental Science & Technology* 40.8 (Apr. 2006), pp. 2635–2643. ISSN: 0013-936X, 1520-5851. DOI: 10.1021/es052297c.
- [63] Ran Zhao. "Aqueous-Phase Organic Chemistry in the Atmosphere". en. PhD thesis. Toronto: University of Toronto, Jan. 2015.
- [64] Hartmut Herrmann. "Kinetics of Aqueous Phase Reactions Relevant for Atmospheric Chemistry". en. In: *Chemical Reviews* 103.12 (Dec. 2003), pp. 4691–4716. ISSN: 0009-2665, 1520-6890. DOI: 10.1021/cr020658q.
- [65] Hartmut Herrmann et al. "Tropospheric Aqueous-Phase Chemistry: Kinetics, Mechanisms, and Its Coupling to a Changing Gas Phase". In: *Chemical Reviews* 115.10 (May 2015), pp. 4259–4334. ISSN: 0009-2665. DOI: 10.1021/cr500447k.
- [66] V. Faye McNeill. "Aqueous Organic Chemistry in the Atmosphere: Sources and Chemical Processing of Organic Aerosols". en. In: *Environmental Science & Technology* 49.3 (Feb. 2015), pp. 1237–1244. ISSN: 0013-936X, 1520-5851. DOI: 10.1021/es5043707.
- [67] Kevin A. Ramazan, Dennis Syomin, and Barbara J. Finlayson-Pitts. "The Photochemical Production of HONO during the Heterogeneous Hydrolysis of NO₂". en. In: *Physical Chemistry Chemical Physics* 6.14 (2004), p. 3836. ISSN: 1463-9076, 1463-9084. DOI: 10.1039/b402195a.
- [68] A.E. Michel, C.R. Usher, and V.H. Grassian. "Reactive Uptake of Ozone on Mineral Oxides and Mineral Dusts". en. In: *Atmospheric Environment* 37.23 (July 2003), pp. 3201–3211. ISSN: 13522310. DOI: 10.1016/S1352-2310(03)00319-4.
- [69] R. Joel Gustafsson et al. "Reduction of NO₂ to Nitrous Acid on Illuminated Titanium Dioxide Aerosol Surfaces: Implications for Photocatalysis and Atmospheric Chemistry". en. In: *Chemical Communications* 37 (2006), p. 3936. ISSN: 1359-7345, 1364-548X. DOI: 10.1039/b609005b.

- [70] V. Faye McNeill et al. "Aqueous-Phase Secondary Organic Aerosol and Organosulfate Formation in Atmospheric Aerosols: A Modeling Study". In: *Environmental Science & Technology* 46.15 (Aug. 2012), pp. 8075–8081. ISSN: 0013-936X. DOI: 10.1021/es3002986.
- [71] Michael P. Tolocka and Barbara Turpin. "Contribution of Organosulfur Compounds to Organic Aerosol Mass". en. In: *Environmental Science & Technology* 46.15 (Aug. 2012), pp. 7978–7983. ISSN: 0013-936X, 1520-5851. DOI: 10.1021/es300651v.
- [72] Amy L. Linsebigler, Guangquan. Lu, and John T. Yates. "Photocatalysis on TiO₂ Surfaces: Principles, Mechanisms, and Selected Results". en. In: *Chemical Reviews* 95.3 (May 1995), pp. 735–758. ISSN: 0009-2665, 1520-6890. DOI: 10.1021/cr00035a013.
- [73] Pierre Pichat, ed. *Photocatalysis and Water Purification: From Fundamentals to Recent Applications*. Materials for Sustainable Energy and Development. OCLC: ocn842359315. Weinheim: Wiley-VCH, 2013. ISBN: 978-3-527-33187-1.
- [74] *Health Effects Institute. 2018. State of Global Air 2018. Special Report. Boston, MA:Health Effects Institute.*
- [75] Institute for Health Metrics and Evaluation, Seattle, USA. *Global Burden of Disease (GBD) Project*. <http://www.healthdata.org/gbd>. Mar. 2019.
- [76] *Health Effects of Particulate Matter*. Tech. rep. DK-2100 Copenhagen, Denmark: World Health Organization (WHO), Regional Office for Europe.
- [77] T. A. Hodgson. "Short Term Effects of Air Pollution on Mortality in New York City". In: *Environmental Science and Technology* 4 (1970), p. 589.
- [78] Michael R. Rampino and Stephen Self. "Sulphur-Rich Volcanic Eruptions and Stratospheric Aerosols". en. In: *Nature* 310.5979 (Aug. 1984), pp. 677–679. ISSN: 0028-0836, 1476-4687. DOI: 10.1038/310677a0.
- [79] J. E. Penner, R. E. Dickinson, and C. A. O'Neill. "Effects of Aerosol from Biomass Burning on the Global Radiation Budget". en. In: *Science* 256.5062 (June 1992), pp. 1432–1434. ISSN: 0036-8075, 1095-9203. DOI: 10.1126/science.256.5062.1432.

- [80] Juping Yan et al. "Review of Brown Carbon Aerosols: Recent Progress and Perspectives". en. In: *Science of The Total Environment* 634 (Sept. 2018), pp. 1475–1485. ISSN: 00489697. DOI: 10.1016/j.scitotenv.2018.04.083.
- [81] Dwayne E. Heard, ed. *Analytical Techniques for Atmospheric Measurement*. OCLC: ocm61362762. Oxford ; Ames, Iowa: Blackwell Pub, 2006. ISBN: 978-1-4051-2357-0.
- [82] Yoshiteru Iinuma et al. "Ozone-Driven Secondary Organic Aerosol Production Chain". en. In: *Environmental Science & Technology* 47.8 (Apr. 2013), pp. 3639–3647. ISSN: 0013-936X, 1520-5851. DOI: 10.1021/es305156z.
- [83] J. Wang et al. "Design of a New Multi-Phase Experimental Simulation Chamber for Atmospheric Photo-smog, Aerosol and Cloud Chemistry Research". en. In: *Atmospheric Measurement Techniques* 4.11 (Nov. 2011), pp. 2465–2494. ISSN: 1867-8548. DOI: 10.5194/amt-4-2465-2011.
- [84] Young J. Kim, ed. *Atmospheric and Biological Environmental Monitoring*. en. OCLC: ocn294887796. Dordrecht ; New York: Springer, 2009. ISBN: 978-1-4020-9673-0 978-1-4020-9674-7.
- [85] Kangwei Li et al. "Smog Chamber Study on Aging of Combustion Soot in Isoprene/SO₂/NO_x System: Changes of Mass, Size, Effective Density, Morphology and Mixing State". en. In: *Atmospheric Research* 184 (Feb. 2017), pp. 139–148. ISSN: 01698095. DOI: 10.1016/j.atmosres.2016.10.011.
- [86] Renee C. McVay et al. "SOA Formation from the Photooxidation of Alpha-Pinene: Systematic Exploration of the Simulation of Chamber Data". en. In: *Atmospheric Chemistry and Physics* 16.5 (Mar. 2016), pp. 2785–2802. ISSN: 1680-7324. DOI: 10.5194/acp-16-2785-2016.
- [87] M Dodge. "Chemical Oxidant Mechanisms for Air Quality Modeling: Critical Review". In: *Atmospheric Environment* 34.12-14 (2000), pp. 2103–2130. ISSN: 13522310. DOI: 10.1016/S1352-2310(99)00461-6.
- [88] C. Vigouroux et al. "Ground-Based FTIR and MAX-DOAS Observations of Formaldehyde at Réunion Island and Comparisons with Satellite and Model Data". en. In: *Atmospheric Chemistry and Physics* 9.24 (Dec. 2009), pp. 9523–9544. ISSN: 1680-7324. DOI: 10.5194/acp-9-9523-2009.

- [89] G. M. B. Dobson and D. N. Harrison. "Measurements of the Amount of Ozone in the Earth's Atmosphere and Its Relation to Other Geophysical Conditions". en. In: *Proceedings of the Royal Society A: Mathematical, Physical and Engineering Sciences* 110.756 (Apr. 1926), pp. 660–693. ISSN: 1364-5021, 1471-2946. DOI: 10.1098/rspa.1926.0040.
- [90] Ulrich Platt and J. Stutz. *Differential Optical Absorption Spectroscopy: Principles and Applications*. en. Physics of Earth and Space Environments. Berlin: Springer, 2008. ISBN: 978-3-540-21193-8 978-3-540-75776-4.
- [91] Matthew T. Parsons et al. "Real-Time Monitoring of Benzene, Toluene, and p-Xylene in a Photoreaction Chamber with a Tunable Mid-Infrared Laser and Ultraviolet Differential Optical Absorption Spectroscopy". en. In: *Applied Optics* 50.4 (Feb. 2011), A90. ISSN: 0003-6935, 1539-4522. DOI: 10.1364/AO.50.000A90.
- [92] Rainer Volkamer. "A DOAS Study on the Oxidation Mechanism of Aromatic Hydrocarbons under Simulated Atmospheric Conditions". In: (2002). DOI: 10.11588/heidok.00001939.
- [93] Keith D. Bartle and Peter Myers. "History of Gas Chromatography". en. In: *TrAC Trends in Analytical Chemistry* 21.9-10 (Sept. 2002), pp. 547–557. ISSN: 01659936. DOI: 10.1016/S0165-9936(02)00806-3.
- [94] A. J. P. Martin and R. L. M. Synge. "A New Form of Chromatogram Employing Two Liquid Phases: A Theory of Chromatography. 2. Application to the Micro-Determination of the Higher Monoamino-Acids in Proteins". en. In: *Biochemical Journal* 35.12 (Dec. 1941), pp. 1358–1368. ISSN: 0264-6021, 1470-8728. DOI: 10.1042/bj0351358.
- [95] A. T. James and A. J. P. Martin. "Gas-Liquid Partition Chromatography: The Separation and Micro-Estimation of Volatile Fatty Acids from Formic Acid to Dodecanoic Acid". en. In: *Biochemical Journal* 50.5 (Mar. 1952), pp. 679–690. ISSN: 0264-6021, 1470-8728. DOI: 10.1042/bj0500679.
- [96] Robert Lee Grob and Eugene F. Barry, eds. *Modern Practice of Gas Chromatography*. en. 4th ed. Hoboken, N.J: Wiley-Interscience, 2004. ISBN: 978-0-471-22983-4.
- [97] C. F. Poole. *Gas Chromatography*. 1st ed. Amsterdam ; Boston: Elsevier, 2012. ISBN: 978-0-12-385540-4.

- [98] Katja Dettmer and W. Engewald. "Ambient Air Analysis of Volatile Organic Compounds Using Adsorptive Enrichment". In: *Chromatographia* 57 (2003), S339–S347.
- [99] Elizabeth Woolfenden. "Monitoring VOCs in Air Using Sorbent Tubes Followed by Thermal Desorption-Capillary GC Analysis: Summary of Data and Practical Guidelines". en. In: *Journal of the Air & Waste Management Association* 47.1 (Jan. 1997), pp. 20–36. ISSN: 1096-2247, 2162-2906. DOI: 10.1080/10473289.1997.10464411.
- [100] E. Massold et al. "Determination of VOC and TVOC in Air Using Thermal Desorption GC-MS – Practical Implications for Test Chamber Experiments". en. In: *Chromatographia* 62.1-2 (July 2005), pp. 75–85. ISSN: 0009-5893, 1612-1112. DOI: 10.1365/s10337-005-0582-z.
- [101] Elizabeth Woolfenden. "Sorbent-Based Sampling Methods for Volatile and Semi-Volatile Organic Compounds in Air: Part 1: Sorbent-Based Air Monitoring Options". In: *Journal of Chromatography A. Extraction Techniques* 1217.16 (Apr. 2010), pp. 2674–2684. ISSN: 0021-9673. DOI: 10.1016/j.chroma.2009.12.042.
- [102] Elizabeth Woolfenden. "Sorbent-Based Sampling Methods for Volatile and Semi-Volatile Organic Compounds in Air. Part 2. Sorbent Selection and Other Aspects of Optimizing Air Monitoring Methods". en. In: *Journal of Chromatography A* 1217.16 (Apr. 2010), pp. 2685–2694. ISSN: 00219673. DOI: 10.1016/j.chroma.2010.01.015.
- [103] Trommsdorf. In: *Ann. Chem. Pharm.* 11 (1834).
- [104] P. L. Yue. "Introduction to the Modelling and Design of Photoreactors". In: *Photoelectrochemistry, Photocatalysis and Photoreactors*. Ed. by Mario Schiavello. Dordrecht: Springer Netherlands, 1985, pp. 527–547. ISBN: 978-90-481-8414-9 978-94-015-7725-0. DOI: 10.1007/978-94-015-7725-0_23.
- [105] C. M. Doede and C. A. Walker. "Photochemical Engineering". In: *Chemical Engineering* 62 (1955), pp. 159–178.
- [106] Paul R. Harris and Joshua S. Dranoff. "A Study of Perfectly Mixed Photochemical Reactors". en. In: *AIChE Journal* 11.3 (May 1965), pp. 497–502. ISSN: 0001-1541, 1547-5905. DOI: 10.1002/aic.690110325.

- [107] Alberto E. Cassano et al. "Photoreactor Analysis and Design: Fundamentals and Applications". en. In: *Industrial & Engineering Chemistry Research* 34.7 (July 1995), pp. 2155–2201. ISSN: 0888-5885, 1520-5045. DOI: 10.1021/ie00046a001.
- [108] Richard Gaertner and J. A. Kent. "Conversion in a Continuous Photochemical Reactor". en. In: *Industrial & Engineering Chemistry* 50.9 (Sept. 1958), pp. 1223–1226. ISSN: 0019-7866. DOI: 10.1021/ie50585a022.
- [109] Benjamin D. A. Hook et al. "A Practical Flow Reactor for Continuous Organic Photochemistry". en. In: *The Journal of Organic Chemistry* 70.19 (Sept. 2005), pp. 7558–7564. ISSN: 0022-3263, 1520-6904. DOI: 10.1021/jo050705p.
- [110] Kerry Gilmore and Peter H. Seeberger. "Continuous Flow Photochemistry: Continuous Flow Photochemistry". en. In: *The Chemical Record* 14.3 (June 2014), pp. 410–418. ISSN: 15278999. DOI: 10.1002/tcr.201402035.
- [111] Dario Cambié et al. "Applications of Continuous-Flow Photochemistry in Organic Synthesis, Material Science, and Water Treatment". en. In: *Chemical Reviews* 116.17 (Sept. 2016), pp. 10276–10341. ISSN: 0009-2665, 1520-6890. DOI: 10.1021/acs.chemrev.5b00707.
- [112] Tiffany Charbouillot et al. "Mechanism of Carboxylic Acid Photooxidation in Atmospheric Aqueous Phase: Formation, Fate and Reactivity". en. In: *Atmospheric Environment* 56 (Sept. 2012), pp. 1–8. ISSN: 13522310. DOI: 10.1016/j.atmosenv.2012.03.079.
- [113] Luisa Schöne et al. "Atmospheric Aqueous Phase Radical Chemistry of the Isoprene Oxidation Products Methacrolein, Methyl Vinyl Ketone, Methacrylic Acid and Acrylic Acid – Kinetics and Product Studies". en. In: *Physical Chemistry Chemical Physics* 16.13 (2014), pp. 6257–6272. DOI: 10.1039/C3CP54859G.
- [114] Annmarie G. Carlton et al. "Atmospheric Oxalic Acid and SOA Production from Glyoxal: Results of Aqueous Photooxidation Experiments". en. In: *Atmospheric Environment* 41.35 (Nov. 2007), pp. 7588–7602. ISSN: 13522310. DOI: 10.1016/j.atmosenv.2007.05.035.

- [115] Rod S. Mason. "Atmospheric Photochemistry". en. In: *Applied Photochemistry*. Ed. by Rachel C. Evans, Peter Douglas, and Hugh D. Burrow. Dordrecht: Springer Netherlands, 2013, pp. 217–246. ISBN: 978-90-481-3829-6 978-90-481-3830-2. DOI: 10.1007/978-90-481-3830-2_5.
- [116] Christian George et al. "Heterogeneous Photochemistry in the Atmosphere". en. In: *Chemical Reviews* 115.10 (May 2015), pp. 4218–4258. ISSN: 0009-2665, 1520-6890. DOI: 10.1021/cr500648z.
- [117] Ho-Jin Lim, Annmarie G. Carlton, and Barbara J. Turpin. "Isoprene Forms Secondary Organic Aerosol through Cloud Processing: Model Simulations". en. In: *Environmental Science & Technology* 39.12 (June 2005), pp. 4441–4446. ISSN: 0013-936X, 1520-5851. DOI: 10.1021/es048039h.
- [118] Y B Lim et al. "Aqueous Chemistry and Its Role in Secondary Organic Aerosol (SOA) Formation". en. In: *Atmos. Chem. Phys.* (2010), p. 19.
- [119] B. Ervens, B. J. Turpin, and R. J. Weber. "Secondary Organic Aerosol Formation in Cloud Droplets and Aqueous Particles (aqSOA): A Review of Laboratory, Field and Model Studies". en. In: *Atmospheric Chemistry and Physics* 11.21 (Nov. 2011), pp. 11069–11102. ISSN: 1680-7324. DOI: 10.5194/acp-11-11069-2011.
- [120] Yi Tan et al. "SOA from Methylglyoxal in Clouds and Wet Aerosols: Measurement and Prediction of Key Products". en. In: *Atmospheric Environment* 44.39 (Dec. 2010), pp. 5218–5226. ISSN: 13522310. DOI: 10.1016/j.atmosenv.2010.08.045.
- [121] B. Ervens and R. Volkamer. "Glyoxal Processing by Aerosol Multiphase Chemistry: Towards a Kinetic Modeling Framework of Secondary Organic Aerosol Formation in Aqueous Particles". en. In: *Atmospheric Chemistry and Physics* 10.17 (Sept. 2010), pp. 8219–8244. ISSN: 1680-7324. DOI: 10.5194/acp-10-8219-2010.
- [122] Nicole K. Richards-Henderson et al. "Aqueous Oxidation of Green Leaf Volatiles by Hydroxyl Radical as a Source of SOA: Kinetics and SOA Yields". en. In: *Atmospheric Environment* 95 (Oct. 2014), pp. 105–112. ISSN: 13522310. DOI: 10.1016/j.atmosenv.2014.06.026.
- [123] E M Elkanzi and Goh Bee Kheng. "H₂O₂-UV Degradation Kinetics of Isoprene in Aqueous Solution". en. In: (2000), p. 8.

- [124] Angela Marinoni et al. "Hydrogen Peroxide in Natural Cloud Water: Sources and Photoreactivity". en. In: *Atmospheric Research* 101.1-2 (July 2011), pp. 256–263. ISSN: 01698095. DOI: 10.1016/j.atmosres.2011.02.013.
- [125] A. Nouri, A.Hedayati Moghaddam, and J. Sargolzaei. "A Mini-Review of Photo Catalytic Process in Wastewater Treatment". en. In: *Recent Innovations in Chemical Engineering (Formerly Recent Patents on Chemical Engineering)* 9.2 (Apr. 2017), pp. 88–97. ISSN: 24055204. DOI: 10.2174/2405520410666170207101914.
- [126] Edward S. Galbavy, Keren Ram, and Cort Anastasio. "2-Nitrobenzaldehyde as a Chemical Actinometer for Solution and Ice Photochemistry". en. In: *Journal of Photochemistry and Photobiology A: Chemistry* 209.2-3 (Jan. 2010), pp. 186–192. ISSN: 10106030. DOI: 10.1016/j.jphotochem.2009.11.013.
- [127] John M. Allen, Sandra K. Allen, and Steven W. Baertschi. "2-Nitrobenzaldehyde: A Convenient UV-A and UV-B Chemical Actinometer for Drug Photostability Testing". en. In: *Journal of Pharmaceutical and Biomedical Analysis* 24.2 (Dec. 2000), pp. 167–178. ISSN: 07317085. DOI: 10.1016/S0731-7085(00)00423-4.
- [128] K. M. Badali et al. "Formation of Hydroxyl Radicals from Photolysis of Secondary Organic Aerosol Material". en. In: *Atmospheric Chemistry and Physics* 15.14 (July 2015), pp. 7831–7840. ISSN: 1680-7324. DOI: 10.5194/acp-15-7831-2015.
- [129] Javier Mateos et al. "A Microfluidic Photoreactor Enables 2-Methylbenzophenone Light-Driven Reactions with Superior Performance". en. In: *Chemical Communications* 54.50 (2018), pp. 6820–6823. ISSN: 1359-7345, 1364-548X. DOI: 10.1039/C8CC01373J.
- [130] Victor M. Monsalvo, ed. *Efficient Management of Wastewater from Manufacturing: New Treatment Technologies*. Waretown, NJ, USA: Apple Academic Press, 2015. ISBN: 978-1-77188-171-5.
- [131] Natalia De la Cruz et al. "O-Nitrobenzaldehyde Actinometry in the Presence of Suspended TiO₂ for Photocatalytic Reactors". en. In: *Catalysis Today* 209 (June 2013), pp. 209–214. ISSN: 09205861. DOI: 10.1016/j.cattod.2012.08.035.

- [132] Chelsea D. Cote et al. "Photochemical Production of Singlet Oxygen by Urban Road Dust". en. In: *Environmental Science & Technology Letters* 5.2 (Feb. 2018), pp. 92–97. ISSN: 2328-8930, 2328-8930. DOI: 10.1021/acs.estlett.7b00533.
- [133] O. Alizadeh Choobari, P. Zawar-Reza, and A. Sturman. "The Global Distribution of Mineral Dust and Its Impacts on the Climate System: A Review". en. In: *Atmospheric Research* 138 (Mar. 2014), pp. 152–165. ISSN: 01698095. DOI: 10.1016/j.atmosres.2013.11.007.
- [134] Manish Shrivastava et al. "Recent Advances in Understanding Secondary Organic Aerosol: Implications for Global Climate Forcing: Advances in Secondary Organic Aerosol". en. In: *Reviews of Geophysics* 55.2 (June 2017), pp. 509–559. ISSN: 87551209. DOI: 10.1002/2016RG000540.
- [135] Erika von Schneidemesser et al. "Chemistry and the Linkages between Air Quality and Climate Change". en. In: *Chemical Reviews* 115.10 (May 2015), pp. 3856–3897. ISSN: 0009-2665, 1520-6890. DOI: 10.1021/acs.chemrev.5b00089.
- [136] J. P. D. Abbatt, A. K. Y. Lee, and J. A. Thornton. "Quantifying Trace Gas Uptake to Tropospheric Aerosol: Recent Advances and Remaining Challenges". en. In: *Chemical Society Reviews* 41.19 (2012), p. 6555. ISSN: 0306-0012, 1460-4744. DOI: 10.1039/c2cs35052a.
- [137] Lynn R. Mazzoleni et al. "Identification of Water-Soluble Organic Carbon in Non-Urban Aerosols Using Ultrahigh-Resolution FT-ICR Mass Spectrometry: Organic Anions". en. In: *Environmental Chemistry* 9.3 (2012), p. 285. ISSN: 1448-2517. DOI: 10.1071/EN11167.
- [138] Philippe Schmitt-Kopplin et al. "Analysis of the Unresolved Organic Fraction in Atmospheric Aerosols with Ultrahigh-Resolution Mass Spectrometry and Nuclear Magnetic Resonance Spectroscopy: Organosulfates As Photochemical Smog Constituents". en. In: *Analytical Chemistry* 82.19 (Oct. 2010), pp. 8017–8026. ISSN: 0003-2700, 1520-6882. DOI: 10.1021/ac101444r.
- [139] A. S. Wozniak et al. "Technical Note: Molecular Characterization of Aerosol-Derived Water Soluble Organic Carbon Using Ultrahigh Resolution Electrospray Ionization Fourier Transform Ion Cyclotron Resonance Mass Spectrometry". en. In: *Atmospheric Chemistry and Physics* 8.17

- (Sept. 2008), pp. 5099–5111. ISSN: 1680-7324. DOI: 10.5194/acp-8-5099-2008.
- [140] Jingyi Zhang et al. “Molecular Characterisation of Ambient Aerosols by Sequential Solvent Extractions and High-Resolution Mass Spectrometry”. en. In: *Environmental Chemistry* 15.3 (2018), p. 150. ISSN: 1448-2517. DOI: 10.1071/EN17197.
- [141] A. S. Willoughby, A. S. Wozniak, and P. G. Hatcher. “A Molecular-Level Approach for Characterizing Water-Insoluble Components of Ambient Organic Aerosol Particulates Using Ultrahigh-Resolution Mass Spectrometry”. en. In: *Atmospheric Chemistry and Physics* 14.18 (Sept. 2014), pp. 10299–10314. ISSN: 1680-7324. DOI: 10.5194/acp-14-10299-2014.
- [142] A. M. K. Hansen et al. “Organosulfates and Organic Acids in Arctic Aerosols: Speciation, Annual Variation and Concentration Levels”. en. In: *Atmospheric Chemistry and Physics* 14.15 (Aug. 2014), pp. 7807–7823. ISSN: 1680-7324. DOI: 10.5194/acp-14-7807-2014.
- [143] Marianne Glasius et al. “Organosulfates in Aerosols Downwind of an Urban Region in Central Amazon”. en. In: *Environmental Science: Processes & Impacts* 20.11 (2018), pp. 1546–1558. ISSN: 2050-7887, 2050-7895. DOI: 10.1039/C8EM00413G.
- [144] Anusha P. S. Hettiyadura et al. “Qualitative and Quantitative Analysis of Atmospheric Organosulfates in Centreville, Alabama”. en. In: *Atmospheric Chemistry and Physics* 17.2 (Jan. 2017), pp. 1343–1359. ISSN: 1680-7324. DOI: 10.5194/acp-17-1343-2017.
- [145] Elizabeth A. Stone et al. “Characterization of Organosulfates in Atmospheric Aerosols at Four Asian Locations”. en. In: *Atmospheric Environment* 47 (Feb. 2012), pp. 323–329. ISSN: 1352-2310. DOI: 10.1016/j.atmosenv.2011.10.058.
- [146] Michael P. Tolocka and Barbara Turpin. “Contribution of Organosulfur Compounds to Organic Aerosol Mass”. en. In: *Environmental Science & Technology* 46.15 (Aug. 2012), pp. 7978–7983. ISSN: 0013-936X, 1520-5851. DOI: 10.1021/es300651v.

- [147] Jason D. Surratt et al. "Organosulfate Formation in Biogenic Secondary Organic Aerosol". en. In: *The Journal of Physical Chemistry A* 112.36 (Sept. 2008), pp. 8345–8378. ISSN: 1089-5639, 1520-5215. DOI: 10.1021/jp802310p.
- [148] H. Lukács et al. "Quantitative Assessment of Organosulfates in Size-Segregated Rural Fine Aerosol". en. In: *Atmospheric Chemistry and Physics* 9.1 (Jan. 2009), pp. 231–238. ISSN: 1680-7324. DOI: 10.5194/acp-9-231-2009.
- [149] Barbara Nozière et al. "Radical-Initiated Formation of Organosulfates and Surfactants in Atmospheric Aerosols: ORGANOSULFATES AND SURFACTANTS IN AEROSOLS". en. In: *Geophysical Research Letters* 37.5 (Mar. 2010). ISSN: 00948276. DOI: 10.1029/2009GL041683.
- [150] A. M. K. Hansen et al. "Hygroscopic Properties and Cloud Condensation Nuclei Activation of Limonene-Derived Organosulfates and Their Mixtures with Ammonium Sulfate". en. In: *Atmospheric Chemistry and Physics* 15.24 (Dec. 2015), pp. 14071–14089. ISSN: 1680-7324. DOI: 10.5194/acp-15-14071-2015.
- [151] Armando D. Estillore et al. "Water Uptake and Hygroscopic Growth of Organosulfate Aerosol". en. In: *Environmental Science & Technology* 50.8 (Apr. 2016), pp. 4259–4268. ISSN: 0013-936X, 1520-5851. DOI: 10.1021/acs.est.5b05014.
- [152] Jason D. Surratt et al. "Evidence for Organosulfates in Secondary Organic Aerosol". en. In: *Environmental Science & Technology* 41.2 (Jan. 2007), pp. 517–527. ISSN: 0013-936X, 1520-5851. DOI: 10.1021/es062081q.
- [153] Adam I. Darer et al. "Formation and Stability of Atmospherically Relevant Isoprene-Derived Organosulfates and Organonitrates". en. In: *Environmental Science & Technology* 45.5 (Mar. 2011), pp. 1895–1902. ISSN: 0013-936X, 1520-5851. DOI: 10.1021/es103797z.
- [154] Monica Passananti et al. "Organosulfate Formation through the Heterogeneous Reaction of Sulfur Dioxide with Unsaturated Fatty Acids and Long-Chain Alkenes". en. In: *Angewandte Chemie International Edition* 55.35 (Aug. 2016), pp. 10336–10339. ISSN: 14337851. DOI: 10.1002/anie.201605266.

- [155] Jing Shang et al. "SO₂ Uptake on Oleic Acid: A New Formation Pathway of Organosulfur Compounds in the Atmosphere". en. In: *Environmental Science & Technology Letters* 3.2 (Feb. 2016), pp. 67–72. ISSN: 2328-8930, 2328-8930. DOI: 10.1021/acs.estlett.6b00006.
- [156] X.L. Shen et al. "Heterogeneous Reactions of Glyoxal on Mineral Particles: A New Avenue for Oligomers and Organosulfate Formation". In: *Atmospheric Environment* 131 (2016), pp. 133–140.
- [157] Liubin Huang et al. "Formation of Organosulfur Compounds through Transition Metal Ion-Catalyzed Aqueous Phase Reactions". en. In: *Environmental Science & Technology Letters* 5.6 (June 2018), pp. 315–321. ISSN: 2328-8930, 2328-8930. DOI: 10.1021/acs.estlett.8b00225.
- [158] Mark J. Perri et al. "Organosulfates from Glycolaldehyde in Aqueous Aerosols and Clouds: Laboratory Studies". en. In: *Atmospheric Environment* 44.21-22 (July 2010), pp. 2658–2664. ISSN: 13522310. DOI: 10.1016/j.atmosenv.2010.03.031.
- [159] J. Schindelka et al. "Sulfate Radical-Initiated Formation of Isoprene-Derived Organosulfates in Atmospheric Aerosols". en. In: 165.0 (Dec. 2013), pp. 237–259. ISSN: 1364-5498. DOI: 10.1039/C3FD00042G.
- [160] Paulina Wach et al. "Radical Oxidation of Methyl Vinyl Ketone and Methacrolein in Aqueous Droplets: Characterization of Organosulfates and Atmospheric Implications". en. In: *Chemosphere* 214 (Jan. 2019), pp. 1–9. ISSN: 00456535. DOI: 10.1016/j.chemosphere.2018.09.026.
- [161] K. J. Rudziński, L. Gmachowski, and I. Kuznietsova. "Reactions of Isoprene and Sulphoxy Radical-Anions – a Possible Source of Atmospheric Organosulphites and Organosulphates". en. In: *Atmospheric Chemistry and Physics* 9.6 (Mar. 2009), pp. 2129–2140. ISSN: 1680-7324. DOI: 10.5194/acp-9-2129-2009.
- [162] B. Ervens. "CAPRAM 2.4 (MODAC Mechanism): An Extended and Condensed Tropospheric Aqueous Phase Mechanism and Its Application". en. In: *Journal of Geophysical Research* 108.D14 (2003). ISSN: 0148-0227. DOI: 10.1029/2002JD002202.

- [163] Kai Chung Kwong et al. "Importance of Sulfate Radical Anion Formation and Chemistry in Heterogeneous OH Oxidation of Sodium Methyl Sulfate, the Smallest Organosulfate". en. In: *Atmospheric Chemistry and Physics* 18.4 (Feb. 2018), pp. 2809–2820. ISSN: 1680-7324. DOI: 10.5194/acp-18-2809-2018.
- [164] Michael R. Hoffmann et al. "Environmental Applications of Semiconductor Photocatalysis". en. In: *Chemical Reviews* 95.1 (Jan. 1995), pp. 69–96. ISSN: 0009-2665, 1520-6890. DOI: 10.1021/cr00033a004.
- [165] Mohammad. Abdullah, Gary K. C. Low, and Ralph W. Matthews. "Effects of Common Inorganic Anions on Rates of Photocatalytic Oxidation of Organic Carbon over Illuminated Titanium Dioxide". en. In: *The Journal of Physical Chemistry* 94.17 (Aug. 1990), pp. 6820–6825. ISSN: 0022-3654, 1541-5740. DOI: 10.1021/j100380a051.
- [166] Jiwen Fan and Renyi Zhang. "Atmospheric Oxidation Mechanism of Isoprene". en. In: *Environmental Chemistry* 1.3 (2004), p. 140. ISSN: 1448-2517. DOI: 10.1071/EN04045.
- [167] K. Sindelarova et al. "Global Data Set of Biogenic VOC Emissions Calculated by the MEGAN Model over the Last 30 Years". en. In: *Atmospheric Chemistry and Physics* 14.17 (Sept. 2014), pp. 9317–9341. ISSN: 1680-7324. DOI: 10.5194/acp-14-9317-2014.
- [168] D. van Pinxteren et al. "Schmücke Hill Cap Cloud and Valley Stations Aerosol Characterisation during FEBUKO (II): Organic Compounds". en. In: *Atmospheric Environment* 39.23-24 (July 2005), pp. 4305–4320. ISSN: 13522310. DOI: 10.1016/j.atmosenv.2005.02.014.
- [169] Haihan Chen, Charith E. Nanayakkara, and Vicki H. Grassian. "Titanium Dioxide Photocatalysis in Atmospheric Chemistry". en. In: *Chemical Reviews* 112.11 (Nov. 2012), pp. 5919–5948. ISSN: 0009-2665, 1520-6890. DOI: 10.1021/cr3002092.
- [170] Cort Anastasio and Keith G. McGregor. "Chemistry of Fog Waters in California's Central Valley: 1. In Situ Photoformation of Hydroxyl Radical and Singlet Molecular Oxygen". en. In: *Atmospheric Environment* 35.6 (Jan. 2001), pp. 1079–1089. ISSN: 13522310. DOI: 10.1016/S1352-2310(00)00281-8.

- [171] Bruce C. Faust and John M. Allen. "Aqueous-Phase Photochemical Sources of Peroxyl Radicals and Singlet Molecular Oxygen in Clouds and Fog". en. In: *Journal of Geophysical Research* 97.D12 (1992), p. 12913. ISSN: 0148-0227. DOI: 10.1029/92JD00843.
- [172] Peter Warneck and Jonathan Williams. *The Atmospheric Chemist's Companion: Numerical Data for Use in the Atmospheric Sciences*. en. OCLC: 784077792. Dordrecht: Springer, 2012. ISBN: 978-94-007-2274-3.
- [173] A. P. S. Hettiyadura et al. "Determination of Atmospheric Organosulfates Using HILIC Chromatography with MS Detection". en. In: *Atmospheric Measurement Techniques* 8.6 (June 2015), pp. 2347–2358. ISSN: 1867-8548. DOI: 10.5194/amt-8-2347-2015.
- [174] Alessandro Nalesso et al. "Synthesis and Characterization of Ethyl Sulfate and D5-Ethyl Sulfate as Reference Substances for Applications in Clinical and Forensic Toxicology". en. In: *Rapid Communications in Mass Spectrometry* 19.23 (Dec. 2005), pp. 3612–3614. ISSN: 0951-4198, 1097-0231. DOI: 10.1002/rcm.2233.
- [175] Ru-Jin Huang et al. "Organosulfates in Atmospheric Aerosol: Synthesis and Quantitative Analysis of PM_{2.5} from Xi'an, Northwestern China". en. In: *Atmospheric Measurement Techniques* 11.6 (June 2018), pp. 3447–3456. ISSN: 1867-8548. DOI: 10.5194/amt-11-3447-2018.
- [176] Saber Ahmed et al. "Heterogeneous Photocatalytic Degradation of Phenols in Wastewater: A Review on Current Status and Developments". en. In: *Desalination* 261.1-2 (Oct. 2010), pp. 3–18. ISSN: 00119164. DOI: 10.1016/j.desal.2010.04.062.
- [177] Jean-Marie Herrmann. "Heterogeneous Photocatalysis: Fundamentals and Applications to the Removal of Various Types of Aqueous Pollutants". en. In: *Catalysis Today* 53.1 (Oct. 1999), pp. 115–129. ISSN: 09205861. DOI: 10.1016/S0920-5861(99)00107-8.
- [178] Yoshio Nosaka and Atsuko Y. Nosaka. "Generation and Detection of Reactive Oxygen Species in Photocatalysis". en. In: *Chemical Reviews* 117.17 (Sept. 2017), pp. 11302–11336. ISSN: 0009-2665, 1520-6890. DOI: 10.1021/acs.chemrev.7b00161.

- [179] Y. Tang et al. "Kinetics and Spectroscopy of the SO₄- Radical in Aqueous Solution". In: *Journal of Photochemistry and Photobiology A: Chemistry* 44.3 (1988), pp. 243–258.
- [180] Chenju Liang and Hsin-Wey Su. "Identification of Sulfate and Hydroxyl Radicals in Thermally Activated Persulfate". en. In: *Industrial & Engineering Chemistry Research* 48.11 (June 2009), pp. 5558–5562. ISSN: 0888-5885, 1520-5045. DOI: 10.1021/ie9002848.
- [181] Zhijian Li et al. "Nitrogen-Containing Secondary Organic Aerosol Formation by Acrolein Reaction with Ammonia/Ammonium". en. In: *Atmospheric Chemistry and Physics* 19.2 (Feb. 2019), pp. 1343–1356. ISSN: 1680-7324. DOI: 10.5194/acp-19-1343-2019.
- [182] Martin Brüggemann et al. "Real-Time Detection of Highly Oxidized Organosulfates and BSOA Marker Compounds during the F-BEACH 2014 Field Study". en. In: *Atmospheric Chemistry and Physics* 17.2 (Jan. 2017), pp. 1453–1469. ISSN: 1680-7324. DOI: 10.5194/acp-17-1453-2017.
- [183] Anke Mutzel et al. "Highly Oxidized Multifunctional Organic Compounds Observed in Tropospheric Particles: A Field and Laboratory Study". en. In: *Environmental Science & Technology* 49.13 (July 2015), pp. 7754–7761. ISSN: 0013-936X, 1520-5851. DOI: 10.1021/acs.est.5b00885.
- [184] Hoi Ki Lam et al. "Heterogeneous OH Oxidation of Isoprene-Epoxydiol-Derived Organosulfates: Kinetics, Chemistry and Formation of Inorganic Sulfate". en. In: *Atmospheric Chemistry and Physics* 19.4 (Feb. 2019), pp. 2433–2440. ISSN: 1680-7324. DOI: 10.5194/acp-19-2433-2019.
- [185] Taichu Y. Tanaka and Masaru Chiba. "A Numerical Study of the Contributions of Dust Source Regions to the Global Dust Budget". en. In: *Global and Planetary Change* 52.1-4 (July 2006), pp. 88–104. ISSN: 09218181. DOI: 10.1016/j.gloplacha.2006.02.002.
- [186] Albert Ansmann et al. "Dust and Smoke Transport from Africa to South America: Lidar Profiling over Cape Verde and the Amazon Rainforest". en. In: *Geophysical Research Letters* 36.11 (June 2009). ISSN: 0094-8276. DOI: 10.1029/2009GL037923.
- [187] Alla H. Falkovich. "Adsorption of Organic Compounds Pertinent to Urban Environments onto Mineral Dust Particles". en. In: *Journal of Geophysical Research* 109.D2 (2004). ISSN: 0148-0227. DOI: 10.1029/2003JD003919.

- [188] Min Shao et al. "Volatile Organic Compounds Measured in Summer in Beijing and Their Role in Ground-level Ozone Formation". en. In: *Journal of Geophysical Research* 114 (Apr. 2009). ISSN: 0148-0227. DOI: 10.1029/2008JD010863.
- [189] Yingjun Liu et al. "Isoprene Photochemistry over the Amazon Rainforest". en. In: *Proceedings of the National Academy of Sciences* 113.22 (May 2016), pp. 6125–6130. ISSN: 0027-8424, 1091-6490. DOI: 10.1073/pnas.1524136113.
- [190] R. C. Sullivan et al. "Direct Observations of the Atmospheric Processing of Asian Mineral Dust". en. In: *Atmospheric Chemistry and Physics* 7.5 (Feb. 2007), pp. 1213–1236. ISSN: 1680-7324. DOI: 10.5194/acp-7-1213-2007.
- [191] *World Meteorological Organization, Scientific Assessment of Ozone Depletion: 1994, WMO Global Ozone Research and Monitoring Project - Report No. 37.* en. Tech. rep. Geneva, Switzerland, 1994.
- [192] A Guenther. "Natural Emissions of Non-Methane Volatile Organic Compounds, Carbon Monoxide, and Oxides of Nitrogen from North America". In: *Atmospheric Environment* 34.12-14 (2000), pp. 2205–2230. ISSN: 13522310. DOI: 10.1016/S1352-2310(99)00465-3.
- [193] R Sawyer. "Mobile Sources Critical Review: 1998 NARSTO Assessment". In: *Atmospheric Environment* 34.12-14 (2000), pp. 2161–2181. ISSN: 13522310. DOI: 10.1016/S1352-2310(99)00463-X.
- [194] M Placet. "Emissions of Ozone Precursors from Stationary Sources: A Critical Review". In: *Atmospheric Environment* 34.12-14 (2000), pp. 2183–2204. ISSN: 13522310. DOI: 10.1016/S1352-2310(99)00464-1.
- [195] Roger Atkinson and Janet Arey. "Atmospheric Degradation of Volatile Organic Compounds". en. In: *Chemical Reviews* 103.12 (Dec. 2003), pp. 4605–4638. ISSN: 0009-2665, 1520-6890. DOI: 10.1021/cr0206420.
- [196] A. B. Guenther et al. "The Model of Emissions of Gases and Aerosols from Nature Version 2.1 (MEGAN2.1): An Extended and Updated Framework for Modeling Biogenic Emissions". en. In: *Geoscientific Model Development* 5.6 (Nov. 2012), pp. 1471–1492. ISSN: 1991-9603. DOI: 10.5194/gmd-5-1471-2012.

- [197] Sarah A. Safieddine, Colette L. Heald, and Barron H. Henderson. “The Global Nonmethane Reactive Organic Carbon Budget: A Modeling Perspective: Global Reactive Organic Carbon Budget”. en. In: *Geophysical Research Letters* 44.8 (Apr. 2017), pp. 3897–3906. ISSN: 00948276. DOI: 10.1002/2017GL072602.
- [198] Marianne Glasius and Allen H. Goldstein. “Recent Discoveries and Future Challenges in Atmospheric Organic Chemistry”. en. In: *Environmental Science & Technology* 50.6 (Mar. 2016), pp. 2754–2764. ISSN: 0013-936X, 1520-5851. DOI: 10.1021/acs.est.5b05105.
- [199] “Clouds and Aerosols”. In: *Climate Change 2013 - The Physical Science Basis*. Ed. by Intergovernmental Panel on Climate Change. Cambridge: Cambridge University Press, 2014, pp. 571–658. ISBN: 978-1-107-41532-4. DOI: 10.1017/CB09781107415324.016.
- [200] A. G. Carlton, C. Wiedinmyer, and J. H. Kroll. “A Review of Secondary Organic Aerosol (SOA) Formation from Isoprene”. en. In: *Atmospheric Chemistry and Physics* 9.14 (July 2009), pp. 4987–5005. ISSN: 1680-7324. DOI: 10.5194/acp-9-4987-2009.
- [201] Q. Zhang et al. “Ubiquity and Dominance of Oxygenated Species in Organic Aerosols in Anthropogenically-Influenced Northern Hemisphere Midlatitudes: UBIQUITY AND DOMINANCE OF OXYGENATED OA”. en. In: *Geophysical Research Letters* 34.13 (July 2007). ISSN: 00948276. DOI: 10.1029/2007GL029979.
- [202] J. A. de Gouw. “Budget of Organic Carbon in a Polluted Atmosphere: Results from the New England Air Quality Study in 2002”. en. In: *Journal of Geophysical Research* 110.D16 (2005). ISSN: 0148-0227. DOI: 10.1029/2004JD005623.
- [203] Allen H. Goldstein and Ian E. Galbally. “Known and Unexplored Organic Constituents in the Earth’s Atmosphere”. en. In: *Environmental Science & Technology* 41.5 (Mar. 2007), pp. 1514–1521. ISSN: 0013-936X, 1520-5851. DOI: 10.1021/es072476p.
- [204] Piers Forster et al. *Changes in Atmospheric Constituents and in Radiative Forcing*. en. Tech. rep. Cambridge, United Kingdom and New York, NY, USA: Cambridge University Press, 2007.

- [205] A. Nel. "ATMOSPHERE: Enhanced: Air Pollution-Related Illness: Effects of Particles". en. In: *Science* 308.5723 (May 2005), pp. 804–806. ISSN: 0036-8075, 1095-9203. DOI: 10.1126/science.1108752.
- [206] Peter H. McMurry and Daniel. Grosjean. "Gas and Aerosol Wall Losses in Teflon Film Smog Chambers". en. In: *Environmental Science & Technology* 19.12 (Dec. 1985), pp. 1176–1182. ISSN: 0013-936X, 1520-5851. DOI: 10.1021/es00142a006.
- [207] Jennifer E. Stern et al. "Aerosol Formation and Growth in Atmospheric Aromatic Hydrocarbon Photooxidation". en. In: *Environmental Science & Technology* 21.12 (Dec. 1987), pp. 1224–1231. ISSN: 0013-936X, 1520-5851. DOI: 10.1021/es00165a011.
- [208] Jay R Odum et al. "Gas/Particle Partitioning and Secondary Organic Aerosol Yields". en. In: (), p. 6.
- [209] T. E. Kleindienst et al. "Determination of Secondary Organic Aerosol Products from the Photooxidation of Toluene and Their Implications in Ambient PM_{2.5}". en. In: *Journal of Atmospheric Chemistry* 47.1 (Jan. 2004), pp. 79–100. ISSN: 0167-7764. DOI: 10.1023/B:JOCH.0000012305.94498.28.
- [210] T.E. Kleindienst et al. "Secondary Organic Aerosol Formation from the Oxidation of Aromatic Hydrocarbons in the Presence of Dry Submicron Ammonium Sulfate Aerosol". en. In: *Atmospheric Environment* 33.22 (Sept. 1999), pp. 3669–3681. ISSN: 13522310. DOI: 10.1016/S1352-2310(99)00121-1.
- [211] William PL Carter et al. "A New Environmental Chamber for Evaluation of Gas-Phase Chemical Mechanisms and Secondary Aerosol Formation". In: *Atmospheric Environment* 39.40 (2005), pp. 7768–7788.
- [212] X. Wang et al. "Design and Characterization of a Smog Chamber for Studying Gas-Phase Chemical Mechanisms and Aerosol Formation". en. In: *Atmospheric Measurement Techniques* 7.1 (Jan. 2014), pp. 301–313. ISSN: 1867-8548. DOI: 10.5194/amt-7-301-2014.
- [213] Min Song et al. "The Influence of OH Concentration on SOA Formation from Isoprene Photooxidation". en. In: *Science of The Total Environment* 650 (Feb. 2019), pp. 951–957. ISSN: 00489697. DOI: 10.1016/j.scitotenv.2018.09.084.

- [214] S. Rossignol et al. "Development of a Parallel Sampling and Analysis Method for the Elucidation of Gas/Particle Partitioning of Oxygenated Semi-Volatile Organics: A Limonene Ozonolysis Study". en. In: *Atmospheric Measurement Techniques* 5.6 (June 2012), pp. 1459–1489. ISSN: 1867-8548. DOI: 10.5194/amt-5-1459-2012.
- [215] Levi H. Mielke et al. "Development of a Proton-Transfer Reaction-Linear Ion Trap Mass Spectrometer for Quantitative Determination of Volatile Organic Compounds". en. In: *Analytical Chemistry* 80.21 (Nov. 2008), pp. 8171–8177. ISSN: 0003-2700, 1520-6882. DOI: 10.1021/ac801328d.
- [216] A. Jordan et al. "A High Resolution and High Sensitivity Proton-Transfer-Reaction Time-of-Flight Mass Spectrometer (PTR-TOF-MS)". en. In: *International Journal of Mass Spectrometry* 286.2-3 (Sept. 2009), pp. 122–128. ISSN: 13873806. DOI: 10.1016/j.ijms.2009.07.005.
- [217] A. Jordan et al. "An Online Ultra-High Sensitivity Proton-Transfer-Reaction Mass-Spectrometer Combined with Switchable Reagent Ion Capability (PTR+SRI-MS)". en. In: *International Journal of Mass Spectrometry* 286.1 (Sept. 2009), pp. 32–38. ISSN: 13873806. DOI: 10.1016/j.ijms.2009.06.006.
- [218] Philipp Sulzer et al. "From Conventional Proton-Transfer-Reaction Mass Spectrometry (PTR-MS) to Universal Trace Gas Analysis". en. In: *International Journal of Mass Spectrometry* 321-322 (May 2012), pp. 66–70. ISSN: 13873806. DOI: 10.1016/j.ijms.2012.05.003.
- [219] Tomasz Majchrzak et al. "PTR-MS and GC-MS as Complementary Techniques for Analysis of Volatiles: A Tutorial Review". en. In: *Analytica Chimica Acta* 1035 (Dec. 2018), pp. 1–13. ISSN: 00032670. DOI: 10.1016/j.aca.2018.06.056.
- [220] Somenath Mitra et al. "Characteristics of Microtrap-Based Injection Systems for Continuous Monitoring of Volatile Organic Compounds by Gas Chromatography". en. In: *Journal of Chromatography A* 727.1 (Mar. 1996), pp. 111–118. ISSN: 00219673. DOI: 10.1016/0021-9673(95)01062-9.
- [221] Anthony J. Borgerding and Charles W. Wilkerson. "Cryogenically Cooled Microloop System for Sampling and Injection in Fast GC". en. In: *Analytical Chemistry* 68.4 (Jan. 1996), pp. 701–707. ISSN: 0003-2700, 1520-6882. DOI: 10.1021/ac950853n.

- [222] Michael Holdren et al. "Development and Evaluation of a Thermoelectric Cold Trap for the Gas Chromatographic Analysis of Atmospheric Compounds". In: *Analytical Chemistry* 70.22 (Nov. 1998), pp. 4836–4840. ISSN: 0003-2700. DOI: 10.1021/ac9804184.
- [223] Elizabeth Woolfenden. "Review : Optimising Analytical Performance and Extending the Application Range of Thermal Desorption for Indoor Air Monitoring". en. In: *Indoor and Built Environment* 10.3-4 (May 2001), pp. 222–231. ISSN: 1420-326X, 1423-0070. DOI: 10.1177/1420326X0101000316.
- [224] Ryan B. Wilson et al. "High-Speed Cryo-Focusing Injection for Gas Chromatography: Reduction of Injection Band Broadening with Concentration Enrichment". en. In: *Talanta* 97 (Aug. 2012), pp. 9–15. ISSN: 00399140. DOI: 10.1016/j.talanta.2012.03.054.
- [225] Alina M. Muscalu et al. "Evaluation of a Single-Stage Consumable-Free Modulator for Comprehensive Two-Dimensional Gas Chromatography: Analysis of Polychlorinated Biphenyls, Organochlorine Pesticides and Chlorobenzenes". en. In: *Journal of Chromatography A* 1391 (Apr. 2015), pp. 93–101. ISSN: 00219673. DOI: 10.1016/j.chroma.2015.02.074.
- [226] Florian Obersteiner et al. "A Versatile, Refrigerant- and Cryogen-Free Cryofocusing–Thermodesorption Unit for Preconcentration of Traces Gases in Air". en. In: *Atmospheric Measurement Techniques* 9.11 (Oct. 2016), pp. 5265–5279. ISSN: 1867-8548. DOI: 10.5194/amt-9-5265-2016.
- [227] William A Groves, Edward T Zellers, and Gregory C Frye. "Analyzing Organic Vapors in Exhaled Breath Using a Surface Acoustic Wave Sensor Array with Preconcentration: Selection and Characterization of the Preconcentrator Adsorbent". en. In: *Analytica Chimica Acta* 371.2-3 (Oct. 1998), pp. 131–143. ISSN: 00032670. DOI: 10.1016/S0003-2670(98)00294-3.
- [228] Chia-Jung Lu and Edward T. Zellers. "A Dual-Adsorbent Preconcentrator for a Portable Indoor-VOC Microsensor System". en. In: *Analytical Chemistry* 73.14 (July 2001), pp. 3449–3457. ISSN: 0003-2700, 1520-6882. DOI: 10.1021/ac001524k.
- [229] B. J. Hopkins and Victor Pretorius. "Rapid Evaporation of Condensed Gas Chromatographic Fractions". In: *Journal of Chromatography A* 158 (Oct.

- 1978), pp. 465–469. ISSN: 0021-9673. DOI: 10.1016/S0021-9673(00)89988-4.
- [230] L. A. Lanning et al. “Electrically Heated Cold Trap Inlet System for Computer-Controlled High-Speed Gas Chromatography”. In: *Analytical Chemistry* 60.18 (Sept. 1988), pp. 1994–1996. ISSN: 0003-2700. DOI: 10.1021/ac00169a036.
- [231] Robert F. Mouradian, Steven P. Levine, and Richard D. Sacks. “Evaluation of a Nitrogen-Cooled, Electrically Heated Cold Trap Inlet for High-Speed Gas Chromatography”. In: *Journal of Chromatographic Science* 28.12 (Dec. 1990), pp. 643–650. ISSN: 0021-9665. DOI: 10.1093/chromsci/28.12.643.
- [232] James Harynuk and Tadeusz Górecki. “Design Considerations for a GC×GC System”. en. In: *Journal of Separation Science* 25.5-6 (Apr. 2002), pp. 304–310. ISSN: 1615-9306, 1615-9314. DOI: 10.1002/1615-9314(20020401)25:5/6<304::AID-JSSC304>3.0.CO;2-P.
- [233] Ognjen Panić et al. “Development of a New Consumable-Free Thermal Modulator for Comprehensive Two-Dimensional Gas Chromatography”. en. In: *Journal of Chromatography A* 1218.20 (May 2011), pp. 3070–3079. ISSN: 00219673. DOI: 10.1016/j.chroma.2011.03.024.
- [234] Gary B. Gordon. “Inductively Heated Cold-Trap Analyte Injector”. Pat. US5954860 A. U.S. Classification 95/87, 95/89, 96/102, 96/105; International Classification G01N30/12, G01N30/02; Cooperative Classification G01N30/12, G01N2030/025, G01N2030/121, G01N2030/122; European Classification G01N30/12. Sept. 1999.
- [235] H Beving et al. “Effect on the Uptake Kinetics of Serotonin (5-Hydroxytryptamine) in Platelets from Workers with Long-Term Exposure to Organic Solvents. A Pilot Study.” en. In: *Scandinavian Journal of Work, Environment & Health* 10.4 (Aug. 1984), pp. 229–234. ISSN: 0355-3140, 1795-990X. DOI: 10.5271/sjweh.2337.
- [236] Yuan-Chang Su, Chih-Chung Chang, and Jia-Lin Wang. “Construction of an Automated Gas Chromatography/Mass Spectrometry System for the Analysis of Ambient Volatile Organic Compounds with on-Line Internal Standard Calibration”. en. In: *Journal of Chromatography A* 1201.2 (Aug.

- 2008), pp. 134–140. ISSN: 00219673. DOI: 10.1016/j.chroma.2008.03.071.
- [237] Jia-Lin Wang, Genn-Zhung Din, and Chang-Chuan Chan. “Validation of a Laboratory-Constructed Automated Gas Chromatograph for the Measurement of Ozone Precursors through Comparison with a Commercial Analogy”. en. In: *Journal of Chromatography A* 1027.1-2 (Feb. 2004), pp. 11–18. ISSN: 00219673. DOI: 10.1016/j.chroma.2003.08.099.
- [238] Steven B. Bertman, Martin P. Buhr, and James M. Roberts. “Automated Cryogenic Trapping Technique for Capillary GC Analysis of Atmospheric Trace Compounds Requiring No Expendable Cryogenics: Application to the Measurement of Organic Nitrates”. In: *Analytical Chemistry* 65.20 (1993), pp. 2944–2946.
- [239] Maite de Blas et al. “Automatic On-Line Monitoring of Atmospheric Volatile Organic Compounds: Gas Chromatography–Mass Spectrometry and Gas Chromatography–Flame Ionization Detection as Complementary Systems”. In: *Science of The Total Environment* 409.24 (Nov. 2011), pp. 5459–5469. ISSN: 0048-9697. DOI: 10.1016/j.scitotenv.2011.08.072.
- [240] Detlev Helmig and James P. Greenberg. “Automated in Situ Gas Chromatographic-Mass Spectrometric Analysis of Ppt Level Volatile Organic Trace Gases Using Multistage Solid-Adsorbent Trapping”. en. In: *Journal of Chromatography A* 677.1 (Aug. 1994), pp. 123–132. ISSN: 00219673. DOI: 10.1016/0021-9673(94)80551-2.
- [241] T. E. Kleindienst et al. “The Formation of Secondary Organic Aerosol from the Isoprene + OH Reaction in the Absence of NO_x”. en. In: *Atmospheric Chemistry and Physics* 9.17 (Sept. 2009), pp. 6541–6558. ISSN: 1680-7324. DOI: 10.5194/acp-9-6541-2009.
- [242] J. J. Donovan et al. *Probe for EPMA: Acquisition, Automation and Analysis, Version 11*. Probe Software, Inc. Eugene, Oregon, 2015.
- [243] J. J. Donovan, D. A. Snyder, and M. L. Rivers. “An Improved Interference Correction for Trace Element Analysis”. In: *Microbeam Anal* 2 (1993), pp. 23–28.

- [244] J. T. Armstrong. "CITZAF-a Package of Correction Programs for the Quantitative Electron Microbeam X-Ray-Analysis of Thick Polished Materials, Thin-Films, and Particles". In: *Microbeam Analysis* 4.3 (1995), pp. 177–200.
- [245] E. Jarosewich, J.A. Nelen, and Julie A. Norberg. "Reference Samples for Electron Microprobe Analysis*". en. In: *Geostandards and Geoanalytical Research* 4.1 (Apr. 1980), pp. 43–47. ISSN: 16394488. DOI: 10.1111/j.1751-908X.1980.tb00273.x.

Appendix A

Photochemical reactor development

A.1 Supplementary Figures

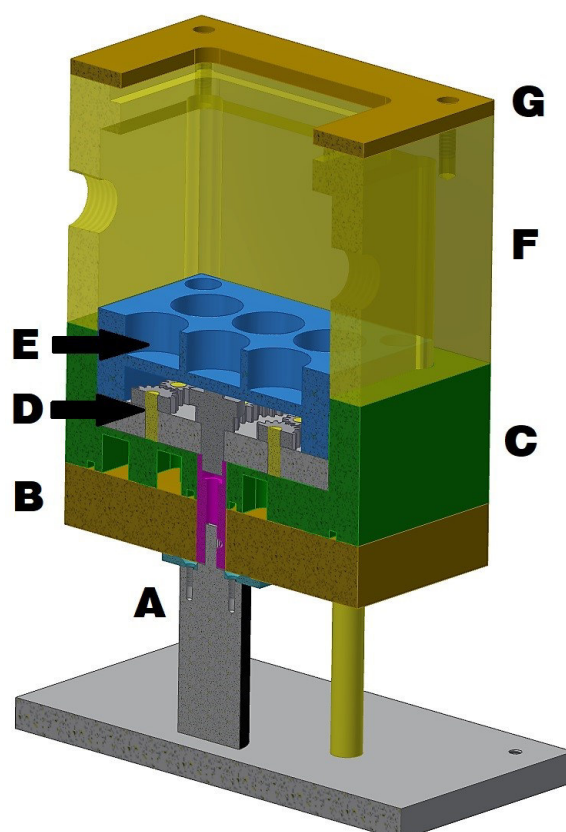


Figure A.1: Cross-section of the reactor setup showing the motor shaft (A), cooling plate (B), adaptor plate (C), stirring mechanism with gears, brass discs and rare earth magnets (D), sample adaptor (E), Teflon box (F) and filter holder (G).

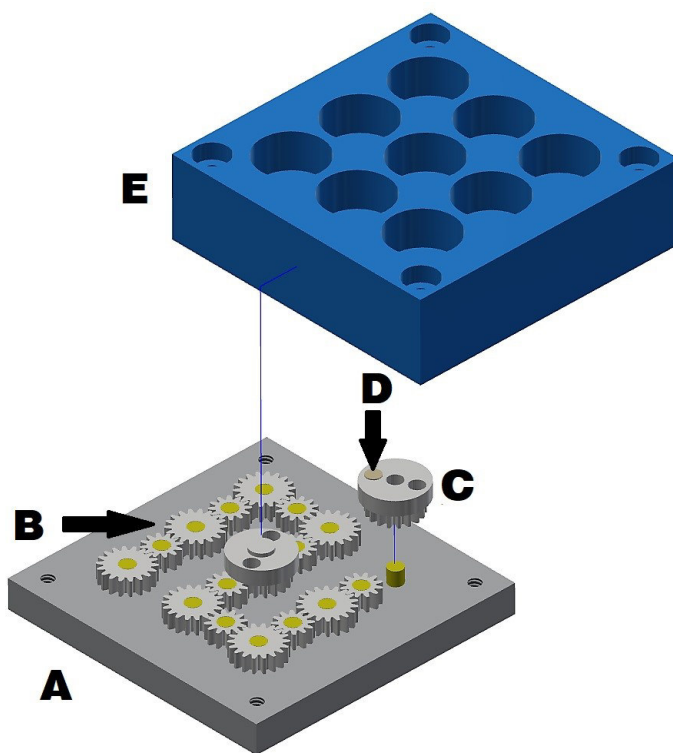


Figure A.2: Cross-section of the reactor setup showing the motor shaft (A), cooling plate (B), adaptor plate (C), stirring mechanism with gears, brass discs and rare earth magnets (D), sample adaptor (E), Teflon box (F) and filter holder (G).

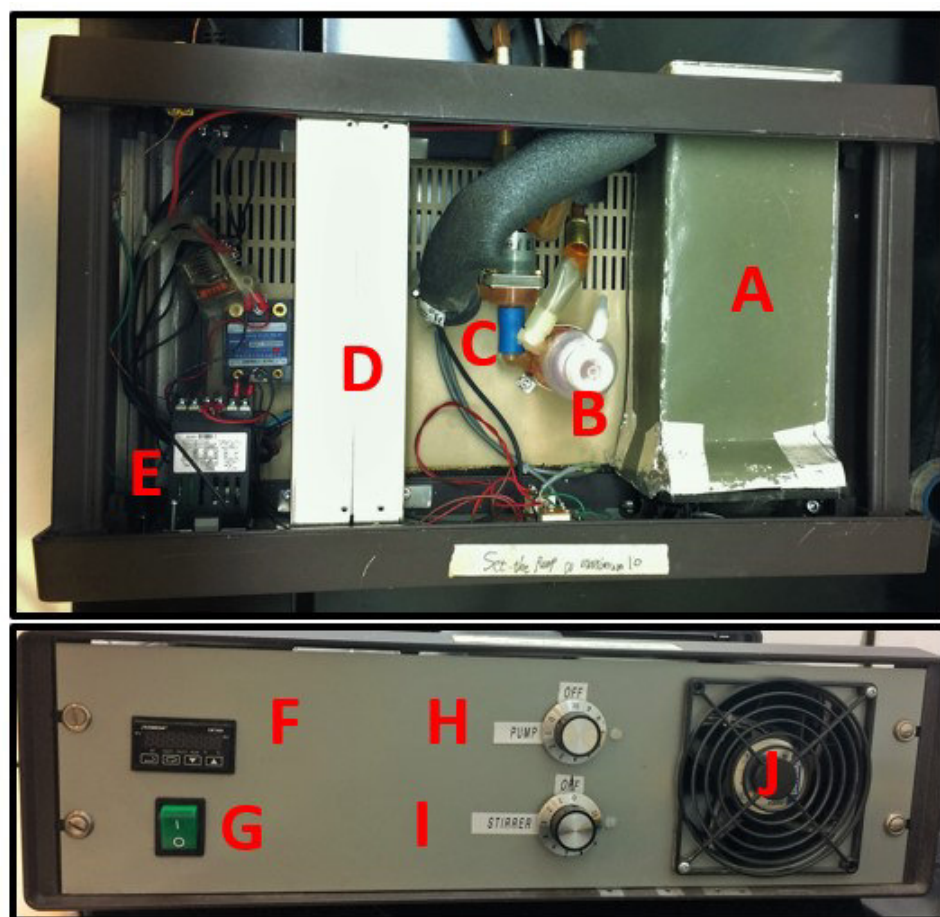


Figure A.3: Overview of the photoreactor control unit including the following parts A (Peltier element cooling unit), B (coolant reservoir), C (liquid pump), D (power supply), E (PID controller), F (PID front interface), G (power switch for liquid pump, cooling unit and stirring motor), H (pump speed adjustment), I (stirring speed adjustment), J (fan for Peltier element heat sink).

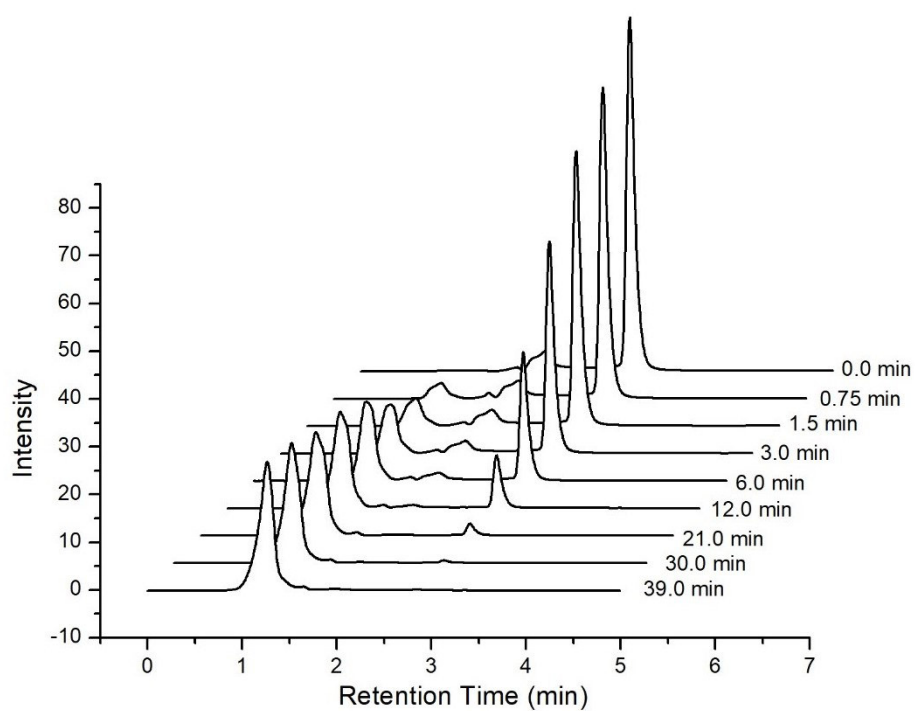


Figure A.4: Chromatograms of time-dependent 2NB ($10 \mu\text{M}$) decay experiments without TiO_2 after illumination between 0 min and 39 min showing 2NB at a retention time of 2.8 min and 2 NB photolysis product at a retention time of 1.3 min.

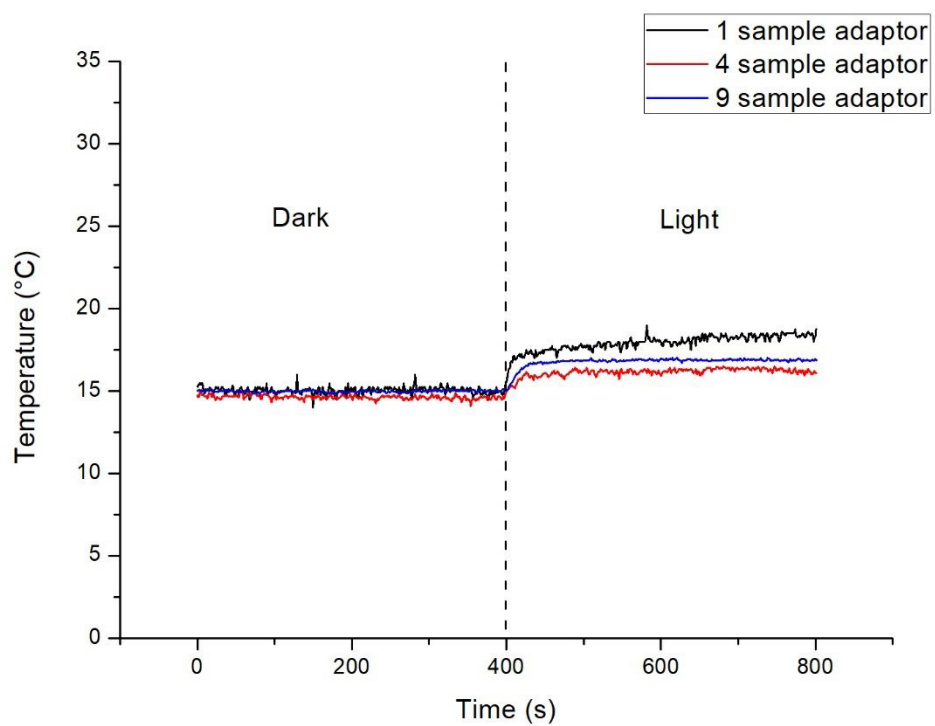


Figure A.5: Temperature monitoring of illuminated (400 s) and non-illuminated (400 s) reactions vessels showing average values for the 1, 4 and 9 sample adaptor.

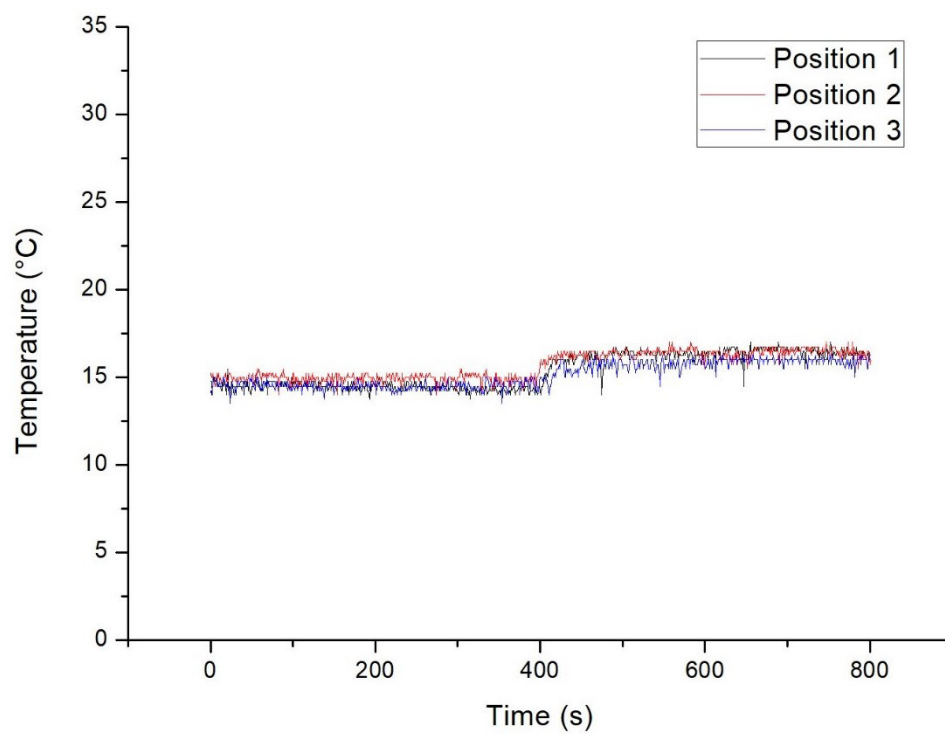


Figure A.6: Temperature dependence on illumination inside all reaction vessels of the 4 sample configuration with illumination for 400 s after dark conditions for 400 s.

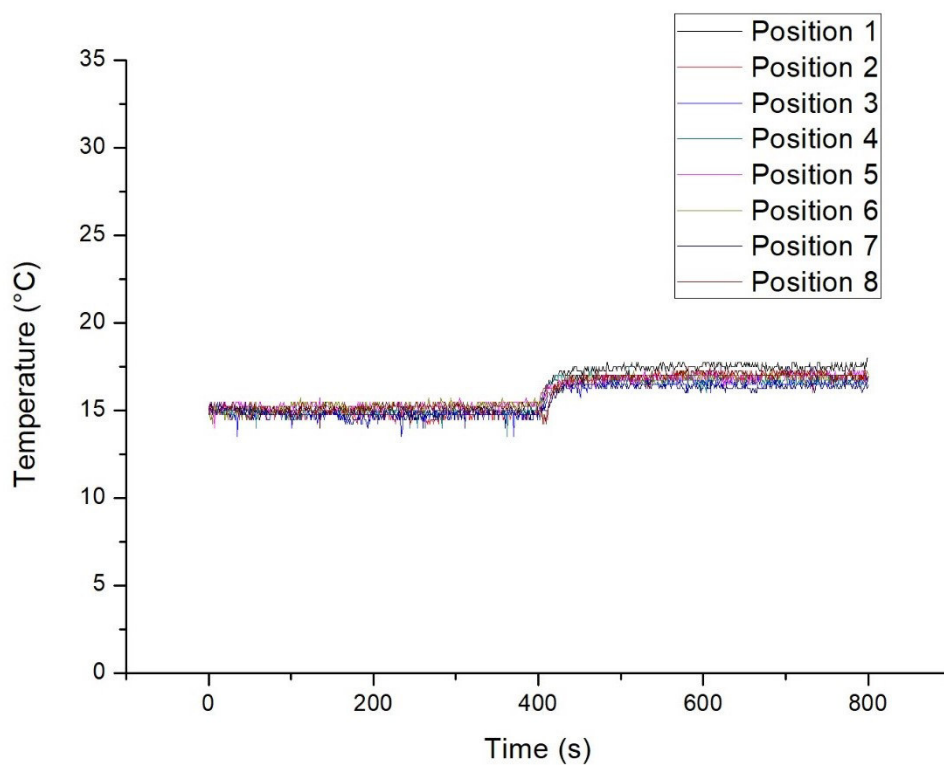


Figure A.7: Temperature dependence on illumination inside all reaction vessels of the 9 sample configuration with illumination for 400 s after dark conditions for 400 s.

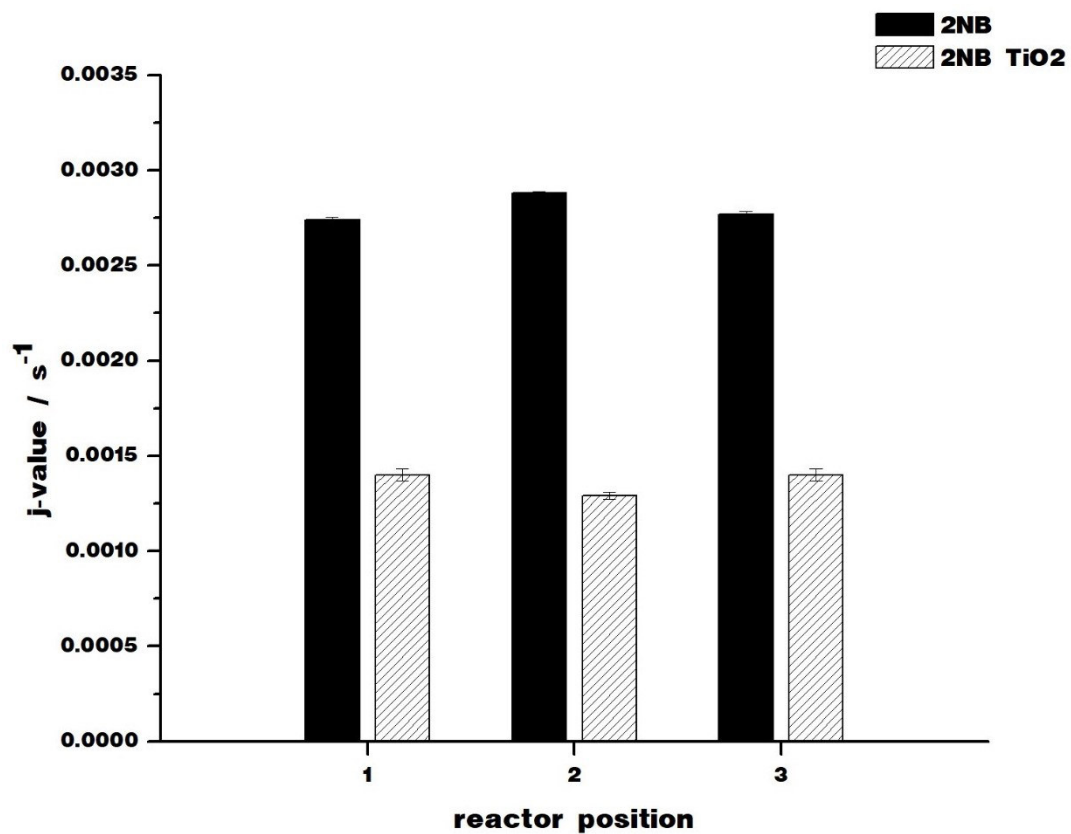


Figure A.8: Comparison of $j(2NB)$ values determined after illumination of $10 \mu\text{M}$ 2NB solutions and TiO_2 (0.25 mg mL^{-1}) suspensions using the 4-sample adaptor configuration.

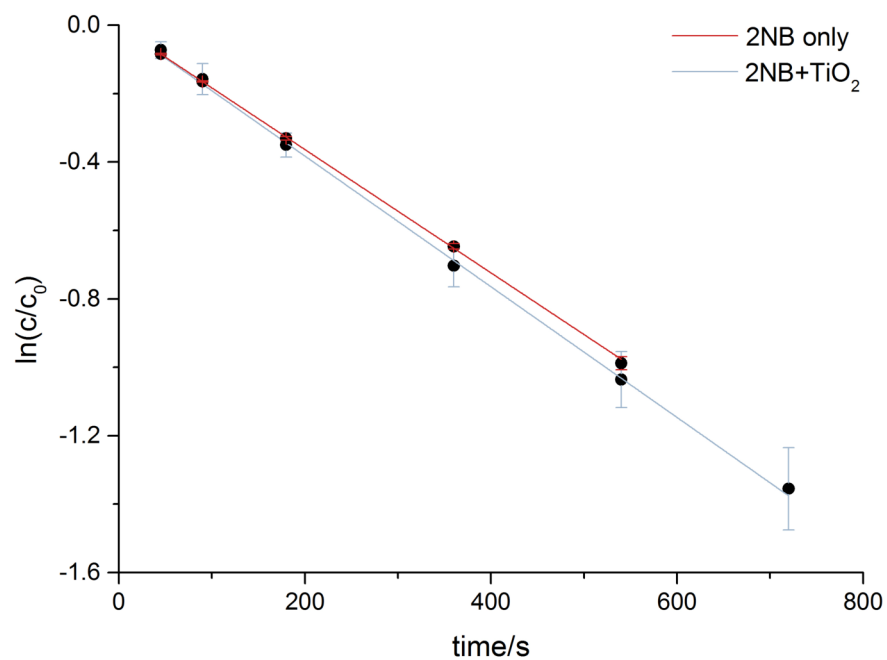


Figure A.9: Linear fit of $\ln(c/c_0)$ vs illumination time for the single sample adaptor with and without TiO_2 in 2NB solution.

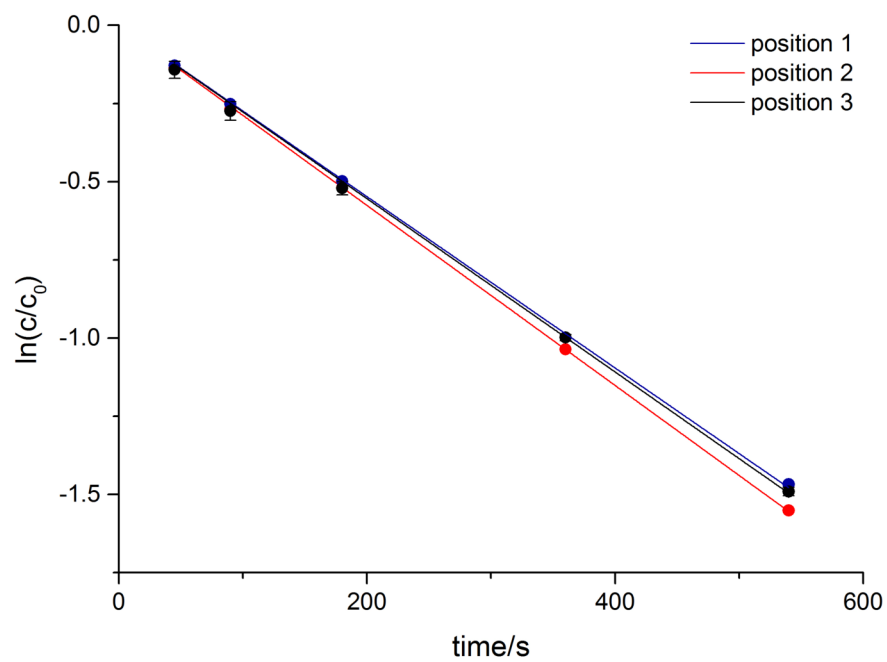


Figure A.10: Linear fit of $\ln(c/c_0)$ vs illumination time for the 4 sample adaptor without TiO_2 in 2NB solution.

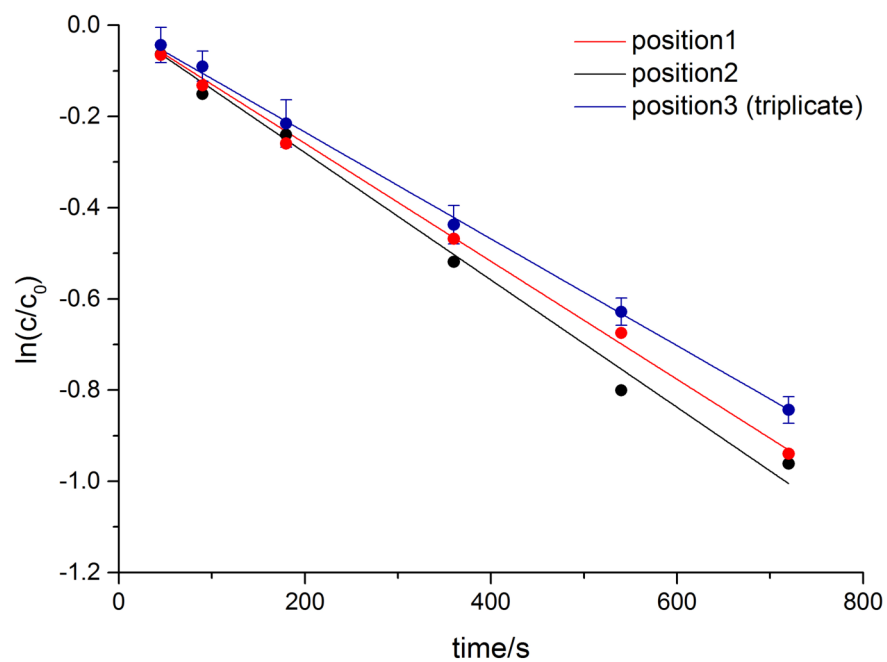


Figure A.11: Linear fit of $\ln(c/c_0)$ vs illumination data for the 4 sample adaptor with TiO_2 in 2NB solution.

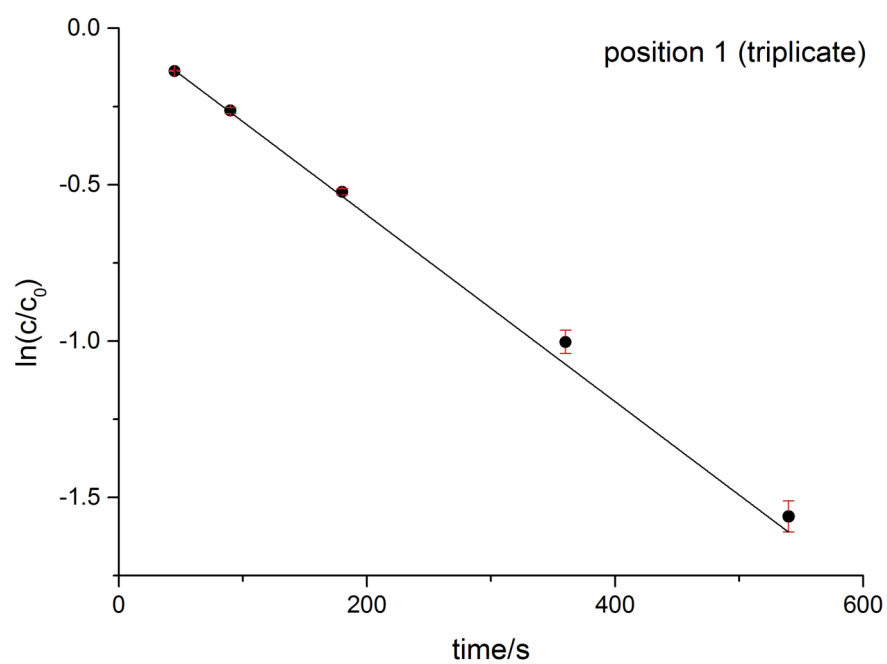


Figure A.12: a) Linear fit for $\ln(c/c_0)$ vs illumination time regarding triplicate experiments in position 1 of the 9 sample adaptor without TiO_2 .

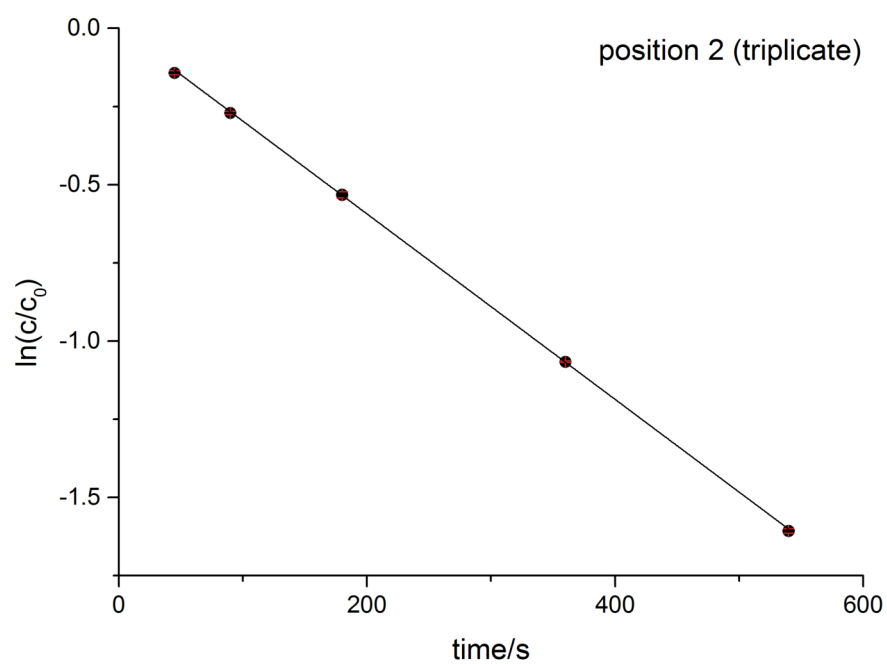


Figure A.12: b) Linear fit for $\ln(c/c_0)$ vs illumination time regarding triplicate experiments in position 2 of the 9 sample adaptor without TiO_2

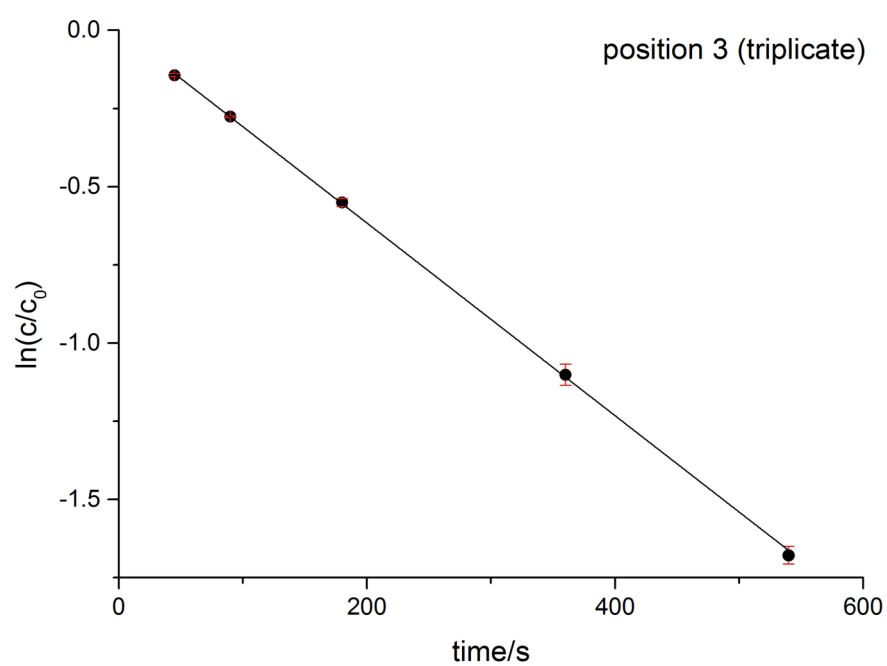


Figure A.12: c) Linear fit for $\ln(c/c_0)$ vs illumination time regarding triplicate experiments in position 3 of the 9 sample adaptor without TiO_2

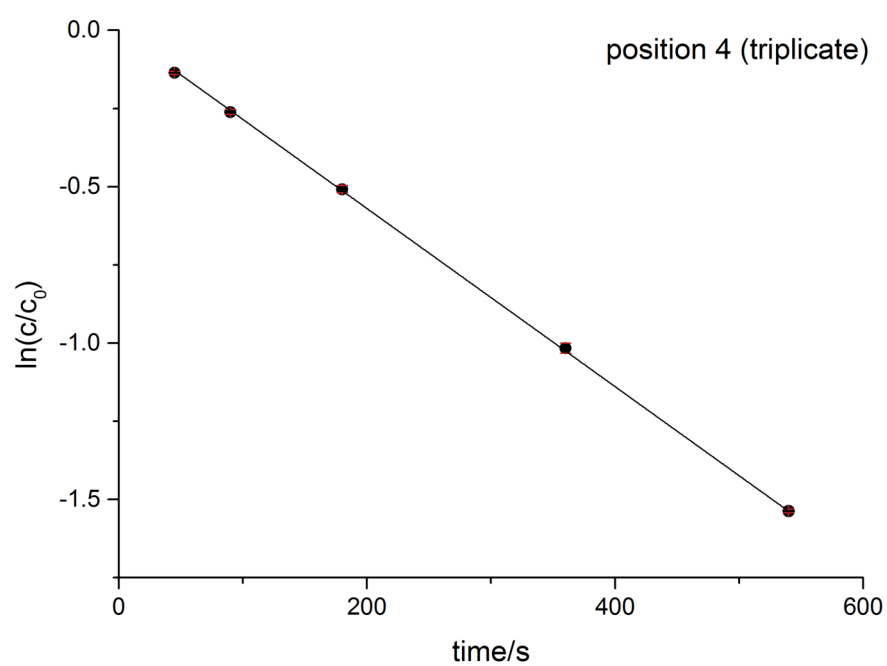


Figure A.12: d) Linear fit for $\ln(c/c_0)$ vs illumination time regarding triplicate experiments in position 4 of the 9 sample adaptor without TiO_2

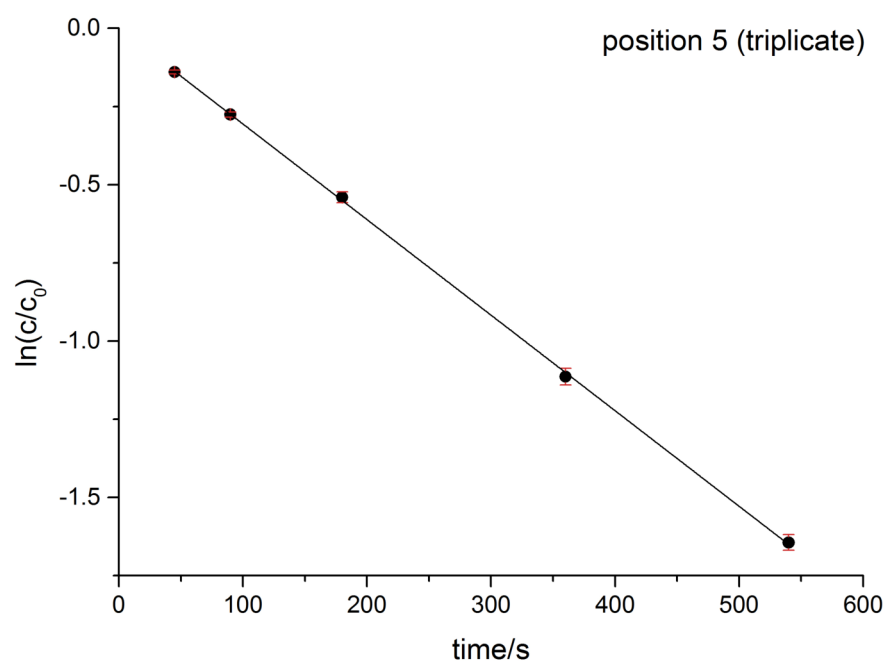


Figure A.12: e) Linear fit for $\ln(c/c_0)$ vs illumination time regarding triplicate experiments in position 5 of the 9 sample adaptor without TiO_2

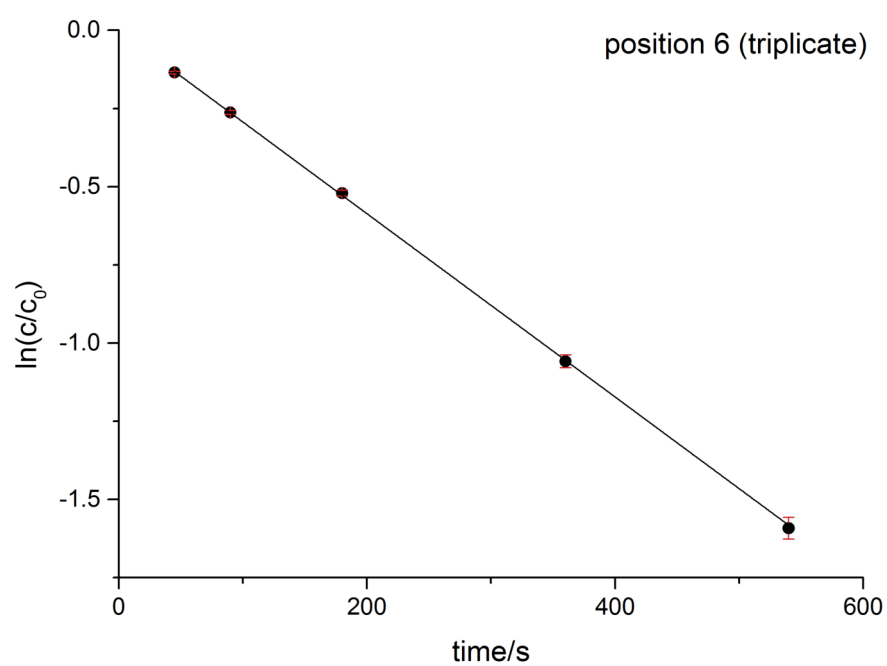


Figure A.12: f) Linear fit for $\ln(c/c_0)$ vs illumination time regarding triplicate experiments in position 6 of the 9 sample adaptor without TiO_2

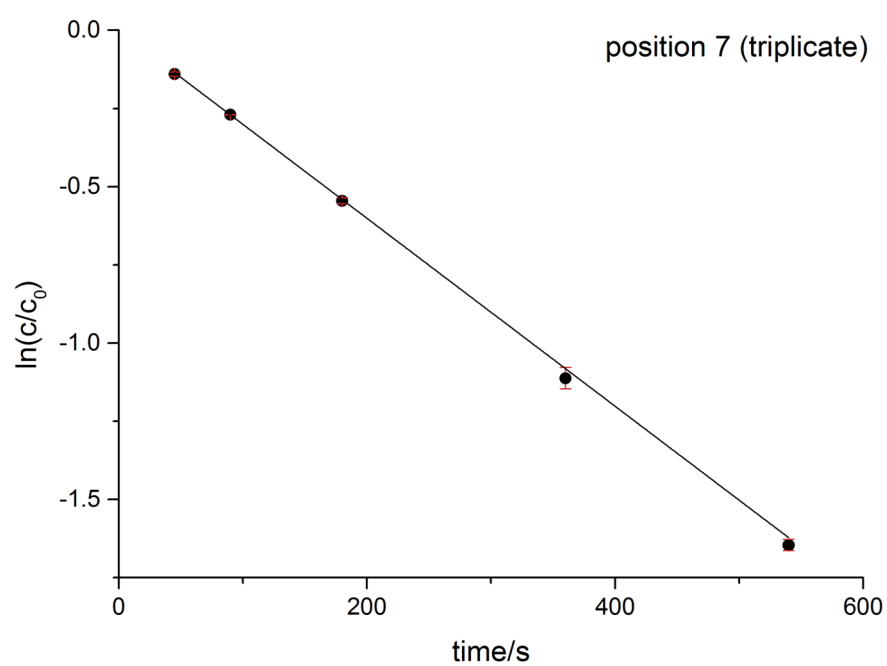


Figure A.12: g) Linear fit for $\ln(c/c_0)$ vs illumination time regarding triplicate experiments in position 7 of the 9 sample adaptor without TiO_2

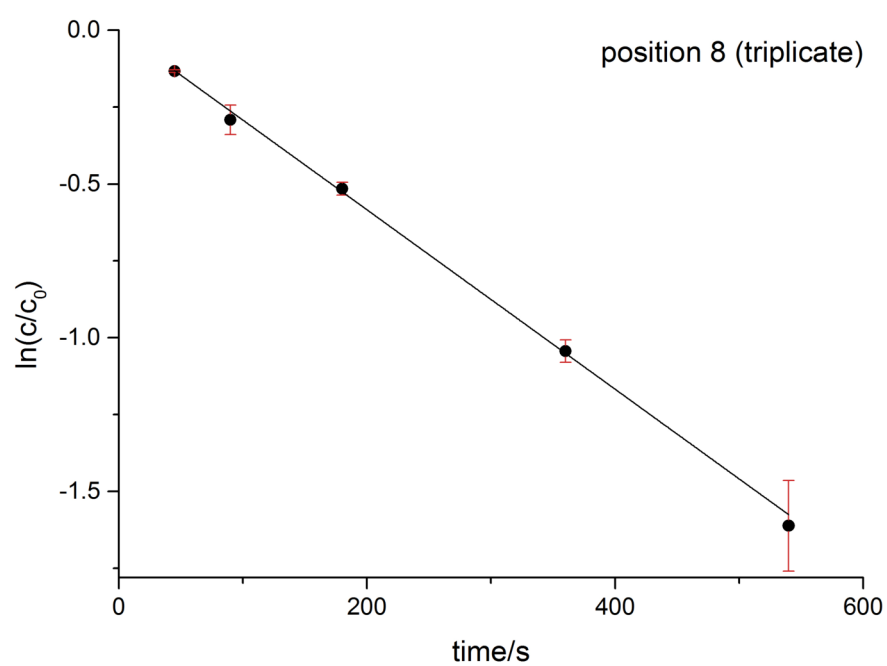


Figure A.12: h) Linear fit for $\ln(c/c_0)$ vs illumination time regarding triplicate experiments in position 8 of the 9 sample adaptor without TiO_2

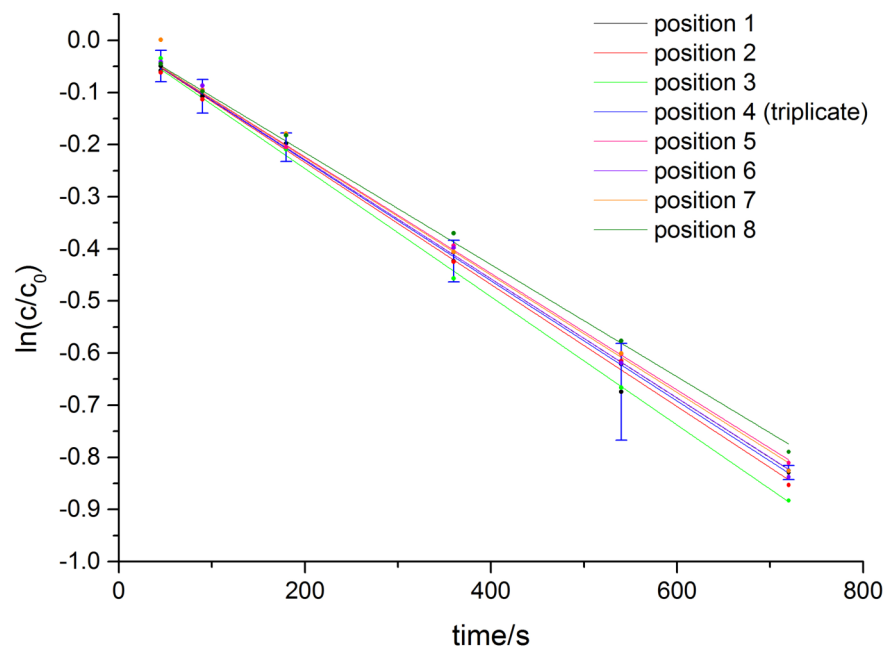


Figure A.13: Linear fits for $\ln(c/c_0)$ vs illumination time regarding single replicate experiments in positions 1,2,3,5,6,7,8 and a triplicate experiment in position 4 of the 9 sample adaptor with TiO_2 .

Appendix B

Mineral-mediated photochemical organosulfate formation

B.1 Experimental and sample characterization details

B.1.1 Solar simulator and photochemical reactor

A schematic of the photochemical reactor set-up employed in these experiments is presented in Figure B.1. The spectral irradiance of the solar simulator employed in the present study (at a working distance of 203 mm) is presented in Figure B.2. The spectral match with the AM1.5G reference spectrum, which reflects the solar radiation spectrum in the mid-latitudes (*i.e.* at a solar zenith angle of 48.2°), is also presented in Figure B.2; according to the specifications of the solar simulator, the spectral fit falls within the Class A limit associated with both the IEC and ASTM standards. However, as shown in Figure B.2, the simulator spectrum exhibits a small tail extending to the blue of the actinic region (the spectral fit standard extends only from 400-1100 nm).

B.1.2 2-Nitrobenzaldehyde (2-NB) chemical actinometry

In order to compare the photon flux in our experiments with that present in the ambient environment, we used chemical actinometry of 2-nitrobenzaldehyde.[126, 170, 171] In these experiments, aqueous solutions of 2-NB (10 μM) were placed in the quartz photochemical reactor and illuminated for 0-540 seconds. Quantification of 2-NB was accomplished using an Agilent 1100 HPLC system equipped with a binary pump, autosampler, thermostatted column compartment held at

48.2°C, and variable wavelength UV absorbance detector set to 258 nm. Separation of 2-NB from its photolysis products was performed using an Atlantis® dC18 column (Waters, 3 µm, 150 × 2.1 mm) under isocratic conditions (60% acetonitrile, 40% ultrapure water) at a flow rate of 0.3 mL min⁻¹. An injection volume of 50 µL was used for all separations. As shown in Figure B3, 2-NB exhibited first-order loss kinetics. The photodecay rate constant for 2-NB, $k(2\text{-NB})$, was $(1.89 \pm 0.02) 10^{-3} \text{ s}^{-1}$ (here, the error reflects the uncertainty associated with the first-order fit of 2-NB loss kinetics).

B.1.3 Control experiments and quality assurance / quality control (QA/QC)

The methanol clean-up procedure described in the main text was validated using recovery tests, the results of which are shown in Figure B.4. In these tests, which were performed in triplicate, 0.142 g Na₂SO₄ was weighed into a 15 mL centrifuge tube; then, 1 mL of a 50 µg mL⁻¹ mixed potassium hydroxyacetone sulfate and potassium propyl sulfate standard was added and the mixture was vortexed to dissolve the sulfate salt. After addition of 2.5 mL of methanol to precipitate sulfate, the tube was vortexed for 30 s and centrifuged for 5 min at 3000 rpm. The supernatant was removed, filtered (0.2 µ nylon filter, VWR), and analyzed as described in the main text. Recoveries are reported as the ratio of (dilution-corrected) peak areas for the processed analyte mix to peak areas for the initial 50 µg mL⁻¹ mix.

In order to verify that the observed organosulfate products arose from photochemistry rather than dark reactions, a comprehensive set of control experiments were performed in stoppered glass vials wrapped in Al foil. For experiments exploring TiO₂ loading (Figure 3.1 in manuscript), the following controls were performed: 0, 20, 40 min stirring; 10 mM methacrolein; 1 M Na₂SO₄; 0.5 mg mL⁻¹ TiO₂. For experiments exploring the sulfate anion concentration dependence (Figure 3.2), the following controls were performed: 0 and 30 min stirring at all Na₂SO₄ and (NH₄)₂SO₄ concentrations shown in Figure 3.2; 10 mM methacrolein; 0.5 mg mL⁻¹ TiO₂. For experiments exploring the methacrolein concentration dependence (Figure 3.3), the following controls were performed: 0 and 30 min stirring at all methacrolein concentrations shown in Figure 3.3; 1 M Na₂SO₄ or (NH₄)₂SO₄; 0.5 mg mL⁻¹ TiO₂. For experiments using natural minerals (Figure 3.4), the

following controls were performed: 0 and 30 min stirring using all minerals shown in Figure 3.3; 10 mM methacrolein; 1 M Na₂SO₄; 0.5 mg mL⁻¹ mineral loading. Prior to analysis, all control samples were subjected to the same clean-up procedure described in Section 3.2 of the main text. No organosulfate production was observed in any of these experiments. In order to verify that organosulfates observed in experiments conducted using natural mineral samples (Figure 3.4) did not arise from photochemistry of mineral-associated organics, we also performed one set of experiments in which minerals were illuminated in the absence of methacrolein (0 and 30 min stirring; 1 M Na₂SO₄; 0.5 mg mL⁻¹ minerals). No organosulfate products were observed in these control experiments.

B.1.4 Sample preparation and characterization

B.1.4.1 Sample preparation

Prior to use, natural minerals were first broken down using a steel percussion mortar; after removing any steel contamination by passing a weighing paper-covered magnet over the samples (in the case of ilmenite, this was not done because some magnetite was interspersed with the sample; see below), samples were ground to a fine powder using an agate mortar and pestle. In order to avoid sample cross-contamination, high-purity Brazilian quartz was ground in ethanol in the steel and agate mortars between samples. After this cleaning procedure, the mortars were rinsed with water and ethanol prior to re-use. Visual inspection, coupled with electron microprobe analysis (see Section B1.4.3) suggested that the mica sample contained calcite and iron oxide (*i.e.* rust). Prior to grinding, therefore, calcite was removed by placing the sample in 1 M HCl for 1.5 h and rust was removed by placing the sample in a solution of Super Iron OUT (56 g in 1.4 L; Summit Brands) for 30 min. A Dremel rotary tool was subsequently used to remove residual contamination. In the case of ilmenite, microscopy was used to aid in the manual removal of contaminants - tentatively identified as goethite/hematite, ferrocolumbite, Ti-bearing magnetite, and possibly anatase/rutile - from the broken-down sample. Anatase did not receive additional treatment beyond grinding.

B.1.4.2 Surface area determination

The Brunauer-Emmett-Teller (BET) surface areas of commercial TiO₂ and the natural minerals anatase and ilmenite were determined using an Autosorb iQ automated gas sorption analyzer (Quantachrome Instruments) with N₂ as adsorbate. Prior to BET analysis, samples were degassed at room temperature for 1.5 h; then, if the rate of pressure increase in the sample cell was less than 26 mTorr min⁻¹, the sample was removed from the degassing station for analysis. Otherwise, the rate of pressure increase was tested every 15 minutes until this condition was met. These results are shown in Table B.2.

B.1.4.3 Electron microprobe analysis

An electron microprobe (JEOL JXA-8900R) was used to examine grains of anatase, ilmenite, and mica. The minerals were mounted in epoxy, polished, and carbon-coated (25 nm thickness) prior to analysis. In addition to back-scattered electron images, quantitative compositional data were acquired from spot analyses of the minerals using wavelength-dispersive spectrometry and Probe for EPMA software.[242] Thirteen elements were measured (Na, Mg, Al, Si, K, Ca, Ti, V, Cr, Mn, Fe, Zn, and Nb) with the following conditions: 20 kV accelerating voltage, 20 nA probe current, and a 1 μm beam diameter for all minerals except mica, for which a 5 μm beam was used. Total count times of 20 s were used for both peaks and backgrounds for all elements except V, Zn, and Nb, for which 30 s was used. The X-ray lines and diffraction crystals were: Na Kα, TAP (thallium hydrogen phthalate); Mg Kα, TAP; Al Kα, TAP; Si Kα, TAP; K Kα, PET (pentaerythritol); Ca Kα, PET; Ti Kα, PET; V Kα, PET; Cr Kα, PET; Mn Kα, LIF (lithium fluoride); Fe Kα, LIF; Zn Kα, LIF; and Nb Lα, PET. Corrections[243] were applied to V for interference by Ti, to Cr for interference by V, and to Mn for interference by Cr. X-ray intensity data were reduced following Armstrong.[244] The reference standards consisted of metals, synthetic inorganic materials, and natural minerals.[245] These results (expressed as oxide weight percent) are shown in Table B.3.

B.1.4.4 Scanning electron microscopy with energy dispersive X-ray spectroscopy (SEM-EDS) analysis

The Edmonton road dust sample was examined using scanning electron microscopy (SEM; JEOL JSM-6010LA) with energy dispersive spectroscopy (EDS) analysis for elemental mapping. A carbon coating was applied to the road dust sample prior to analysis to increase the conductivity of the sample. Three full-field scans were performed, each with a collection time of 3 min. An accelerating voltage of 15 kV was used with a working distance of 9 mm and 300 \times magnification. A sample EDS spectrum is shown in Figure B.7. The following elements were identified using elemental analysis: Na, Mg, Al, Si, K, Ca, Ti, Fe, Cu, and Mo (the latter two elements were present at unexpectedly high levels, and identification of them using this technique is therefore considered tentative at best). Representative elemental mapping results, which are also shown in Figure B.7, highlight the compositional heterogeneity of the road dust sample.

B.1.4.5 X-ray diffraction (XRD) analysis

In order to verify the mineralogy of the natural Ti-containing minerals employed in this study, X-ray diffraction (XRD) patterns were collected using an Inel MPD Multi Purpose Diffractometer System equipped with a CPS 120 curved position sensitive X-ray detector and a Cu $K\alpha_1$ radiation source. The instrument was operated at a beam intensity of 40 kV and 20 mA. Phase identification was accomplished using Jade software (Materials Data, Inc.) in conjunction with the ICDD-PDF2 and ICSD databases. Phase refinement was performed using the TOPAS Academic software package (Bruker AXS), and phase presence was confirmed using Pawley fitting. Refined parameters include scaling, 6-term polynomial background, and cell parameters of the refined structures. Residual difference lines were calculated as the difference between observed intensity and calculated intensity. As shown in Figure B.8, the XRD patterns of the natural minerals were consistent with those of anatase, ilmenite, and mica (identified as phlogopite; $K(Mg,Fe)_3Si_3AlO_{10}(OH)_2$). We note that since Pawley fit refines only peak positions, intensity mismatch is possible. For mica, a strong preferred orientation along the 0 0 2n direction was observed, which resulted in increased intensity of the corresponding peaks (Figure B.8c). Figure B.8 also shows that

the road dust sample was more compositionally complex, with contributions from quartz, microcline, dolomite, albite, scawtite (tentative), and calcite.

B.1.5 Synthesis of calibration standards

Standards were synthesized according to established literature procedures,[173, 174] which are briefly summarized here. NMR spectra, high-resolution mass spectra, and product ion scans of the synthesized standards are presented in Figures B.9-B.12.

B.1.5.1 Potassium hydroxyacetone sulfate

5.6 mL (0.08 mol) of hydroxyacetone was added to a round-bottom flask containing 15 mL of tetrahydrofuran (THF) under nitrogen; then, 14.01 g (0.088 mol) of pyridine sulfur trioxide was added. The resultant cloudy mixture was stirred for 8 hours to yield a clear solution. THF was removed via rotary evaporation to yield a clear light-yellow oil (the pyridinium salt of hydroxyacetone sulfate). Isolation of the potassium salt was accomplished by creating an aqueous slurry of the pyridinium salt with 80 equivalents of Dowex 50WX8-200 cation exchange resin that had been previously charged with potassium ions by passing a 1 M KOH solution through the protonated cation exchanger. The solution was then filtered and water was removed via rotary evaporation. The resultant white solid was recrystallized from boiling 80% ethanol solution; hot filtration under vacuum was used to remove a white precipitate that gave no ^1H or ^{13}C signal. The potassium salt of hydroxyacetone sulfate was formed as colourless needles (29% yield).

^1H NMR (400 MHz, D_2O): δ/ppm 2.23 (s, 3H); 4.474 (s, 2H)

^{13}C NMR (400 MHz, D_2O): δ/ppm 26.67; 72.76; 208.79

B.1.5.2 Potassium propyl sulfate (adapted from a published synthesis of sodium ethyl sulfate[174])

5 mL of concentrated H_2SO_4 was added dropwise to a round-bottom flask containing 20 mL of 1-propanol. The mixture was stirred under reflux for 2 h, cooled by pouring into 250 mL of cold water, and neutralized using calcium carbonate, which converted the sulfuric acid into insoluble calcium sulfate and the propyl

hydrogen sulfate product into its soluble calcium salt. After removal of calcium sulfate via filtration, calcium propyl sulfate was converted to potassium propyl sulfate via addition of 30 g of potassium carbonate. The solution was then filtered and water was removed via rotary evaporation. The resultant crude solid was recrystallized from methanol to produce the pure product as colourless needles (68% yield).

^1H NMR (400 MHz, D_2O): δ /ppm 0.94 (t, $J=7.4$ Hz, 3H); 1.68 (sx, $J=7.9$ Hz, 2H); 4.01 (t, $J=6.4$ Hz, 2 H)

^{13}C NMR (400 MHz, D_2O): δ /ppm 9.26; 21.81; 71.01

B.1.6 Chemicals

Ammonium sulfate (ACS, $\geq 99.0\%$), sodium sulfate (ACS, $\geq 99.0\%$), methacrolein (95%), TiO_2 (99.8% trace metals basis), 2-nitrobenzaldehyde ($\geq 99.9\%$), and tetrahydrofuran (HPLC grade, $\geq 99.9\%$ purity, inhibitor-free) were obtained from Sigma Aldrich. Hydroxyacetone (95%), sulfur trioxide-pyridine complex (98%, active SO_3 ca. 48-50%), and 1-propanol (ACS, $\geq 99.5\%$) were obtained from Alfa Aesar. Acetonitrile (HPLC grade), calcium carbonate (certified ACS powder, 100%), potassium carbonate (certified ACS powder, 100%), formic acid (Optima grade, LC-MS), and methanol (Optima grade, 99.9%) were obtained from Fisher Chemical. Dowex 50WX8-200 ion exchange resin (100-200 mesh) was obtained from ACROS Organics. Concentrated H_2SO_4 (reagent grade) was obtained from Caledon Laboratory Chemicals. 80% ethanol was prepared from ethyl alcohol (100% anhydrous; Commercial Alcohols).

B.2 2 Supplementary figures and tables

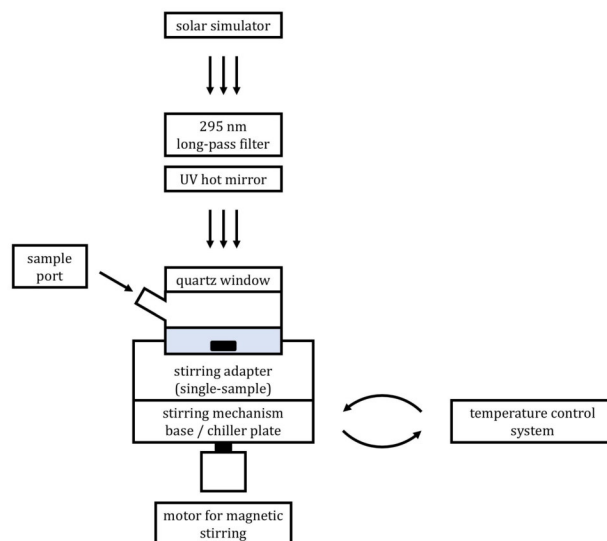


Figure B.1: Schematic drawing of the photochemical reactor employed in these experiments. The reactor itself is constructed from a flat o-ring flange (5 cm ID \times 3.8 cm height) equipped with a 6 mm ID sampling port. The top of the reactor is equipped with a quartz window (76 mm diameter \times 6 mm thickness), which is held in place using a horseshoe clamp. Samples are stirred using a custom-built two-part modular stirring apparatus*, both parts of which are contained within aluminum housings. The exchangeable upper part of the apparatus comprises the stirring mechanism itself, which consists of a brass disc equipped with four rare earth magnets. A milled depression in the aluminum housing serves as a sample holder. The upper and lower parts of the apparatus are interfaced via a fixed socket, which protrudes upward from the bottom part of the apparatus. The fixed socket, in turn, is mounted to a motor beneath the apparatus, which drives the mechanism. The temperature of the samples is controlled using a custom-built digital Peltier temperature control system, in which cooling fluid is circulated through channels in the bottom part of the apparatus. Sample temperature input to the control system is provided by a probe inserted through the reactor sampling port. * *Note: The stirring apparatus also has four- and nine-sample configurations. In these configurations, the upper part of the apparatus is exchanged for versions containing four and nine brass gears, respectively.*

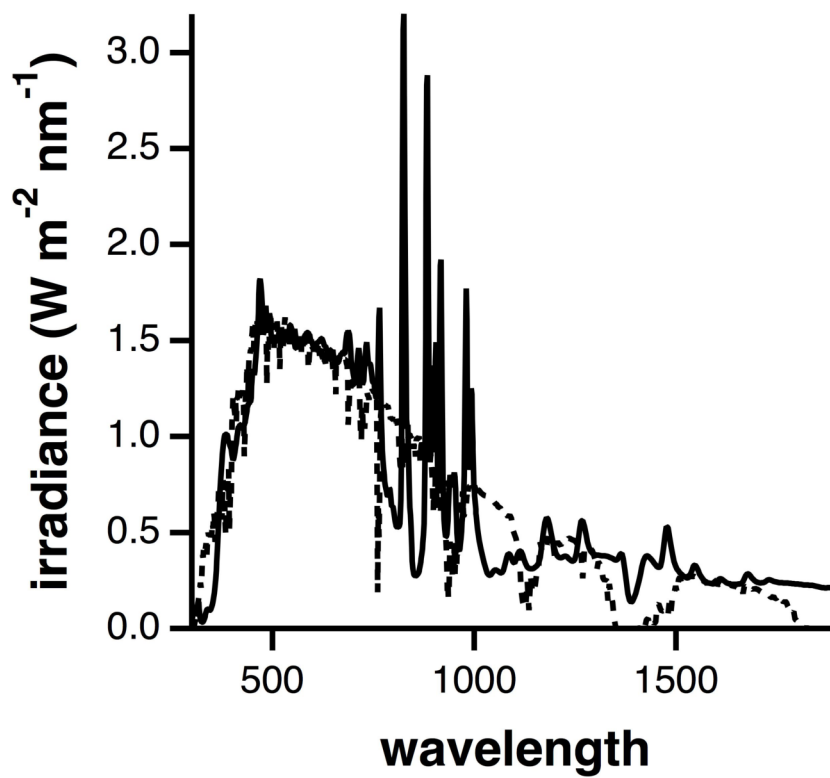


Figure B.2: Spectral irradiance of the solar simulator employed in the present study at a working distance of 203 nm (solid line) as compared to the AM1.5 reference spectrum (dashed line). Data provided by the solar simulator manufacturer (Abet Technologies). In the present experiments, the working distance was 190 mm. In order to compare the photon flux in our experiments with those in the ambient environment, we used chemical actinometry.

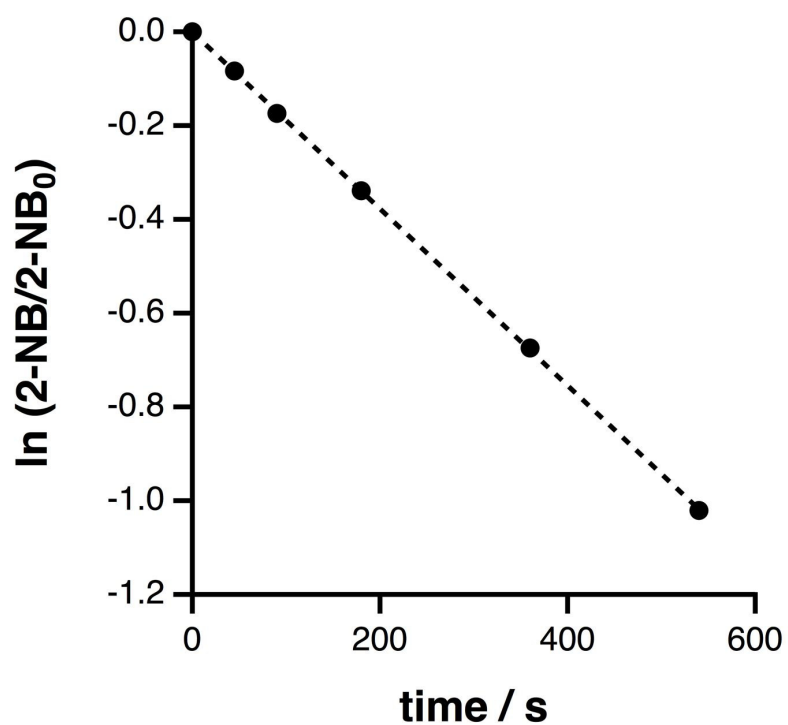


Figure B.3: Loss of the chemical actinometer 2-nitrobenzaldehyde (2-NB) in our photochemical reactor as a function of illumination time. Each data point represents the mean of three experimental trials, with $1\text{-}\sigma$ error bars (here, the error bars are too small to be seen). The dashed line is a linear fit to the experimental data.

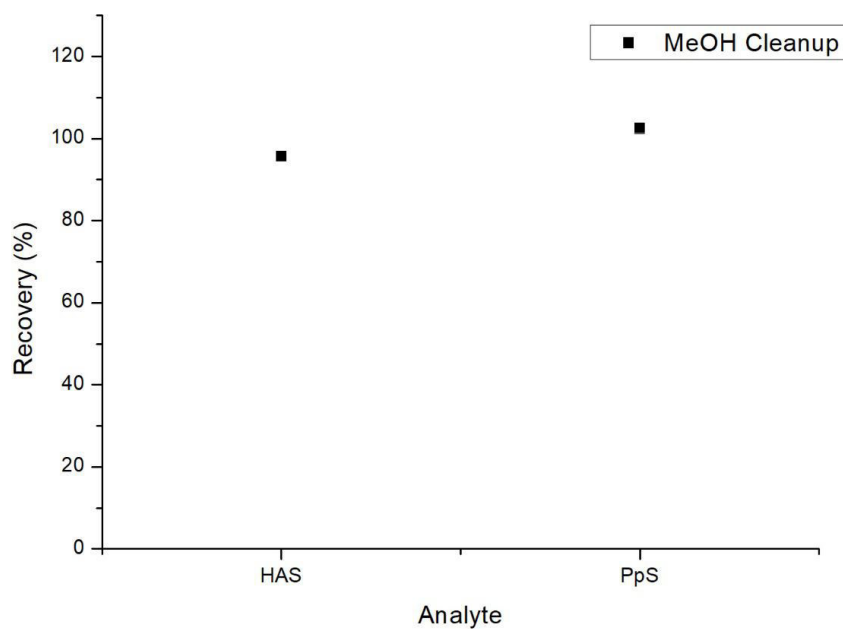


Figure B.4: Recovery of hydroxyacetone sulfate (HAS) and propyl sulfate (PpS) using the MeOH cleanup procedure described in Appendix B text. Each data point represents the mean of three experimental trials, with $1-\sigma$ error bars (here, the error bars are too small to be seen).

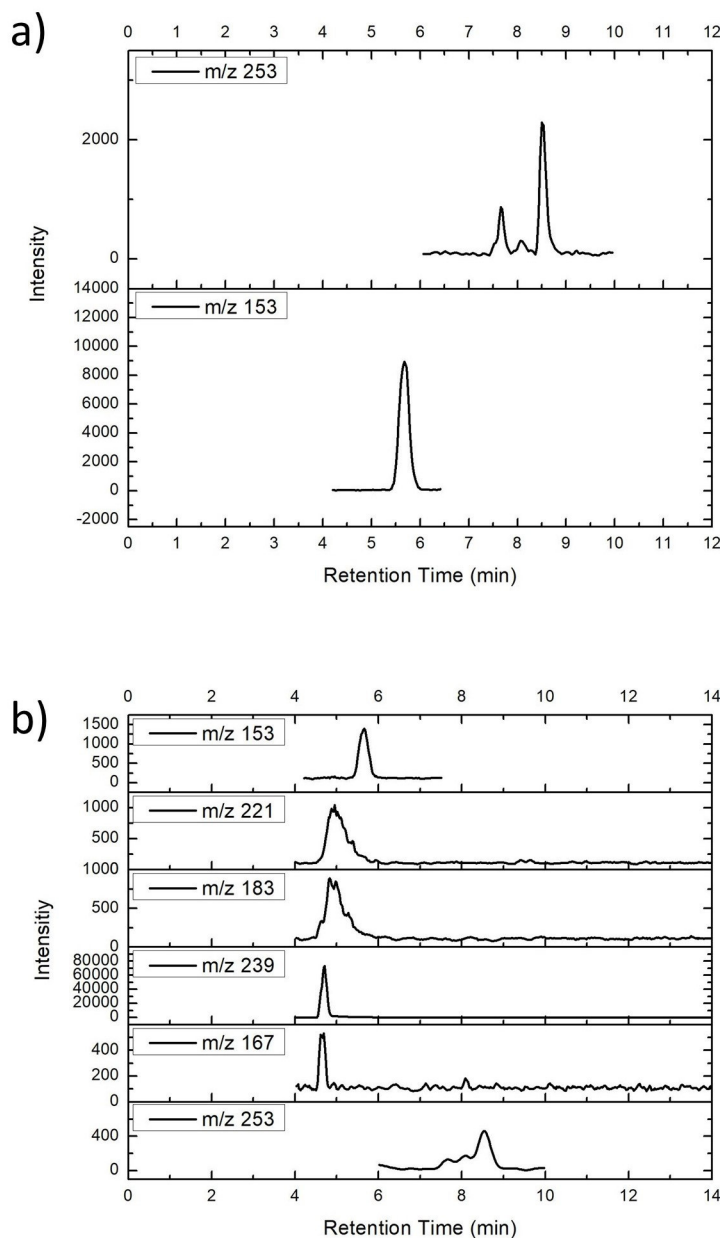


Figure B.5: Representative chromatograms showing organosulfate products: a) 1M Na₂SO₄ (adjusted to pH 5 using 50 mM aqueous H₂SO₄), 10 mM methacrolein, 1 mg mL⁻¹ TiO₂, 30 min illumination; b) 1M Na₂SO₄ (adjusted to pH 5 using 50 mM aqueous H₂SO₄), 10 mM methacrolein, 0.5 mg mL⁻¹ mica, 30 min illumination. Samples were run in multiple reaction monitoring (MRM) mode; in all cases, the [M-H]⁻ → m/z 97 transition was employed for analysis and quantification.

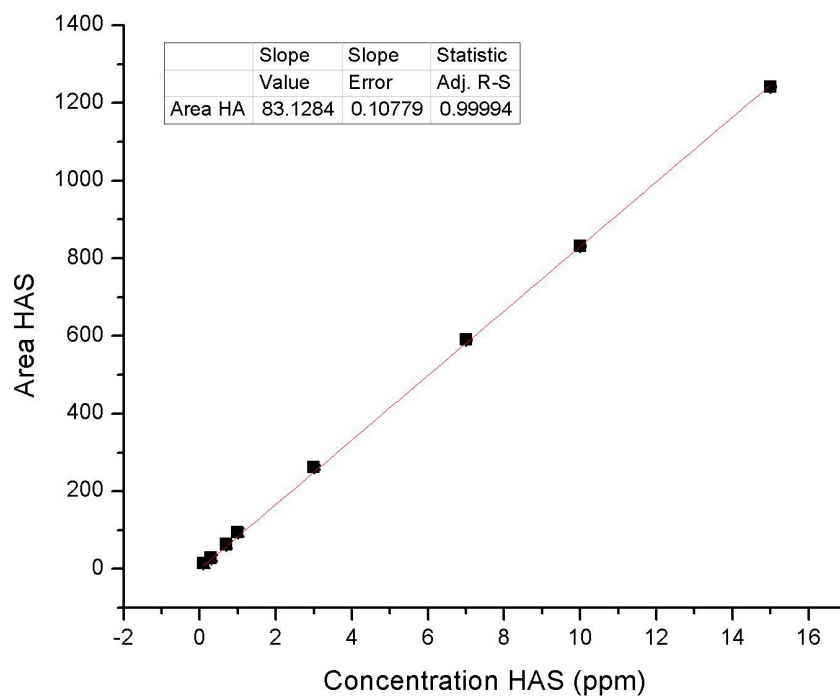


Figure B.6: External calibration curve for hydroxyacetone sulfate (HAS). All standards were run in selected reaction monitoring (SRM) mode; the $[M-H]^- \rightarrow m/z$ 97 transition was employed for analysis and quantification. Each data point represents the mean of triplicate injections, with $1-\sigma$ error bars (here, the error bars are too small to be seen).

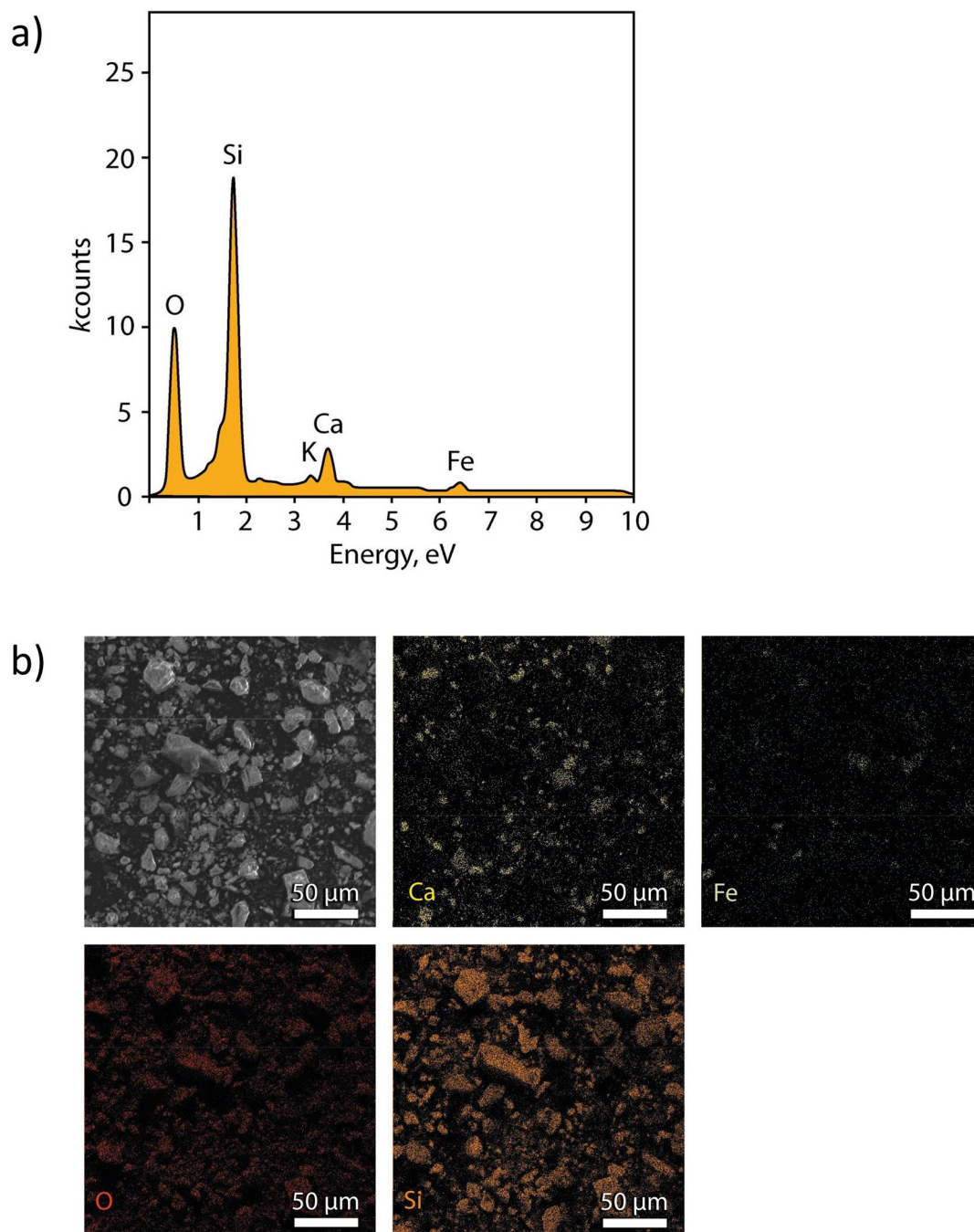


Figure B.7: Analysis of Edmonton road dust using scanning electron microscopy with energy dispersive X-ray spectroscopy (SEM-EDS) analysis: a) sample EDS spectrum and b) elemental mapping.

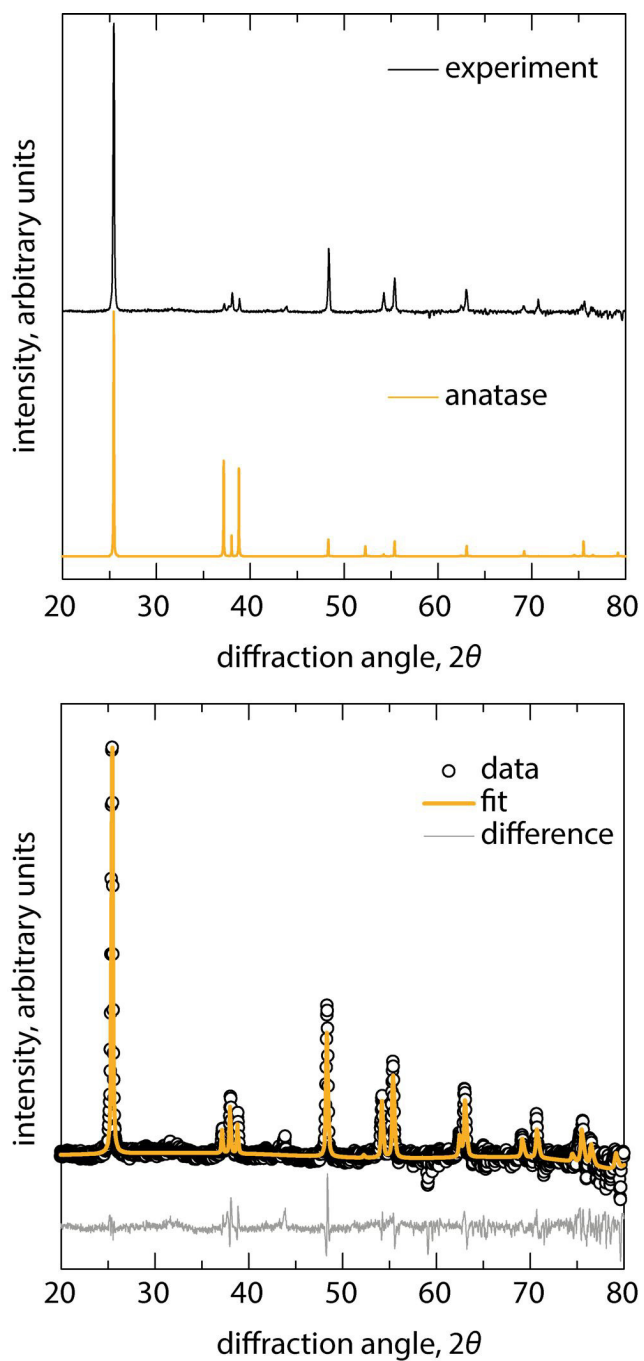


Figure B.8: a) XRD diffractograms of anatase

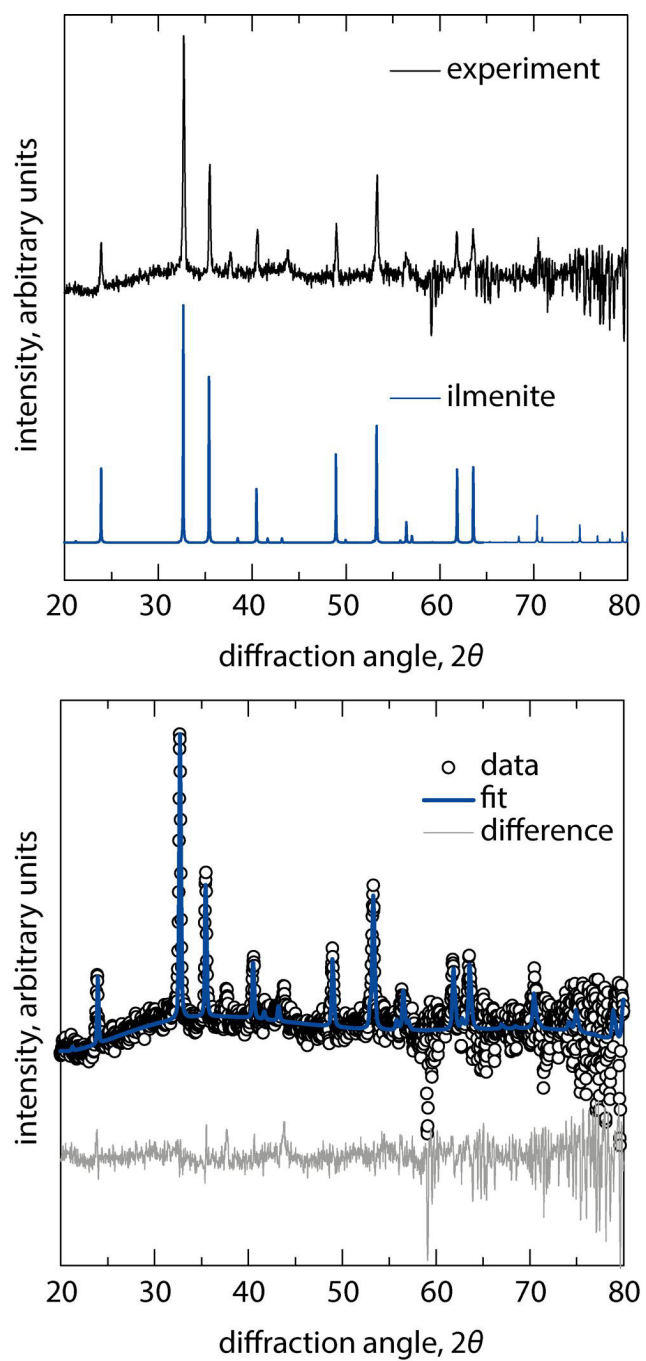


Figure B.8: b) XRD diffractograms of ilmenite

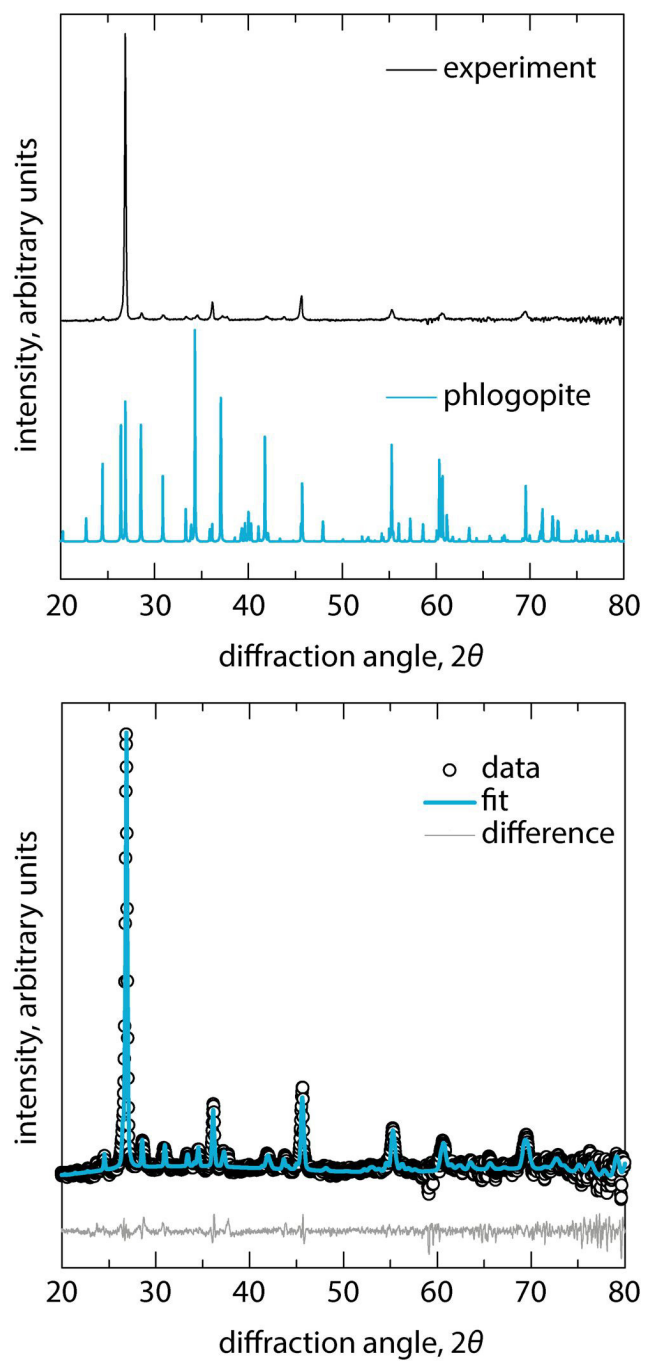


Figure B.8: c) XRD diffractograms of mica

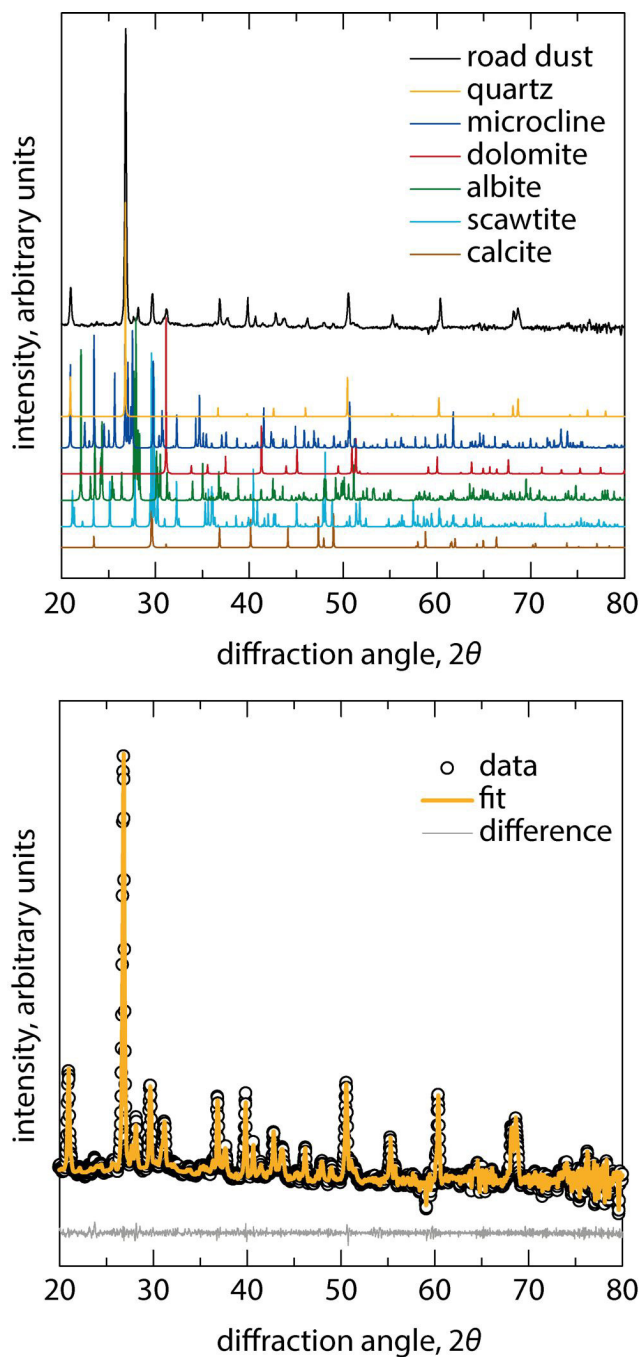


Figure B.8: d) XRD diffractograms of Edmonton road dust

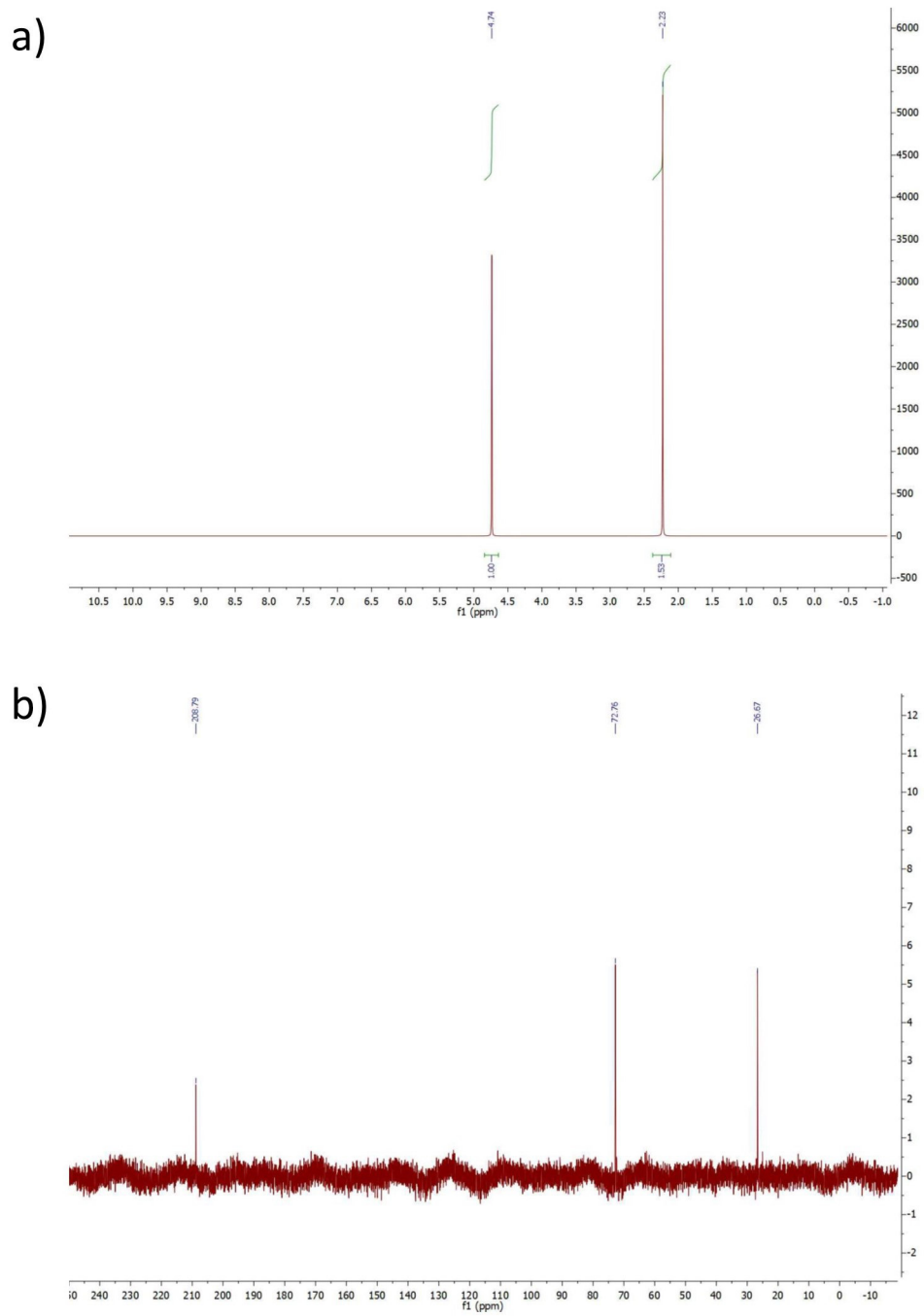


Figure B.9: 1H and b) ^{13}C NMR spectra of hydroxyacetone sulfate in D_2O .

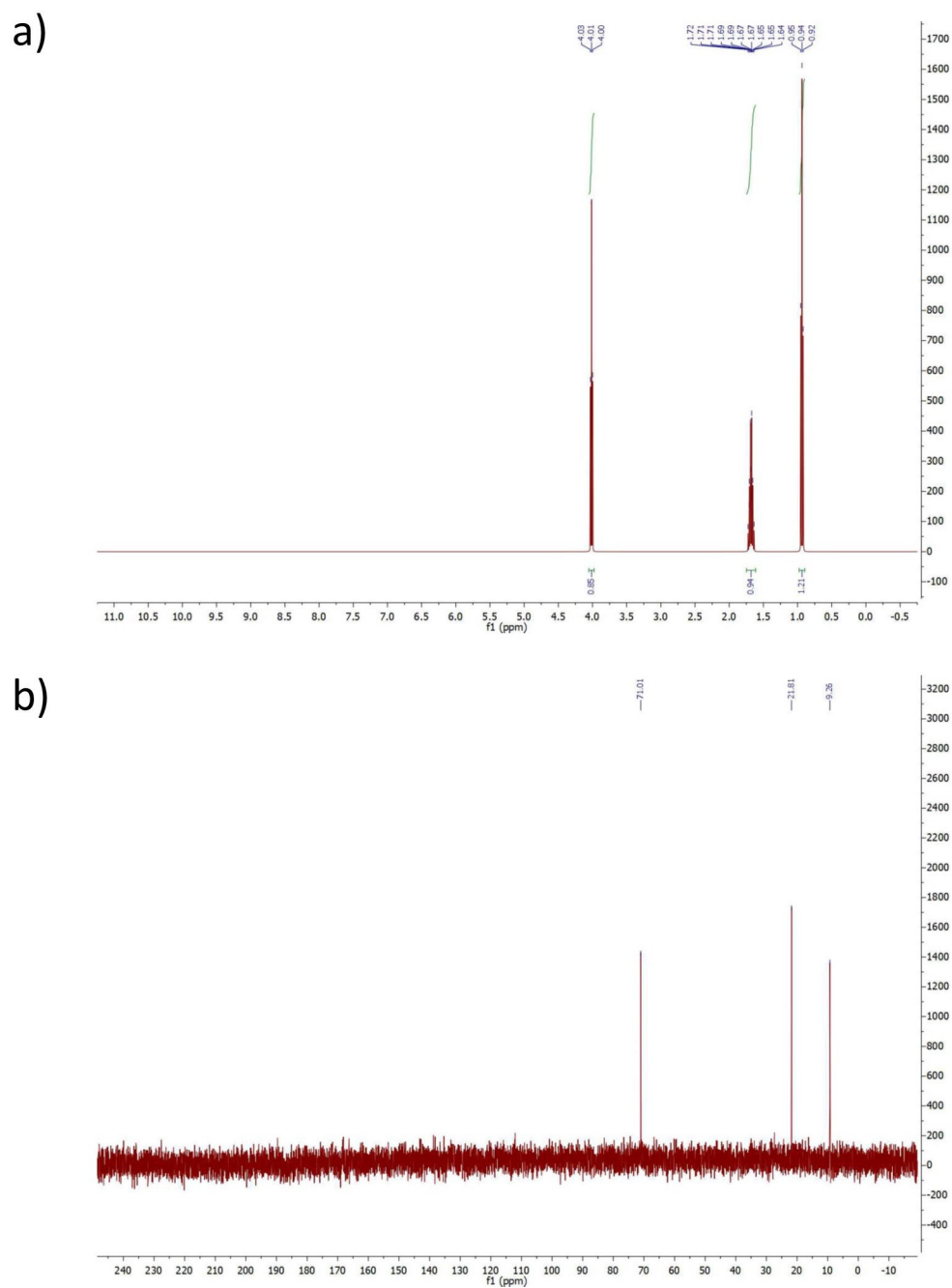


Figure B.10: 1H and b) ^{13}C NMR spectra of propyl sulfate in D_2O .

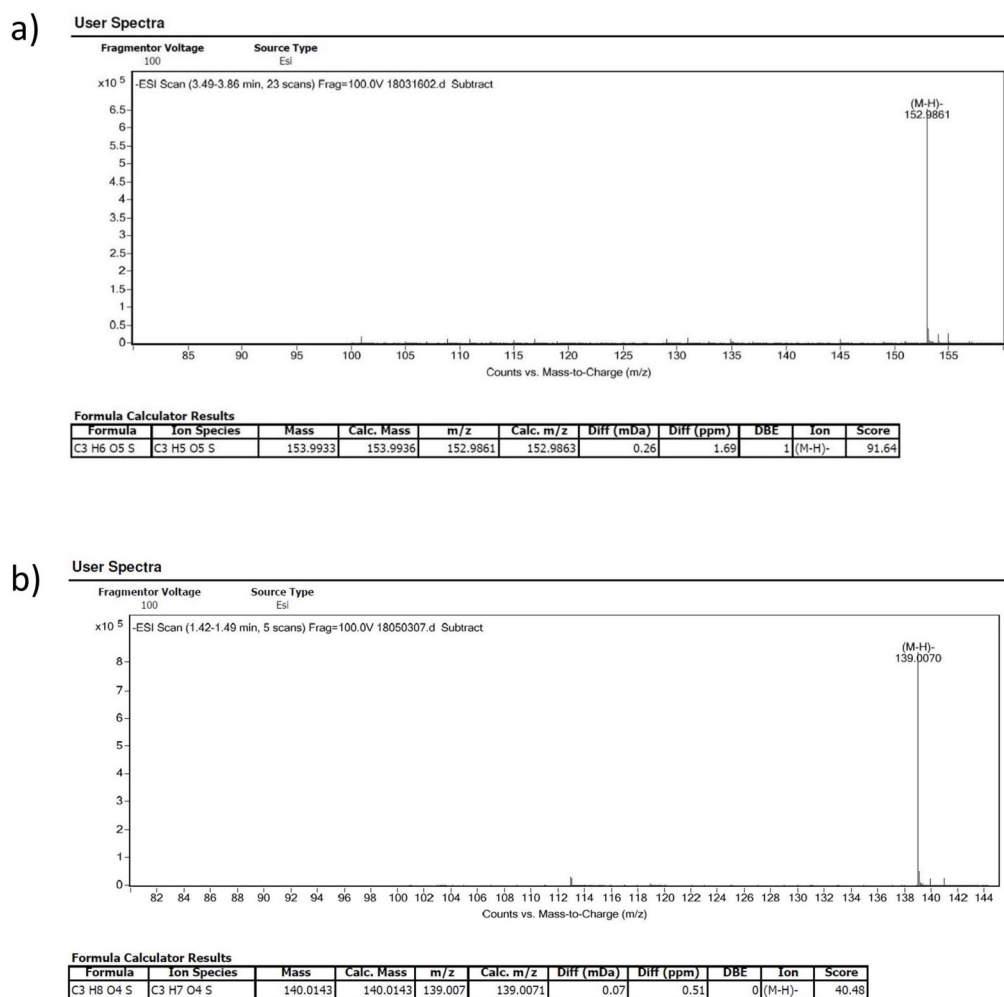


Figure B.11: High-resolution mass spectra of a) hydroxyacetone sulfate and b) propyl sulfate synthesized standards.

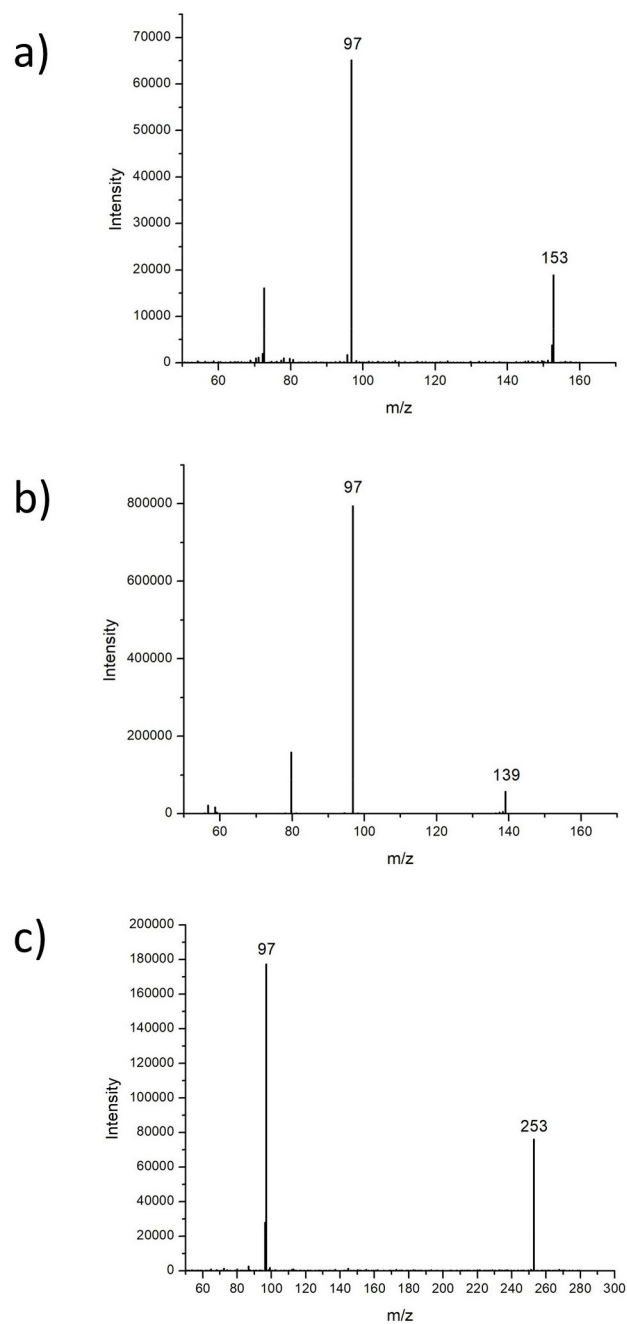


Figure B.12: Product ion scans for a) hydroxyacetone sulfate, b) propyl sulfate, and c) the m/z 253 organosulfate; all show m/z 97 (HSO_4^-).

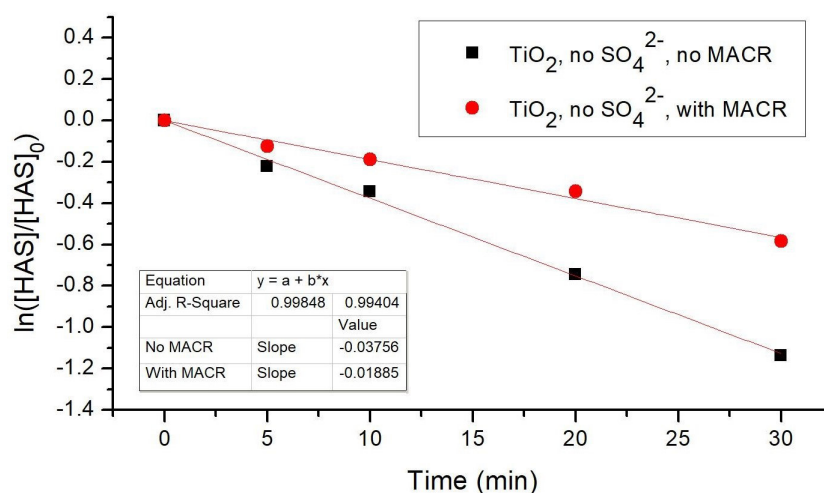


Figure B.13: TiO_2 -catalyzed (0.5 mg mL^{-1}) loss of hydroxyacetone sulfate (HAS; 7 ppm) in the presence and absence of methacrolein (10 mM) as a function of illumination time. Experiments were performed in the absence of sulfate salts. Each experiment was performed once; the solid lines are linear fits to the experimental data. No HAS loss was observed under dark conditions (*i.e.* HAS concentrations were identical after 30 min stirring; results not shown).

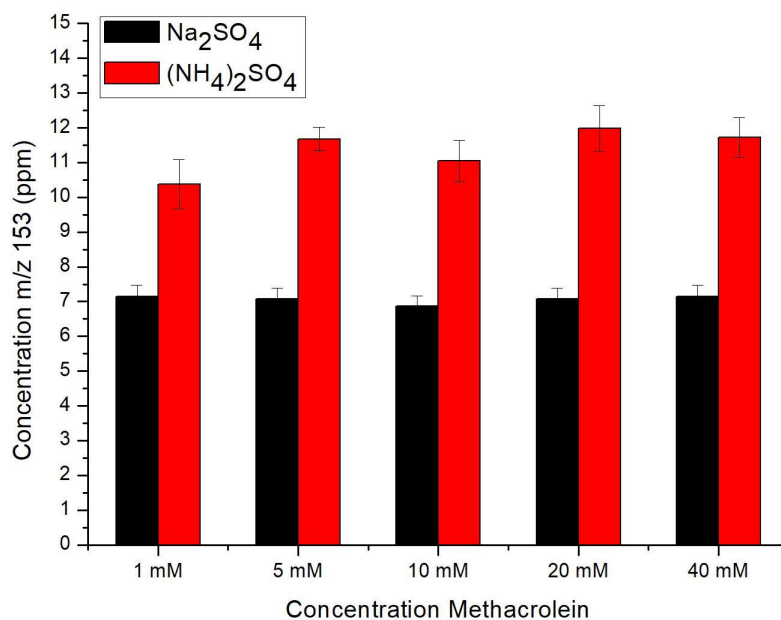


Figure B.14: Formation of hydroxyacetone sulfate (m/z 153) upon 30 min illumination in 1 M Na₂SO₄ (adjusted to pH 5 using 50 mM aqueous H₂SO₄) or 1 M (NH₄)₂SO₄ in the presence of 0.5 mg mL⁻¹ TiO₂ as a function of methacrolein concentration. Each data point represents the mean of three experimental trials, with 1- σ error bars.

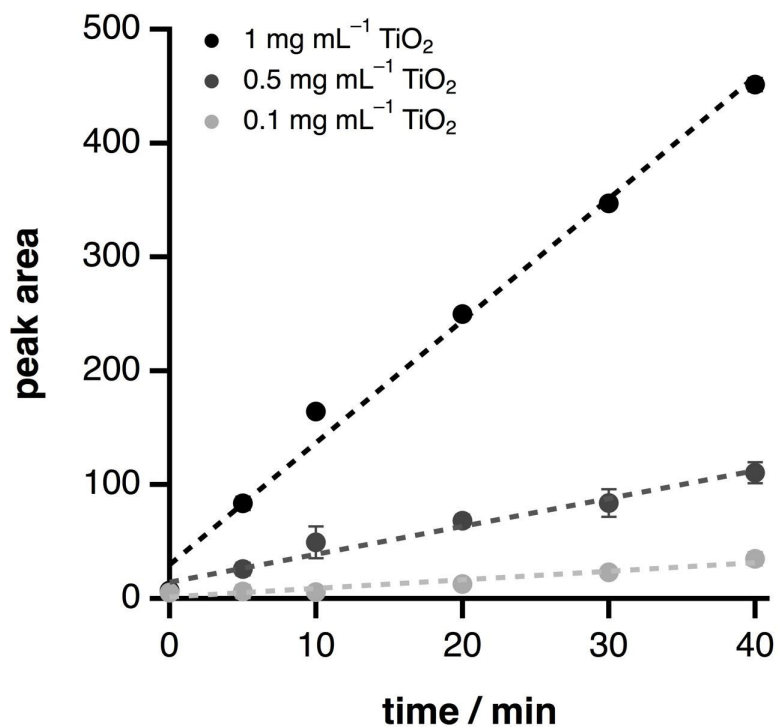


Figure B.15: Time-dependent production of a set of organosulfates with m/z 253 from methacrolein (10 mM) in illuminated suspensions of TiO₂ in aqueous Na₂SO₄ (1 M; adjusted to pH 5). In all cases, data points represent the mean of three trials, with 1- σ error bars. The dashed lines are linear fits to the experimental data.

Table B.1: Summary of mass spectrometric parameters.

Parameters	Value
ESI voltages	
Capillary	2.8 kV
Cone	25 V
Extractor	1
RF Lens	0.9
Temperatures	
Source	120 °C
Desolvation	275 °C
Gas Flow	
Desolvation (N ₂)	300 L h ⁻¹
Collision (Ar)	30 L h ⁻¹
MRM method	
Transition to product ion	[M-H] ⁻ → m/z 97
Dwell time	0.1 sec
Cone voltage	25 V
Collision energy	20 eV

Table B.2: Specific surface areas (BET; m²g⁻¹) of three of the samples employed in these experiments.

Sample	Specific surface area (BET; m² g⁻¹)
TiO ₂ (commercial)	11.22
anatase	5.172
ilmenite	2.152

Table B.3: Elemental composition of a) anatase, b) ilmenite, and c) mica samples obtained via electron microprobe analysis. The point numbers in the tables correspond to the points labelled in the back-scattered-electron images for each mineral sample provided below the tables. In all cases, results below the estimated limits of detection at 99% confidence have been set to zero.

Anatase														
point #	Nb ₂ O ₅	SiO ₂	TiO ₂	ZnO	Al ₂ O ₃	V ₂ O ₃	Cr ₂ O ₃	Fe ₂ O ₃ total	MnO	MgO	CaO	Na ₂ O	K ₂ O	Total
193	0.09	0.00	99.63	0.00	0.00	0.03	0.00	0.03	0.00	0.00	0.00	0.00	0.00	99.78
194	0.07	0.00	100.12	0.00	0.00	0.08	0.00	0.00	0.00	0.00	0.00	0.00	0.00	100.27
195	0.08	0.00	99.19	0.00	0.00	0.10	0.00	0.09	0.00	0.00	0.00	0.00	0.00	99.46
196	0.07	0.00	99.70	0.00	0.00	0.00	0.00	0.00	0.00	0.00	0.00	0.00	0.00	99.77
197	0.12	0.02	99.51	0.00	0.00	0.04	0.00	0.03	0.00	0.00	0.00	0.00	0.00	99.72
198	0.00	0.00	99.30	0.00	0.02	0.06	0.00	0.03	0.00	0.00	0.00	0.00	0.00	99.41
199	0.00	0.00	99.14	0.00	0.00	0.11	0.00	0.03	0.00	0.00	0.01	0.00	0.00	99.29
200	0.10	0.00	99.14	0.00	0.00	0.10	0.00	0.05	0.00	0.00	0.00	0.00	0.00	99.39
Average	0.07	0.00	99.47	0.00	0.00	0.07	0.00	0.03	0.00	0.00	0.00	0.00	0.00	99.64
Std Dev	0.04	0.01	0.34	0.00	0.01	0.04	0.00	0.03	0.00	0.00	0.00	0.00	0.00	0.32
Min	0.00	0.00	99.14	0.00	0.00	0.00	0.00	0.00	0.00	0.00	0.00	0.00	0.00	99.29
Max	0.12	0.02	100.12	0.00	0.02	0.11	0.00	0.09	0.00	0.00	0.01	0.00	0.00	100.27

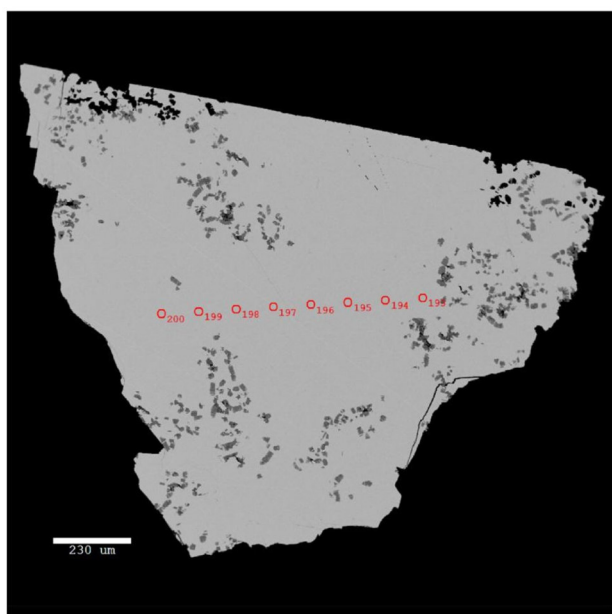


Table B.3: Elemental composition of a) anatase, b) ilmenite, and c) mica samples obtained via electron microprobe analysis. The point numbers in the tables correspond to the points labelled in the back-scattered-electron images for each mineral sample provided below the tables. In all cases, results below the estimated limits of detection at 99% confidence have been set to zero.

Ilmenite	FeTiO ₃														
point #	Nb ₂ O ₅	SiO ₂	TiO ₂	ZnO	Al ₂ O ₃	V ₂ O ₅	Cr ₂ O ₃	FeO _{total}	MnO	MgO	CaO	Na ₂ O	K ₂ O	Total	
209	0.00	0.02	50.01	0.04	0.00	0.00	0.00	46.09	0.66	0.00	0.00	0.00	0.00	96.82	
210	0.00	0.00	50.73	0.00	0.00	0.00	0.00	46.03	0.71	0.00	0.00	0.00	0.00	97.47	
211	0.00	0.00	50.94	0.04	0.00	0.00	0.00	45.86	0.69	0.00	0.00	0.00	0.00	97.53	
212	0.00	0.01	50.10	0.03	0.00	0.00	0.00	46.43	0.69	0.00	0.00	0.00	0.00	97.26	
214	0.47	0.00	51.44	0.00	0.00	0.00	0.00	44.53	0.71	0.00	0.00	0.00	0.00	97.15	
215	0.00	0.00	50.49	0.03	0.00	0.00	0.00	45.87	0.71	0.00	0.00	0.00	0.00	97.10	
216	4.48	0.00	53.50	0.00	0.02	0.06	0.00	38.96	0.60	0.03	0.00	0.00	0.00	97.65	
Average	0.71	0.00	51.03	0.02	0.00	0.01	0.00	44.82	0.68	0.00	0.00	0.00	0.00	97.27	
Std Dev	1.67	0.01	1.19	0.02	0.01	0.02	0.00	2.65	0.04	0.01	0.00	0.00	0.00	0.29	
Min	0.00	0.00	50.01	0.00	0.00	0.00	0.00	38.96	0.60	0.00	0.00	0.00	0.00	96.82	
Max	4.48	0.02	53.50	0.04	0.02	0.06	0.00	46.43	0.71	0.03	0.00	0.00	0.00	97.65	
<i>Impurity in sample, not used in average</i>															
213	0.00	3.47	14.82	0.00	1.53	0.04	0.00	66.95	0.39	0.14	0.00	0.00	0.00	87.34	

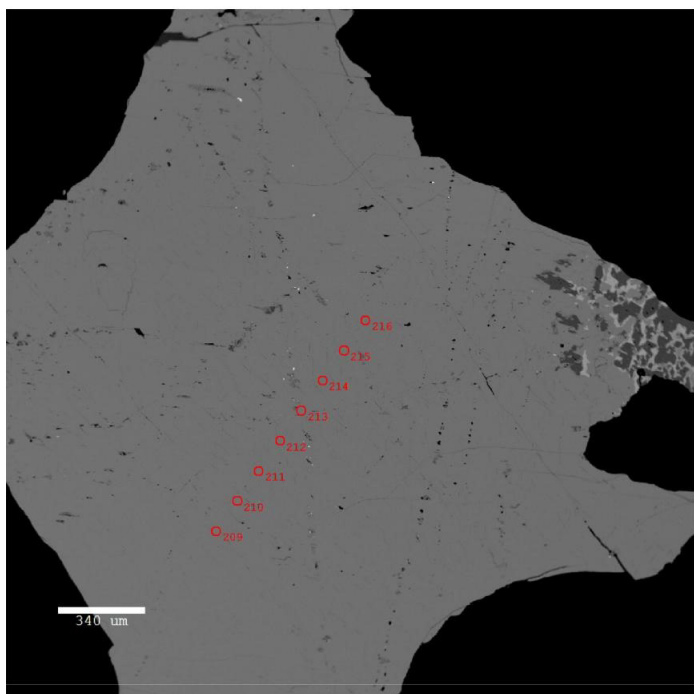
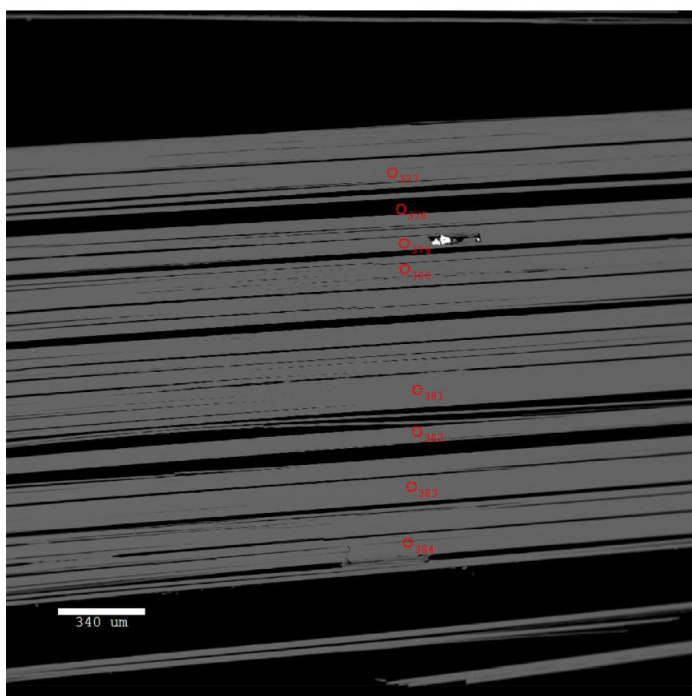


Table B.3: Elemental composition of a) anatase, b) ilmenite, and c) mica samples obtained via electron microprobe analysis. The point numbers in the tables correspond to the points labelled in the back-scattered-electron images for each mineral sample provided below the tables. In all cases, results below the estimated limits of detection at 99% confidence have been set to zero.

Mica	$(K_{0.95}Na_{0.04})_{\Sigma 0.99}(Mg_{2.39}Fe_{0.41}Ti_{0.06}Al_{0.03}Mn_{0.01})_{\Sigma 2.90}(Si_{3.08}Al_{0.92})_{\Sigma 4}O_{16}(OH)_2$													
point #	Nb ₂ O ₅	SiO ₂	TiO ₂	ZnO	Al ₂ O ₃	V ₂ O ₃	Cr ₂ O ₃	FeO _{total}	MnO	MgO	CaO	Na ₂ O	K ₂ O	Total
377	0.00	42.82	0.92	0.08	11.08	0.00	0.00	6.66	0.13	22.43	0.00	0.43	10.07	94.62
379	0.00	42.80	0.98	0.08	11.02	0.00	0.00	6.60	0.13	22.23	0.00	0.18	10.51	94.53
380	0.00	42.85	1.05	0.07	11.20	0.00	0.00	6.80	0.13	22.05	0.00	0.25	10.31	94.71
381	0.00	42.53	1.02	0.09	11.19	0.00	0.00	6.79	0.12	22.26	0.00	0.34	10.17	94.51
382	0.00	42.83	1.04	0.07	11.10	0.00	0.00	6.68	0.12	22.13	0.00	0.25	10.39	94.61
383	0.00	42.68	1.05	0.08	10.95	0.00	0.00	6.79	0.12	22.05	0.00	0.33	10.25	94.30
384	0.00	42.23	1.07	0.06	11.17	0.00	0.00	6.88	0.14	22.15	0.00	0.36	10.17	94.23
Average	0.00	42.68	1.02	0.08	11.10	0.00	0.00	6.74	0.13	22.19	0.00	0.31	10.27	94.52
Std Dev	0.00	0.23	0.05	0.01	0.09	0.00	0.00	0.10	0.01	0.13	0.00	0.08	0.15	0.18
Min	0.00	42.23	0.92	0.06	10.95	0.00	0.00	6.60	0.12	22.05	0.00	0.18	10.07	94.23
Max	0.00	42.85	1.07	0.09	11.20	0.00	0.00	6.88	0.14	22.43	0.00	0.43	10.51	94.71



Appendix C

TD-GC-FID/MS system

C.1 Instrument Operation

There are several basic steps that need to be followed before any thermal desorption experiment can be started involving either the smog chamber or the calibration generation. Initially, all instruments are at least in standby mode or are turned off, especially emphasizing a turned off Korad DC power supply to ensure a safe instrumental setup. Additionally, under no circumstances, the mass spectrometer should be turned off without the application of a proper software-initiated shutdown process. The GC-FID/MS can be set into the operational mode by turning on all necessary flow rates or terminating gas saving modes for all gas supplies of the gas chromatograph and the flame ionization detector, which include zero air, helium, nitrogen and hydrogen using the corresponding software (Chromeleon). The availability of continuous gas supplies by opening any 2-stage valves of gas cylinders or by turning on the zero air generator is expected at this point. The FID flame can be ignited when all gases are properly supplied. To check the function of the mass spectrometer, it is recommended to first perform an air and water tune to check for any leaks followed by an EI smart tune. After the successful completion of these tasks, only the GC-FID/MS as an instrumental unit can be considered as being ready for measurements. The 10-port valve then needs to be set to valve position A to create a closed cycle of helium flowing into the trap towards the GC inlet. At the same time, the sampling line and valve tube heating can be turned on. After that, the ATX power supply can be turned on to start Peltier cooling to a set temperature value at the Peltier controller. Furthermore, both Arduino UNO R3 units for measuring the trap temperature and controlling the relay-mediated heating are turned on by plugging in both USB cables into the corresponding USB hub. As soon as the trap relay receives a signal

for the valve position A, it will turn on the high current trap heating. After carefully checking all electrical connections that are established between the Korad DC power supply and the alligator clips connected to the NiCr wire wrapped around the trap tube, the Korad DC power supply can be manually turned on to heat and bake out the sorbent inside the trap tube for 5 minutes under instrumental default He carrier gas conditions. Afterward, the Korad DC power supply needs to be turned off for the benefit of a safe workspace until remaining instruments are prepared for starting experiments. Moreover, valve position A is maintained to keep the sorbent bed clean during the trap tube cool down by flushing He through the trap tube. The GC-FID/MS and the thermal desorption trap are prepared for experiments at this point. However, either the calibration gas generator or the smog chamber needs to be activated. The calibration gas generator demands an air supply, which is already given by the zero air generator turned on for the FID. The installation of the permeation tube is expected at this point and the device is set to the so-called zero mode to flush clean air through the sampling line. The necessary flow rate for the final span gas mode is then set up during a maintained zero mode by changing the shown flow rate to a required (span flow) value less a flow rate of 0.1 L min^{-1} . The generation gas generator is kept in zero mode for following blank measurements using the thermal desorption unit. The GC-FID/MS, thermal desorption unit and the calibration gas generator are prepared for experiments at this point. The sampling pump can be turned on now to draw clean zero air through the sampling lines towards the vent by-passing the trap tube still using position A of the 10-port valve. Eventually, the metering valve-controlled pump flow rate needs to be checked or adjusted. Since flow rates for trap tube sampling are limited by the flow resistance of the packed tube to 22 mL min^{-1} , the sampling flow through the trap tube can be operated at maximum flow rates without any valve adjustment. The flow rate for sampling line flushing via an integrated jumper during thermal desorption processes needs to be limited by the metering valve (*e.g.* 200 mL min^{-1}) using the bubble flow meter by directing the flow output of the micropump towards the bubble flow meter input. Afterward, the micropump output is relocated to the general vent to avoid VOC exposure, when gas-phase samples are taken. At this point the 10-port valve is still set to A (inject), the Korad power supply is still turned off and all remaining instrumental parts are ready for experiments. After setting up a sequence list in Chromeleon for the following experiments, the 10-port valve can be changed to

position B, which draws zero air from the zero air generator in zero mode through the trap tube and the Korad DC power supply can be turned on. Time needs to be monitored as soon as position B is chosen to generate a blank measurement that is equal in sampling time according to the following sequence-controlled samples. If for example 5 minutes of sampling time is set in the GC method, the start button for beginning the Chromeleon sequence needs to be pushed after 4 minutes and 48 seconds of sampling to initiate the injection and hence the following automated sampling and desorption process. The Chromeleon chromatography software will then change the 10-port valve to position A and starts the first GC-FID/MS run. Since position A initiates the trap tube heating, a high current is flushed through the alligator clip electrodes and the trap tube NiCr wire. After the separation step/compound analysis has been finished, the 10-port valve position will be automatically changed to position B for sampling for the specific set time in the GC method. Trap tube heating will be automatically turned off during this time. Consequently, the GC method contains the separation and compound analysis via thermal desorption (first step) and the sampling process (second step) afterward.

C.2 Supplementary figures and schemes

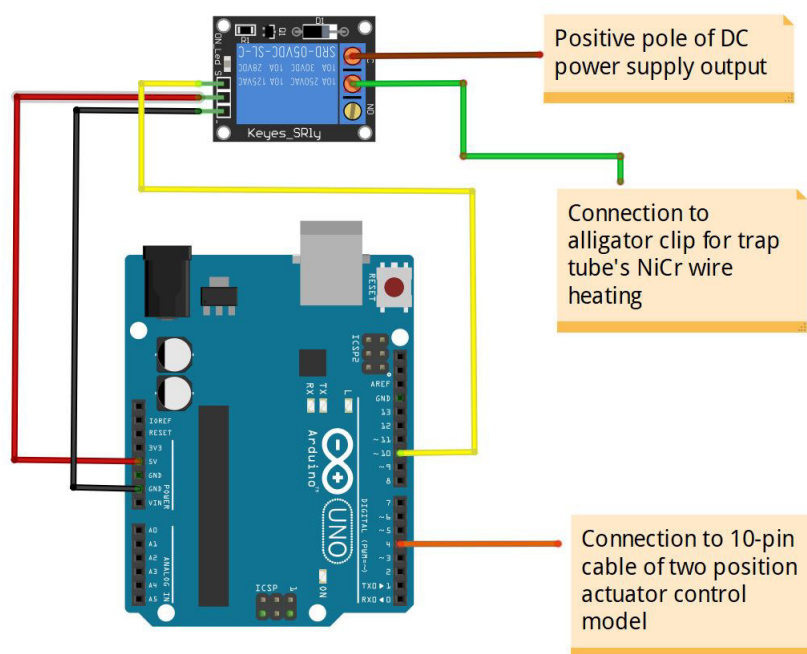


Figure C.1: Illustrated description of the Arduino UNO R3 board wiring to establish a relay-controlled heating mechanism depending on an incoming signal from the 10-port valve.

```
int ValvePin = 4; // Pin of 10 port valve

int relayPin = 10; // Pin of Relay Module

void setup() {

  Serial.begin(9600);

  pinMode(relayPin, OUTPUT); // Set Pin connected to Relay as an OUTPUT

  digitalWrite(relayPin, LOW); // Set Pin to LOW to turn Relay OFF

}

void loop() {

  while (digitalRead(ValvePin) == HIGH) { // If 10-port valve is set to position A

    delay(10000); // Wait 10000 ms until relay turned on

    digitalWrite(relayPin, HIGH); // Turn Relay ON

    Serial.println("Relay is ON");

    delay(500);

  }

  digitalWrite(relayPin, LOW); // Turn Relay OFF

  Serial.println("Relay is OFF");

  delay(500);

}
```

Figure C.2: Arduino sketch (code) for the relay-controlled heating mechanism presented in Figure C.1

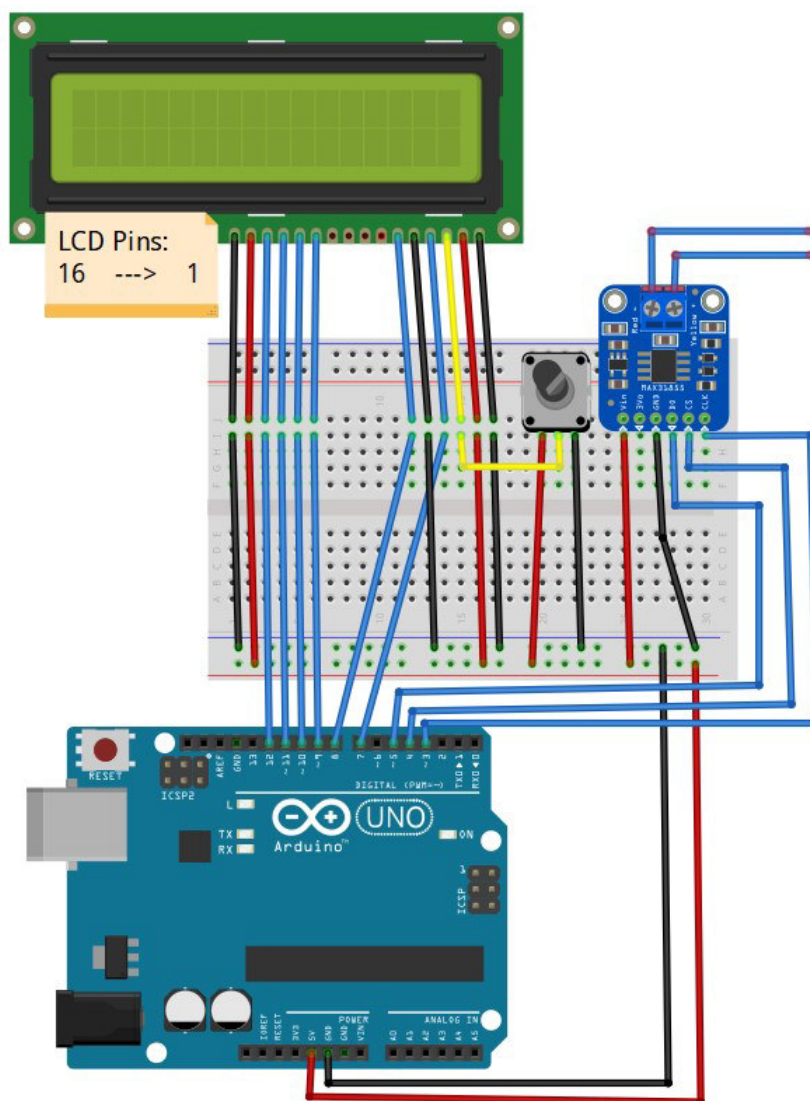


Figure C.3: Illustrated description of the Arduino UNO R3 board wiring to establish a trap tube temperature measurement indicated on an LCD display and monitored using a PLX-DAQ addon for Microsoft Excel; further including a potentiometer and a MAX31855 thermocouple amplifier.

```
#include <SPI.h>
#include <Wire.h>
#include "Adafruit_MAX31855.h"
#include <LiquidCrystal.h>
#define MAXDO 5
#define MAXCS 4
#define MAXCLK 3
Adafruit_MAX31855 thermocouple(MAXCLK, MAXCS, MAXDO);
LiquidCrystal lcd(7, 8, 9, 10, 11, 12);
#if defined(ARDUINO_ARCH_SAMD)
#define Serial SerialUSB
#endif
void setup() {
  Serial.begin(9600);
  Serial.println("CLEARDATA");
  Serial.println("LABEL,Date,Time,Timer,millis, TempC");
  lcd.begin(16, 2);
  lcd.clear();
  lcd.print("MAX31855 test");
  delay(500);}
void loop() {
  Serial.println( (String) "DATA,DATE,TIME,TIMER," + millis() + "," + thermocouple.readCelsius());
  lcd.clear();
  lcd.setCursor(0, 0);
  lcd.print("Int. Temp = ");
  lcd.println(thermocouple.readInternal());
  Serial.print("Int. Temp = ");
  Serial.println(thermocouple.readInternal());
  double c = thermocouple.readCelsius();
  lcd.setCursor(0, 1);
  if (isnan(c))
  {lcd.print("T/C Problem"); }
  else
  {lcd.print("C = ");
  lcd.print(c);
  lcd.print(" ");
  Serial.print("Thermocouple Temp = ");
  Serial.println(c);}
  delay(1000);
}
```

Figure C.4: Arduino sketch (code) for the temperature acquisition procedure presented in Figure C.3.

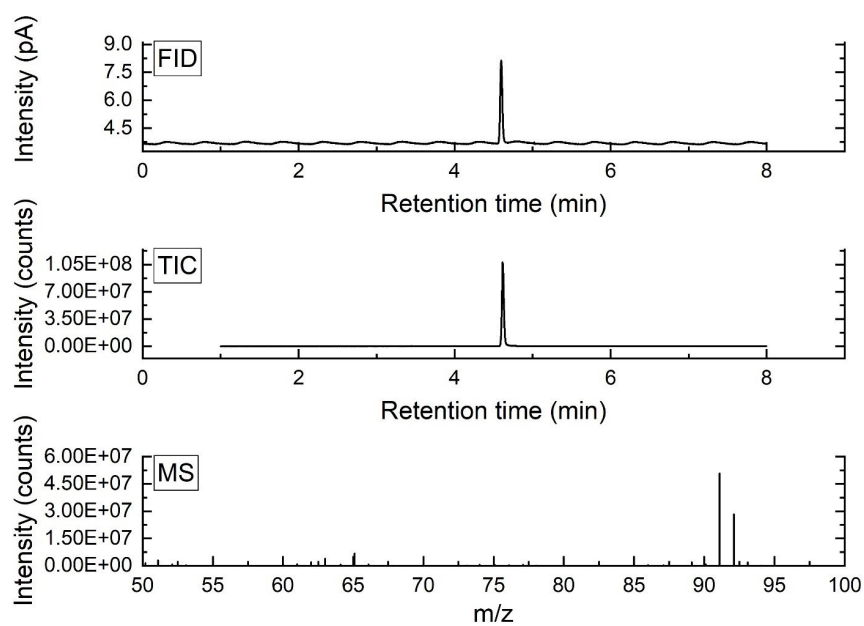


Figure C.5: Exemplary FID chromatogram and total ion current for the injection of a preconcentrated toluene sample using a gas-phase concentration of 1 ppm toluene with a corresponding EI mass spectrum showing a base peak at m/z 92.

Table C.1: Overview of the parameters for generating toluene gas-phase concentrations between 0.2 ppm and 1.0 ppm using a fixed permeation oven temperature of 80°C. The constant K is defined as molar constant to convert permeation rates at standard temperature and pressure (STP) conditions into ambient conditions and is calculated by the division of the molar volume (22.4 L mol⁻¹) over the molecular weight of the chemical compound. The span flow rate is defined as the product of the emissions rate and the molar constant over the product of the desired concentration in ppm and the numerical value of 1000 to finally achieve a concentration in ppm.

Compound	Toluene	Toluene	Toluene	Toluene	Toluene
Concentration [ppm]	0.2	0.4	0.6	0.8	1.0
Molecular mass [g/mol]	92.14	92.14	92.14	92.14	92.14
K _o	0.243108313	0.24310831	0.24310831	0.24310831	0.24310831
Temperature [°C]	80	80	80	80	80
Emission rate [ng/min]	2263	2263	2263	2263	2263
Span flow [L/min]	2.750770567	1.37538528	0.91692352	0.68769264	0.55015411

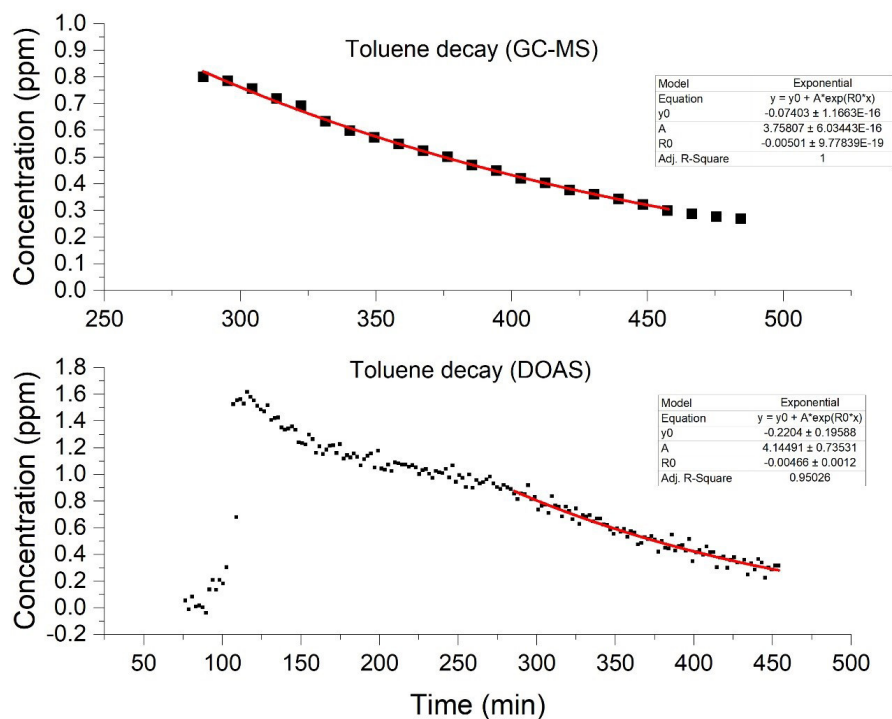


Figure C.6: Exponentially fitted graphs for the decay of toluene in the atmospheric reaction chamber monitoring with DOAS and TD-GC-FID/MS between 286.39 min and 484.35 min of total chamber experiment run time including the generation of DOAS background reference spectra over 76 min.

Appendix D

Conclusions and future directions

D.1 Supplementary figures

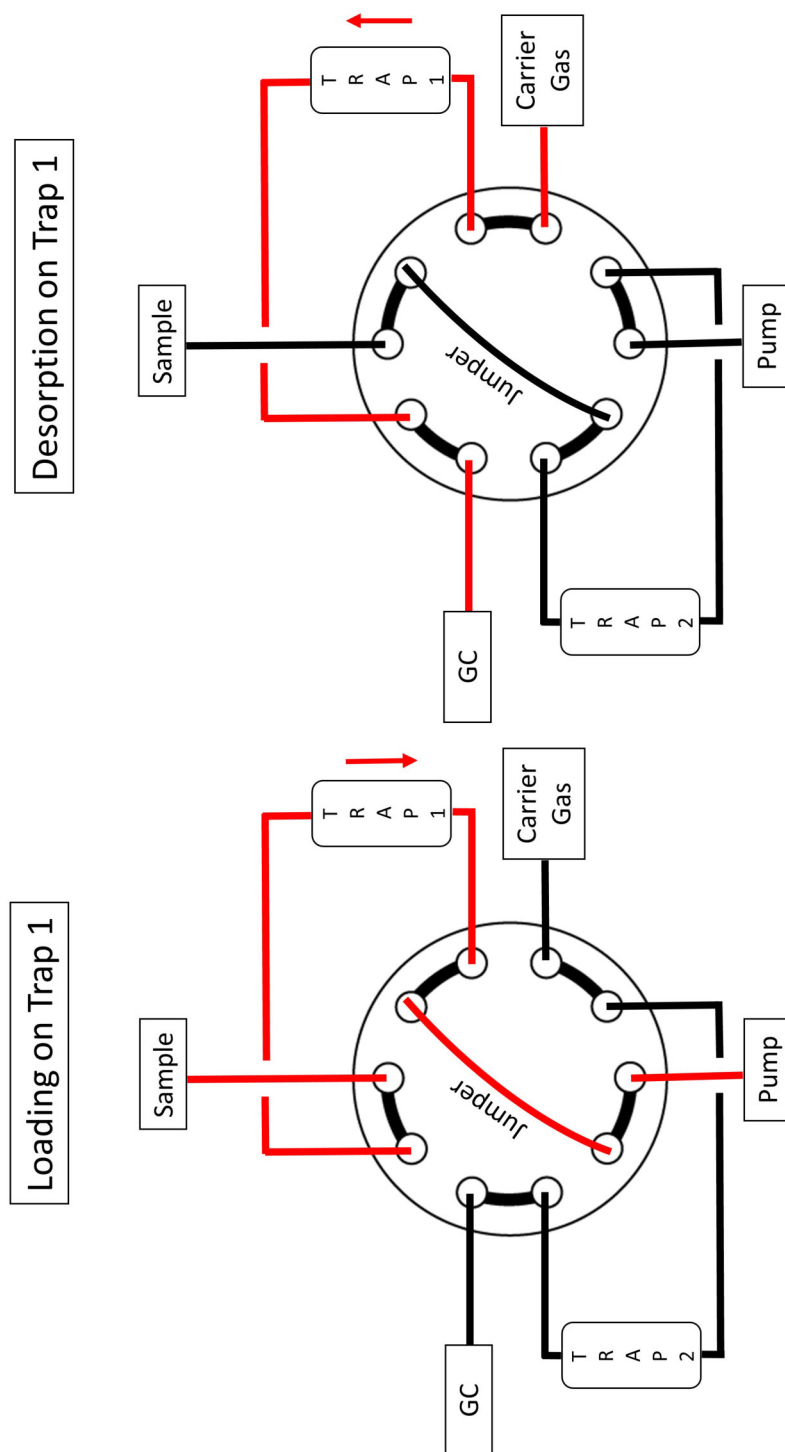


Figure D.1: Possible design for a simultaneous TD trap loading and desorption process to increase the time resolution.

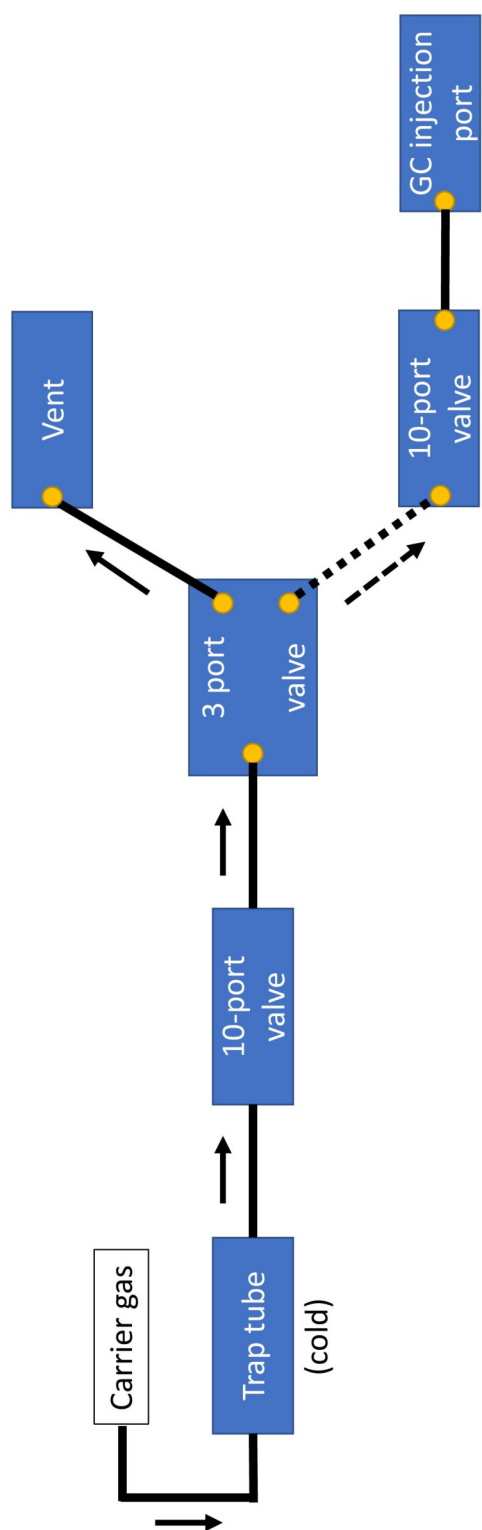


Figure D.2: Optional addition of a dry purge valve to remove trapped water vapor.

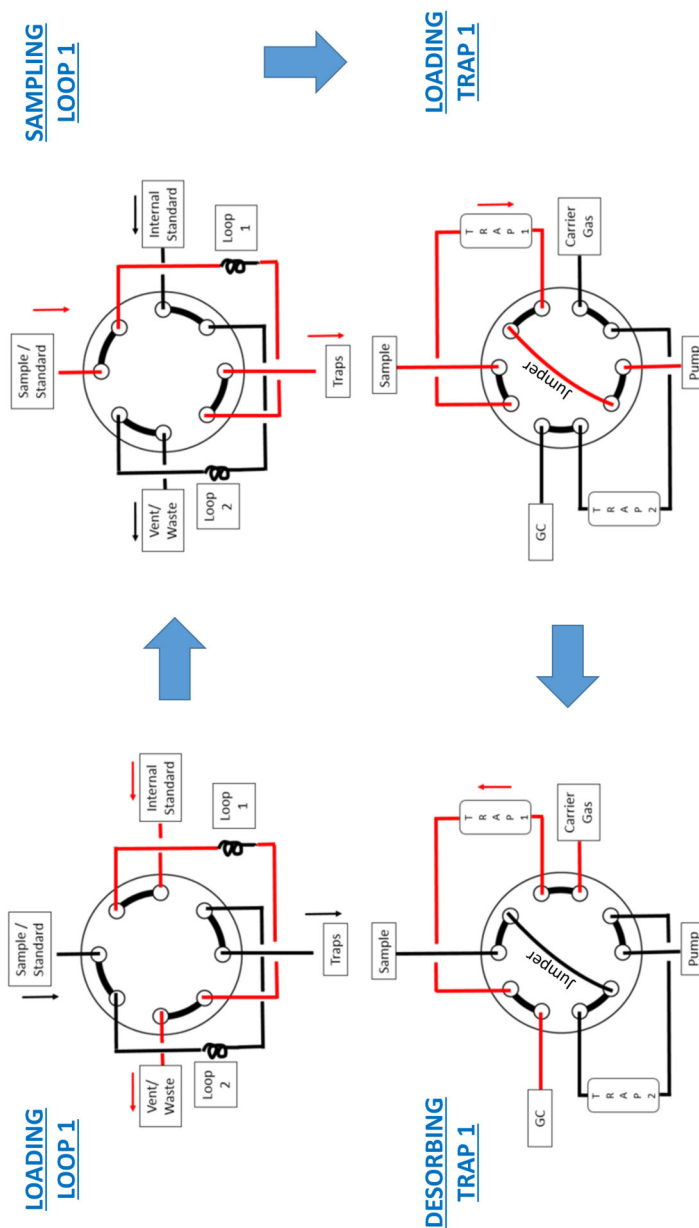


Figure D.3: Schematic description of the introduction of an 8-port valve for loop-mediated internal standard injection connected to the established 10-port valve. A double trap, double loop system is shown. Each loop is filled with a specific amount of an internal standard gas mixture. After switching the 8-port valve position to sampling mode, the internal standard (filled loop) and the actual sample from the smog chamber are drawn towards the 10-port trap valve and through the sorbent filled trap for trap loading. Simultaneously, the second loop is filled with the internal standard gas mixture to load the second trap sorbent filled trap tube after the desorption is finished.